

**Measurement of the Time Reversal  
Asymmetry for the Decay  $\bar{B}^0 \rightarrow \Lambda \bar{p} \pi^+$   
and Observation of the Decay  
 $\bar{B}_s^0 \rightarrow \Lambda \bar{p} K^+$  with the LHCb  
Experiment**

Dissertation

zur  
Erlangung des akademischen Grades  
Doctor rerum naturalium (Dr. rer. nat.)  
der Mathematisch-Naturwissenschaftlichen Fakultät  
der Universität Rostock

vorgelegt von Christian Voß, geb. am 17. Mai 1985 in Rostock



**Gutachter:**

1. Gutachter  
Priv.-Doz. Dr. Roland Waldi  
Institut für Physik, Universität Rostock
2. Gutachter  
Prof. Dr. Michael Schmelling  
Max-Planck-Institut für Kernphysik, Heidelberg

**Datum der Einreichung:** 18.Mai 2016

**Datum der Verteidigung:** 23.September 2016

## Abstract

This Analysis presents the measurement of the time reversal asymmetry in the decay  $\bar{B}^0 \rightarrow \Lambda \bar{p} \pi^+$  based on a triple product given by

$$\mathcal{O} = \mathbf{s}_\Lambda \cdot (\mathbf{p}_\Lambda \times \mathbf{p}_{\pi^+}) \quad ,$$

where  $\mathbf{s}_\Lambda$  is the  $\Lambda$  spin vector,  $\mathbf{p}_\Lambda$  and  $\mathbf{p}_{\pi^+}$  are the momentum vectors of the  $\Lambda$  and  $\pi^+$ , respectively. The triple product is evaluated in the  $\bar{B}^0$  rest frame. The Time reversal asymmetry is determined to be

$$\mathcal{A}_T = (7.6 \pm 27.0 \text{ (stat)} \pm 1.1 \text{ (syst)})\% \quad .$$

Allowing for CP violation in the  $\Lambda$  decay, the asymmetry is determined to be

$$\mathcal{A}_T^{\text{CPV}} = (4.3_{-22.0}^{+22.1} \text{ (stat)} \pm 1.2 \text{ (syst)})\% \quad .$$

Both are in agreement with the theoretical predictions [1, 2] but also with  $\mathcal{A}_T = 0$ .

The decays  $\bar{B}_s^0 \rightarrow \Lambda \bar{p} K^+$  and  $\bar{B}_s^0 \rightarrow \bar{\Lambda} p K^-$  are observed for the first time and their combined statistical significance corresponds to 17.2 Gaussian standard deviations. The branching fraction for the sum of  $\bar{B}_s^0 \rightarrow \Lambda \bar{p} K^+$  and  $\bar{B}_s^0 \rightarrow \bar{\Lambda} p K^-$  is measured to be

$$\mathcal{B}(\bar{B}_s^0 \rightarrow \Lambda \bar{p} K^+) + \mathcal{B}(\bar{B}_s^0 \rightarrow \bar{\Lambda} p K^-) = \left[ 4.75_{-0.49}^{+0.53} \text{ (stat)} \pm 0.20 \text{ (syst)} \pm 0.28(f_s/f_d) \pm 0.44(\mathcal{B}) \right] \times 10^{-6} \quad .$$

For each result the first uncertainty is statistical and the second systematic, further additional external uncertainties are labelled accordingly. In addition to these results, the Dalitz plot for  $\bar{B}^0 \rightarrow \Lambda \bar{p} \pi^+$  and  $\bar{B}_s^0 \rightarrow \Lambda \bar{p} K^+$  has been studied and shows the familiar behaviour with a pronounced enhancement at the threshold of the invariant baryon antibaryon mass.

Finally, the angular distribution for the proton from the  $B^0$  and  $\Lambda$  decays have been studied. For the  $\bar{B}^0 \rightarrow \Lambda \bar{p} \pi^+$  the first shows a large asymmetry not expected from naive meson pole models. The angular distribution for the  $\bar{B}_s^0 \rightarrow \Lambda \bar{p} K^+$  and  $\bar{B}_s^0 \rightarrow \bar{\Lambda} p K^-$  exhibit no significant asymmetry. The angular distribution of the proton from the  $\Lambda$  decay allows to determine the  $\Lambda$  polarisation in these decays and its dependence on the  $\Lambda$  energy in the  $\bar{B}^0$  rest frame was investigated. No significant polarisation was found for either decay mode.

## Kurzfassung

In der vorliegenden Arbeit wird die Messung der Verletzung der Zeitspiegel-Symmetrie im Zerfall  $\bar{B}^0 \rightarrow \Lambda \bar{p} \pi^+$  präsentiert. Diese wurde mit Hilfe des folgenden Spatproduktes bestimmt,

$$\mathcal{O} = \mathbf{s}_\Lambda \cdot (\mathbf{p}_\Lambda \times \mathbf{p}_{\pi^+}) \quad ,$$

wobei  $\mathbf{s}_\Lambda$  den  $\Lambda$  Spinvektor und  $\mathbf{p}_\Lambda$  sowie  $\mathbf{p}_{\pi^+}$  die Impulsvektoren des  $\Lambda$  and des Pions darstellen. Die Zeitspiegel-Symmetrie wurde bestimmt zu

$$\mathcal{A}_T = (7.6 \pm 27.0 \text{ (stat)} \pm 1.1 \text{ (syst)})\% \quad .$$

Unter Vernachlässigung der CP-Erhaltung im  $\Lambda$ -Zerfall wird die Asymmetrie bestimmt zu

$$\mathcal{A}_T^{\text{CPV}} = (4.3_{-22.0}^{+22.1} \text{ (stat)} \pm 1.2 \text{ (syst)})\% \quad .$$

Die Ergebnisse stimmen im Rahmen der Unsicherheiten sowohl mit der theoretischen Erwartung als auch der Hypothese einer verschwindenden Asymmetrie überein.

Desweiteren wurden die baryonischen  $\bar{B}_s^0$ -Zerfälle  $\bar{B}_s^0 \rightarrow \Lambda \bar{p} K^+$  und  $\bar{B}_s^0 \rightarrow \bar{\Lambda} p K^-$  zum ersten Mal beobachtet und deren Summenverzweigungsverhältnis bestimmt zu

$$\mathcal{B}(\bar{B}_s^0 \rightarrow \Lambda \bar{p} K^+) + \mathcal{B}(\bar{B}_s^0 \rightarrow \bar{\Lambda} p K^-) = \left[ 4.75_{-0.49}^{+0.53} (\text{stat}) \pm 0.20 (\text{syst}) \pm 0.28 (f_s/f_d) \pm 0.44 (\mathcal{B}) \right] \times 10^{-6} \quad .$$

Dabei stellt die erste Unsicherheit die statistische Unsicherheit, die zweite die systematische Unsicherheit und die verbleibenden Unsicherheiten die externen systematischen Unsicherheiten dar. Zusätzlich wurden die Dalitz-Verteilungen der untersuchten Zerfälle studiert. Sie zeigen eine ausgeprägte Anhäufung nahe der  $m(\Lambda \bar{p})$ -Schwelle.

Zum Abschluss wurden die Winkelverteilungen für die Protonen aus den  $\bar{B}_{(s)}^0$  Zerfällen und den  $\Lambda$ -Zerfällen bestimmt. Die Winkelverteilung der Protonen aus dem  $\bar{B}^0 \rightarrow \Lambda \bar{p} \pi^+$ -Zerfall zeigt eine starke, unerwartete Asymmetrie, wohingegen die Winkelverteilung für  $\bar{B}_s^0 \rightarrow \Lambda \bar{p} K^+$  mit der Erwartung aus Mesonpol-Modellen übereinstimmt. Die Winkelverteilung der Protonen aus den  $\Lambda$ -Zerfällen erlaubt es, die Polarisierung der  $\Lambda$ -Hyperonen zu bestimmen. Keine signifikante Polarisierung konnte gemessen werden.





# Preface

Over the course of history the role of time in physics has changed. In Newtonian physics time was an external parameter upon which the kinematic functions such as the momentum  $p$  depended. In the classical electrodynamics the equations of motion for electromagnetic waves contain partial derivatives in both time and space. Time governed the evolution of any physical system and allowed setting references to before and after, similar to the understanding of the common man. In classical mechanics time was not only an external parameter but it had no direction. Changing the direction of time does not impede a game of snooker, the equations of motion for two rolling balls do not change when time is moving backwards. This is in stark contrast to the experience of the common man, to him time is only moving forward, people grow older rather than younger. Time seems to have a fixed direction. This contradiction is now understood within the scope of Statistical Physics and its influence on Thermodynamics. The concept of entropy gave time its direction. Behind the scenes, however, nothing changed. The ideal gas model is still applicable to a lot of problems using nothing more than elastic collisions of point like particles moving randomly through a volume, thus it is basically a random game of snooker using very small balls and a three dimensional snooker table. It should be noted that, once the players start to pot the balls, this analogy breaks down.

The 20th century saw two major revolutions in physics, some of them changed how we perceive time itself. The first major change came with the Theory of Relativity. Time is no longer separated from space but both are part of a four dimensional space time and the flow of time depends upon the relative motion between two objects and on the distribution of mass near an object. Relativistic effects allow particles with life times at the order of pico-seconds to travel macroscopic distances due to their large momenta. The particles analysed in this thesis have mean life times of nano-seconds but pass the whole LHCb detector, a distance of roughly 20 m. In addition to that, an observer at a geostationary orbit measures time differently compared to an earthbound observer. Time passes slower in the vicinity of a massive object. This behaviour is described by the laws of General Relativity.

The other revolution was the theory of quantum mechanics. Elementary particles are described within Quantum Field Theories such as Quantum Electrodynamics, complementing the classical theory of electrodynamics, or Quantum Chromodynamics, the theory describing the strong interaction between quarks. A fundamental principle of all these theories is the CPT theorem upon which Lorentz invariance is based, the principle of Special Relativity. This means that any experimental result is independent with respect to any Lorentz transformation. The CPT theorem requires the theory to be invariant with respect to the product of charge conjugation  $C$ , parity operation  $P$ , and time reversal  $T$ . The first two can be combined to describe the transformation of a particle to its antiparticle. Time reversal involves changing the sign of time thus running time backwards. As mentioned before, classical mechanics is invariant with respect to  $T$ , thus  $CP$  must be conserved as well. The discovery of  $CP$  violation in the weak interaction in 1964 [3] required  $T$  violation in order to conserve CPT. Similar to Thermodynamics time has a preferred direction in weak processes. This allows a definition of before and after depending on the asymmetry between the directions of time. Due to the CPT theorem, the asymmetry between the directions of time must have the same size as the asymmetry between particle and antiparticle.

From an experimental standpoint, measuring  $T$  violation is quite challenging. The peculiar nature of the  $T$  operator in Quantum mechanics leaves us without eigenvalues to be measured. Many  $T$  violation measurements depend on CPT conservation, thus they often measure  $CP$  violation indirectly. However, it took until 1998 before the first experimental evidence for  $T$  violation was claimed by the CPLEAR experiment [4] and took another 14 years until the *BABAR* collaboration claimed a CPT independent measurement [5]. In recent years measuring  $T$  asymmetries

based on triple products became popular. These, however, are not fully CPT independent and usually are constructed using momentum vectors and, therefore, are not exclusively sensitive to T violation but also to P violation. Theorists C.Q. Geng and Y.K. Hsiao [1, 2] proposed using the spin vectors of baryons in the construction of these triple products making them only sensitive to T violation. This thesis is based on an analysis using such a triple product and searches for T violation in the decay  $\bar{B}^0 \rightarrow \Lambda \bar{p} \pi^+$ .

# Contents

<b>1</b>	<b>Theoretical introduction</b>	<b>1</b>
1.1	Symmetries in Physics	1
1.1.1	Space-time Symmetries	2
1.1.2	Symmetries of Fields	3
1.1.3	Parity, Charge Conjugation, Time Reversal, and the CPT Theorem	3
1.2	Standard Model - an Overview	5
1.2.1	Theory of the Standard Model	5
1.2.2	Charmless Baryonic $B$ -Decays within the Standard Model	7
1.2.3	Discrete Symmetries within the Standard Model	11
1.2.4	Time Reversal Asymmetry within the Standard Model	11
1.3	Experimental Determination of the Triple Product	14
1.4	The Dalitz Plot	15
<b>2</b>	<b>The LHCb-experiment</b>	<b>17</b>
2.1	Large Hadron Collider	18
2.2	LHCb Detector	19
2.2.1	Vertex Locator – VELO	19
2.2.2	Planar Tracking Stations	20
2.2.3	Rich Imaging Cherenkov (RICH) Detectors	22
2.2.4	Calorimeters	23
2.2.5	Muon System	24
2.2.6	Dipole Magnet	24
2.3	Event Reconstruction	25
2.3.1	Track Reconstruction	25
2.3.2	Momentum and Mass Resolution	26
2.3.3	Vertex Reconstruction	26

2.4	Particle Identification . . . . .	27
2.4.1	Calorimeter and Muon System Based Particle Identification . . . . .	28
2.4.2	RICH System Based Particle Identification . . . . .	28
2.4.3	Combined Particle Identification . . . . .	28
2.5	LHCb Trigger Ensemble . . . . .	29
2.5.1	Level-0 Hardware Trigger . . . . .	30
2.5.2	High Level Trigger . . . . .	30
2.6	LHCb Software Environment . . . . .	31
2.7	LHCb Recorded and Simulated Data . . . . .	31
2.7.1	Differences between Recorded Data and Simulated Data . . . . .	33
2.7.2	Available Simulated Data Sets and Their Relative Normalisation . . . . .	33
<b>3</b>	<b>Analysis of <math>\bar{B}^0_{(s)} \rightarrow A\bar{p}h^+</math></b>	<b>35</b>
3.1	Event Selection . . . . .	36
3.1.1	Trigger selection . . . . .	36
3.1.2	Stripping Selection . . . . .	37
3.1.3	Particle Substitution Procedure . . . . .	39
3.1.4	Decay Tree Fitter . . . . .	39
3.1.5	Pre-selection Cuts . . . . .	39
3.1.6	Multivariate Selection . . . . .	40
3.1.7	Particle Identification . . . . .	48
3.1.8	Multiple Candidates . . . . .	48
3.2	Background Studies . . . . .	49
3.2.1	Charm Veto Selection . . . . .	49
3.2.2	Background from Charged Particle Misidentification . . . . .	51
3.2.3	Partially Reconstructed Backgrounds . . . . .	52
3.2.4	Background from Decays Containing $K^0_S$ Mesons . . . . .	53
3.2.5	Summary of Background Contributions . . . . .	54
3.3	Efficiency Calculations . . . . .	55
3.4	Variance of the Efficiencies Across the Dalitz Plane . . . . .	57
3.5	Mass Fits . . . . .	58
3.5.1	Fit Strategy . . . . .	59
3.5.2	Fit Components . . . . .	62
3.5.3	Fit Summary . . . . .	68

<b>4</b>	<b>Calculation of <math>\mathcal{B}(\bar{B}_s^0 \rightarrow \Lambda \bar{p} K^+)</math> and <math>\mathcal{A}_T</math></b>	<b>71</b>
4.1	Dalitz Plots for $\bar{B}_{(s)}^0 \rightarrow \Lambda \bar{p} h^+$ Decays and Efficiency Recalculation . . . . .	71
4.2	Branching Fraction of the Decays $\bar{B}_s^0 \rightarrow \Lambda \bar{p} K^+$ and $\bar{B}_s^0 \rightarrow \bar{\Lambda} p K^-$ . . . . .	78
4.3	Time Reversal Asymmetry $\mathcal{A}_T$ Determination . . . . .	79
4.3.1	Correction Factors for the Time Reversal Asymmetry . . . . .	80
4.4	Systematic uncertainties for $\mathcal{A}_T$ . . . . .	82
4.4.1	Fit model . . . . .	83
4.4.2	Selection . . . . .	88
4.4.3	$\Lambda$ Decay and $\Lambda$ Decay Constant . . . . .	90
4.5	Systematic Uncertainties for the $\bar{B}_s^0 \rightarrow \Lambda \bar{p} K^+$ Branching Fraction . . . . .	91
4.5.1	Fit Model . . . . .	91
4.5.2	Selection . . . . .	92
4.5.3	External Systematic Uncertainties . . . . .	92
<b>5</b>	<b>Results and Conclusion</b>	<b>95</b>
5.1	Asymmetries $\mathcal{A}_T$ and $\mathcal{A}_T^{\text{CPV}}$ . . . . .	96
5.2	Observation of the Baryonic $B_s^0$ Decay $\bar{B}_s^0 \rightarrow \Lambda \bar{p} K^+$ . . . . .	96
	<b>List of figures</b>	<b>101</b>
	<b>Appendices</b>	<b>107</b>
<b>A</b>	<b>Study of Trigger Lines</b>	<b>109</b>
<b>B</b>	<b>Distribution of the MVA Input Variables for the Individual Data Samples</b>	<b>111</b>
B.1	MVA Training for the 2011 LL Data . . . . .	112
B.2	MVA Training for the 2011 DD Data . . . . .	116
B.3	MVA Training for the 2012 LL Data . . . . .	120
B.4	MVA Training for the 2012 DD Data . . . . .	124
<b>C</b>	<b>Effect of the Trigger Configuration in 2012</b>	<b>129</b>
<b>D</b>	<b>Hadronisation Fractions</b>	<b>139</b>
<b>E</b>	<b>Correlation between the MVA Input Variables</b>	<b>141</b>

---

<b>F Breakdown of the Selection Efficiencies</b>	<b>145</b>
F.1 Generator Efficiencies . . . . .	145
F.2 Stripping Efficiencies . . . . .	146
F.3 Trigger Efficiencies . . . . .	147
F.4 Selection Efficiencies . . . . .	148
F.5 PID Efficiencies . . . . .	149
F.6 Variation of the Efficiency Across the Dalitz Plot . . . . .	150
<b>G List of Shape Parameters</b>	<b>153</b>
<b>H Additional Fit information</b>	<b>155</b>
H.1 Fit to the Full Data with Dalitz Plot Corrected Efficiencies . . . . .	155
H.2 Fit to the Full Data with Dalitz Plot Corrected Efficiencies for the Enhancement Only. . . . .	157
H.3 Fit to the Full Data in Order to Determine for $\mathcal{A}_T$ with Dalitz Plot Corrected Efficiencies Including Dilution Effects . . . . .	159
<b>Bibliography</b>	<b>163</b>
<b>Acknowledgements</b>	<b>167</b>

# Chapter 1

## Theoretical introduction

Three of the four known fundamental forces are described within the “Standard Model of elementary particle physics”. This excludes gravity, as approaches towards quantum gravity have been in vain so far. Gravity, however, can be neglected at the energy scale of today’s experiments due to its very small coupling constant.

The remaining three – strong, electromagnetic and weak interaction – are included. The mathematical concept behind those three is very similar, which would imply a common mechanism and thus a unification at a higher scale. Weak and electromagnetic forces have been unified into the Quantum Flavour Dynamics. This was a major success in theoretical physics. A further unification into a Grand Unified Theory (GUT), which would be a single model for those three fundamental forces is still on the agenda. Within the Standard Model the combined electro-weak and strong interactions are represented by a direct product between the fundamental symmetry groups. A GUT would make use of a single group and the three forces are represented as one broken symmetry.

The next step, the unification with gravity, would lead to a so called “Theory of Everything”. There are several attempts to realise that, most notably String Theories. But the effect of gravity should stay negligible until the Planck scale is reached, *i.e.* at  $\approx 10^{19}$  GeV.

Since much of the standard model is based on symmetries, within the next sections the general concept will be introduced before the Standard Model is summarised shortly. Afterwards the properties of the decays at hand will be presented in detail. Finally, the theoretical predictions and the experimental extraction for the time reversal asymmetry are introduced.

### 1.1 Symmetries in Physics

In the description describing of physical systems symmetries play a vital role. The usage of symmetries is even more pronounced in modern day physics ranging from lattice symmetries in solid state physics to proposed symmetries between elementary particles up to GUT-scale. A system  $S$  is said to be symmetrical with respect to a transformation  $\mathbf{T}$ , if

$$\mathbf{T}(S) = S \quad . \quad (1.1)$$

In contrast to the geometrical properties in the lattice of a solid, one of the foci body we are interested in the symmetries of the laws of Physics. Connected to these is Noether’s theorem, which relates the symmetry of a system to a conserved current. In classical mechanics rotational symmetry results in the conservation of angular momentum and the independence of the laws of physics on the orientation of the coordinate system.

In general we distinguish two different kind of symmetries, space-time symmetries, also known as external symmetries, and symmetries of the fields representing the elementary particles, also known as internal symmetries. Furthermore, we can distinguish between continuous and discrete symmetries.



### 1.1.1 Space-time Symmetries

In special relativity, the laws of physics are described in the four-dimensional pseudo-euclidean Minkowski space. Transformations in this space are translations in space and time, rotations and boosts referred to as Lorentz transformations. These operations form the Poincaré group. In order to be invariant under these transformations, physical objects need to fall into representations of this group. Neither energy nor the momentum are invariant, but the momentum four-vector  $p^\mu = (E, \mathbf{p})$  is invariant with respect to the Poincaré group. As a result, it is not sensible to use the Hamiltonian, since it transforms like the time-like component of a four-vector, but instead to look for a scalar quantity with respect to transformations of the Poincaré group. One such scalar can be found by using the scalar product of two four-vectors, such as<sup>1</sup>

$$m^2 = p^\mu p_\mu = E^2 - \mathbf{p}^2 \quad , \quad (1.2)$$

which is the invariant mass of the particle described by  $p^\mu$  and is independent of the frame of reference chosen to measure its properties. In a similar way it is useful to require the action  $\mathcal{S}$  to be a scalar as well. Thus we get

$$\mathcal{S} = \int dt L = \int dt d\mathbf{r} \mathcal{L} = \int dx^\mu \mathcal{L} \quad . \quad (1.3)$$

Here  $L$  is the Lagrangian and  $\mathcal{L}$  the Lagrangian density. From eq. (1.3) one finds, that  $\mathcal{L}$  needs to be a scalar if the action is a scalar. Therefore, it is adequate to describe the properties of a physical system using the Lagrange formalism.

Apart from continuous symmetries, there are the discrete space-time symmetries parity  $P$  and time reversal  $T$ . Parity inverts the space like coordinates. For the position vector this leads to

$$P\mathbf{r} = -\mathbf{r} \quad . \quad (1.4)$$

Since the mass of a particle is a scalar we find for the momentum vector

$$P\mathbf{p} = -\mathbf{p} \quad . \quad (1.5)$$

The angular momentum, however, does not change its sign under parity. It is an angular vector defined by the outer product of two polar vectors namely the position and momentum vectors. Parity is a multiplicative operation, since both  $\mathbf{r}$  and  $\mathbf{p}$  change sign, the product does not. A similar difference exists between scalars and pseudo scalars. A classical example would be the magnitude of the momentum

$$p^2 = \mathbf{p} \cdot \mathbf{p} \quad , \quad (1.6)$$

which transforms like a scalar with respect to parity. The helicity, a commonly used quantity in latter measurement, is defined as

$$h = \frac{\mathbf{s} \cdot \mathbf{p}}{|\mathbf{s}||\mathbf{p}|} \quad . \quad (1.7)$$

The spin  $\mathbf{s}$  is an angular momentum, and therefore an angular vector. Since parity is multiplicative, the helicity is odd with respect to parity transformations.

The time reversal changes the sign of time

$$Tt = -t \quad . \quad (1.8)$$

Similar to parity, time reversal is also multiplicative. The position vector is even with respect to  $T$ , but the momentum is odd since

$$\mathbf{p} = m \frac{d\mathbf{r}}{dt} \quad . \quad (1.9)$$

This can also be easily understood when taking into account, that the momentum describes a directed motion instead of just a point in space, so that it naturally needs to flip its direction with respect to time reversal. The same is true for the angular momentum.

<sup>1</sup>Throughout the theoretical introduction natural units are used, *i.e.*  $\hbar = 1$  and  $c = 1$

### 1.1.2 Symmetries of Fields

In addition to space time symmetries, physical objects also have internal symmetries. A simple example is the Lagrangian of the free fields of the QED, the theory of Quantum Electrodynamics,

$$\mathcal{L} = \bar{\psi}(i\gamma^\mu \partial_\mu - m)\psi - \frac{1}{4}\mathbf{F}^{\mu\nu}\mathbf{F}_{\mu\nu} \quad , \quad (1.10)$$

with  $\psi$  being the electron spinor,  $\mathbf{F}_{\mu\nu}$  the electromagnetic field tensor, and  $\gamma^\mu$  the Dirac matrices. Since it only contains the electron spinor  $\psi$  in bilinear terms  $\bar{\psi}\psi$ , it is invariant under a global phase transformation of  $\psi \rightarrow \psi e^{i\phi}$ . This, however, is not true for local phase transformations  $\psi \mapsto \psi e^{i\phi(x_\mu)}$  since  $\bar{\psi}\partial_\mu\psi \mapsto \bar{\psi}\partial_\mu\psi + i\bar{\psi}(\partial_\mu\phi(x_\mu))\psi$ . These are more physical and do not require any observer in the universe to make the same choice for an arbitrary phase. The gauge potential is not unambiguously defined either. The equations of motion for the electromagnetic field are invariant with respect to the transformation  $A_\mu \mapsto A_\mu + \frac{1}{e}\partial_\mu\phi(x_\mu)$ . Modifying the Lagrangian to read

$$\mathcal{L} = \bar{\psi}(i\gamma^\mu(\partial_\mu - ieA_\mu) - m)\psi - \frac{1}{4}\mathbf{F}^{\mu\nu}\mathbf{F}_{\mu\nu} \quad (1.11)$$

leads to a cancellation of these extra terms. Furthermore, an additional term appears,

$$\mathcal{L}_{\text{int}} = -ie\bar{\psi}\gamma^\mu A_\mu\psi \quad , \quad (1.12)$$

which describes the electron-photon interaction. By demanding invariance with respect to a local gauge transformation it is possible to introduce interaction terms. In a formal approach Yang and Mills have developed a formalism to introduce interaction terms by requiring local gauge invariance [6]. Starting from a global symmetry of the Lagrangian it is required to be a local symmetry as well. These symmetries are usually represented by  $SU(N)$  groups. The number of generators of these groups corresponds to the number of gauge particles. The QED is a Young-Mills theory with a  $U(1)$  symmetry. The  $U(1)$  group has one generator, therefore, there exists only one gauge field, the photon field. Another special property of the  $U(1)$  is its abelian nature, *i.e.* it is commutative. Non-abelian groups such as the  $SU(N)$  are not commutative, which means that the generators do not commute with each other and leading directly to self-interaction between the gauge fields. Examples for these are the colour  $SU(3)$  of QCD in which the gluons interact with each other or the weak isospin  $SU(2)$  in which the  $W^\pm$  bosons can couple to each other.

### 1.1.3 Parity, Charge Conjugation, Time Reversal, and the CPT Theorem

The parity and time reversal operations have been introduced as space time symmetries in sec. 1.1.1. It is also interesting to study the behaviour of the elementary particles with respect to P and T.

For any field holds true,

$$\mathbf{P}\phi(x) = \phi'(x') \quad . \quad (1.13)$$

The parity operator changes the location as well as the spatial orientation of the fields. Scalar or pseudo scalar fields have no spacial orientation, so that the transformation is simply

$$\mathbf{P}\phi(x) = \pm\phi(x') \quad . \quad (1.14)$$

The pseudo scalar changes its sign, the scalar does not. Other fields, like spinors, vectors and tensors behave in a more complicated manor. Spinors, for example, have a spin orientation in space and vector fields are represented by a spatial four-vector. The parity transformation turns a covariant four-vector into a contravariant four-vector. The parity of a fermion is not given by first principles, however, the parity of a fermion needs to be opposite to that of an anti-fermion. As a result, the parity of a fermion is defined to be positive and negative for an anti-fermion. From that we can deduce the parity for bound states as well. The  $\pi^+$  is a bound state of an up quark and an anti-down quark. So its parity should be negative since

$$\mathbf{P}\pi^+ = \mathbf{P}u\mathbf{P}\bar{d} = (+1)(-1) = -1 \quad . \quad (1.15)$$

In addition to the intrinsic parity of quarks or leptons it is necessary to look at the spacial wave function. The parity of the spherical harmonics depend on the orbital angular momentum  $L$  of the two particles with respect to each other. An odd orbital angular momentum is odd with respect to the parity transformation, even values for  $L$  are even with respect to parity. Eq. (1.16) needs to be modified

$$\mathbf{P}\pi^+ = \mathbf{P}u \mathbf{P}\bar{d} (-1)^L = (+1)(-1)(-1)^0 = -1 \quad . \quad (1.16)$$

This formula is true for all fermion anti-fermion bound states.

Noether's theorem implies that any symmetry of the Lagrangian leads to a conserved current and charge. This is also true for local gauge theories. The generators are the charges conserved in these theories, again for the QED, the electric charge is the generator of the  $U(1)$  symmetry and it is conserved in all interactions. Only fields, that carry a specific charge can interact with each other. Neutrinos have no electric charge and therefore do not couple to photons. It is now interesting what happens when the sign of the charge is changed. This operation is denoted  $C$ . In general, the charge conjugation changes the sign of all additive quantum numbers. It turns an electron into a positron. Charge conjugation on fermions leads to peculiar things. In contrast to  $P^2 = 1$  there is  $C^2 = -1$ . This behaviour leads to an additional term when calculating the eigenvalue of  $C$  of a system of fermions

$$\mathbf{C}|q\bar{q}, S, L\rangle = (-1)^{L+S}|q\bar{q}, S, L\rangle \quad , \quad (1.17)$$

$L$  being the orbital angular momentum and  $S$  the spin of the particle. This allows to use charge conjugation to distinguish between pseudo scalar and vector particles.

The operation  $T$  is more complicated than parity or even charge conjugation and this can already be seen on the level of classical mechanics and classical electrodynamics. In classical mechanics time reversal is considered an anti-canonical transformation since the Poisson brackets change sign. In general, a system is considered time reversal symmetric in case  $\mathbf{x}_T(t) = \mathbf{x}(-t)$  is also a solution of  $H_T$  with  $H(\mathbf{x}, \mathbf{p}) \mapsto H_T(\mathbf{x}_T, \mathbf{p}_T)$ . Most Hamiltonians are quadratic in  $\mathbf{p}$  and thus time reversal invariant. The Hamiltonian of classical electrodynamics introduces terms linear in  $\mathbf{p}$  in a quadratic Hamiltonian

$$H(\mathbf{x}, \mathbf{p}) = 1/2m(\mathbf{p} - e\mathbf{A})^2 + e\phi \quad , \quad (1.18)$$

$\mathbf{A}$  being the vector potential and  $\phi$  the scalar potential. For electrodynamics to be time reversal invariant the vector potential needs to transform like  $\mathbf{A}(\mathbf{x}, t) \mapsto -\mathbf{A}(\mathbf{x}, -t)$  and since  $\mathbf{B} = \nabla \times \mathbf{A}$  the magnetic field  $\mathbf{B}$  needs to be odd with respect to time reversal as well. This can easily be understood since the magnetic field is generated by a moving charge and a similar argument as for the momentum holds true.

The definition of the time reversal operator in quantum mechanics leads to several complications. First of all it is desirable to have correspondence to classical physics. This, however, leads to a contradiction in the commutator relation  $[\mathbf{x}, \mathbf{p}]$  and in the definition of the momentum operator  $\mathbf{p} = -i\hbar\partial_{\mathbf{x}}$ . Furthermore, the time reversed eigenstates  $|n\rangle$  of a Hamiltonian would have negative eigenvalues. In order to solve these problem, the time reversal operator needs to include complex conjugation and needs to be an anti-unitary operator such as

$$T\psi(\mathbf{x}, t) = \psi_T(\mathbf{x}, t) = \psi^*(\mathbf{x}, -t) \quad . \quad (1.19)$$

Additional complications arise in quantum field theory, due to the operator nature of the fields. The  $T$  operator needs to transform the creation and annihilation operators as well. In general  $T$  time-reverses field operators and complex conjugates complex numbers and leads to the following transformation behaviour

$$\begin{aligned} S(\mathbf{x}, t) &\mapsto +S(\mathbf{x}, -t) && \text{(Scalar)} \\ P(\mathbf{x}, t) &\mapsto -P(\mathbf{x}, -t) && \text{(Pseudo-Scalar)} \\ V^\mu(\mathbf{x}, t) &\mapsto +V_\mu(\mathbf{x}, -t) && \text{(Vector)} \\ A^\mu(\mathbf{x}, t) &\mapsto +A_\mu(\mathbf{x}, -t) && \text{(Axial-Vector)} \\ T^{\mu\nu}(\mathbf{x}, t) &\mapsto -T_{\mu\nu}(\mathbf{x}, -t) && \text{(Tensor)} \end{aligned} \quad (1.20)$$

## 1.2 Standard Model - an Overview

### 1.2.1 Theory of the Standard Model

The Standard Model is a combined theory of strong and electro-weak interactions between the known elementary particles. The Standard Model is represented by local gauge invariant quantum field theories and the fundamental gauge group is given by

$$\mathcal{F} = \text{SU}(3) \otimes \text{SU}(2) \otimes \text{U}(1) \quad , \quad (1.21)$$

and includes both strong and electro-weak forces. But as this group is created by a direct product, it offers no further physical insight, as there is no linkage between those two interactions.

The electro-weak interaction is the unified theory of electromagnetism and weak processes as the neutron decay. It is represented by a local gauge invariant quantum field theory called Quantum Flavourdynamics (QFD), whose gauge group is given by  $\text{SU}(2) \otimes \text{U}(1)$ . The  $\text{SU}(2)$  of the weak isospin has three and the  $\text{U}(1)$  of the weak hypercharge has one generators. This results in four gauge boson fields, three  $\mathbf{W}_\mu^i$  and  $\mathbf{B}_\mu$ , for the weak isospin  $\text{SU}(2)$  and weak hyper-charge  $\text{U}(1)$  gauge groups, respectively. In order for the Lagrangian to be gauge invariant the fields need to be arranged in representations of the gauge group. Due to the  $(V - A)$  structure<sup>2</sup> of the coupling, the weak interaction only couples to left handed fermions and right handed anti-fermions. As a result, the left-handed particles form iso-doublets with respect to the  $\text{SU}(2)$  group and the right handed particles form iso-singlets. All in all there are three quark and three lepton doublets.

In general it is useful to introduce ladder operators  $\mathbf{W}_\mu^\pm$  in order to transform one doublet state into the other, *i.e.* an  $u$  quark into a  $d$  quark. These are constructed by using two linearly independent combinations of  $\mathbf{W}_\mu^1$  and  $\mathbf{W}_\mu^2$ . The  $\mathbf{W}_\mu^3$  and  $\mathbf{B}_\mu$  fields mix with each other. This mixing can be described by a  $2 \times 2$  rotation matrix with the mixing angle  $\theta_W$ . The rotated fields are the  $\mathbf{Z}_\mu$  and the  $\mathbf{A}_\mu$ . The  $\mathbf{W}_\mu^\pm$ , the  $\mathbf{Z}_\mu$ , and the photon  $\mathbf{A}_\mu$  are the observable states.

So far all fields have zero masses, thus the weak currents couple only to fields from the same iso-doublet. Introducing ad-hoc mass terms for the gauge fields into the Lagrangian breaks the gauge invariance. The same reason requires the fermions to be massless due to the  $(V-A)$  structure. In order to achieve massive  $W^\pm$  and  $Z$  bosons, a mass-less photon, as well as massive fermions, the concept of a spontaneously broken symmetry can be applied. This mechanism requires two additional scalar fields,  $\Phi = (\phi^+, \phi^0)$ , which break the  $\text{SU}(2) \otimes \text{U}(1)$  symmetry down to the  $\text{U}(1)_{\text{EM}}$  and thus apply masses to the  $W^\pm$  and  $Z$  bosons. In a generalized approach of the Yukawa coupling the fermions couple to the Higgs field. It is desirable to express the Lagrangian with the mass eigenstates. To achieve that, it is necessary to introduce matrices to diagonalize the fermion coupling matrices. This can be found for the coupling to the weak neutral and electromagnetic currents, but not for the charged weak current, *i.e.* the coupling to the  $W^\pm$  bosons. As a result, the weak neutral and the electro-magnetic current conserve the fermion flavour. The charged current is not diagonal and changes the flavour of the fermions. The amplitudes of these interactions are given by a non-diagonal, unitary  $3 \times 3$  matrix, the Cabibbo-Kobayashi-Maskawa (CKM) matrix. This matrix can be interpreted as a rotation matrix that transforms the mass eigenstates into the flavour eigenstates. By definition the up-type quarks mass eigenstates are also the flavour eigenstates whereas the down-type quark mass eigenstates are rotated by the CKM matrix. Therefore, the charged weak current is also diagonal using the flavour eigenstates and is given by

$$\mathbf{J}_\mu^{\text{CC}} = (\bar{u}, \bar{c}, \bar{t}) \gamma_\mu (1 - \gamma_5) \begin{pmatrix} d' \\ s' \\ b' \end{pmatrix} = (\bar{u}, \bar{c}, \bar{t}) \gamma_\mu (1 - \gamma_5) \mathbf{V}_{\text{CKM}} \begin{pmatrix} d \\ s \\ b \end{pmatrix} \quad , \quad (1.22)$$

with

$$\mathbf{V}_{\text{CKM}} = \begin{pmatrix} V_{ud} & V_{us} & V_{ub} \\ V_{cd} & V_{cs} & V_{cb} \\ V_{td} & V_{ts} & V_{tb} \end{pmatrix} \quad . \quad (1.23)$$

<sup>2</sup>In contrast to the vector coupling of the QED, the weak charged current contains a vector ( $\gamma^\mu$ ) and an axial vector component ( $\gamma^5$ ) which projects the left handed components of a spinor. This leads to a suppression of meson decays into a pair of leptons as well, due to the helicity suppression

The elements of the matrix being arbitrary complex numbers, it is not possible to derive the values of the matrix elements within the theory of the Standard Model, but they can be determined by experiments [7].

The strong interaction is described by Quantum Chromodynamics (QCD), a local gauge invariant quantum field theory, whose symmetry group is the colour-SU(3). The SU(3) has eight generators, therefore, one finds eight corresponding gauge fields called gluons. Compared to the electromagnetic charge, the colour charge is more complicated. There are three different colour charges, red, green and blue. Only quarks couple to the strong interaction and each quark forms an SU(3) triplet. Since leptons do not carry colour charge, they are described as colour singlets. The QCD is a textbook example of a strong interacting non-abelian local gauge theory. Compared to the SU(2)  $\otimes$  U(1) symmetry of the QED the colour-SU(3) is an unbroken symmetry. The non-abelian nature of the SU(3) leads to terms in the Lagrangian in which the gauge fields couple to each other. This does not appear in the QED since the U(1) of electromagnetism is an abelian group. In general, the strength of the coupling depends on the energy scale. Compared to the electromagnetic interaction, where the coupling strength increases with the energy scale, the coupling strength of the strong interaction decreases. In the limit of a vanishing momentum transfer the coupling diverges and in the limit of infinite momentum transfer the coupling vanishes. This effects are called confinement and asymptotic freedom. Due to confinement there are neither free quarks nor free gluons, physical states are colour-SU(3) singlet states.

The pretence of QCD is to be able to describe all interaction between quarks and gluons. The hadrons, which are observed in collider experiments, are bound states of the strong interaction and colour singlets. There is, however, no closed theory to describe the masses and spectra of hadrons using the QCD. Due to the large coupling at small energy scales it is impossible to use perturbation theory, that has been applied to both QED and QFD very successfully. Calculations on processes in which hadrons appear have to either rely on effective descriptions such as the operator product expansion or QCD sum rules or on numerical calculations performed by the lattice QCD. At high energies, perturbative calculations are reasonable and have shown that QCD can be very successful in describing the interaction between quarks and gluons. The weak decays of hadrons containing heavy  $b$  and  $c$  quarks are the main interest of the field of Flavour physics and QCD corrections play a vital part in these studies. For example, the absolute values of CKM matrix elements and its complex phase are difficult to extract from the experimental data without a deep understanding of the underlying QCD effects.

The fermions of the Standard Model, *i.e.* the quarks and leptons, can be arranged in the following representations of the gauge groups,

$$\ell_L^i = (\mathbf{1}, \mathbf{2})_{-1} \quad i = 1, 2, 3 \quad (1.24)$$

$$\nu_R = (\mathbf{1}, \mathbf{1})_0 \quad \nu = \nu_e, \nu_\mu, \nu_\tau \quad (1.25)$$

$$\ell_R^i = (\mathbf{1}, \mathbf{1})_{-2} \quad i = e^-, \mu^-, \tau^- \quad (1.26)$$

$$q_L^i = (\mathbf{3}, \mathbf{2})_{\frac{1}{3}} \quad i = 1, 2, 3 \quad (1.27)$$

$$u_R = (\mathbf{3}, \mathbf{1})_{\frac{4}{3}} \quad u = u, c, t \quad (1.28)$$

$$d_R = (\mathbf{3}, \mathbf{1})_{-\frac{2}{3}} \quad d = d, s, b \quad (1.29)$$

$\ell$  and  $q$  represent the lepton and quark generation, respectively, and  $L$ (eft) and  $R$ (ight) denote the handedness of the fields. The first number is the representation with respect to the colour-SU(3), the second the representation with respect to the weak isospin, and the subscript is the weak hypercharge of the states.

There are three left handed leptons, three left handed quarks. Due to the electro-weak symmetry breaking the degeneracy of the fermion doublets is removed. The right handed fermions are singlets with respect to the electro-weak symmetry. Quarks are triplets with respect to the colour-SU(3). Each quark appears in three different colour states. Leptons do not interact strongly and are, therefore, put into singlets.

## 1.2.2 Charmless Baryonic $B$ -Decays within the Standard Model

Charmless  $B$  decays in general are defined as rare decays, whose final states contain neither open charm, *i.e.* there is final state particle with either a  $c$  or  $\bar{c}$ , nor hidden charm, *i.e.* a final state particle comprised of a  $c\bar{c}$  pair. For example, the decays  $B^0 \rightarrow \bar{D}^0 K_S^0$  and  $B^0 \rightarrow J/\psi K_S^0$  are an open charm and a hidden charm  $B$  decay, respectively. Decays such as  $B^0 \rightarrow K^+ \pi^-$  are charmless decays, whose dominant amplitudes are usually given by a  $b \rightarrow u$  tree and a  $b \rightarrow s$  penguin diagram, *cf.* the diagrams in 1.1.

As mentioned in the previous section, reactions involving quarks and gluons are difficult to calculate within the usual perturbation framework. In case a hadron decays into a pair of leptons or into a hadron and a pair of leptons, the latter case is referred to as a semi-leptonic decay, the theoretical framework is working quite well making use of different formalisms to describe the QCD effects. The decays of heavy quarks, however, are dominated by non-leptonic modes due to the  $(V - A)$  coupling and the resulting helicity suppression. In order to describe hadronic decays new methods have been developed. A successful and widely used method is the Operator-Product-Expansion (OPE). The OPE is an effective theory. Instead of describing the system at all energy scales, effective theories only describe the physics at a certain low energy scale. A prime example would be nuclear physics, where it is sufficient to describe the interaction between hadrons not the interaction of the quarks within the hadrons. An effective Lagrangian is introduced and new Feynman rules are derived to model the low energy behaviour whereas the high energy effects are absorbed by separate coefficients or functions.

In the OPE formalism low energy dynamics are described by effective four quark operators and the high energy effects are described by the Wilson coefficients. By a factorisation ansatz the short distance interactions, *i.e.* the high energy component of the interaction, and the long distance, *i.e.* low energy part, are separated. This approach is very similar to the effective Fermi theory for the weak interaction. The relevant operators for the  $b \rightarrow u$  tree amplitude are shown in Fig. 1.1(a). The  $W^-$  propagator can be reduced to a point in case the momentum transfer  $q_\mu, q^\mu = q^2$  is small compared to the  $W$  mass squared  $m_W^2$ , the result is identical to the Fermi theory for weak decays. The coupling is described by the two operators  $\mathcal{O}_{1,2}$ . Both operators contain the CKM coupling elements, in this case  $V_{ub}V_{us}^*$ , and information on the colour structure of the final state. Since the final states have to be colour singlets there are two different ways to match the colour charges for the quarks, coupling the  $\bar{u}$  and the  $s$  is referred to as an external graph, as the quarks produced by the  $W^-$  decay are grouped together, this behaviour is described by  $\mathcal{O}_1$ . Coupling the  $u\bar{u}$  together leads to a different colour structure, often referred to as internal graph, and is described by  $\mathcal{O}_2$ .

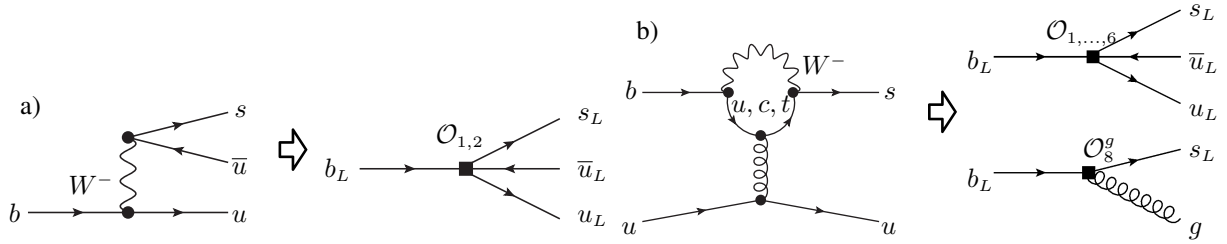


Figure 1.1: Feynman diagrams for the Standard Model process  $b \rightarrow su\bar{u}$  and the diagrams in the reduced theory assuming  $q^2 \ll m_W^2$ . The subscript  $L$  denotes, that the vector currents are left-handed following the Fermi theory of the weak interaction. The Operators  $\mathcal{O}_i$  denote the interactions in the effective low energy regime.

As the weak neutral current conserves the fermion flavour, the  $b \rightarrow s$  penguin amplitude needs to be loop diagram. These are expected to be suppressed due to the GIM mechanism [8]. But since  $m_t \gg m_u, m_c$  and  $|V_{tb}| \gg |V_{ub}|, |V_{cb}|$  the GIM suppression almost cancels and the contribution of the penguin amplitude to the overall decay rate is usually larger than the contribution from the  $b \rightarrow u$  tree diagram. The OPE reduction for the  $b \rightarrow s$  penguin with a gluon coupling to a  $u\bar{u}$  pair is shown in Fig. 1.1(b).

This easy picture, however, is misleading, due to loop corrections. In these the  $W$  boson is part of the internal loop and its momentum is integrated out in accordance to the Feynman rules and its momentum  $q$  can have arbitrarily

large or small values. The assumption of  $q^2 \ll m_W^2$  is no longer valid and the theory cannot be expanded in terms of  $q^2/m_W^2$ . The full theory needs to be split into an infra-red regime ( $m_W \rightarrow \infty$ ) and an ultra-violet regime ( $m_q \rightarrow 0$ ). Both are calculated with respect to a renormalisation scale  $\mu$  at which both regimes diverge.

Unfortunately the quark transitions are not observable at the experiments, but rather the hadronic decays of mesons and baryons governed by hadronic matrix elements that pose an additional difficulty to the calculation of the decay rates. Popular methods to calculate the hadronic matrix elements are QCD sum and counting rules [9, 10] as well pole models or similar power series expansions [11]. Additional approximations are often made as well, one that is frequently used in the calculation of mesons decaying into baryons is the factorisation ansatz. Hereby it is assumed, that the whole amplitude can be factorised into two independent matrix elements, each of which can be calculated independently. Usually, one amplitude describes the decay of the initial particle in one or more final state particles while the other amplitudes describes the creation of the remaining final state particles from the vacuum.

Before any factorisation is applied it is useful to write down and look at each leading order Feynman diagrams for  $\bar{B}^0 \rightarrow \Lambda \bar{p} \pi^+$ . In Figure 1.2 the leading order diagrams for  $\bar{B}^0 \rightarrow \Lambda \bar{p} \pi^+$  are shown, the gluon lines have been omitted to improve readability. This is the main decay of interest for this analysis. There are two major classes, there are four  $b \rightarrow u$  tree amplitudes and two  $b \rightarrow s$  penguin amplitudes. The diagram in Fig. 1.2(d) is related to the operator  $\mathcal{O}_1$  described before, the other three correspond to internal graphs. It is obvious that the structure of baryonic decays is more complicated than decays into mesons. Normally, the internal graphs are colour suppressed with respect to the external graphs since the quarks produced by the  $W$  need to match the colour charges of the quarks contained in the initial state particle. Due to the additional quark pairs produced, this effect is less pronounced than in two body meson decays, *cf.* decay rates for  $D^0$  mesons such as  $\Gamma(D^0 \rightarrow K_s^0 \pi^0)/\Gamma(D^0 \rightarrow K^- \pi^+) = (30.5 \pm 0.9)\%$  [12]. Recent results on the search for  $B^- \rightarrow \Lambda_c^+ \bar{p} \ell^- \bar{\nu}_\ell$  [13] suggest, that the external graph is suppressed with respect to the internal graphs.

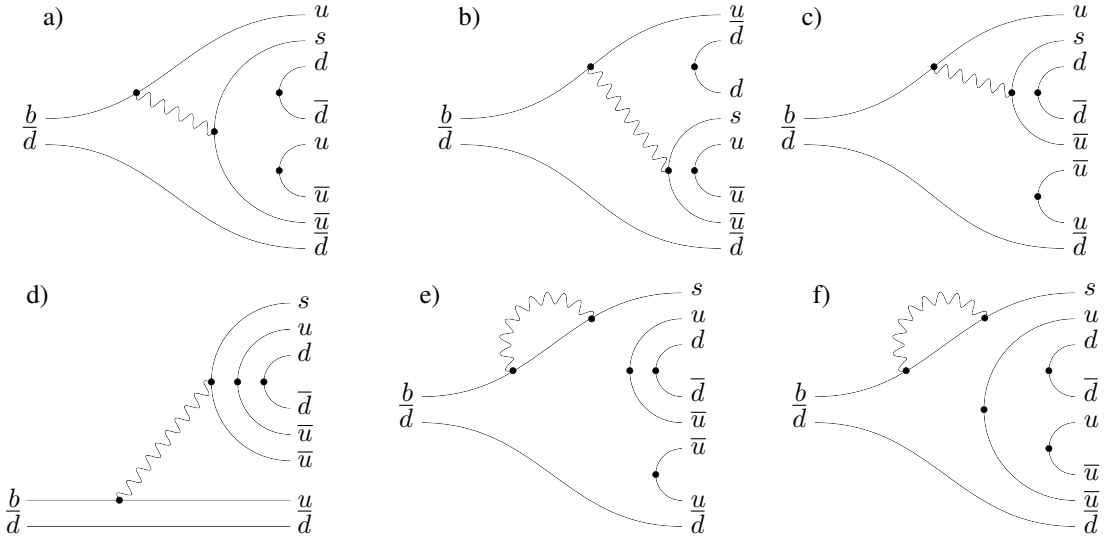


Figure 1.2: Leading order diagrams for the  $\bar{B}^0 \rightarrow \Lambda \bar{p} \pi^+$  decay. Gluon lines are omitted. The amplitudes are proportional to  $V_{ub}V_{us}^*$  (a,b,c,d) and  $V_{tb}V_{ts}^*$  (e,f).

The  $\bar{B}^0 \rightarrow \Lambda \bar{p} \pi^+$  penguin amplitudes are shown in Figs. 1.2(e) and (f). As for Figs. 1.2(a) to (c) the diagrams differ in the fragmentation into the final state particles. Assuming the  $u\bar{u}$  pair is produced first in the fragmentation, there are two different initial states possible,

$$(b\bar{d}) \rightarrow (s\bar{u})(u\bar{d}) \quad (1.30)$$

$$(b\bar{d}) \rightarrow (su)(\bar{u}\bar{d}) \quad , \quad (1.31)$$

the first leading to an initial state of two mesons quite similar to the decay  $\bar{B}^0 \rightarrow K^- \pi^+$ , the latter consists of a pair of diquarks, a pair of two quarks or antiquarks, each initial state leading to different dynamics in the final

fragmentation step. For the initial state Eq. 1.31 the pion is on-shell (a physical pion), and the kaon is off-shell (a virtual kaon), further fragmenting into the  $\Lambda\bar{p}$  pair. This picture directly corresponds to the pole model formalism. The  $B$  meson decays into a pair of mesons, one space-like the other time-like, and the space-like meson further decays into a baryon antibaryon pair. This should lead to an interesting phenomenon, as the invariant baryon antibaryon mass distribution should be centred at the threshold due to the virtual meson pole [14–17].

For the diquark initial state, a different behaviour is expected. While a quark and an antiquark can combine to form a colour singlet, an (anti-)diquark cannot be in a colour singlet state, only in combination with another (anti-)quark thus producing a baryon antibaryon pair, both of which can be virtual or physical. In case the  $d\bar{d}$  pair is produced first in the fragmentation, the following final state can be found,

$$\bar{B}^0 \rightarrow \Lambda\bar{N} \quad \text{with } \bar{N} \rightarrow \bar{p}\pi^+ \quad , \quad (1.32)$$

$\bar{N}$  being any nucleon resonance decaying into  $\bar{p}\pi^+$ . Within the theoretical framework diquark initial states can be described using baryon poles. Since both processes lead to different dynamics the Dalitz plot for  $\bar{B}^0 \rightarrow \Lambda\bar{p}\pi^+$  should yield evidence which process dominates the fragmentation, an enhancement at the threshold of the invariant  $m(\Lambda\bar{p})$  mass supports the meson pole hypothesis and the appearance of resonances in either  $m(\Lambda\pi^+)$  or  $m(\bar{p}\pi^+)$  support the baryon pole hypothesis. Similar arguments allow to categorise the  $b \rightarrow u$  tree amplitudes in a similar fashion.

In contrast to the first and second generation  $e^+e^-B$  factories DORIS II, CESR, PEP-II, and KEKB operating predominantly at the  $\Upsilon(4S)$  resonance producing only  $B^0$  and  $B^-$  mesons, the LHC produces  $B_s^0$  mesons in a similar order of magnitude as  $B^0$  mesons. Naively, swapping the  $\bar{d}$  from the  $\bar{B}^0$  with an  $\bar{s}$ , one would find the baryonic  $\bar{B}_s^0$  decay  $\bar{B}_s^0 \rightarrow \Lambda\bar{p}K^+$ . This is more of an experimental concern, because the channel  $\bar{B}_s^0 \rightarrow \Lambda\bar{p}K^+$  is a possible source of background to the  $\bar{B}^0 \rightarrow \Lambda\bar{p}\pi^+$  decay mode due to kaon-pion misidentification. Since both the  $\bar{d}$  and  $\bar{s}$  are the spectator quarks, one would assume the decay rates and dynamics to be very similar between the  $\bar{B}^0 \rightarrow \Lambda\bar{p}\pi^+$  and  $\bar{B}_s^0 \rightarrow \Lambda\bar{p}K^+$  decay modes [18, 19]. However, a detailed look at the diagrams for  $\bar{B}_s^0 \rightarrow \Lambda\bar{p}K^+$  reveals several key differences compared to the  $\bar{B}^0 \rightarrow \Lambda\bar{p}\pi^+$  decay, *cf.* Fig. 1.3.

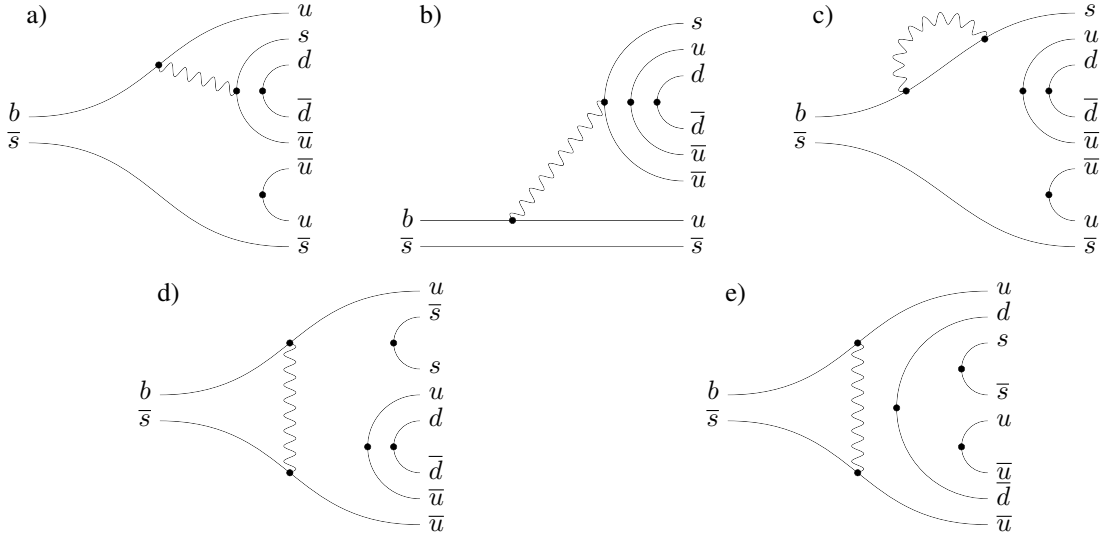


Figure 1.3: Leading order diagrams for the  $\bar{B}_s^0 \rightarrow \Lambda\bar{p}K^+$  decay. Gluon lines are omitted. The amplitudes are proportional to  $V_{ub}V_{us}^*$  (a,b,d,e) and  $V_{tb}V_{ts}^*$  (c).

The internal graph in Fig. 1.3(a) yields an initial state of

$$\bar{B}_s^0 \rightarrow \Lambda\bar{\Lambda}^* \quad \text{with } \bar{\Lambda}^* \rightarrow \bar{p}K^+ \quad , \quad (1.33)$$



fitting into the baryon pole model. The decay  $\bar{B}^0 \rightarrow \Lambda \bar{\Lambda}(1520)$  was observed by the LHCb collaboration [20] as a resonant decay of  $B^+ \rightarrow p \bar{p} K^+$ , and an observation of this mode in  $\bar{B}_s^0 \rightarrow \Lambda \bar{p} K^+$  would support the baryon pole model. The external graph in Fig.1.3(b) clearly supports the meson pole hypothesis,

$$\bar{B}_s^0 \rightarrow K^+ K^{-*} \quad \text{with } K^{-*} \rightarrow \Lambda \bar{p} \quad . \quad (1.34)$$

It should be pointed out that the notation  $K^{-*}$  is misleading, as in general there are several meson poles possible. Basically any charged kaon can contribute to the overall decay rate and needs to be taken into account. Theoretical analyses often assume a pole at  $m(\Lambda \bar{p}) = 0$  in order to avoid the influence of several different poles interfering with each other. The penguin amplitude in Fig.1.3(c) supports both hypotheses depending on the choice of the leading fragmentation process. As can be seen, the number of  $b \rightarrow u$  tree and  $b \rightarrow s$  penguin amplitudes for  $\bar{B}_s^0 \rightarrow \Lambda \bar{p} K^+$  is only half the number of  $\bar{B}^0 \rightarrow \Lambda \bar{p} \pi^+$  diagrams and, depending on the strong phases, this can lead to a larger or smaller overall decay rate compared to  $\bar{B}^0 \rightarrow \Lambda \bar{p} \pi^+$ . An additional contribution to the  $\bar{B}_s^0 \rightarrow \Lambda \bar{p} K^+$  decay mode is due to two  $W$  exchange diagrams, cf. Figs.1.3(d) and (e). The influence of these two amplitudes is difficult to assess. Theorists often claim these to be negligible while experimental results for  $D^0 \rightarrow K_s^0 \phi$  dominated by the  $W$  exchange amplitude reveal a surprisingly large decay rate [21]. In general, the  $W$  amplitudes are difficult to assess theoretically since they are not factorisable and therefore usually not included.

Finally, another decay mode needs to be considered, due to the presence of an  $s\bar{s}$  pair in  $\bar{B}_s^0 \rightarrow \Lambda \bar{p} K^+$  it is possible to rearrange the final state particles to find the CP conjugated decay mode  $\bar{B}_s^0 \rightarrow \bar{\Lambda} p K^-$  with similar penguin and  $W$  exchange diagrams. For the external graph in Fig.1.4(a) the fragmentation is reversed with respect to  $\bar{B}_s^0 \rightarrow \Lambda \bar{p} K^+$ , here the meson is produced in the  $W$  decay and the  $\bar{B}_s^0$  decays into the  $\Lambda \bar{p}$  pair but still supporting the meson pole hypothesis, while the internal graph should be dominated by baryon poles. Experimentally, it is not possible to distinguish between  $\bar{B}_s^0 \rightarrow \Lambda \bar{p} K^+$  and  $\bar{B}_s^0 \rightarrow \bar{\Lambda} p K^-$  without explicitly tagging the  $\bar{B}_s^0$  flavour, which is not part of this analysis, therefore, only a sum of both decay modes will be measured. The appearance of both  $\bar{B}_s^0 \rightarrow \Lambda \bar{p} K^+$  and  $\bar{B}_s^0 \rightarrow \bar{\Lambda} p K^-$  is interesting for another reason, as it allows to measure time dependent CP violation in a future dedicated analysis. CP violation in general in the Standard Model will be discussed in more detail in the following section.

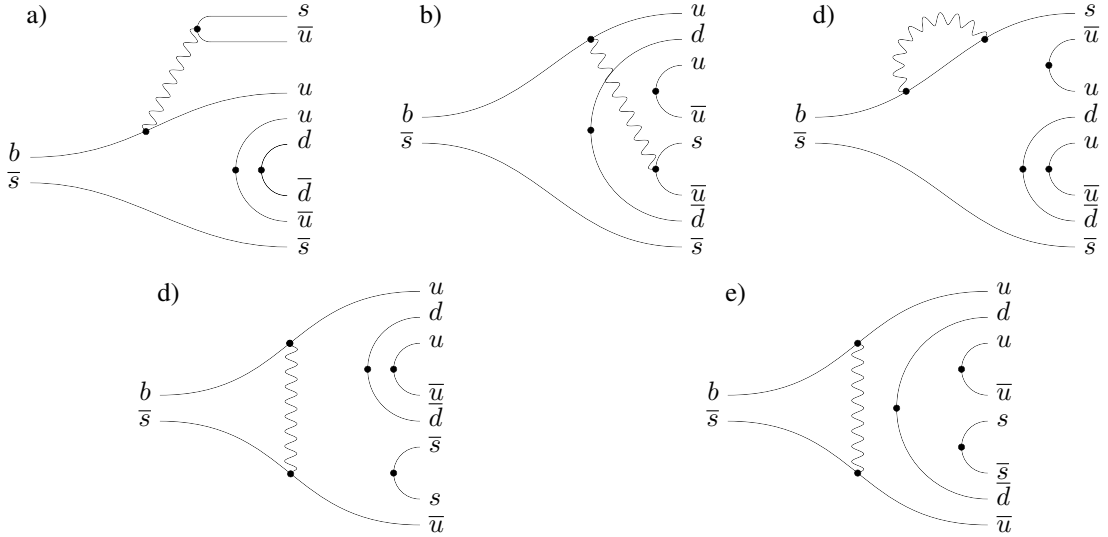


Figure 1.4: Leading order diagrams for the  $\bar{B}_s^0 \rightarrow \bar{\Lambda} p K^-$  decay. Gluon lines are omitted. The amplitudes are proportional to  $V_{ub}V_{us}^*$  (a,b,d,e) and  $V_{tb}V_{ts}^*$  (c).

Within the factorisation and meson pole framework predictions are made for the branching fraction for  $\bar{B}^0 \rightarrow \Lambda \bar{p} \pi^+$  and  $\bar{B}^0 \rightarrow \Sigma^0 \bar{p} \pi^+$  [16]. The latter shares the quark content and amplitudes with  $\bar{B}^0 \rightarrow \Lambda \bar{p} \pi^+$ , but instead of the  $\Lambda$

isospin singlet the  $\Sigma^0$  isospin triplet state is produced. One finds,

$$\begin{aligned} \mathcal{B}(\bar{B}^0 \rightarrow \Lambda \bar{p} \pi^+) &\sim 0.5 \times 10^{-6} \\ \mathcal{B}(\bar{B}^0 \rightarrow \Sigma^0 \bar{p} \pi^+) &\sim 0.9 \times 10^{-6} \end{aligned} \quad (1.35)$$

The predicted branching fraction for the  $\bar{B}^0 \rightarrow \Sigma^0 \bar{p} \pi^+$  mode is larger than for the  $\bar{B}^0 \rightarrow \Lambda \bar{p} \pi^+$  mode. The  $\bar{B}^0 \rightarrow \Lambda \bar{p} \pi^+$  decay mode was observed by the *BABAR* and *BELLE* collaborations [12], for the  $\bar{B}^0 \rightarrow \Sigma^0 \bar{p} \pi^+$  decay mode the *BELLE* collaboration determined an upper limit [22],

$$\begin{aligned} \mathcal{B}(\bar{B}^0 \rightarrow \Lambda \bar{p} \pi^+) &= (3.14 \pm 0.29) \times 10^{-6} \\ \mathcal{B}(\bar{B}^0 \rightarrow \Sigma^0 \bar{p} \pi^+) &< 3.8 \times 10^{-6} \end{aligned} \quad (1.36)$$

The experimental branching fraction is significantly larger than the theoretical prediction, which indicates the limits of the factorisation approach and hints to large non-factorisable contributions. The inference between the penguin and tree amplitude scales with the CKM angle  $\gamma$ , therefore, larger values for  $\gamma$  increase the decay rates for the  $B_{(s)}^0 \rightarrow p \bar{\Lambda}(\Sigma^0) \pi^-$  decays. While not being of interest in this analysis,  $\bar{B}_{(s)}^0 \rightarrow \Sigma^0 \bar{p} h^+$  events need to be considered as a background to both the  $\bar{B}^0 \rightarrow \Lambda \bar{p} \pi^+$  and  $\bar{B}_s^0 \rightarrow \Lambda \bar{p} K^+$  decay modes. The predicted and experimental dependence of the branching fraction on the invariant baryon antibaryon mass is shown in Fig. 1.5. The appearance of an enhancement near the threshold indicates a dominance of the meson pole like dynamics.

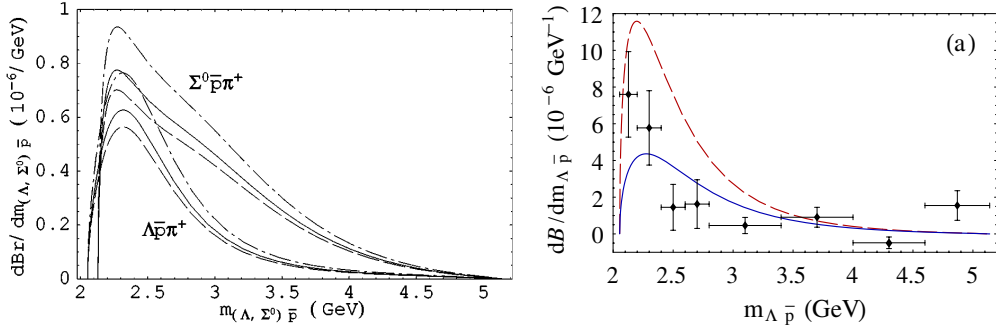


Figure 1.5: Dependence of the branching fraction for  $\bar{B}^0 \rightarrow \Lambda \bar{p} \pi^+$  and  $\bar{B}^0 \rightarrow \Sigma^0 \bar{p} \pi^+$  on the invariant baryon antibaryon mass. The left plot shows the prediction from [16] for different number of colours, The dashed, solid, and dot-dashed lines correspond to  $N_c = 2, 3, \infty$ , respectively. The right plot shows two extreme cases for the dependence calculated in [23] overlaid with the *BELLE* data from [22].

### 1.2.3 Discrete Symmetries within the Standard Model

The standard model is a collection of two Yang-Mills-theories, namely the QCD and QFD, and as such conserves CPT, the product of parity, charge conjugation and time reversal. Since particles are described by field operators, each can be categorised according to its behaviour with respect to the discrete symmetries, *cf.* Section 1.1.3.

Quantum chromodynamics conserves in addition to CPT each symmetry on its own. There is no difference between a coloured quark and an anti-coloured antiquark. The QCD is left-right symmetric as well. Quantum flavour dynamics consists of three different currents, the electro-magnetic, the neutral, and the charged current. The electro-magnetic current conserves CPT as well as each discrete symmetry on its own. The neutral and charged current, however, only conserve CPT.

### 1.2.4 Time Reversal Asymmetry within the Standard Model

The time reversal symmetry is only violated in the weak interaction and arises due to the existence of at least three families of fermions. As a consequence of the Higgs mechanism, the weak down-type quarks are a mixture of the

mass eigenstates of the down-type quarks. The mixing between the down-type quarks is described by the CKM matrix, *cf.* Eq. (1.23). The CKM matrix is a unitary  $3 \times 3$ , matrix with four physical parameters, three Euler angles and one complex phase, the standard parametrisation leaving  $V_{ud}$  and  $V_{cb}$  real is given as

$$\mathbf{V}_{\text{CKM}} = \begin{pmatrix} 1 & 0 & 0 \\ 0 & c_{23} & s_{23} \\ 0 & -s_{23} & c_{23} \end{pmatrix} \begin{pmatrix} c_{13} & 0 & s_{13}e^{-i\delta_{13}} \\ 0 & 1 & 0 \\ -s_{13}e^{i\delta_{13}} & 0 & c_{13} \end{pmatrix} \begin{pmatrix} c_{12} & s_{12} & 0 \\ -s_{12} & c_{12} & 0 \\ 0 & 0 & 1 \end{pmatrix}, \quad (1.37)$$

with  $c_{ij} = \cos \theta_{ij}$ ,  $s_{ij} = \sin \theta_{ij}$ , and  $\theta_{ij} \in [0, \pi/2]$ . For the CKM matrix to be unitary twelve unitarity relations between the matrix elements have to be fulfilled. These can be used to construct two unitary triangles, leading to the introduction of six angles describing the unitarity triangles together with six edges. These unitary triangles are a measure for CP and T violation, hence it is useful to express Eq. (1.37) in terms of the edges, *i.e.* the quark transition probabilities, and the angles to read

$$\mathbf{V}_{\text{CKM}} = \begin{pmatrix} |V_{ud}| & |V_{us}| & |V_{ub}|e^{-i\tilde{\gamma}} \\ -|V_{cd}|e^{i\tilde{\phi}_4} & |V_{cs}|e^{-i\tilde{\phi}_6} & |V_{cb}| \\ |V_{td}|e^{-i\tilde{\beta}} & -|V_{ts}|e^{i\tilde{\phi}_2} & |V_{td}| \end{pmatrix}. \quad (1.38)$$

Using the definition of Eq.1.38 CP and T violation for the decay  $\bar{B}^0 \rightarrow A\bar{p}\pi^+$  can be explained. Taking the  $b \rightarrow uW^-$  transition from Figs. 1.2(a) to (d) the decay rate depends on  $V_{ub}$  and can be simplified to the Feynman diagram shown in Fig. 1.6(a) since  $V_{us}$  contains no phase information in this parametrisation. The time reversed process is shown in Fig. 1.6(b), where the  $u$  quark picks up the  $W$  boson to form the  $b$  quark in the final state. The important point is the complex conjugation of the CKM matrix element  $V_{ub}$  into  $V_{ub}^*$  for the time reversed process. In the absence of an additional amplitude no T violation will be seen since the decay rate is proportional to the square of the matrix element  $V_{ub}$ .

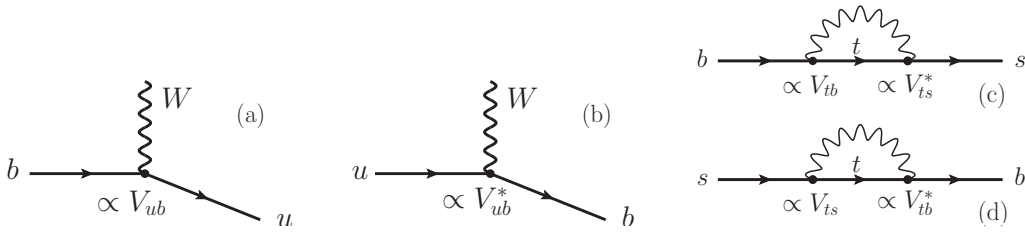


Figure 1.6: Decay of a  $b$  quark into a  $u$  quark by emission of a  $W$  boson (a), and the time reversed process (b). The diagram in (c) shows the  $b \rightarrow s$  penguin decay and (d) its time reversed process.

The picture changes with the existence of the second  $b \rightarrow s$  penguin amplitude. The two decay amplitudes interfere and the interference is given as

$$|A^{\text{Total}}|^2 = |A^{b \rightarrow u}|^2 + |A^{b \rightarrow s}|^2 + |A^{b \rightarrow u}||A^{b \rightarrow s}| \cos(\gamma' + \Delta\delta) \quad (1.39)$$

$$|A_T^{\text{Total}}|^2 = |A_T^{b \rightarrow u}|^2 + |A_T^{b \rightarrow s}|^2 + |A_T^{b \rightarrow u}||A_T^{b \rightarrow s}| \cos(-\gamma' + \Delta\delta) \quad (1.40)$$

for the decay and its T reversed process where  $\gamma'$  is the weak phase difference between the amplitudes and  $\Delta\delta$  the difference between the strong phases. Under time reversal the weak phases flip their sign, while the strong phases remain unchanged. Subtracting both rates yields

$$|A_T^{\text{Total}}|^2 - |A^{\text{Total}}|^2 = |A^{b \rightarrow u}||A^{b \rightarrow s}| \sin \gamma' \sin \Delta\delta. \quad (1.41)$$

In the case of non vanishing phase differences the violation of the time reversal symmetry can be observed. However, the whole argument is also true for CP violation, the weak phase changes its sign with respect to CP as well, which is based on CPT invariance. So any such measurement of T violation is also a measurement of CP violation. The dependence of the branching fraction on the CKM angle  $\gamma'$  is shown in Fig. 1.7. The theoretical predictions used

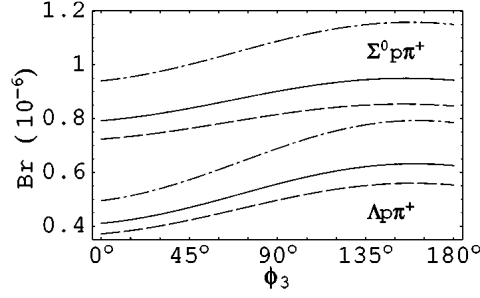


Figure 1.7: Dependence of the branching fraction for  $\bar{B}^0 \rightarrow \Lambda \bar{p} \pi^+$  and  $\bar{B}^0 \rightarrow \Sigma^0 \bar{p} \pi^+$  on the CKM angle  $\gamma$ , here noted as  $\phi_3$  [16]. The current value of  $\gamma$  is  $\gamma = 73.2^{+6.3}_{-7.0}^\circ$  [7]. The notation is the same as in Fig. 1.5.

$\gamma' \approx \gamma = 54^\circ$ , however, even using the most recent results for  $\gamma$  from the CKM fitter [7], the predictions deviate significantly from the experimental results [22, 24, 25].

The measurement of time reversal violation without measuring CP violation as well is experimentally quite challenging. First, since the time reversal operator is an anti-unitary operator, there are no observable eigenvalues to measure, second in contrast to classical mechanics the decay of a particle cannot be time reversed in the sense, that the mother particle can be produced by colliding two beams of the decay products. The particles produced in the decay of a particle are in a coherent state, whereas two colliding particles are in an incoherent state. Therefore, T violation can only be measured under additional assumptions. A popular method is to construct triple products using the momentum of the daughter particle of a decay meson. In recent years there have been several analyses of  $D$  meson decays [26] using this approach. Several theoretical analyses proposed probing  $B$  decays as well using these triple products to measure CP and T violation [27, 28]. Usually the triple products are constructed as

$$\mathcal{O} = \mathbf{p}_1 \cdot (\mathbf{p}_2 \times \mathbf{p}_3) \quad . \quad (1.42)$$

Since  $\mathbf{p}$  is odd with respect to T, the triple product itself is odd with respect to T as well. In order to measure T violation it is useful to define the following asymmetry,

$$A_T = \frac{\Gamma(\mathcal{O} > 0) - \Gamma(\mathcal{O} < 0)}{\Gamma(\mathcal{O} > 0) + \Gamma(\mathcal{O} < 0)} \quad , \quad (1.43)$$

counting the number of events with a positive and negative sign. A non vanishing expectation value for the asymmetry is a sign of T violation. These triple products, however, are also odd with respect to parity and as a result sensitive to CP violation as well. So in order to be only sensitive to T violation, a different kind of triple product can be constructed containing the spin vector of at least one daughter, such as

$$\mathcal{O} = \mathbf{s}_\Lambda \cdot (\mathbf{p}_\Lambda \times \mathbf{p}_{\pi^+}) \quad (1.44)$$

for the  $\bar{B}^0 \rightarrow \Lambda \bar{p} \pi^+$  decay. The  $\Lambda$  is chosen instead of the proton, because its spin vector can be estimated in its decay. Since the angular momentum is even with respect to parity but odd under T reversal the asymmetry defined in Eq. (1.43) is only sensitive to T violation. This approach was suggested by C.Q. Geng and Y.K. Hsiao [1, 2]. Experimentally, there are several challenges using the operator defined in Eq. (1.44), which will be subject of the next section. There remains an additional problem in interpreting the measured asymmetry. A non-vanishing expectation value for the asymmetry defined in Eq. (1.43) is only a sign for T violation in absence of final state interaction between the daughter particles. Final state interaction is QCD rescattering and can mock a fake asymmetry. Using an additional assumption allows to circumvent this issue. The QCD is CP invariant and, therefore, the final state interaction should be CP invariant as well. Calculating the asymmetry  $A_T$  only for the particle, a separate asymmetry for the CP conjugated decay and then taking the difference between these should cancel the QCD contributions, in

case for the  $\bar{B}^0 \rightarrow \Lambda \bar{p} \pi^+$  the asymmetries take the form of

$$A_T = \frac{N^{\bar{B}^0 \rightarrow \bar{p} \Lambda \pi^+}(\mathcal{O} > 0) - N^{\bar{B}^0 \rightarrow \bar{p} \Lambda \pi^+}(\mathcal{O} < 0)}{N^{\bar{B}^0 \rightarrow \bar{p} \Lambda \pi^+}(\mathcal{O} > 0) + N^{\bar{B}^0 \rightarrow \bar{p} \Lambda \pi^+}(\mathcal{O} < 0)} \quad (1.45)$$

$$\bar{A}_T = \frac{N^{B^0 \rightarrow p \bar{\Lambda} \pi^-}(\mathcal{O} > 0) - N^{B^0 \rightarrow p \bar{\Lambda} \pi^-}(\mathcal{O} < 0)}{N^{B^0 \rightarrow p \bar{\Lambda} \pi^-}(\mathcal{O} > 0) + N^{B^0 \rightarrow p \bar{\Lambda} \pi^-}(\mathcal{O} < 0)} \quad (1.46)$$

$$\mathcal{A}_T = 1/2(A_T - \bar{A}_T) \quad . \quad (1.47)$$

The asymmetry  $A_T$  refers to the  $b$  quark in the  $\bar{B}^0$  meson and  $\bar{A}_T$  to the  $\bar{b}$  quark of the  $B^0$  meson. The difference between the two asymmetries  $\mathcal{A}_T$  depends on the weak and strong phase difference

$$\mathcal{A}_T \propto \sin \gamma' \cos \Delta\delta \quad , \quad (1.48)$$

and is maximal for a vanishing strong phase difference in contrast to the asymmetry given in Eq. (1.41) which is null for a vanishing strong phase difference. The predictions for  $A_T$ ,  $\bar{A}_T$ , and  $\mathcal{A}_T$  given in [1, 2] are list in Tab. 1.1.

Table 1.1: Prediction for  $A_T$ ,  $\bar{A}_T$ , and  $\mathcal{A}_T$  given in [1, 2]. The calculations have been performed assuming  $\gamma' \approx \gamma = 57^\circ$  for a vanishing and non-vanishing strong phase difference.

$A_T, \bar{A}_T, \mathcal{A}_T$	$\gamma = 57^\circ$
$\Delta\delta \neq 0$	(12.0, -8.4, 10.2)%
$\Delta\delta = 0$	(10.4, -10.4, 10.4)%

### 1.3 Experimental Determination of the Triple Product

Usually, analyses only use momentum vectors to construct triple products and measure the CP or T asymmetry, *cf.* the previous section. This is usually caused by the choice of the decay under investigation. Decays such as  $B^- \rightarrow K^- \pi^+ \pi^-$  consists only of pseudo scalar particles in the final state and using the momentum vectors is the only option to construct the triple product. In contrast to pseudo scalar mesons, baryons such as the  $\Lambda$  baryon have spin, which can be used to construct the triple product. The determination of the spin, however, is experimentally very challenging. Only intermediate baryons can be utilised in such analyses. The theorists C.Q. Geng and Y.K. Hsiao proposed using  $\Lambda$  baryons in the charmless  $B$  decay  $\bar{B}^0 \rightarrow \Lambda \bar{p} \pi^+$ . The advantage of using  $\Lambda$  baryons instead of protons is that the  $\Lambda$  decay will be utilised to estimate the spin vector of the  $\Lambda$ .

The triple product defined in Eq. (1.44) is calculated in the  $B$  rest frame. The momentum vectors are determined in the lab frame, *i.e.* the LHCb detector, and the  $\Lambda$  spin vector in the  $\Lambda$  rest frame. Making use of Lorentz transformations these vectors are boosted into the  $B^0$  rest frame. This is trivial for the momentum vectors, since the energy of each daughter is well known and can be used to construct the momentum four vector, which is then boosted to the  $B^0$  rest frame. In order to transform the  $\Lambda$  spin vector, the polarisation four vector has to be constructed. Any polarisation four vector  $\varepsilon^\mu$  needs to fulfil

$$\varepsilon^\mu p_\mu = 0 \quad . \quad (1.49)$$

Since  $p_\mu = (m, \mathbf{0})$  in the rest frame of any massive particle, the time like component of  $\varepsilon_\mu$  is given by

$$\varepsilon^0 = 0 \quad . \quad (1.50)$$

For the space like components of  $\varepsilon_\mu$  the direction of the proton from the  $\Lambda$  decay is taken. The  $\Lambda$  polarisation vector is then given by

$$\varepsilon_\mu = (0, \mathbf{s}) = (0, \mathbf{p}_p/2|\mathbf{p}_p|) \quad (1.51)$$

in the  $\Lambda$  rest frame. Unfortunately this assumption is only correct for some  $\Lambda$  decays. The  $\Lambda$  decay rate is given by

$$\Gamma \propto 1 + \gamma \hat{\omega}_f \cdot \hat{\omega}_i + (1 - \gamma) [\hat{\omega}_f \cdot \hat{n}] [\hat{\omega}_i \cdot \hat{n}] + \alpha ([\hat{\omega}_f \cdot \hat{n}] + [\hat{\omega}_i \cdot \hat{n}]) + \beta (\hat{n} \cdot [\hat{\omega}_f \times \hat{\omega}_i]) \quad , \quad (1.52)$$

where  $\alpha$ ,  $\beta$ , and  $\gamma$  are the  $\Lambda$  decay parameters,  $\hat{n}$  is the unit vector in the direction of the proton momentum, and  $\hat{\omega}_i$  and  $\hat{\omega}_f$  are unit vectors in the direction of  $\Lambda$  and  $p$  baryon spins, respectively.

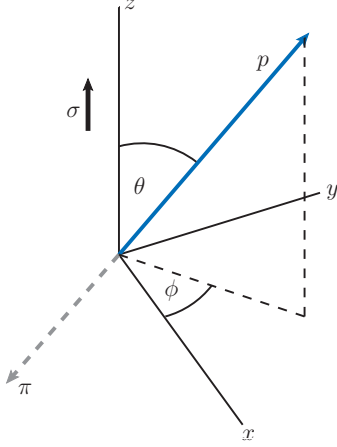


Figure 1.8: Illustration of the  $\Lambda$  rest frame,  $\sigma$  being the  $\Lambda$  spin  $p$  the proton momentum.

Since a single  $\Lambda$  baryon is always polarised, the equation can be simplified to read

$$\Gamma \propto 1 + \alpha (\hat{\omega}_i \cdot \hat{n}) \quad . \quad (1.53)$$

The scalar product  $\hat{\omega}_i \cdot \hat{n}$  product is equivalent to the cosine of the angle between the  $\Lambda$  spin and the proton momentum, *cf.* Fig. 1.8, one finds

$$\Gamma \propto 1 + \alpha \cos \theta \quad . \quad (1.54)$$

The decay parameter  $\alpha$  describes the parity violation in the  $\Lambda$  decay. The decay parameters for the  $\Lambda$  and  $\bar{\Lambda}$  are known [12],

$$\alpha(\Lambda \rightarrow p\pi^-) = +0.642 \pm 0.013 \quad (1.55)$$

$$\alpha(\bar{\Lambda} \rightarrow \bar{p}\pi^+) = -0.71 \pm 0.08 \quad (1.56)$$

and agree within the uncertainty, which means CP is not violated by the  $\Lambda$  decay. In the final fit, both hypotheses, CP conservation and CP violation in the  $\Lambda$  decay will be tested.

The expectation value for  $\cos \theta$  is given by

$$\langle \cos \theta \rangle = \frac{1}{2} \int_{-1}^{+1} \cos \theta (1 + \alpha \cos \theta) d \cos \theta = +\frac{\alpha}{3} \quad . \quad (1.57)$$

This angular dependency results in a large dilution factor that needs to be taken into account when calculating the triple product asymmetry. A final remark has to be made on the CP behaviour of the spin. For any angular momentum vector one finds

$$CP \mathbf{s} = +\mathbf{s} \quad , \quad (1.58)$$

whereas for the momentum vector one finds

$$CP \mathbf{p} = -\mathbf{p} \quad . \quad (1.59)$$

As a result the  $\Lambda$  flavour needs to be taken into account and an additional minus sign needs to be applied for the CP conjugated decay. Additional dilution factors arise from the experimental determination, these will be discussed in detail later. Since only the sign of the triple product is relevant, it is calculated using the unit vectors instead of the full momentum and spin vectors.

## 1.4 The Dalitz Plot

The Dalitz plot, first introduced by R.H. Dalitz [29], allows studies of the dynamic structure of three body decays. For a pseudo scalar particle decaying into three final state particles the partial decay width can be expressed by

$$d\Gamma = \frac{1}{(2\pi)^3 32\sqrt{s^3}} |\mathcal{M}|^2 dm_{12}^2 m_{23}^2 \quad , \quad (1.60)$$

with  $s$  being the mass of the mother particle,  $m_{ij}^2 = p^\mu(i)p_\mu(j)$  the invariant two body daughter masses, and  $|\mathcal{M}|^2$  is the quantum mechanical matrix element for the decay. The scatter plot between  $m_{ij}^2$  and  $m_{ik}^2$  ( $j \neq k$ ) is called the

Dalitz plot and can be used to visualise the matrix element  $|\mathcal{M}|^2$ . Resonant intermediate states appear as bands in the corresponding two body invariant mass and the density distribution allows to determine the angular quantum numbers of the intermediate state. In its relativistic invariant formulation the Dalitz plot appears in a triangular shape in case all daughter particles are massless and its edges are determined by the mass of the mother particle. In case the daughter particles are massive, the shape of the Dalitz plot changes accordingly. In Fig. 1.9 the kinematically allowed Dalitz plot for the  $\bar{B}^0 \rightarrow \Lambda \bar{p} \pi^+$  decay is shown, the maximum values are indicated and the overall allowed range is also shown. The kinematic borders can be calculated using

$$m(\bar{p}\pi^+)_{\pm}^2 = m_{\pi^+}^2 + m_{\bar{p}}^2 + \frac{1}{2m(\Lambda\bar{p})^2} \left[ (m_{\bar{B}^0}^2 - m(\Lambda\bar{p})^2 - m_{\pi^+}^2)(m(\Lambda\bar{p})^2 - m_{\Lambda}^2 + m_{\bar{p}}^2) \pm \sqrt{\lambda(m(\Lambda\bar{p})^2, m_{\bar{B}^0}^2, m_{\pi^+}^2)} \sqrt{\lambda(m(\Lambda\bar{p})^2, m_{\Lambda}^2, m_{\bar{p}}^2)} \right] \quad (1.61)$$

with the kinematic function  $\lambda(x, y, z)$  defined as,

$$\lambda(x, y, z) = x^2 + y^2 + z^2 - 2xy - 2yz - 2zx \quad . \quad (1.62)$$

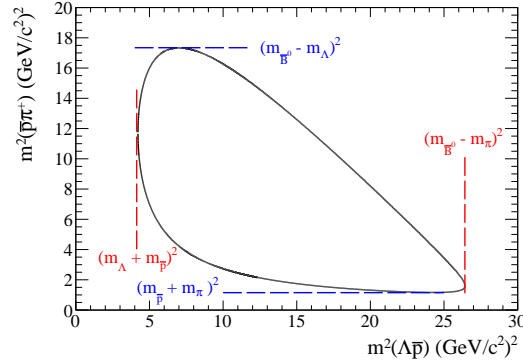


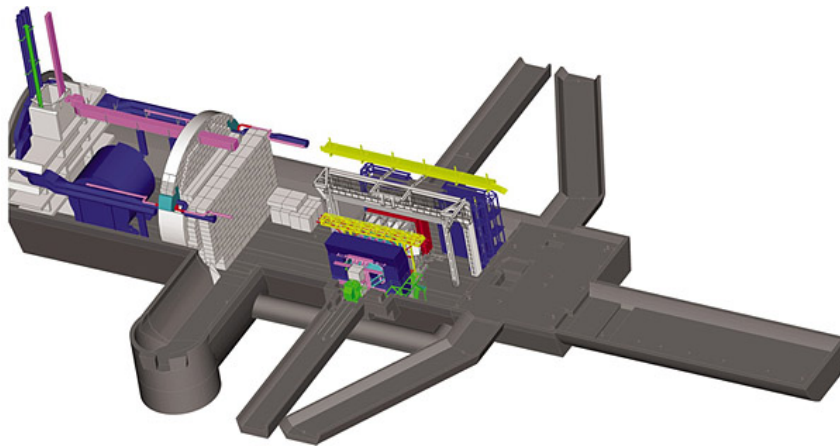
Figure 1.9: Shape of the kinematically allowed Dalitz plot for the  $\bar{B}^0 \rightarrow \Lambda \bar{p} \pi^+$  decay. The edges of the Dalitz plot are determined by the  $B$  mass and the individual daughter masses.

In general, the Dalitz plot of three body baryonic  $B_{(s)}^0$  decays can have a multitude of interesting structures. These include the known threshold enhancement (*cf.* Fig. 1.5) and intermediate baryon resonances like  $\Delta$  or nucleon resonances decaying in to  $p\pi^-$ . A recent LHCb analysis [20] revealed the  $\Lambda(1520)$  resonance decaying into  $pK^-$  as an intermediate resonance. Contribution from charmed decays can also appear in the Dalitz plot, for example the decay  $\Lambda_c^+ \rightarrow \Lambda \pi^+$  can be found. In contrast to the broad resonances, charm decays appear as very small bands due to their long lifetimes. Finally, there are more exotic states such as glueballs, bound states of gluons, which can appear in decays containing two baryons of identical flavour. Another, possible explanation of the threshold enhancement is a bound state of two baryons, the baryonium. Neither glueballs nor baryonium states have been found experimentally. Apart from all these intermediate decays, there is usually also a contribution from non resonant decays, *i.e.* true three body decays.

For the decays at hand, possible structures to be found in the  $\bar{B}^0 \rightarrow \Lambda \bar{p} \pi^+$  Dalitz are the threshold enhancement, the  $\Lambda_c^+ \rightarrow \Lambda \pi^+$  contribution from  $\bar{B}^0 \rightarrow \Lambda_c^+ \bar{p}$ , and the  $\bar{\Delta}$  or nucleon resonances decaying in to  $\bar{p}\pi^+$ . According to the previous measurements of  $\bar{B}^0 \rightarrow \Lambda \bar{p} \pi^+$  the only contribution seen is the threshold enhancement, there is no evidence for any other resonant structures and even the non resonant decays are suppressed [24, 25]. The Dalitz plot for  $\bar{B}_s^0 \rightarrow \Lambda \bar{p} K^+$  should also contain a pronounced threshold enhancement, as the decay is quite similar to the  $\bar{B}^0 \rightarrow \Lambda \bar{p} \pi^+$  decay. Instead of  $\Delta$  or nucleon resonances, the  $\Lambda(1520)$  and similar resonances can contribute to the overall decay rate. The  $\Lambda_c^+$  could also appear through the decay  $\Lambda_c^+ \rightarrow \Lambda K^+$ , this mode, however, is Cabibbo suppressed. For both decays the  $\Lambda_c^+$  contribution is due to the  $b \rightarrow c$  tree decay  $\bar{B}^0 \rightarrow \Lambda_c^+ \bar{p}$ , which is a different process than the penguin and  $b \rightarrow u$  contribution for  $\bar{B}_{(s)}^0 \rightarrow \Lambda \bar{p} h^+$ , it is, therefore, vetoed in the selection and only contributions from charm less decays are considered.

## Chapter 2

# The LHCb-experiment



The LHCb (LHCbeauty) experiment consists of the LHCb detector and the Large Hadron Collider (LHC). The LHCb experiment is a dedicated heavy flavour experiment whose goal is to search for effects of new physics in decays of beauty and charm quarks. The LHCb experiment is a third generation  $B$  factory. The first generation were the ARGUS and CLEO experiments and the second generation the *BABAR* and Belle experiments. All of these were  $e^+e^-$  machines operating at the  $\Upsilon(4S)$  resonance corresponding to a centre of mass energy of  $\sqrt{s} = 10.58$  GeV. Experimentally there are a lot of advantages in doing so. A significant disadvantage of these  $B$  factories is the low  $b\bar{b}$  production cross-section of only  $\sigma(e^+e^- \rightarrow b\bar{b}) = 1.09$  nb [30]. During the lifetime of the *BABAR* experiment about 470 million  $B\bar{B}$  pairs were produced. At  $pp$  interactions at  $\sqrt{s} = 7$  TeV the  $b\bar{b}$  cross-section in the geometric region of the LHCb detector is  $\sigma(pp \rightarrow b\bar{b}X) = (75.3 \pm 5.4 \pm 13.0)$   $\mu\text{b}$ . Together with the luminosity of the LHC, about  $10^{12}$   $b\bar{b}$  pairs are produced per year. In addition to that, all kind of  $b$  hadrons are produced compared to only  $B^0$  and  $B^+$  at the  $\Upsilon(4S)$  resonance. This leads to a higher sensitivity compared to the previous experiments and allows to probe the Standard Model with unprecedented precision.



## 2.1 Large Hadron Collider

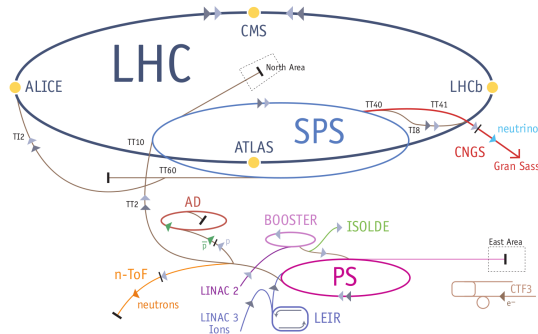


Figure 2.1: Layout of the LHC accelerator complex. The layout shows the four major experiments. The energy of the protons is ramped up through several smaller accelerators. Additional experiments also receive their protons from these.

The Large Hadron Collider (LHC) is a  $pp$  storage ring located in the former LEP tunnel at CERN, the European Organisation for Nuclear Research. At the LHC two proton beams collide each with a design energy of 7 TeV, however, during the 2011 and 2012 data taking periods the beam energy was limited to 3.5 TeV and 4 TeV, respectively. The design luminosity of  $\mathcal{L} = 2 \times 10^{32} \text{ cm}^{-2}\text{s}^{-1}$  was superseded during most of the 2011 and 2012 data taking. Most of the data taking took place at  $\mathcal{L} = 3.5 \times 10^{32} \text{ cm}^{-2}\text{s}^{-1}$  and  $\mathcal{L} = 4 \times 10^{32} \text{ cm}^{-2}\text{s}^{-1}$  in 2011 and 2012, respectively. In 2011 a luminosity scaling procedure was introduced. Its goal was to keep the instantaneous luminosity constant during a fill of the LHC. This minimised the luminosity decay usually observed during a fill and allowed to maintain the same trigger configuration during the whole fill.

Another problem that all LHC experiments had to cope with was pile-up. Pile-up is the average number of visible  $pp$  interactions per bunch crossing. During Run I the average bunch spacing was 50 ns instead of the planned 25 ns. In order to achieve the designated luminosity the number protons per bunch was increased. This also led to an increased pile up rate. Fig. 2.2(a) shows the variance of the instantaneous luminosity and the pile-up over a time period from July 2010 till December 2012.

The data sample available for physics analyses contains  $L = 38 \text{ pb}^{-1}$  (7 TeV),  $1.11 \text{ fb}^{-1}$  (7 TeV), and  $2.08 \text{ fb}^{-1}$  (8 TeV) for 2010, 2011, and 2012, respectively. Fig. 2.2(b) shows the integrated luminosity during Run I of the LHC.

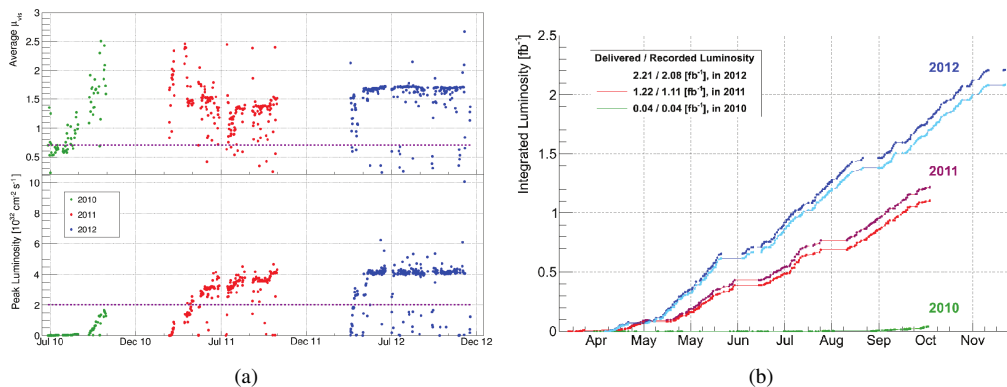


Figure 2.2: (a) Distribution of the average number of visible interactions (top) and the instantaneous luminosity over Run I at the LHCb interaction point. The dotted lines show the design values. (b) Integrated luminosity of the LHCb experiment taken during the Run I of the LHC.

## 2.2 LHCb Detector

The LHCb detector is a single arm spectrometer that covers the range from 15 mrad to 300 mrad in the bending and from 15 mrad to 250 mrad in the non bending plane. The detector geometry is dictated by the production of the  $b\bar{b}$  pairs which are produced predominately into a small forward or backward cone along the  $pp$  beam axis. In order to measure the momentum of the charged particles a magnetic field is necessary. The spectrometer magnet provides an integrated field of about 4Tm deflecting charged particles in the horizontal plane. The magnet influences the proton beams and three dipole magnets are dedicated to compensate the effect and stabilise the beams.

The LHCb tracking system consists of the Vertex Locator (VELO) placed around the interaction region inside a vacuum tank and four planar tracking stations, one, the TT, located upstream and three Tracking stations T1-T3 downstream of the magnet. Silicon strip detectors are employed in the TT and the inner sections of T1-T3. The outer sections of T1-T3 consist of straw tubes. Charged particles require a minimum momentum of 1.5 GeV/c to pass the magnet and reach the tracking stations T1-T3. Downstream of the tracking system are the electromagnetic and hadronic calorimeters whose main task is to contribute to the trigger system followed by the muon system. Particle identification is performed by two Cherenkov detectors. The individual detector components are introduced in the next sections followed by a description about the track reconstruction, the trigger system and the data structure of the LHCb experiment.

The LHCb coordinate is an orthogonal right-handed system defined as follows,  $\hat{z}$  along the  $z$  axis, the  $x$  parallel to the cavity ground and the  $y$  axis perpendicular to the  $x$ - $z$  plane, *cf.* Fig. 2.3.

A detailed review of all components and their operational status can be found in [31] and [32].

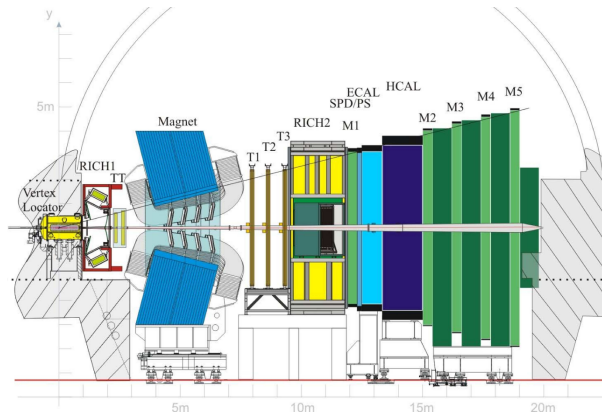


Figure 2.3: Schematic representation of the LHCb detector. The coordinate system is indicated.

### 2.2.1 Vertex Locator – VELO

The Vertex Locator, short VELO, is designed to provide precise measurement of tracks near the interaction point and designated to use these to identify primary, *i.e.* from  $pp$  interactions, and secondary vertices originating from long lived beauty and charm hadrons. This task requires a high signal-to-noise ratio in each element to ensure an efficient trigger performance as well as a high efficiency of each channel. An excellent spatial resolution is needed as well in order to achieve the required impact parameter resolution allowing to distinguish tracks originating from secondary vertices from those from the primary vertex. The impact parameter is the perpendicular between the path of the particle, *i.e.* the track, and the centre of the interaction, *i.e.* the  $pp$  interaction. The design of the LHCb detector places geometrical constraints on the VELO, detecting charged particles with a pseudorapidity  $\eta \in (1.6, 4.9)$  emerging from primary vertices within  $|z| < 10.6$  cm, a polar angle coverage of 15 mrad for a track with  $z = 10.6$  cm, a minimum distance of 7 mm to the beam axis. In general any track in the angular acceptance of 300 mrad should pass through at least two VELO modules.

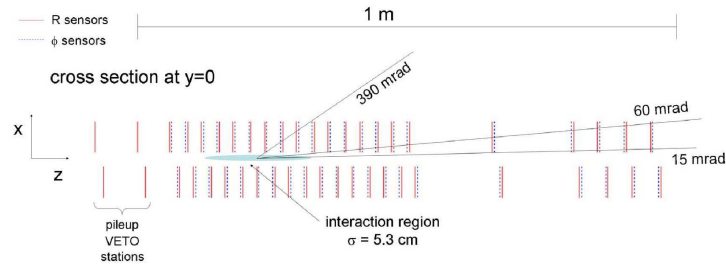


Figure 2.5: Layout of the two VELO halves and the individual modules in the  $x$ - $z$  plane [31].

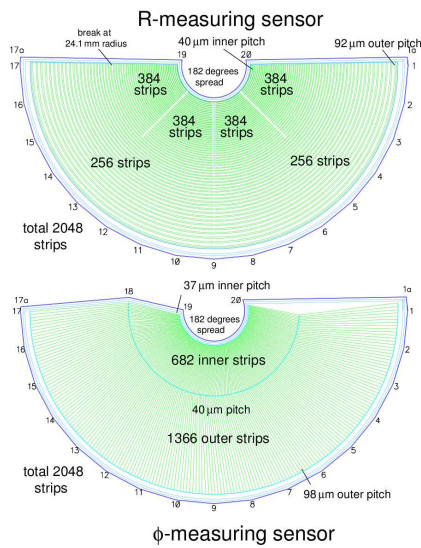


Figure 2.4: Layout of the VELO modules in the  $x$ - $y$  plane in the closed state [33].

The VELO consists of two 21 back-to-back silicon strip detector modules. Fig. 2.4 shows the layout of two VELO modules in the  $x$ - $y$  plane. The VELO uses a cylindrical coordinate system with  $\hat{r}$ ,  $\hat{\phi}$ ,  $\hat{z}$ . The modules provide a measurement of the  $r$  and  $\phi$  coordinates at a fixed value of  $z$ . The choice of cylindrical coordinates allows for the fast track reconstruction needed in the software stage of the trigger (sec. 2.5). The pitch between the silicon modules increases with  $r$  so that the spatial resolution is best near the interaction point and decreases towards the edge of the modules.

The modules are placed along the  $pp$  beam axis. Fig.2.5 shows the assembly of the VELO modules. The VELO modules need to be very close to the interaction region to fulfil the geometric requirements, however, the aperture of the LHC increases during the injection of a new fill requiring the VELO modules to retract by 3 cm. This is achieved by retracting both halves during the injection of a new fill and once a stable beam is declared the halves are closed again.

In the closed state the two detector halves overlap providing full azimuthal coverage and aiding the alignment process. The distance needed to be smaller than 5 cm in the central region reducing the average extrapolation distance between the first hit in the detector and the vertex. The distance of the modules increases with  $z$ . Upstream of the interaction point there are two additional modules perpendicular to the  $pp$  beam axis. This is the pile-up-veto system designed to veto events with multiple primary vertices. The VELO modules are mounted in a vessel in order to maintain a vacuum around the sensors. It is separated from the machine vacuum by a thin aluminium foil. This arrangement was chosen to minimise the amount of material traversed by the charged particles before interacting with the sensors.

The spacial resolution of the VELO has been determined using data taken in 2010. The resolution depends on the pitch between the silicon strips as shown in Fig. 2.6 [32].

## 2.2.2 Planar Tracking Stations

The planar tracking stations consist of three different detectors arranged in one station upstream of the magnet, the TT station, and three stations downstream of the magnet, the T1-T3 stations (see Fig.2.7).

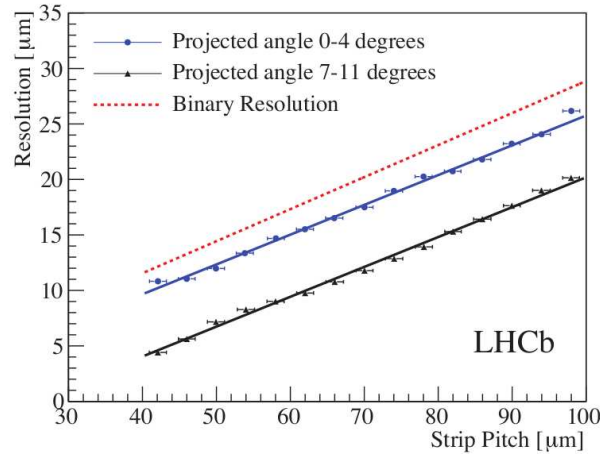


Figure 2.6: The VELO hit resolution as a function of the pitch between the silicon strips for the R sensors. Results are shown for two angle ranges and a single-hit binary system [32].

### 2.2.2.1 Silicon Tracker

The Silicon Tracker (ST) consists of the TT the Inner Tracker IT, which are the sections close to the beam axis of the T1-T3 stations. Both detectors are made of silicon strip detectors with a pitch of about  $200\ \mu\text{m}$ . This allows for a single-hit resolution of about  $50\ \mu\text{m}$ . The TT is located upstream of the magnet and covers the whole acceptance of the LHCb experiment. The IT covers a  $120\ \text{cm} \times 40\ \text{cm}$  cross shaped area at the centre of the downstream tracking stations. Each of the four ST stations consists of four detection layers in an  $(x-u-v-x)$  pattern. The  $x$  layers are made of vertical strips. In the  $u$  and  $v$  layer the strips are rotated by a stereo angle of  $-5^\circ$  and  $+5^\circ$ , respectively. The momentum resolution is dominated by multiple scattering, so that it is necessary to keep the material budget as small as possible.

The three IT stations consist of four individual detector boxes. The right hand side of Fig. 2.7 shows the arrangement of the IT detector modules. Each box consists of four sections with seven detector modules each. The silicon sensors used in the modules have a pitch of  $198\ \mu\text{m}$  between each other.

The hit resolution in data was found to be  $52.6\ \mu\text{m}$  and  $50.3\ \mu\text{m}$  for the IT and TT detectors, respectively.

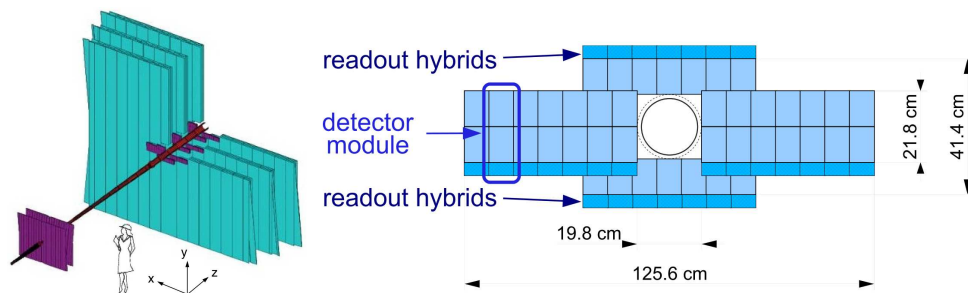


Figure 2.7: Layout of the planar tracking stations (left). Arrangement of the IT around the beam pipe covering the more active central region [31].

### 2.2.2.2 Outer Tracker

The Outer Tracker OT is designed as an array of gas tight straw tube modules. The hits are determined by measurement of the drift time of the electrons from the ionised gas molecules to the wire located at the centre of the straw tube. The recorded drift time is proportional to the distance of the particle trajectory to the wire and can be used to reconstruct the trajectory of the charged particle. The gas mixture is chosen to be Argon (70%) and CO<sub>2</sub> (30%). The detector modules are arranged in three stations (T1-T3, *cf.* Fig. 2.7). Each station consists of four modules, arranged in a  $(x-u-v-x)$  pattern similar to the TT. The maximum drift-time is about 35 ns but in order to account for variations in the time of flight of the particles, signal propagation through the wire and offsets in the electronics three consecutive bunch crossings are read out of a positive L0 trigger on the first bunch crossing. This time window is approximately 75 ns. The drift time distributions are shown in Fig. 2.8. Using data the single hit resolution was determined to be 205  $\mu\text{m}$  which is close to the design value of 200  $\mu\text{m}$ .

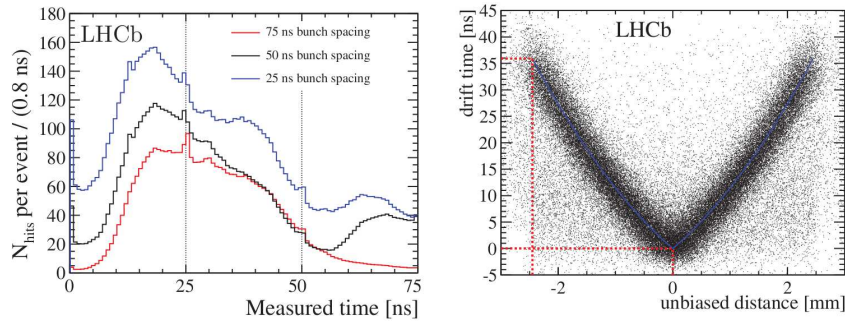


Figure 2.8: Drift-time distribution for the modules closest to the beam for three different bunch crossing rates (left). Drift time versus distance (right). The dotted lines indicate the centre and the edge of the wire, corresponding to a drift-time of 0 ns and 36 ns, respectively [31].

### 2.2.3 Rich Imaging Cherenkov (RICH) Detectors

The Cherenkov effect is used to identify the charged tracks in the LHCb detector. The unique layout of the LHCb detectors poses special conditions on the RICH detector. At large polar angles the momentum spectrum is softer than at small polar angles. It is difficult to cover the whole momentum range from a few GeV to 100 GeV, hence the particle identification (PID) system consists of two detectors covering different momentum ranges. The upstream detector, RICH1, covers the low momentum of  $\approx 1 \text{ GeV}/c$  up to  $60 \text{ GeV}/c$  using aerogel and C<sub>4</sub>F<sub>10</sub> radiators. The downstream detector, RICH2, covers the high momentum range from  $\approx 15 \text{ GeV}/c$  up to and beyond  $100 \text{ GeV}/c$  using a CF<sub>4</sub> radiator. The RICH1 located upstream of the magnet covers the whole angular acceptance of the LHCb detector. The RICH2 located downstream of the magnet covers a limited angular acceptance from  $\pm 15 \text{ mrad}$  to  $\pm 120 \text{ mrad}$  ( $x$ - $z$  plane) and  $\pm 100 \text{ mrad}$  ( $x$ - $y$  plane). In both detectors a combination of flat and spherical mirrors are used to focus the Cherenkov light out of the detector acceptance into Hybrid Photo Detectors (HPD). The HPDs are covered by an external iron shield in order to reduce the influence of the field created by the bending magnet.

Charged particles originating from or near the  $pp$  interaction point are followed through the radiator. Cherenkov photons are emitted uniformly along each track in the aerogel and gas radiators. The Cherenkov photons are ray-traced through the optical system and the impact points in the plan of the HPDs are recorded. The Cherenkov angle is reconstructed assuming the photon emission occurred at the centre of the RICH detector.

Aerogel is the ideal radiator in the range of refractive indices between gas and liquid. Silica aerogel is made of quartz and is solid but has a very small density. The refractive index  $n$  can be tuned in the range of  $n \in [1.01, 1.10]$  and is ideally suited for particle identification of particles with a momentum of a few  $\text{GeV}/c$ . The refractive index of the aerogel in the RICH1 was chosen to be  $n = 1.03$  at  $\lambda = 400 \text{ nm}$ . The number of detected photo-electrons



for a particle with  $\beta = 1$  passing through the aerogel is  $\sim 6.5$ . After the first run it was decided to remove the aerogel from the RICH1. The fluorocarbon gases were chosen because their refractive indices match the momentum spectrum of particles in the LHCb detector. The refraction indices are  $n = 1.0014$  and  $n = 1.0005$  at  $\lambda = 400 \text{ nm}$  for  $\text{C}_4\text{F}_{10}$  and  $\text{CF}_4$ , respectively, and the estimated number of photo-electrons is  $\sim 30$  and  $\sim 22$  for particles with  $\beta = 1$ . The layout of the RICH detectors can be found in Fig. 2.9.

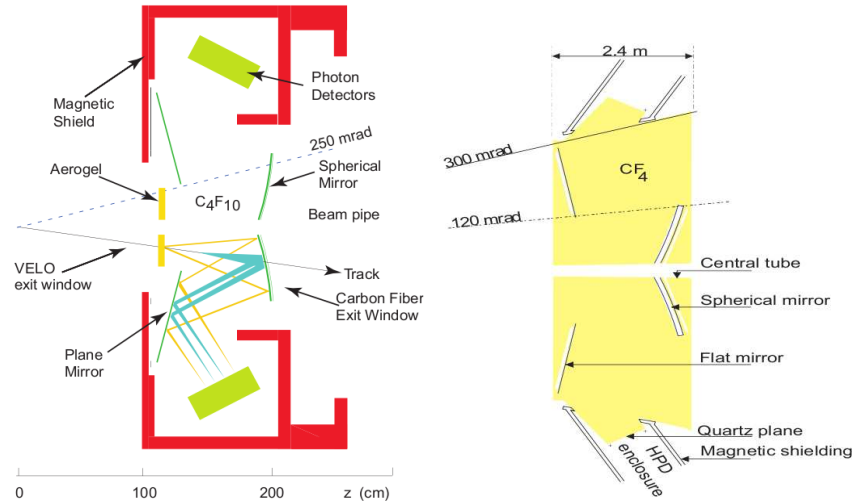


Figure 2.9: Layout of the RICH detectors, on the left hand side the RICH1 and on the right hand side the RICH2 [31].

### 2.2.4 Calorimeters

The calorimeter-system consists of four elements, the Scintillating Pad Detector (SPD), the Preshower Detector (PS), the Electromagnetic Calorimeter (ECAL), and the Hadronic Calorimeter (HCAL) and fulfills several functions. The main purpose is selecting transverse energy hadron, electron and photon candidates for the first trigger level. In addition the calorimeters provide single photon and  $\pi^0$  reconstruction and electron identification capabilities.

The SPD and PS are both made of a plane of scintillator tiles separated by a thin lead layer. The ECAL and HCAL have shashlik and sampling constructions. All four detectors follow the same principle, light from the organic scintillators is transmitted via optical fibers to photo multipliers. Since the hit density varies over the calorimeter surface, a variable lateral segmentation is adopted. The calorimeter segmentation is illustrated in Fig. 2.10.

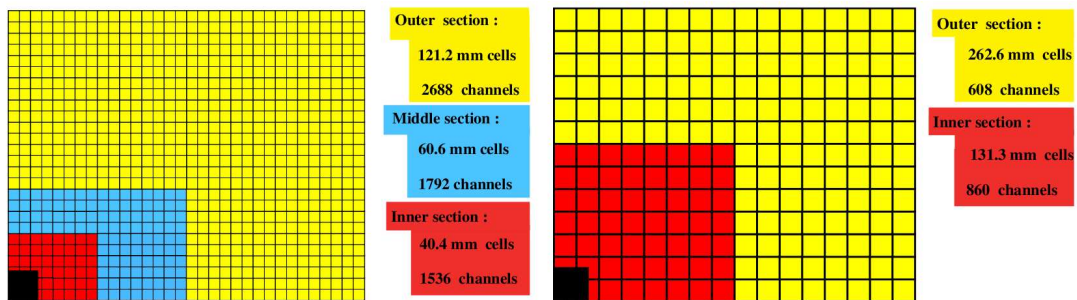


Figure 2.10: Lateral segmentation for the SPD, PS, and ECAL (left) and the HCAL (right). A quarter of the detector front face is shown and the dimensions are given for the ECAL and HCAL [31].

### 2.2.5 Muon System

Muons are of special interest for the LHCb experiment. Muons cannot be produced in strong processes that dominate the hadronic environment of the LHC so that any event in which a muon appears is interesting. Muons are present in the final states of many  $CP$  sensitive decays, *e.g.*  $B^0 \rightarrow J/\psi K_S^0$  and  $B_s^0 \rightarrow J/\psi \phi$  with  $J/\psi \rightarrow \mu^+ \mu^-$ . Muons from semileptonic  $B$  decays provide a tag for the initial  $B$  flavour for oscillation and  $CP$  analyses. In addition, muons appear in rare flavour changing neutral currents, which probe physics beyond the Standard Model. Because of these arguments a high muon detection efficiency is demanded of the LHCb detector.

The layout of the muon system is shown Fig. 2.11 and it is composed of five stations M1–M5 placed along the beam axis.

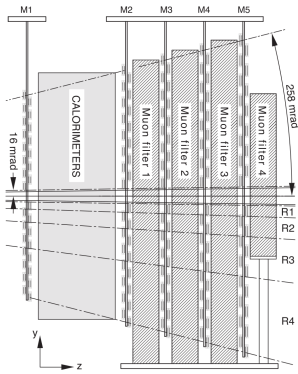


Figure 2.11: Layout of the muon system [31].

The angular acceptances of the muon system are 20 mrad (16 mrad) and 306 mrad (258 mrad) in the bending (non-bending) plane. This allows for an acceptance of about 20% for muon from semileptonic beauty hadron decays. The stations M2–M5 are placed downstream of the calorimeters and are interleaved with iron absorbers in order to prevent non muon particle to pass through the stations. The minimum momentum for a muon to pass all stations is 6 GeV/c. The first station M1 is placed in front of the calorimeter system in order to improve the transverse momentum measurement in the trigger. All stations of a projected geometry, *i.e.* all transverse dimensions scale with the distance from the interaction point. Stations M1–M3 have a high spatial resolution along the bending plane and are used to define the track direction and calculate the transverse momentum of the muon candidate with a resolution of about 20%. The remaining stations have limited spatial resolution, as their main purpose is identification of penetrating muons.

Muti-wire proportional chambers are used throughout the station except for the centre region of station M1 in which the expected particle flux exceeds the safety limits for ageing and, therefore, triple gas electron multiplier (GEM) detectors are used.

### 2.2.6 Dipole Magnet

The LHCb uses a warm magnet with a saddle-shaped coil design in a window frame yoke with sloping poles. The constraints of the LHCb detector pressed for this design. It has to have an integrated field of 4Tm for a track with a length of 10 m but the magnetic field inside the RICH1 needs to be smaller than 2mT yet the field between the VELO and the TT should be as high as possible for a precise momentum measurement. The layout of the magnet is shown in the left hand side of Fig. 2.12.

The magnetic field may have two configurations,  $\mathbf{B}(z) = \pm B(z)\hat{y}$ . Any single choice results in charge asymmetries in the detector and in order to prevent these, each magnet configuration is used and the data taking is split equally among the magnet polarities. The Polarities are defined as

$$\begin{aligned} \mathbf{B}(z) &= +B(z)\hat{y} && \text{(Magnet - Up)} \\ \mathbf{B}(z) &= -B(z)\hat{y} && \text{(Magnet - Down)} \end{aligned}$$

and the  $z$  dependence of both configurations is shown in Fig. 2.12.

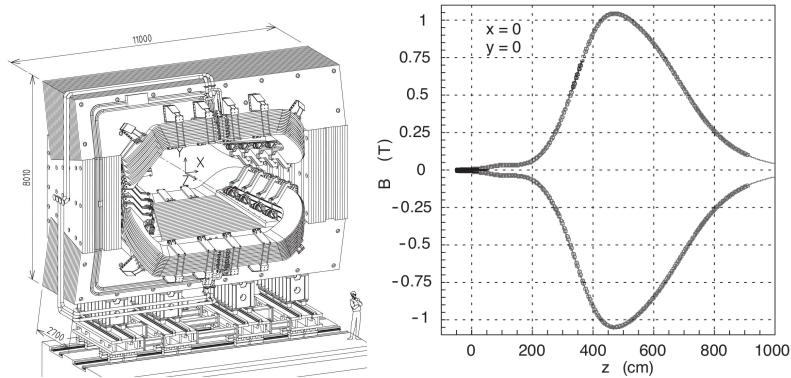


Figure 2.12: Layout of the LHCb magnet (left);  $z$  dependence of the magnetic field (right) [31].

## 2.3 Event Reconstruction

### 2.3.1 Track Reconstruction

Charged particles traversing the tracking system are reconstructed from hits in the VELO, TT, IT, and OT detectors. Depending upon their interaction with these detectors the following track types are defined, *cf.* Fig. 2.11

**Long tracks** pass through the complete tracking system having hits in both the VELO and the T stations, and optionally in the TT station. Long tracks have the most precise momentum estimate and are the most important set of tracks for physics analyses.

**Downstream tracks** pass only through the TT and T stations. These are important for the reconstruction of long-lived neutral  $V^0$  particles such as  $K_S^0$  mesons and  $\Lambda$  baryons. Due to the long lifetimes most  $K_S^0$  and  $\Lambda$  particles decay outside the VELO.

**Upstream tracks** pass only through the VELO and the TT station. In general those tracks' momentum is too low to transverse the magnet but they can generate Cherenkov photons in case  $p > 1 \text{ GeV}/c$ . As a result they can be used to understand backgrounds in the particle identification algorithms of the RICH1.

**T tracks** have only hits in the T station and are usually caused by particles produced in secondary interactions. Similar to upstream tracks these are useful for the particle identification with the RICH2.

**VELO tracks** pass only through the VELO and are typically large-angle or backward tracks, that are useful for the reconstruction of the primary vertices.

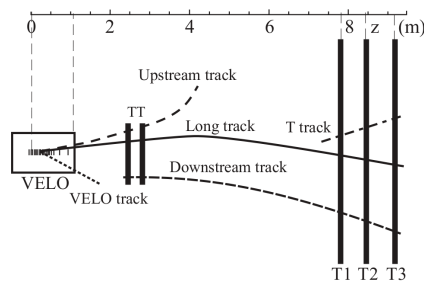


Figure 2.13: Illustration of the various track types, the  $z$  coordinate position is also indicated [32].



The long track reconstruction starts in the VELO. The track finding algorithm searches for straight line trajectories with at least three hits in  $R$  and  $\phi$  sensors. Afterwards two additional algorithms take over, the first algorithm, the `forward tracking`, combines the VELO tracks with information from the T stations. The VELO information and a single hit in the T stations fully determine the trajectory and momentum of a particle. The algorithm then searches for additional hits in the T stations along the trajectory in order to find the best combination of hits to define the `long track`. The second algorithm, called `track matching`, combines the VELO tracks with track segments from the T stations provided by a standalone track finding algorithm. A T track segment needs at least one hit in the  $x$  layers and one in the stereo layers in each T station. The `long tracks` created by both algorithms are then combined and duplicates are removed. Finally, hits in the TT station consistent with the trajectories of each track are added in order to improve the momentum measurement.

The `downstream tracks` are reconstructed by starting with T track segments which are extrapolated through the magnetic field into the TT station. The algorithm then searches for corresponding TT hits.

In a final step, all tracks are refitted with a `Kalman filter` [34]. The fit accounts for multiple scattering and energy loss effects. The quality of the fit is determined by the  $\chi^2$  per degrees of freedom. Due to the large extrapolation distance between the tracking stations, it is inevitable to have false combinations of track segments called `ghost tracks`. The fake rate is typically 6.5% but can increase up to 20% in events with high multiplicities. The fake rate is significantly reduced by application of neural network classifier (*cf.* sec. 3.1.6.3) using the results of the track fit, the track kinematics and number of measured hits with expected hits. The classifier output is called `Ghost probability`.

### 2.3.2 Momentum and Mass Resolution

As a preliminary study being part of a service task the momentum resolution for `long tracks` was investigated. In a data driven method  $J/\psi \rightarrow \mu^+ \mu^-$  decays are used. Due to the small lifetime of the  $J/\psi$  the invariant dimuon mass resolution is defined by the momentum resolution of the two muons. In addition to that, the  $J/\psi \rightarrow \mu^+ \mu^-$  offers a very good signal-to-background ratio increasing the statistical precision. Since the invariant  $J/\psi$  mass is given by

$$m^2(\mu^+, \mu^-) = p^2(\mu^+)p^2(\mu^-)(1 - \cos \theta) \quad , \quad (2.1)$$

assuming ultra-relativistic muons, the momentum resolution of the muons is given by

$$\left(\frac{\sigma_{p_{\mu^+}}}{p_{\mu^+}}\right)^2 + \left(\frac{\sigma_{p_{\mu^-}}}{p_{\mu^-}}\right)^2 = 4 \left(\frac{\sigma_m}{m}\right)^2 - \left(\frac{\sigma_{\cos \theta}}{1 - \cos \theta}\right)^2 \quad . \quad (2.2)$$

Eq. (2.2) is used to determine the absolute momentum resolution  $\delta p/p$  by fitting the invariant  $\mu^+ \mu^-$  mass in a grid of  $22 \times 22$  bins in order to determine  $\sigma_m/m$ . The mass resolution for  $p(\mu^+) \approx p(\mu^-)$  is shown in the left plot of Fig. 2.14. For each bin the values for  $\sigma_{\cos \theta}/1 - \cos \theta$  are determined by using the mean value its distribution in each bin. The values of  $\sigma_{\cos \theta}$  are determined by the track fit. The right hand side of eq. (2.2) is calculated for each bin and a binned two-dimensional likelihood fit is used to determine  $\delta p/p$ . The resulting momentum resolution is shown in the right plot of Fig. 2.14. The momentum resolution is about 5% for momenta below 20 GeV/ $c$  and increases to about 8% for momenta  $\sim 100$  GeV/ $c$ .

### 2.3.3 Vertex Reconstruction

In the context of the LHCb experiment two kinds of vertices need to be distinguished, primary vertices (PVs) and secondary vertices (SVs). Primary vertices correspond to the  $pp$  interaction; secondary vertices are the decay vertices of  $b$  and  $c$  hadrons or interactions of charged particles with the detector. Vertices with at least 5 tracks are considered primary vertices. The `pile-up VETO` stations located upstream of the  $pp$  interaction in the VELO are used to determine the number of tracks in each primary vertex and are used to veto events with more than one primary vertex. A primary vertex with 25 tracks has a resolution of 13  $\mu\text{m}$  in  $x$  and  $y$  and 71  $\mu\text{m}$  in  $z$ . Closely

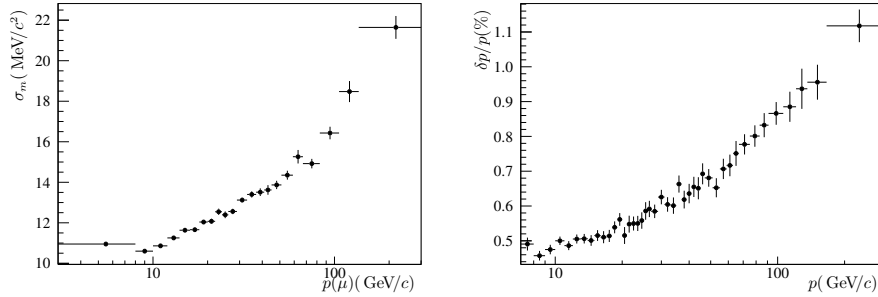


Figure 2.14: Mass (left) and momentum (right) resolution for  $J/\psi \rightarrow \mu^+ \mu^-$  decays. The momentum resolution is about 5‰ for momenta below 20  $\text{GeV}/c$  and about 8‰ for momenta about 100  $\text{GeV}/c$ .

related to the primary vertex is the impact parameter (IP). The IP of a track is defined as the distance between a PV and the point of closest approach (POCA). A track originating from a PV should have  $\text{IP} = 0$  within the uncertainties. Tracks from SVs, on the other hand, should have a non-zero IP with respect to the PV. This fact is used heavily in LHCb data analyses including the current one and it is therefore vital to have an optimal IP resolution. The IP resolution is dominated by the effects of multiple scattering of particles with the detector components, the resolution of the position of the track, and the extrapolation distance of the track, *i.e.* the distance from the first measured hit to the interaction point. The overall VELO layout was designed with these points in mind. The IP resolution depends linearly on  $1/p_T$  due to multiple scattering and the VELO geometry and is 13  $\mu\text{m}$  for a particle with an asymptotically high transverse momentum.

Secondary vertices are constructed by fitting the decay products of  $b$  or  $c$  hadrons. In a decay chain like  $\bar{B}^0 \rightarrow \Lambda \bar{p} \pi^+$  this is done for the  $\Lambda$  and  $B^0$  decay individually. As an alternative it is useful to fit the whole decay chain in a single fit. This is done by the Decay Tree Fitter (DTF) algorithm [35]. Using a Kalman filter algorithm the whole decay tree is fitted with the mass hypothesis of each daughter particle. Unlike usual vertex fit algorithms, the DTF also uses information upstream of a given vertex by fitting the whole decay chain instead of individual decays. This improves the invariant mass resolution. In addition the DTF package allows the usage of mass and vertex constraints that further improve the resolution and help suppress background candidates. The decays of  $V^0$  particles such as  $\Lambda \rightarrow p \pi^-$  and  $K_S^0 \rightarrow \pi^+ \pi^-$  pose additional challenges. With lifetimes at the order of  $10^{-10}$  s and momenta of about 30  $\text{GeV}/c$  only one third of the  $V^0$  particle decay in the VELO, *i.e.* the decay products are long tracks, the other two thirds decay before the TT station, *i.e.* the decay products are downstream tracks. In general, the invariant mass resolution for long track  $V^0$  particles is about a factor of two smaller compared to downstream track  $V^0$  particles.

## 2.4 Particle Identification

Particle identification (PID) is crucial in flavour experiments. Identifying a track as an electron, kaon, muon, or a proton allows to calculate the energy of the given particle rather than relying on the measurement of the energy deposition in the calorimeters. This greatly improves the resolution of the invariant mass of intermediate particles such as  $B$  and  $D$  mesons. In addition to that, particle identification allows to determine the flavour of decaying hadrons. At the large track momenta of the LHCb experiment it is impossible to distinguish between kaons and pions in the decay  $\bar{B}^0 \rightarrow K^- \pi^+$  and, in order to measure the direct CP violation in this decay, it is vital to be able to tag, *i.e.* identify the flavour, the  $B$  meson decay. Measurements of time dependent CP violation also need information on the  $B$  flavour at its production, which can be provided by a kaon or pion in the jet close by the  $b$  hadron, again being able to identify the pion or kaon is crucial.

At the LHCb experiment PID is provided by four detectors, the calorimeters, the RICH detectors, and the muon system.

### 2.4.1 Calorimeter and Muon System Based Particle Identification

The role of the calorimeter in terms of particle identification is to provide information on electrons, photons and neutral pions. Neutral particles are distinguished from charged particles by searching for the absence of a track in front of the energy disposition. The shape of the energy cluster is used to differentiate between photons and  $\pi^0$ -mesons. In case the energy cluster is associated with a charged track, the electron hypothesis is constructed to allow separation of electrons and hadrons.

Muon identification is based on the extrapolation of trajectories found in the tracking system into the muon system and searches for hits in the muon system within rectangular intervals around the extrapolation points. The intervals depend on the momentum and their parameters are tuned to maximise the muon efficiency while still provide low misidentification rates. Likelihoods for the muon and non-muon hypotheses are calculated for each muon candidate based on the average squared distance of hits closest to the interpolation points.

### 2.4.2 RICH System Based Particle Identification

The primary role of the RICH system is to identify charged hadrons, *i.e.* pions, kaons, and protons, and it is used on the the analysis level and the software trigger stage, *cf.* Sec. 2.5. Apart from hadron identification, the RICH system also provides additional information for the lepton identification.

The identification procedure follows a likelihood based approach. The observed hits in the photo-detectors are compared to the expected pattern for a given particle hypothesis. The likelihood is constructed by calculating the effective emission angle for all hit-track combinations and maximised by varying the particle hypotheses. The likelihood includes all tracks of the event and all radiator simultaneously.

The performance of the RICH detector is governed by the resolution  $\sigma(\theta_C)$  with which the Cherenkov angle of the emitted photons can be reconstructed. Using isolated high momentum tracks the resolution is determined to be  $\sigma(\theta_C) = (1.618 \pm 0.002)$  mrad for the RICH1 and  $\sigma(\theta_C) = 0.68 \pm 0.02$  for the RICH2, respectively [32]. Since the opening angle of the Cherenkov cone depends on the refractive index and the velocity of the passing object distinctive bands are formed when plotted as a function of the momentum, which can be used to determine the mass of the passing particle. Figure 2.15 shows the distinctive bands for the Cherenkov angles for different particles.

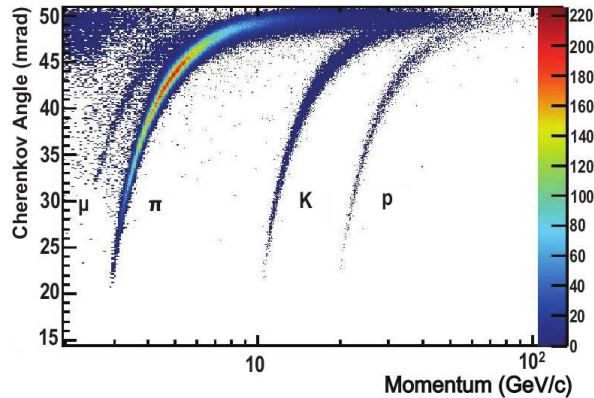


Figure 2.15: Reconstructed Cherenkov angle for isolated tracks as a function of the track momentum for the  $C_4F_{10}$  radiator [32].

### 2.4.3 Combined Particle Identification

The PID information gathered in the sub-detectors is combined in order to provide a single powerful variable. This combination follows two different approaches, the first implements a log likelihood approach and the second is based on an artificial neural net.

The log likelihood approach sums the individual likelihoods of each sub-system linearly into a combined log likelihood  $\Delta L(X)$ , where  $X$  represents either the electron, muon, kaon, or proton hypothesis. It is useful to compare these individual likelihoods with the pion likelihood as a reference value by calculating the difference,

$$\Delta \log L(X - \pi) = \log L(X) - \log L(\pi) \quad , \quad (2.3)$$

that offers a measure how likely the  $X$ -mass hypothesis for a given track is compared the the  $\pi$ -mass hypothesis. The neural net approach is designed to improve the upon the likelihood approach by taking into account correlations between the individual sub-detectors and including additional information from the event. The neural net variables are usually denoted as `ProbNNX`, where  $X$  again represents either the electron, muon, kaon, or proton hypothesis.

An important aspect of the particle identification is the calibration of both the likelihood and the neural net variable. In order to determine the exact behaviour of kaon, pions, and protons clean sources of these particle are needed. These should be obtained via kinematic selections only in order to avoid any biases due to `PID` preselections. Naively there are several easy choices, but each comes with own challenges.

Samples with a high kaon purity can be obtained from excited  $D^+$  meson decays. The  $D^0 \rightarrow K^- \pi^+$  candidates from the  $D^{*+} \rightarrow D^0 \pi^+$  decay are very clean and the  $\pi^+$  can be used to tag the  $D^0$  flavour and therefore determine which track belongs to the kaon without any `PID` requirement. The cross feed from the double Cabibbo suppressed  $D^0 \rightarrow K^+ \pi^-$  is negligible. Since the  $D^{*+}$  mesons are produced in charm jets as well as  $b$  hadron decays, the coverage of the  $(p, \eta)$  spectrum for tracks coming from both charm and beauty hadron decays is good.

A good source for charged pions are  $K_s^0$  meson decay into a pair of oppositely charged pions. Due to the long life-time and the secondary vertex the purity of the sample is very high. The long life-time is reduced the efficiency as usually only the  $K_s^0$  candidates reconstructed from `Long` tracks are used. The statistics are sufficient and the coverage is good as well.

The natural choice for protons are  $\Lambda$  baryons with the decay  $\Lambda \rightarrow p \pi^-$ . The long life-time and the clean vertex separation reduces the number of background events to a negligible level. Using the Armenteros-Podolanski plot [36], described in detail in Sec 3.2.4, it is possible to distinguish  $\Lambda$ ,  $\bar{\Lambda}$ , and  $K_s^0$  candidates on merits of kinematic variables only and no `PID` information need to be applied beforehand to distinguish between the proton and the pion. However, as mentioned earlier, the long life-time of the  $\Lambda$  baryons is problematic and usually only the  $\Lambda$  candidates reconstructed from `Long` tracks are used. Another, more serious issue, is the coverage of the large  $(p, \eta)$  spectrum observed in hadronic  $b$  and  $c$  decays. The  $\Lambda \rightarrow p \pi^-$  decays cover only the low momentum region sufficiently. In order to overcome this problem, an additional source for protons is used, the decay  $\Lambda_c \rightarrow p K^- \pi^+$ . Using the same technique as for the  $D^{*+}$  candidates, *i.e.* using the  $\Sigma_c^{++/0}$  resonance decaying into  $\Lambda_c \pi^\pm$ , the background is reduced but remains sizeable compared to the other control modes. Therefore, additional selection criteria need to be applied in order to reduce cross feed from related decays of charged  $D^+$  and  $D_s^+$  mesons including a `PID` selection on the kaons. Adding this reference channel improves the coverage, but does not solve the problem entirely. As a result, the systematic uncertainty on the proton `PID` is larger than for pions or kaons.

A final issue rests with the simulated events, the simulated data underestimate the amount of tracks produced in the  $pp$  collisions and as a result overestimate the `PID` performance since more tracks increase the difficulty to match each track to the correct Cherenkov ring.

## 2.5 LHCb Trigger Ensemble

For any hadron collider experiment the trigger is a crucial component selecting interesting events compared to noise events. As mentioned before, the LHCb experiment is dedicated to study weak decays of  $b$  and  $c$  hadrons as well as  $\tau$  leptons. In general, events without one of these characteristics is considered a noise event. Due to the high data rates it is not feasible to collect all events and the trigger should filter all interesting events while rejecting the noise events. The LHCb trigger consists of two dedicated stages, the Level-0 (L0) and the High Level Trigger (HLT). During the first run of the LHC the trigger reduced the data rate from 20 MHz based on a proton-proton bunch crossing every 50 ns to 2 – 5 kHz [32]. These triggered events are the basis for the physics analyses.

The L0 trigger is hardware based and uses information from the calorimeters and the muon system to reduce the event rate below 1 MHz, at which the whole detector can be read out. The HLT is software based. It is run on a dedicated event filter farm. During 2012 a fraction of L0 accepted events was deferred to disk to be analysed by the HLT during the inter-fill times thus optimising the usage of the available resources. After being accepted by the HLT the events are saved to disk and later fully reconstructed using a more accurate alignment and information from all sub-detectors.

### 2.5.1 Level-0 Hardware Trigger

The L0 trigger system is divided into three independent systems, the L0 calorimeter trigger, the L0 muon trigger, and the L0 pile up trigger. The latter is only used for the determination of the luminosity. The L0 trigger is synchronous with the proton-proton bunch crossing of the LHC.

The L0 calorimeter trigger builds three types of candidates based on the deposited transverse energy  $E_T$ .  $L0_{Hadron}$  is the highest  $E_T$  HCAL cluster,  $L0_{Photon}$  is the highest  $E_T$  ECAL cluster with one or two hits in the pre shower detector and no hits in the silicon pad detector in front of the HCAL. The  $L0_{Electron}$  share the requirements with the  $L0_{Photon}$  with an additional condition of at least one hit in the silicon pad detector. The transverse energy is compared to a fixed threshold and events with at least one candidate above the threshold fire the L0 trigger.

The L0 muon trigger looks for the two muon tracks with the highest  $p_T$  in each quadrant and either triggers on the largest transverse momentum of a single muon or the product of the two largest transverse momenta.

### 2.5.2 High Level Trigger

Events accepted by the L0 trigger are analysed by a software application similar to the overall LHCb software framework. The HLT application considers several independent trigger lines each applying a specific selection based on a specific event class, *e.g.*  $b$  hadron decays. The high level trigger consists of two stages. During the first level, the HLT1, a partial event reconstruction is performed, whereas in the second stage, the HLT2, a complete event reconstruction is employed.

The VELO plays a central role during the HLT1 stage. The full offline VELO track reconstruction is applied and vertices are reconstructed from intersection VELO tracks as well. Based on the L0 decision several track based trigger lines are employed. Relevant for the analysis at hand is the inclusive beauty and charm trigger line. It is based on the properties of one good quality track candidate and its selection is based on the transverse momentum (about 1.6 GeV/ $c$ ) and the displacement with respect to the primary vertex ( $IP > 0.1$  mm). The output rate is about 58 kHz and is the largest contributor to the overall HLT1 bandwidth. It is overall the most efficient trigger line not requiring a lepton in the event.

The HLT1 reduces the data rate to about 80 kHz, which is low enough to allow forward tracking for all VELO tracks, however, in 2011 only long tracks were considered lowering the efficiency to trigger  $V^0$  particles significantly. The topological inclusive beauty lines make up a significant portion of the HLT2 output rate. These lines cover all  $b$  hadron decays with at least two charged tracks in the final state and a displaced secondary vertex motivated by the long life-time of the  $b$  quark. The track selection is based on the track fit quality, the impact parameter and lepton identification. Vertices are reconstructed using either two-, three-, or four-body decays based on the distance of closest approach between the individual tracks. The pseudo  $n$ -body  $b$  hadron candidates are selected using the transverse momentum of the daughters, the minimal transverse momentum among all daughters, the  $n$ -body invariant mass, the distance of closest approach, the  $IP$   $\chi^2$ , and the  $\chi^2$  of the flight distance. The overall output rate of the inclusive topological trigger lines is 2 kHz. During the 2012 data taking the trigger performance for  $V^0$  was increased significantly, however, during the start of the 2012 run, there was a bug in the trigger software, and it was fixed during the technical stop during June 2012. This, however, complicates matters for any analysis containing  $K_S^0$  or  $\Lambda$  particles need to split their data into three independent samples according to the trigger conditions, namely 2011, 2012 pre-June, and 2012 post-June.

## 2.6 LHCb Software Environment

The LHCb software environment is comprised of different program environments suited to perform their individual purpose. In line with current approaches on software design the LHCb software contains several framework layers each providing a basic functionality for its designed purpose.

The basic framework is called `Gaudi` and is shared with the ATLAS experiment and provides elemental functionality for reading data, booking histograms and tuples, and provides a lot of mathematical operations and objects such as matrix multiplication or four-vectors. The latter are generally based on the CERN `ROOT` software package, which is heavily used in the LHCb software.

All other LHCb software applications are based on `Gaudi`, the most widely used are `Gauss`, implementing the simulation of specific decay modes, `Brunel`, implementing the basic reconstruction of tracks and vertices, `Moore`, implementing the trigger, and `DaVinci` implementing the reconstruction and analysis of reconstructed particles.

The raw data passing the L0 trigger stage are analysed by `Brunel` and `Moore` in order to decide whether the events pass the software stage of the trigger. Afterwards `DaVinci` generates lists of reconstructed particles. Each element in these lists contains a track together with PID information to form a particle candidate. Additional `DaVinci` algorithms then use these lists to reconstruct unstable composite particles such as the  $\Lambda$  baryons and later the  $B$  mesons.

Due to the large amount of data collected with the LHCb detector the whole reconstructed data is not accessible for the common LHCb user. Instead a preselection is run on dedicated computing farms. The working groups provide a set of algorithms containing the reconstruction of interesting decays and certain selection criteria designed to limit the necessary computing and storage resources. This process is called `stripping` and each individual preselection algorithms is called a `stripping line`.

Depending on the analysis, two different data formats are available. In case the analyst needs information on the whole event the `DST` format is chosen, in which each event is completely stored including all charged particles and vertices. Examples are analyses which need to `tag` the flavour of the individual  $b$  hadron. The more common case is, that the analyst is only interested in the particles contained in the decay chain listed in the `stripping line`. In this case the data are stored in  $\mu$ `DST` files. Here, only the particles contained in the decay and the corresponding vertices are stored.

Since  $\mu$ `DST` files use less amount of storage space compared to the `DST` files, the users are discouraged to use `DST` files. In general, `stripping lines` implementing `DST` files have to meet narrow bandwidth requirements usually limiting the available statistics due to the tight preselection necessary.

The  $\bar{B}^0_{(s)} \rightarrow \Lambda \bar{p} h^+$  decays can be tagged by their decay products, therefore, the information from the remaining event is not needed, therefore, the `StrippingLb2V0hhLLLine` and `StrippingLb2V0hhDDLLine`, see sec. 3.1.2, use the  $\mu$ `DST` format.

Afterwards, additional `DaVinci` algorithms are used to refine the preselection, improve the vertex fit and substitute particle hypotheses. The refinement of the event selection is done via multivariate analysis (MVA) techniques using the `TMVA` package of `ROOT`. The selected candidates are written into `RoodataSets`, which is a tuple based format of the `Roofit` package of `ROOT`. These are used to plot variables such as the invariant  $\Lambda \bar{p} h$  mass and finally to extract the number of signal decays by means of fits.

## 2.7 LHCb Recorded and Simulated Data

This analysis makes use of the combined 2011 and 2012 data samples comprising of an integrated luminosity of  $L = 3 \text{ fb}^{-1}$  taken at  $\sqrt{s} = 7 \text{ TeV}$  and  $\sqrt{8} \text{ TeV}$ , respectively. The data taken in 2011 of about  $L = 1 \text{ fb}^{-1}$  is not further split into individual runs, as no major changes were implemented during the year. The recorded data have been `restripped` using the `Reco14` version of the reconstruction software also employed in the 2012 data set

including several small changes compared to the original reconstruction. In contrast the technical stop in June 2012 saw several changes to the trigger configuration increasing the  $V^0$  reconstruction efficiency. Therefore, the 2012 data sample is split in two, a pre-June sample (2012a) and a post-June sample (2012b). The luminosities for the two 2012 sample are

$$\begin{aligned} L(2012a) &= 0.641 \text{ fb}^{-1} \\ L(2012b) &= 1.359 \text{ fb}^{-1} \end{aligned} \quad , \quad (2.4)$$

and this split will be used when the efficiencies for the different 2012 samples are combined. In the final fit the data is not split into two different samples as all effects are accounted for beforehand.

Since it is often necessary to study the behaviour of signal events without background contributions, having simulated events is very important. The events are generated using Monte Carlo (MC) methods [37]. The event generation is a three step process. The first step includes the simulation of the primary  $pp$  interaction. This step is done by `Pythia8` [38] with a dedicated LHCb configuration [39]. The most recent version contains the most recent updates on the parton distribution function of the proton, `Pythia` simulates the parton-parton interactions in which the  $b$  quarks are produced and hadronise into the different  $b$  hadrons. As a result `Pythia` is responsible for the generation of the underlying event as well as well the kinematic distribution if the  $b$  hadrons. The second is the simulation actual  $b$  hadron decay performed by `EvtGen` [40]. Dedicated decay files allow the analyst to configure decays into almost any final state include intermediate particles. A global `EvtGen` data base allows for generic decays to occur as well. In addition, `EvtGen` allows using different decay models. For example, the Dalitz plot for  $D^0 \rightarrow K_s^0 \pi^+ \pi^-$  is included allowing for a realistic generation of this  $D^0$  decay. The most general option is to use a constant matrix element. This model is called phase space and it is used in this analysis. As an example the Dalitz plot for phase space simulated events of  $\bar{B}^0 \rightarrow \Lambda \bar{p} \pi^+$  is shown in Fig. 2.16. Additional radiative processes are simulated by `PHOTOS` [41].

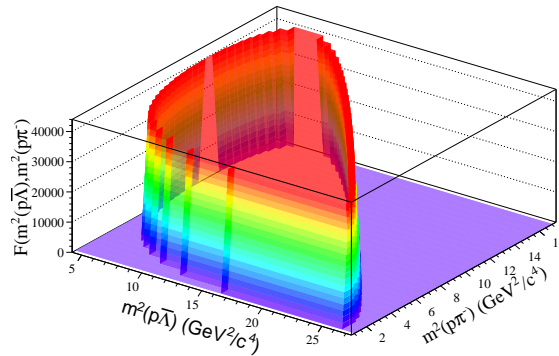


Figure 2.16: Dalitz plot for the  $\bar{B}^0 \rightarrow \Lambda \bar{p} \pi^+$  decay mode assuming a constant matrix element across the Dalitz plane before the application of the `DecProdCut`.

The third and final step includes the detector simulation based on a dedicated configuration [42] of the `Geant4` detector simulation tool kit [43]. Due to disk space limitation, only decays, whose daughters are located with the active detector volume are saved. This option is called `DecProdCut` and all analysts are encouraged to use it. Roughly four out of five events are discarded. These has several implications for the analyst, first he has to correct for the number of discarded events when calculating the overall efficiencies. This loss of events is referred as generator efficiency. The second effect is, that despite having the events generated flat across the Dalitz plot, the Dalitz plot for the generated events already includes these geometric acceptances. There are several ways to account for these effects. The method chosen for this analysis is to calculate the initial number of events before the `DecProdCut` and constructing the initially generated Dalitz plot by hand.

In general, there are three relevant official MC sample available. For given decay file 2011, 2012a, and 2012b MC data set can be generated each simulating a trigger condition that fit closely to the average conditions in each run. Usually having 2011 and 2012b samples is sufficient for analyses without  $V^0$  particles but due to the changes during the technical stop in June 2012 simulated samples are available using the conditions before and after June 2012, referred to as 2012a and 2012b samples.

### 2.7.1 Differences between Recorded Data and Simulated Data

The simulation of both the physics taking place at a centre of mass energy of  $\sqrt{8}$  TeV and the detector response for up to two hundred tracks is challenging and cannot be expected to match the data perfectly.

Beginning with the aspect of event generation, compared to an  $e^+e^-$  machine operating at lower energies, the environment on a  $pp$  machine is quite different. The cross section for  $e^+e^-$  into a pair of fermions can be calculated within Quantum Electrodynamics down to the angular distributions. The following hadronisation into  $b$  and  $c$  hadrons is also well known. The same is true for the average multiplicity in typical events. This allows the simulated events to match the physical distributions quite well and differences between the recorded and simulated data are usually second order effects. At the LHC the picture is different: the initial state is not a pair of point like fermion interacting at an energy scale, where only one process is dominant, but rather the interaction between two hadrons comprised not only of three valence quarks each but an infinite number of gluon and virtual  $q\bar{q}$  pairs. The energy regime between the interactions also covers a wide range, collisions between valence quarks usually have a large centre of mass energy, whereas collision between sea quarks or gluons typically cover a wide range of energies from a few GeV up to 100 GeV or from the non-perturbative QCD up to scales that allow perturbative calculations. It is very challenging to cover both ranges sufficiently well. As a result, the  $p_T$  and  $\eta$  distributions of the produced hadron do not fully match the data and have to be modified. The spectra of  $B^0$  and  $B_s^0$  mesons are modelled quite well, however, for  $\Lambda_b^0$  baryons the distributions are not well matched. These problems propagate into other related variables and require modifications to the simulated samples. In addition to the properties of individual particles, the overall events is not matched well to the data. The simulation in general underestimates the number of tracks per events which is related to the limited knowledge of the small angle QCD scattering that dominate the LHCb environment. This has far reaching consequences, the most relevant for this analysis is an overestimation of the PID performance in the simulated data. The more tracks pass through the RICH detectors, the more difficult it is to match the Cherenkov rings to each track. This has an impact on the trigger as well. It is not possible to select any trigger in data and be sure the simulation predicts the correct trigger efficiencies. It is common practise to only apply the trigger to the tracks from the signal decay at hand.

Another aspect is the detector simulation itself. Basically, the simulated detector is the ideal LHCb detector, whereas the real detector has deficiencies, that need to be addressed within the simulation as well to have a reliable prediction. An example would be the absolute momentum scale, due to the misalignment of the tracking detectors and an incorrect gauge of the magnetic field the absolute momentum scale is incorrect in both data and the simulation. This is a major source for systematic uncertainties for absolute mass measurements. Unfortunately, the scales between the data and the simulation are also different from one another requiring the analyst to introduce a global shift parameter to their fits if they cannot establish the signal shapes in data directly. The simulation often overestimates the invariant mass resolution as well, again this can be mitigated in case the statistics are large enough, if not a systematic uncertainty on the incorrect shape predicted by the simulation needs to be applied.

Combining these flaws many analysis rely on a high statistic calibration channel, which can be used to train their selection and determine the signal shape. There are also many data driven methods to calculate the PID efficiencies using large control samples are use data tables to determine the trigger rates.

### 2.7.2 Available Simulated Data Sets and Their Relative Normalisation

In order to conclude the section on simulated events, the simulated samples used in this analysis are listed. These are used to perform four main tasks of the analysis: to determine the relative efficiencies between the  $\bar{B}^0_{(s)} \rightarrow \Lambda\bar{p}h^+$



Table 2.1: Scaling factors for the simulated datasets; each mode is scaled according to the number of generated  $\bar{B}^0 \rightarrow \Lambda\bar{p}\pi^+$  and  $B_s^0 \rightarrow \Lambda\bar{p}K^+$  events, to the production ratio relative to  $\bar{B}^0 \rightarrow \Lambda\bar{p}\pi^+$  and  $B_s^0 \rightarrow \Lambda\bar{p}K^+$ , and finally to the different branching fraction. Decays marked with (\*) indicate that the branching fraction is not known and a value guessed from a similar decay was used. The different PID efficiencies between data and simulations is accounted for as well.

Mode	Total number of MC events			Prod. fract.	$\mathcal{B}$ ( $\times 10^{-6}$ )	PID corr.	
	2011	2012a	2012b			$\pi$	$K$
$\bar{B}^0 \rightarrow \Lambda\bar{p}\pi^+$	4076761	2070550	8012691	$f_d$	3.14	0.978	1.3
$B_s^0 \rightarrow \Lambda\bar{p}K^+$	4036546	1022711	8006536	$f_s$	3.0(*)	1.03	0.998
$\bar{B}^0 \rightarrow \Sigma^0\bar{p}\pi^+$	779748	1092787	1522745	$f_d$	3.0(*)	0.98	1.2
$\bar{B}_s^0 \rightarrow \Sigma^0\bar{p}K^+$	1555852	1015741	3029707	$f_s$	3.0(*)	1.02	1.0
$\bar{B}^0 \rightarrow \Lambda\bar{p}\rho^+$	1549166	–	3023124	$f_d$	3.0(*)	0.96	1.52
$\bar{B}_s^0 \rightarrow \Lambda\bar{p}K^{*+}$	1551639	–	3077618	$f_s$	3.0(*)	1.05	0.998
$\Lambda_b^0 \rightarrow \Lambda p\bar{p}$	506500	–	2057993	$f_\Lambda$	0.05(*)	1.56	0.93

signal modes and the  $\bar{B}^0_{(s)} \rightarrow \Sigma^0\bar{p}h^+$  background modes. The relative efficiencies are used in the final fit to allow using physical constraints to stabilise the global fit and reduce the number of free parameters. Furthermore, the simulated data takes the role as the signal sample source in the multivariate selection during the training process. The fit function are also based on the predicted line shapes from the Monte Carlo simulations. These choices are based on the lack of a high statistic reference decay mode and the differences between the data and MC simulation are investigated and assigned as systematic uncertainties.

Finally, the simulated samples are investigated to estimate the contributions of the various charmless background modes in comparison to the signal modes. In order to compare the different contributions, each mode has to be scaled according to number of generated events, the relative branching fractions, and the hadronisation fractions. Due to the difference between the PID selection efficiency for simulated and recorded data an additional correction factor is applied to correct for that difference.

Each mode was generated with a different number of candidates, so, as a first step, the number of generated events is scaled to the number of generated  $\bar{B}^0 \rightarrow \Lambda\bar{p}\pi^+$  and  $\bar{B}_s^0 \rightarrow \Lambda\bar{p}K^+$  events, respectively.

Since the background modes contain not just  $B^0$  modes but  $B_s^0$  and  $\Lambda_b^0$  modes as well, it is necessary to include the different fragmentation probabilities in the scale factor. Again this is done with respect to the corresponding  $\bar{B}^0_{(s)} \rightarrow \Lambda\bar{p}h^+$  mode. The values for the hadronisation probabilities of  $B^0$  mesons,  $f_d$ ,  $B_s^0$  mesons,  $f_s$ , and  $\Lambda_b^0$  baryons,  $f_\Lambda$ , have been measured by the LHCb experiment [44, 45] and a detailed listing can be found in Appendix D.

Finally, the relative branching fractions are included in the scale factor. Only  $\bar{B}^0 \rightarrow \Lambda\bar{p}\pi^+$  has been measured before by *BABAR* [25] and *Belle* [22, 24]. There is a limit  $\bar{B}^0 \rightarrow \Sigma^0\bar{p}\pi^+$  set by the *Belle* experiment [22], the latter being consistent with the assumption of  $\mathcal{B}(\bar{B}^0 \rightarrow \Sigma^0\bar{p}\pi^+) = \mathcal{B}(\bar{B}^0 \rightarrow \Lambda\bar{p}\pi^+)$ . There are predictions for  $\bar{B}^0 \rightarrow \Sigma^0\bar{p}\pi^+$  [46] and  $\Lambda_b^0 \rightarrow \Lambda p\bar{p}$  [47]. In case of  $\bar{B}^0 \rightarrow \Sigma^0\bar{p}\pi^+$  the limit will be used to estimate the background and for  $\Lambda_b^0 \rightarrow \Lambda p\bar{p}$  the theoretical predictions will be used. For all other modes assumptions based on the other known modes are made. Although  $\bar{B}^0 \rightarrow \Lambda\bar{p}\pi^+$  and  $\bar{B}_s^0 \rightarrow \Lambda\bar{p}K^+$  having different contributing diagrams the branching fraction should be at the same order of magnitude, so it is assumed that  $\mathcal{B}(\bar{B}^0 \rightarrow \Lambda\bar{p}\pi^+) = \mathcal{B}(\bar{B}_s^0 \rightarrow \Lambda\bar{p}K^+)$ . There is no differentiation made between  $\bar{B}_s^0 \rightarrow \Lambda\bar{p}K^+$  and  $\bar{B}_s^0 \rightarrow \bar{\Lambda}pK^-$  since only the sum is measured here. Assessing the branching fraction for  $\bar{B}_s^0 \rightarrow \Sigma^0\bar{p}K^+$  the following assumption is made,  $\mathcal{B}(\bar{B}^0 \rightarrow \Sigma^0\bar{p}\pi^+) = \mathcal{B}(\bar{B}_s^0 \rightarrow \Sigma^0\bar{p}K^+)$ .

The resulting scale factors are listed in Tab. 2.1 and applied to the simulated datasets. The overall size is also listed and split into the three main data periods, 2011, 2012a, and 2012b. Dedicated 2012a MC samples have been only generated for the relevant samples used in the fit in order to extract their efficiencies.

## Chapter 3

# Analysis of $\bar{B}_{(s)}^0 \rightarrow \Lambda \bar{p} h^+$

As mentioned in the detector chapter only stable particles such as pions, kaons, protons, electrons, muons, and photons can be measured in the LHCb detector<sup>1</sup>. The  $\Lambda$  baryons as intermediate hadrons<sup>2</sup>, however, need to be reconstructed. In the context of experimental particle physics an intermediate particle is reconstructed by combining several charged tracks searching for a common origin, *i.e.* the decaying mother particle, and calculate the invariant mass of the combination. Each combination is referred to as a candidate. In case of the  $\Lambda$  baryons, a  $\Lambda$  ( $\bar{\Lambda}$ ) candidate is any combination of two oppositely charged tracks, one being associated with a proton (antiproton) the other with a  $\pi^-$  ( $\pi^+$ ) meson. Furthermore, due to the statistical nature of the approach, it is impossible to distinguish a true  $\Lambda$  candidate from a random  $p\pi^-$  combination. By making use of the properties of the  $\Lambda$  baryon the probability of finding a true  $\Lambda$  baryon compared to a random combination can be increased. As a next step, all  $\Lambda$  candidates found in an event are combined with two additional tracks of opposite charge, again one should be consistent with the  $p$  hypothesis, the other either with a pion or a kaon. Most combinations are background candidates, *i.e.* either random combinations referred to as combinatorial background or different decays incorrectly associated with  $\bar{B}_{(s)}^0 \rightarrow \Lambda \bar{p} h^+$  decays<sup>3</sup>.

Both the  $\Lambda$  and  $B$  reconstruction is performed during the `stripping` (*cf.* sec. 2.6). The selection applied during the `stripping` is not sufficient to isolate  $\bar{B}_{(s)}^0 \rightarrow \Lambda \bar{p} h^+$  decays from the remaining combinatorial background candidates. The following chapter describes the selection criteria necessary to isolate the  $\bar{B}_{(s)}^0 \rightarrow \Lambda \bar{p} h^+$  candidates from the remaining background. The first step includes the selection of the event triggers followed the application of a `DecayTreeFit` (*cf.* sec. 2.3.3) and additional cuts to prepare the data samples for the multivariate analysis designed to maximise the separation between signal and background. After applying the selection the number of  $B$  signal candidates in each event is checked to exclude multiple candidates.

The selection is followed by studies of sources of non-combinatorial background and afterwards the methods of extracting the number of signal events and the T-Asymmetry are described.

---

<sup>1</sup>In the context of this document stable particles are particles, that do not decay within the LHCb detector.

<sup>2</sup>Throughout this document the charge conjugated decay is always included if not stated otherwise.

<sup>3</sup>Throughout this document the notation  $\bar{B}_s^0 \rightarrow \Lambda \bar{p} K^+$  always refers to the sum of the decays  $\bar{B}_s^0 \rightarrow \Lambda \bar{p} K^+$  and  $\bar{B}_s^0 \rightarrow \bar{\Lambda} p K^-$  and their charge conjugated decays if not stated otherwise.

## 3.1 Event Selection

This analysis investigates the data collected by the LHCb experiment during the years 2011 and 2012. Due to the different centre-of-mass energies and detector conditions during these years the data is split per year. An additional split is necessary due to the  $\Lambda$  baryons. Due to the long life-time of the  $\Lambda$  baryon, some  $\Lambda$  baryons decay within the VELO, others outside. According to the track conventions the first sample is referred to as long-long (LL) sample and the latter as down-down (DD) sample.

A further split of the 2012 data sample is investigated due to significant changes to the trigger implementation during the June technical stop in view of a significant increase of the performance for  $V^0$  particles such as the  $\Lambda$  baryon. These pre- and post-June trigger configurations will hereafter be referred to as 2012a and 2012b. Overall the data is hence split in three sets of conditions as far as the trigger is concerned: 2011, 2012a and 2012b.

### 3.1.1 Trigger selection

Instead of using all available trigger lines it is useful to select trigger lines that are sensitive to the decay studied. This is useful to suppress background but more importantly it increases the liability of the available Monte Carlo generated signal events. In case of selecting all available trigger lines it would be necessary to rely on the assumption, that the generated event has the exact same properties. As this is not the case, it is useful to use trigger lines that resemble the decay independent of the surrounding event.

Table 3.1: Trigger lines used to select events, the `Hlt2Topo{2, 3, 4}BodySimple_TOS` trigger lines are used in 2011 data only.

Trigger level	Requirements
L0	<code>L0Hadron_TOS</code> or <code>L0Global_TIS</code>
HLT1	<code>Hlt1TrackAllL0_TOS</code>
HLT2	<code>Hlt2Topo2BodyBBDT_TOS</code> or <code>Hlt2Topo3BodyBBDT_TOS</code> or <code>Hlt2Topo4BodyBBDT_TOS</code> or <code>Hlt2Topo2BodySimple_TOS</code> or <code>Hlt2Topo3BodySimple_TOS</code> or <code>Hlt2Topo4BodySimple_TOS</code>

In Table 3.1, the trigger lines used to select the events are listed. It is required that either one of the decay products fired the L0 hadron trigger (Trigger On Signal) or that the event was triggered independently of any of the decay products (Trigger Independent of Signal). The `Hlt1TrackAllL0` selects tracks based on their transverse momenta and displacement from the primary vertex. The topological HLT2 triggers combine several tracks into a composite particle and select the events upon the invariant mass of the combination and the vertex displacement from the primary vertex. In 2011 the cut based trigger lines `Hlt2TopoNBodySimple` were used as backup for an algorithm based on a multi-variate analysis (MVA). This was only used in 2011 and was removed during the 2012 data taking period. It is required that one of these lines was fired by one of the decay products. Usually the proton and the light hadron in the decay  $\bar{B}^0_{(s)} \rightarrow \Lambda \bar{p} h^+$  successfully trigger the `Hlt2Topo2Body` line since the  $\Lambda$  decays further downstream, but short lived  $\Lambda$  baryons can also trigger the three- and four-body lines similar to  $B$  decays containing charmed particles. A summary of the performance of each trigger stage on the  $\bar{B}^0 \rightarrow \Lambda \bar{p} \pi^+$  mode can be found in Appendix A.

The influence of the 2012a and 2012b trigger configurations on the input variables is shown in Appendix C and found to be insignificant and it was decided to use the same selection for the whole 2012 data-set. This decision is also corroborated by the otherwise limited statistics in the size of the training and test samples for signal and

background. The same argument applies to the common strategy at LHCb to split the data further to train two independent selectors for each data period.

### 3.1.2 Stripping Selection

As mentioned before, the LHCb data is usually only available to the analyst in form of stripped  $\mu$ DST files. The line chosen for this analysis is the `StrippingLb2V0hh` which reconstructs the decay  $\Lambda_b \rightarrow \Lambda \pi^+ \pi^-$  allowing for a broad window of the invariant mass of the  $\Lambda \pi^+ \pi^-$  system. This stripping line was initially developed by the LHCb group at the University of Warwick [48]. When substituting a charged pion for a proton and correcting for the different life time of the  $B_{(s)}^0$  it is possible to search for  $\bar{B}_{(s)}^0 \rightarrow \Lambda \bar{p} h^+$  using this stripping line. In Table 3.2 the list of stripping lines used as well as the selected stripping cycle is shown. The number 20 denotes the release cycle, p2 shows, that it was the second incremental restripping, *i.e.* adding of additional lines to the original stripping release, and r1 marks the 2011 data and r0 the 2012 dataset. Again data samples are split according to the  $\Lambda$  being reconstructed in the VELO, *i.e.* its daughters are long-tracks, and behind the VELO, *i.e.* its daughters are downstream-tracks.

Table 3.2: Stripping lines used in this analysis

Data period	Stripping release	Stripping lines
2011	20r1p2	<code>StrippingLb2V0hhLLLine</code> ,
2012	20r0p2	<code>StrippingLb2V0hhDDLLine</code>

Detailed information on the selection in the stripping is summarised in Tables 3.3 and 3.4.

The LHCb stripping lines usually consist of three different selection stages. The first stage refines the selection on the predefined  $\Lambda$  particles. The second and third step are part of the  $B^0$  reconstruction, the first placing restrictions on the simple combination of the input variables and the latter on the fitted  $b$  hadron candidate.

The `StdLooseLambdaLL` list is used as input for the `StrippingLb2V0hhLLLine` and the selection criteria are included in Tab. 3.3. The  $\chi^2(\text{IP})$  is the squared ratio between the impact parameter (IP) divided by its error and  $\chi^2(\text{IP}) > 9$  means, that each daughter is displaced from the primary vertex (PV) by  $3\sigma$ . Similarly the distance between the  $\Lambda$  and its associated PV is required to be larger than  $\sqrt{50}\sigma$ .

The combination selection places restrictions on the individual transverse momenta as well as the sum of the absolute value of the daughter transverse momenta. Finally only  $\Lambda\pi\pi$  combinations within a given mass window are selected and, in order to speed up the vertex fit, the  $\chi^2$  of the distance of closest approach (DOCA) between any combination of  $\Lambda_b^0$  daughters with respect to each other should be  $\chi^2(\text{DOCA}) < 5$ .

The mother selection concludes with the selection on the fitted  $\Lambda_b^0$  candidate such as the  $\chi^2$  of the vertex fit and the transverse momentum of the  $\Lambda_b^0$ . In addition, the angle between the  $\Lambda_b^0$  momentum vector and the vector connecting the PV and the  $\Lambda_b^0$  decay vertex, called  $\theta_{\text{DIRA}}$  (*cf.* direction angle), is required to be close to zero and the IP of the  $\Lambda_b^0$  should be consistent with originating from a PV and its distance to any PV should be consistent with a displaced vertex expected from a  $b$  hadron decay.

The `StrippingLb2V0hhDDLLine` configuration for the DD  $\Lambda$  candidates is similar to the `StrippingLb2V0hhLLLine`. There are additional requirements for the  $\Lambda$  candidates and an additional selection on the  $\Lambda\pi\pi$  combinations in the form, that the daughter with the largest transverse momentum should have a minimal IP of  $\text{IP} > 0.05$  mm. In order to reduce the bandwidth of the stripping line the momentum cuts are larger as well compared to the LL stripping.

Table 3.3: Configuration of the StrippingLb2V0hhLLLine stripping line.

$\Lambda$ filter	$\Lambda$ daughter track momentum Daughter $\chi^2$ (IP) wrt any PV Mass difference wrt $\Lambda$ mass $\Lambda$ daughter track fit $\chi^2$ /nDoF $\chi^2$ of $\Lambda$ vertex fit $\Lambda$ -PV separation $\chi^2$	$p > 2000 \text{ MeV}/c^2$ $\chi^2(\text{IP}) > 9$ $ m(p\pi) - m(\Lambda)  < 15 \text{ MeV}/c^2$ $\chi^2(\text{Trk})/\text{nDoF} < 3$ $\chi^2(\Lambda) < 12$ $\chi^2(\Lambda - \text{PVVD}) > 50$
Combination	Charged daughter track fit $\chi^2$ /nDoF Sum over daughter $p_T$ $p_T$ of at least two $\Lambda_b^0$ daughters $p_T$ of the combination four-vector Mass of the $\Lambda_b^0$ candidate $\chi^2$ (DOCA) of any two daughters	$\chi^2(\text{Trk})/\text{nDoF} < 3$ $\sum_{\Lambda, \pi, \pi} p_T > 3000 \text{ MeV}/c$ $p_T > 800 \text{ MeV}/c$ $p_T > 1 \text{ GeV}/c$ $m(\Lambda\pi\pi) \in (4301, 6120) \text{ MeV}/c^2$ $\chi^2(\text{DOCA}) < 5$
Mother cut	$\Lambda_b^0$ transverse momentum $\chi^2$ of $\Lambda_b^0$ vertex fit Cosine of the DIRA angle $\Lambda_b^0$ IP $\chi^2$ wrt any PV $\Lambda_b^0$ vertex distance $d$ wrt any PV $\chi^2$ separation of $\Lambda_b^0$ vertex and PV	$p_T > 1500 \text{ MeV}/c$ $\chi^2(\Lambda_b^0) < 12$ $\cos \theta_{\text{DIRA}} > 0.995$ $\chi^2(\text{IP}) < 8$ $d > 1 \text{ mm}$ $\chi^2(\Lambda_b^0 - \text{PVVD}) > 50$

Table 3.4: Configuration of the StrippingLb2V0hhDDLLine stripping line.

$\Lambda$ filter	$\Lambda$ daughter track momentum Daughter $\chi^2$ (IP) wrt any PV $\Lambda$ daughter track fit $\chi^2$ /nDoF Mass difference wrt $\Lambda$ mass $\chi^2$ of $\Lambda$ vertex fit $\Lambda$ -PV separation $\chi^2$ $\Lambda$ flight distance wrt any PV $\Lambda$ momentum $\chi^2$ (DOCA) between daughters	$p > 2000 \text{ MeV}/c^2$ $\chi^2(\text{IP}) > 4$ $\chi^2(\text{Trk})/\text{nDoF} < 3$ $ m(p\pi) - m(\Lambda)  < 20 \text{ MeV}/c^2$ $\chi^2(\Lambda) < 12$ $\chi^2(\Lambda - \text{PVVD}) > 50$ $r > 300 \text{ mm}$ $p > 8000 \text{ MeV}/c$ $\chi^2(\text{DOCA}) < 25$
Combination	Charged daughter track fit $\chi^2$ /nDoF Sum over daughter $p_T$ $p_T$ of at least two $\Lambda_b^0$ daughters $p_T$ of the combination four-vector Mass of the $\Lambda_b^0$ candidate IP of the $\Lambda_b^0$ daughter with highest $p_T$ $\chi^2$ (DOCA) of any two daughters	$\chi^2(\text{Trk})/\text{nDoF} < 3$ $\sum_{\Lambda, \pi, \pi} p_T > 4200 \text{ MeV}/c$ $p_T > 800 \text{ MeV}/c$ $p_T > 1 \text{ GeV}/c$ $m(\Lambda\pi\pi) \in (4301, 6120) \text{ MeV}/c^2$ IP $> 0.05 \text{ mm}$ $\chi^2(\text{DOCA}) < 5$
Mother cut	$\Lambda_b^0$ transverse momentum $\chi^2$ of $\Lambda$ vertex fit Cosine of the DIRA angle $\Lambda_b^0$ IP $\chi^2$ wrt any PV $\Lambda_b^0$ vertex distance $d$ wrt any PV $\chi^2$ separation of $\Lambda_b^0$ vertex and PV	$p_T > 1500 \text{ MeV}/c$ $\chi^2(\Lambda) < 12$ $\cos \theta_{\text{DIRA}} > 0.995$ $\chi^2(\text{IP}) < 8$ $d > 1 \text{ mm}$ $\chi^2(\Lambda - \text{PVVD}) > 50$

### 3.1.3 Particle Substitution Procedure

The StrippingLb2V0hh stripping lines introduced in the previous section reconstruct the decay  $\Lambda_b^0 \rightarrow \Lambda\pi^+\pi^-$ . The incorrect hypothesis for the charged  $B$  daughters leads to a distorted invariant mass and needs to be corrected. The  $\Lambda$  flavour is used to determine the  $B$  flavour, *e.g.* a  $\bar{B}^0$  decays into a  $\Lambda$  baryon. Depending on the  $B$  flavour either the  $\pi^+$  ( $B^0$ ) or the  $\pi^-$  ( $\bar{B}^0$ ) is the proton or antiproton, respectively, and the energy is calculated using the  $p$  mass hypothesis instead of the  $\pi$  mass. Finally the decay is refitted with the  $B^0$  hypothesis. In case of the  $\bar{B}_s^0 \rightarrow \Lambda\bar{p}K^+$  decay, an additional substitution for the remaining pion is made. Fig. 3.1 illustrates the effect of the particle substitution.

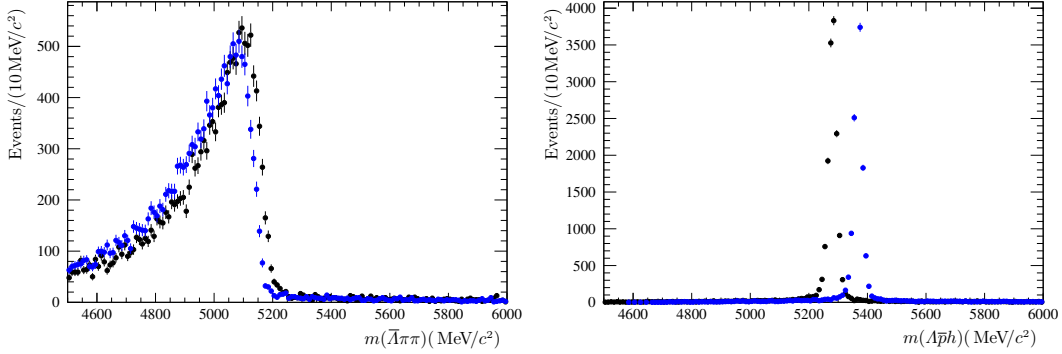


Figure 3.1: Distribution of  $m(\Lambda\pi^+\pi^-)$  (left) using the  $\pi$  mass hypothesis and using the correct mass hypotheses (right) for the  $\bar{B}^0 \rightarrow \Lambda\bar{p}\pi^+$  (black data points) and  $B_s^0 \rightarrow \Lambda\bar{p}K^+$  (blue data points) modes. The data shown in both plots are simulated events only.

### 3.1.4 Decay Tree Fitter

The stripped candidates are refitted with the Decay Tree Fitter (DTF) package, see sec. 2.3.3, in order to improve the resolution and to calculate useful variables such as the  $B$  and  $\Lambda$  lifetimes. This refit is performed for each candidate twice using the pion and kaon hypothesis, respectively. In addition, the  $\Lambda$  is constrained to its nominal mass [12]. This also improves the mass resolution. The resulting  $m(\Lambda\bar{p}h)$  invariant mass is used later to determine the number of signal candidates.

In a second DTF the  $B$  candidates are mass constrained to the  $B_{(s)}^0$  meson mass [12]. Doing so leads to well defined borders of the Dalitz plot, which will be of interest later on.

### 3.1.5 Pre-selection Cuts

In preparation for the MVA a loose preselection of the data is necessary. This rejects the most obvious background events and restricts the input variables of the MVA to its signal region to maximise the performance of the MVA. The following preselection is applied based on the signal distribution predicted by the simulation and a commonly applied section criterion for the Ghost probability.

- Ghost probability (*cf.* sec. 2.3.1) of all charged final-state tracks,  $P_{\text{Ghost}} < 0.5$ ,
- Loose proton PID pre-selection,  $\text{ProbNNPIDp}(p) > 0.05$ ,
- The  $B$  vertex  $\chi^2$  over its degree of freedom,  $\chi^2(\text{DTF})/\text{nDoF}(\text{DTF}) < 5$ ,

- Logarithm of the significance of the  $\Lambda$  flight length  $r$ ,  $\log_{10} \chi^2(r) > 0.75$ , i.e.  $\chi^2(r) \approx 5.6$ ,
- Distance of closest approach (DOCA) between the  $p$  and the bachelor ( $\pi^+$  or  $K^+$ ),  $r(\overline{p}, h) < 0.15$  mm,
- Direction angle of the  $B$  candidate,  $\theta_{\text{DIRA}} < 0.04$ .

### 3.1.6 Multivariate Selection

Experiments in the field of particle physics are basically counting experiments with billions of repetitions. Therefore, not only the processes studied but also the experimental environment is dominated by statistical processes.

In past experiments it was common practise to use cut-based analysis methods. In these, several key variables were selected to distinguish between signal and background. The quality of this method depends on the variables available. In the case of low separating power of the variables simply applying cuts in these variables does not lead to a good signal-to-background ratio and it is useful to use multivariate methods. These take a given set of variables and transform them into a new variable that can maximise the separation of signal and background.

#### 3.1.6.1 Variable selection for the MVA Training

The final event selection is done with a multivariate analysis (MVA) using the algorithms provided by the TMVA software package [49]. As method a multilayer perceptron (MLP) is chosen which is described in sec. 3.1.6.3.

Since the Dalitz plot is of interest as well in the analysis, it is necessary to choose variables that are insensitive to the position in the Dalitz plot. Therefore, the focus is on topological variables. The following variables are selected and explained below:

- The logarithm of the impact parameter (IP) calculated with respect to the associated primary vertex (PV),  $\log_{10} \text{IP}$ , for all particles,
- The sum over the  $\chi^2$  of the IPs for the charged tracks,  $\sum_{\overline{p}, h} \log_{10} \chi^2(\text{IP})$ ,
- The distance of closest approach (DOCA) between the two charged  $B$  daughters,  $r(\overline{p}, h)$ ,
- The  $\chi^2/\text{nDoF}$  of the `DecayTreeFit`,  $\chi^2/\text{nDoF}(\text{DTF})$ ,
- The fit probability of the `DecayTreeFit` calculated with `ROOT: TMath :: Prob(\chi^2(\text{DTF}), \text{ndof}(\text{DTF}))`,
- $B$ -mother kinematic variables  $p_{\text{T}}$  and  $\eta$ , the transverse momentum and the pseudo-rapidity,
- The logarithm of the flight-significance,  $\log_{10} \chi^2(r)$ ,
- The logarithm of the lifetime,  $\log_{10}(c\tau)$ , of both the  $B$  and  $\Lambda$  candidates,
- $\theta_{\text{DIRA}}(B)$ , the angle between the momentum vector and the vector connecting the associated PV with the decay vertex,
- $\theta_{\text{DIRA}}(\Lambda)$ , the angle between the momentum vector and the vector connecting the  $B$  decay vertex with the decay vertex calculated in  $B$  rest frame,
- Angle between  $\Lambda$  momentum in the  $B$  rest-frame and the boost axis of the  $B$ , which is given by the  $B$  momentum in the lab frame,
- Pointing variable defined as

$$P = \frac{\sum_{\Lambda \overline{p} h} p \times \sin \theta_{\text{DIRA}}(B)}{\sum_{\Lambda \overline{p} h} p \times \sin \theta_{\text{DIRA}}(B) + \sum_{\Lambda \overline{p} h} p_{\text{T}}} . \quad (3.1)$$

The IPs of the daughter particles make use of the fact that the  $B$  meson is long lived and, therefore, the daughters should have a non-zero IP compared to  $\Lambda$ ,  $\bar{p}$ ,  $\pi$  candidates originating from the associated PV. The same argument is true for using the flight-significance and the lifetime of the  $B$  meson and  $\Lambda$  baryon. Since all  $B$  daughters have a non-zero IP, the sum of all three IPs should discriminate against random combinations of two particles from the  $B$  decay and one particle with different origin. In addition to that, there is a correlation between the individual IPs and the sum, which is different between signal and background candidates. Since the IP resolution for a neutral composite particle is worse compared to charged tracks, only proton and pion are considered and used.

The DOCA is the minimal spacial distance between two tracks measured in the LHCb detector. Using the DOCA of proton and pion allows to discriminate against random  $p\pi^-$  combinations. This variable is calculated before the `DecayTreeFit` since this algorithms nullifies the effect of the DOCA variable.

Using both the  $\chi^2/n\text{DoF}$  and the fit probability allows to discriminate random  $p\bar{\Lambda}\pi^-$  combination from those coming from a  $B$  meson. Tracks from different origins may be successfully fit to a common vertex, however, the fit needs not to be good, hence its  $\chi^2$  is worse compared to tracks actually having the same point of origin, *i.e.* the  $B$  meson. This variable cannot distinguish between tracks from the  $B$  vertex and from a primary vertex.

The opening angle  $\theta_{\text{DIRA}}$  discriminates against decays with additional particles since the sum of the daughter momentum vectors does not point to the corresponding production vertex, *i.e.* the PV for the  $B$  candidate and the  $B$  meson decay vertex for the  $\Lambda$  baryon. In order to improve the separation between signal and background  $\theta_{\text{DIRA}}(\Lambda)$  is calculated in the  $B$  meson rest frame using the  $\Lambda$  lifetime in the laboratory frame to construct the space-time four-vector.

Both the  $\bar{B}^0$  and the  $\bar{B}_s^0$  meson are spin 0 states. As a result the decay products are produced uniformly in the  $B$  rest frame. The  $B$  momentum is very close to the  $z$ -axis, background  $\Lambda$  baryons are similarly produced with small  $p_T$  and are therefore close to the  $z$ -axis as well. When boosting into the  $B$  rest frame, background  $\Lambda$  baryons retain their small angle compared to the boost axis, *i.e.* the  $B$  momentum, whereas signal  $\Lambda$  candidates have a uniform distribution.

The pointing variable combines information on the direction of the  $B$  candidate in form of the  $\theta_{\text{DIRA}}$  angle and the daughter momenta. Random  $\Lambda\bar{p}\pi$  combinations from the primary vertex have small opening angles as well but the sum of their transverse momenta is small compared to the decay products of a heavy particle such as a  $B$  meson. This again allows for a separation between these two kinds of events and yield additional information in form of the correlation to the  $\theta_{\text{DIRA}}$  angle. This variable has been used by several LHCb analyses before such as the analysis of  $B^+ \rightarrow p\bar{p}h^+$  [50].

Appendix B shows the distributions of these variable for signal and background for all data periods and data samples. It was decided to use the same MVA classifier for  $\bar{B}^0 \rightarrow \Lambda\bar{p}\pi^+$  and  $\bar{B}_s^0 \rightarrow \Lambda\bar{p}K^+$ . This choice helps to minimise the systematic uncertainty later on. The correlations among the input variables for signal and background in case of the 2012 LL training can be found in Fig. 3.2. The remaining correlation matrices can be found in Appendix E.

### 3.1.6.2 Comparison of the Variable Between the 2012 Trigger Periods

As mentioned in Sec. 3.1, there were significant changes in the trigger configuration during the technical stop in June 2012. In order to investigate this effect two independent MC samples are studied, produced using the pre-June conditions and the post-June conditions, respectively. Compared to the expected statistical uncertainties these differences are negligible. In Fig. 3.6 the resulting MVA selectors for LL and DD for 2012a and 2012b are shown, respectively. The distribution of the input variables are shown in Appendix C. The different efficiencies of the two trigger periods will be addressed (*cf.* Sec. 3.3).

### 3.1.6.3 Training Configuration

Any attempt of separating signal and background needs a sample consisting of signal candidates and a sample of background candidates. There are different opinions on these samples. Monte-Carlo generated signal events



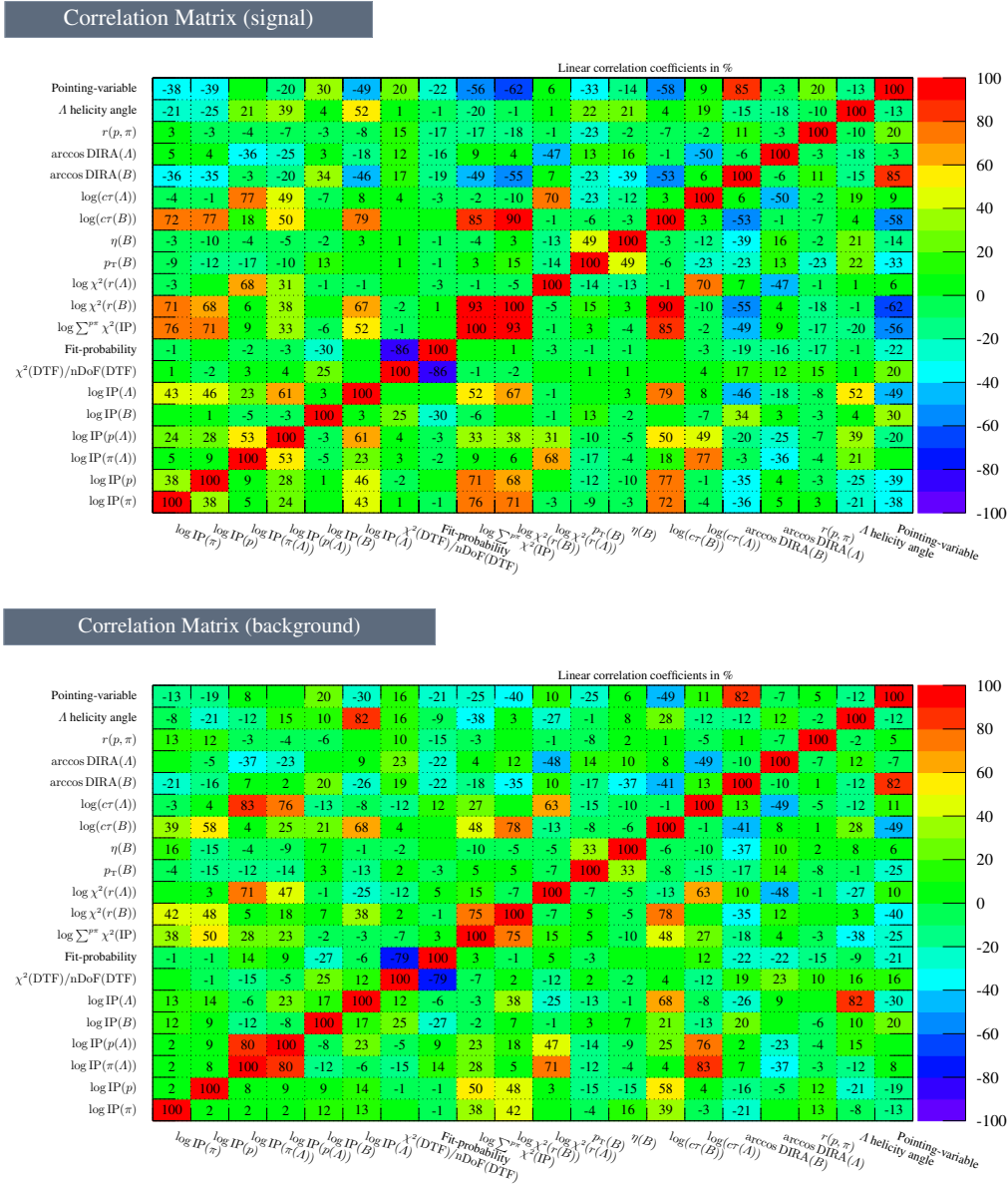


Figure 3.2: Correlations among the MVA input variables for the 2012 LL signal (top) and background (bottom) sample.

are usually used as signal sample and dedicated simulated background events are often used as well. This choice has certain advantages such as exact knowledge and control over the composition of background modes, and it is possible to check very specific sources of background. But this whole procedure depends on the quality of the simulation both in generating the event and modelling the detector response. The  $B$  factories  $BABAR$  and  $Belle$  could rely heavily on simulation both for signal and background as the  $e^+e^-$  interaction and hadronisation is quite well understood. At the LHC with its  $pp$  collisions and the following hadronisation of the decay particles the situation is different. Since it is very difficult to model the whole event, simulated data is only available for the signal sample.

A different approach is to use recorded data for both signal and background. If a similar decay with large statistics is available, it can be used to emulate the signal decay. It is possible to select sideband data as source of background assuming the combinatorial background behaves similar in the signal region. Due to the lack of a

control channel with large statistics a mixed approach was chosen for this analysis. Simulated events are chosen as signal and the right sideband of the invariant  $\Lambda\bar{p}\pi$ -mass as background sample. The right sideband is defined as  $m(\Lambda\bar{p}\pi^+) \in [5400, 5600] \text{ MeV}/c^2$ . The left sideband should not be used since decays with additional pions are located there, a more detailed descriptions on these modes will be given in Section 3.2.3. These are very similar to the  $\bar{B}^0_{(s)} \rightarrow \Lambda\bar{p}h^+$  decays and the purpose of the training is not to discriminate against these but against combinatorial background.

After selecting the signal and background sample the trigger,  $\Lambda$ , PID, and preselection criteria are applied and the refined samples are put into TMVA and the training is commenced. The performance of several different classifier configurations was tested and the following was found to have superior performance: a Multilayer Perceptron with

- one hidden layer with  $N + 1$  neurons,  $N$  being the number of input variables,
- uniformly transformed variables,
- the tanh as neuron-activation function,
- product of output neuron and its weights summing over all output neurons as synapse function.

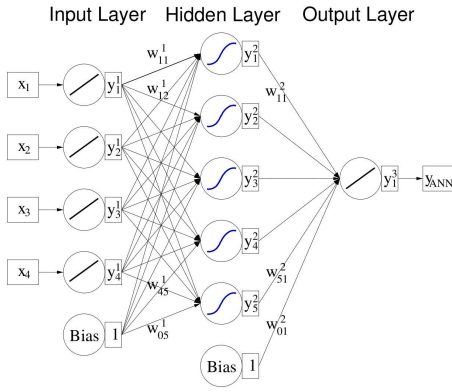


Figure 3.3: Exemplary network layout similar to the one used in the analysis [51].

The Multilayer Perceptron (MLP) is a special case of an artificial neural network (ANN). An ANN is basically a collection of interconnected neurons with each neuron producing a response due to a given input dataset, *cf.* Fig. 3.3. Applying an external signal to the input neurons puts the neural network into a defined state, which can be measured by the response of the output neurons. So in general, a neural network maps the space of input variables  $(x_1, \dots, x_k)$  either to a one dimensional or multidimensional space. The first case is basically a signal-versus-background problem, the idea is to have a single variable with which signal and background can be separated. The latter case maps the input variables  $(x_1, \dots, x_k)$  to output variables  $(y_1, \dots, y_m)$ . These can then be used as additional layers in the neural network. The mapping between input and output variables can be non-linear in case one or more neurons have a non-linear response to the input variables.

In principle a neural network with  $k$  neurons can have  $k^2$  directional connections to other neurons. This leads to very complex structures. Alternatively the neurons can be organised into layers and only allowing connection from a given layer to the next. This type of neural network is called a forward feeding Multilayer Perceptron. The initial layer is represented by the input variables, followed by an arbitrary number of layers, called hidden layers, and the final layer, the output layer, contains only one neuron, the output variable, which is used to separate signal and background (see. fig. 3.3).

The configuration chosen is very similar to what is shown in fig. 3.3, the number of neuron is also  $N + 1$ , but the number of input variables in this case is twenty. Furthermore, the MLP performance is improved by a transformation of the input variables into uniform distributions. In fig. 3.4 the transformation for the  $\Lambda$  impact parameter  $\log \text{IP}(\Lambda)$  is illustrated. The transformation improves the performance by about 5%.

The neuron response function  $\rho$  maps the neuron input to the neuron output. It can often be factorised into a synapse function  $\kappa$  responsible for propagating weights from one layer to the next and a neuron activation function  $\alpha$  such that  $\rho = \alpha \circ \kappa$ . The following definitions are chosen for  $\alpha$  and  $\kappa$

$$\alpha : x_i \mapsto \frac{e^{x_i} - e^{-x_i}}{e^{x_i} + e^{-x_i}} \quad (3.2)$$

$$\kappa : \left( y_1^{(l)}, \dots, y_n^{(l)} | w_{0,j}^{(l)}, \dots, y_{n,j}^{(l)} \right) \mapsto w_{0,j}^{(l)} + \sum_{i=1}^n y_i^{(l)} w_{i,j}^{(l)} \quad , \quad (3.3)$$

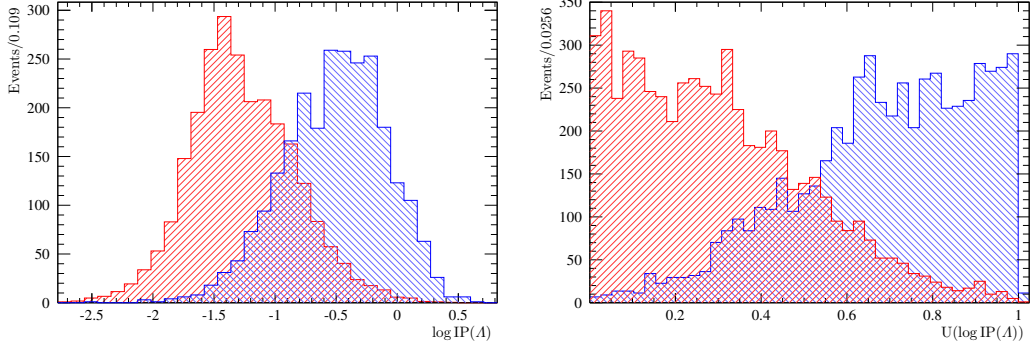


Figure 3.4: Comparison between the  $\log \text{IP}(A)$  before (left) and after (right) the uniform transformation. The blue histogram represent the signal sample and the red histogram the background sample.

with  $x_i, \dots, x_k$  being the input variables,  $y_1^{(l)}, \dots, y_n^{(l)}$  the neurons of the  $l$ th layer and  $w_{i,j}^{(l)}$  the weights for the connection from neuron  $y_i^{(l)}$  to the neuron  $y_j^{(l+1)}$ . The output of the MLP within this configuration is calculated as follows

$$y_{\text{MLP}} = \sum_{j=1}^n y_j^{(2)} w_{j,1}^{(2)} = \sum_{j=1}^n \tanh \left( \sum_{i=1}^k x_i w_{i,j}^{(2)} \right) w_{j,1}^{(2)}, \quad (3.4)$$

where  $k$  and  $n$  are the number of neurons in the input and hidden layer, respectively. The TMVA package then generates random samples from the input data to determine the weights for maximum signal-to-background separation.

Once the training is finished the performance of the MLP is evaluated. A useful tool for that is the Receiver Operating Characteristic (ROC) curve. This graphical plot illustrates the performance of a binary classification system by plotting the true positive rate, *i.e.* selecting a  $\bar{B}^0_{(s)} \rightarrow \Lambda \bar{p} h^+$  candidate, against the true negative rate, *i.e.* reject a background candidate. A perfect training would lead to a ROC curve, that is 1 for all true positive rates, which means for any efficiency to select a  $\bar{B}^0_{(s)} \rightarrow \Lambda \bar{p} h^+$  candidate it would reject any background candidate. In any realistic application the background rejection decreases with an increased signal efficiency.

A general problem of any attempt to separate signal and background is the influence of statistical fluctuations. In case of low statistics in either or both the signal and background sample it is possible to select candidates based on statistical fluctuations in the input variables. In cut based analyses these effects are easier to spot than in dedicated high dimensional MVA methods. Depending in the configuration, 1000 signal candidates can be enough for a successful training, but in other configurations it might be completely inadequate. In order to address this issue an additional statistically independent sample of signal and background candidates is used to evaluate this effect. This sample is labeled the test sample. The classifier is applied to this dataset and is compared to the result obtained for the training sample. The two distributions should be identical. A KOLMOGOROV-SMIRNOV test is applied to check the equality by comparing the empirical distribution function of the test sample and the cumulative distribution function of the training distribution. A non-zero value indicates good agreement.

In Fig. 3.5 the ROC curve and the training output is shown for the 2011 and 2012 data sets for both LL and DD. The result of the Kolmogorov-Smirnov test is shown as well. Finally the effect of the 2012 trigger configuration is investigated. In fig. 3.6 the application of the MLP on the 2012a and 2012b signal samples is shown. The effect is small compared to the statistical uncertainty expected.

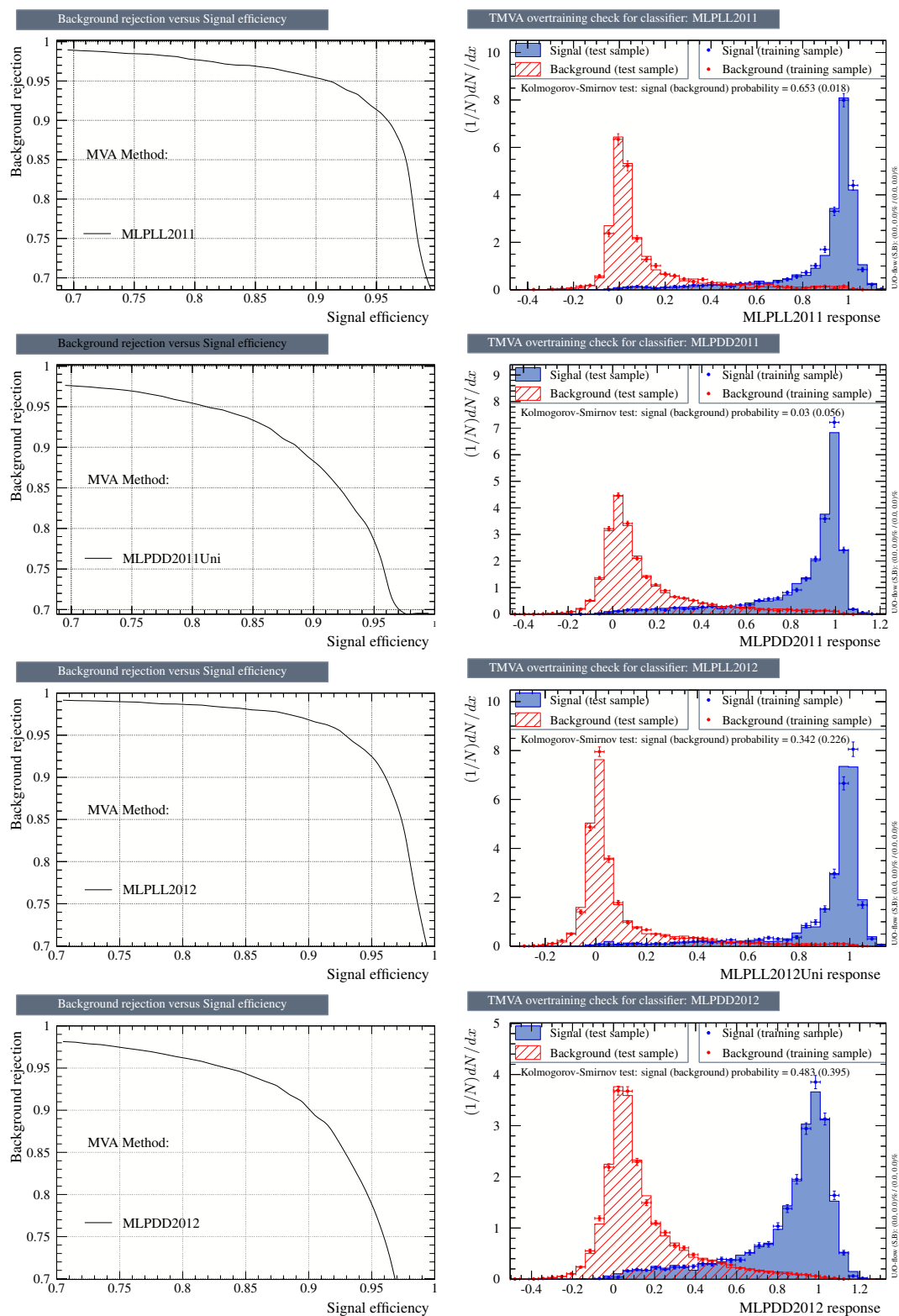


Figure 3.5: ROC curve (left) and comparison between the test and training sample (right) obtained for, from top to bottom, the 2011 LL, 2011 DD, 2012 LL, and 2012 DD data samples.

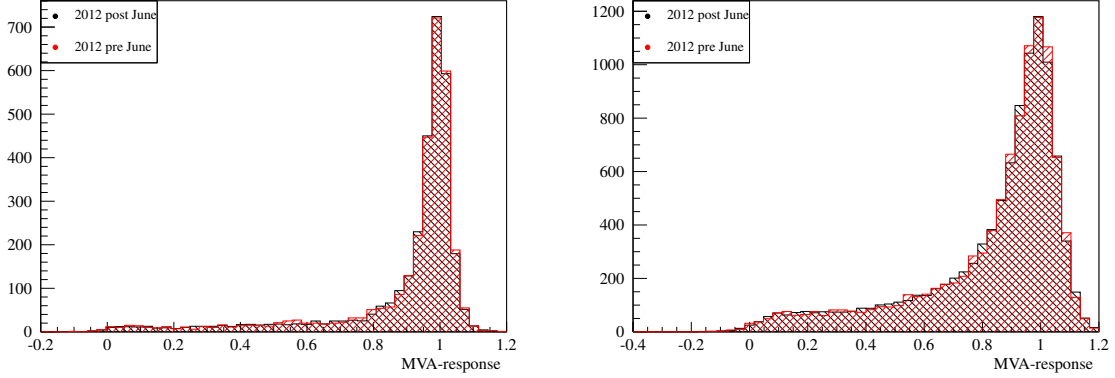


Figure 3.6: Comparison between the MVA-response for the two 2012 periods for LL (left) and the DD (right) sample. The red (black) histogram represent the pre-(post-)June trigger conditions.

### 3.1.6.4 MVA Selection Optimisation

In order to determine the best selection criteria on the MVA classifiers a Figure of Merit (FoM) needs to be introduced. Naively, one could use the ROC curve and calculate the optimal ratio between the signal and background contributions. A problem with that arises once the the number of signal and backgrounds candidates are different. Usually, the number of background candidates far exceeds the number of signal candidates, it is, therefore, useful to use the signal significance as a Figure of Merit,

$$\text{FoM} = \mathcal{S} = \frac{\varepsilon S}{\sqrt{\varepsilon S + B}} \quad , \quad (3.5)$$

where  $S$  and  $B$  are the number of signal and background candidates after a certain selection, respectively. Unfortunately, neither  $S$  nor  $B$  are usually accessible. Here, the FoM is maximised with respect to a loose selection of 0.45 chosen together with a proton neural net PID selection of  $\text{NNPID}(p) > 0.15$ . In a simple fit model to data of a sum of an Novosibirsk (cf. Eq. (3.39)) and an exponential the number of  $\bar{B}^0 \rightarrow \Lambda \bar{p} \pi^+$  signal events  $S_{0.45}^{\text{MVA}}$  is determined by the normalisation of the Novosibirsk. Using the information from the simulated  $\bar{B}^0 \rightarrow \Lambda \bar{p} \pi^+$  data sets, the selection efficiency  $\varepsilon_{0.45}^{\text{MVA}}$  can be determined and the initial number of events  $S_0^{\text{MVA}}$  is calculated as follows

$$S_{0.45}^{\text{MVA}} = \varepsilon_{0.45}^{\text{MVA}} S_0^{\text{MVA}} \quad . \quad (3.6)$$

Therefore, the number of events after any MVA selection can be calculated using  $S_0$  and the corresponding efficiency from the simulation. The number of background events,  $B^{\text{MVA}}$ , is estimated from the right-hand sideband data, fitting with an exponential function, and extrapolating into the signal region. The overall Figure of Merit is thus given by

$$\text{FoM} = \frac{\varepsilon^{\text{MVA}} S_0^{\text{MVA}}}{\sqrt{\varepsilon^{\text{MVA}} S_0^{\text{MVA}} + B^{\text{MVA}}}} \quad . \quad (3.7)$$

The  $m(\Lambda \bar{p} \pi^+)$  invariant mass distributions used to determine  $S_0$  as well as the fits are shown in Fig. 3.7 for the 2011 and 2012 data sets, respectively and Figure 3.8 presents the distributions of the FoM for all four selectors for the 2011 and 2012 LL and DD samples. The optimised selection criteria are indicated by the vertical lines corresponding to

$$\text{MLP} - \text{value}_{11, \text{LL}} > 0.93 \quad \text{MLP} - \text{value}_{12, \text{LL}} > 0.85 \quad (3.8)$$

$$\text{MLP} - \text{value}_{11, \text{DD}} > 0.9 \quad \text{MLP} - \text{value}_{12, \text{DD}} > 0.8 \quad . \quad (3.9)$$

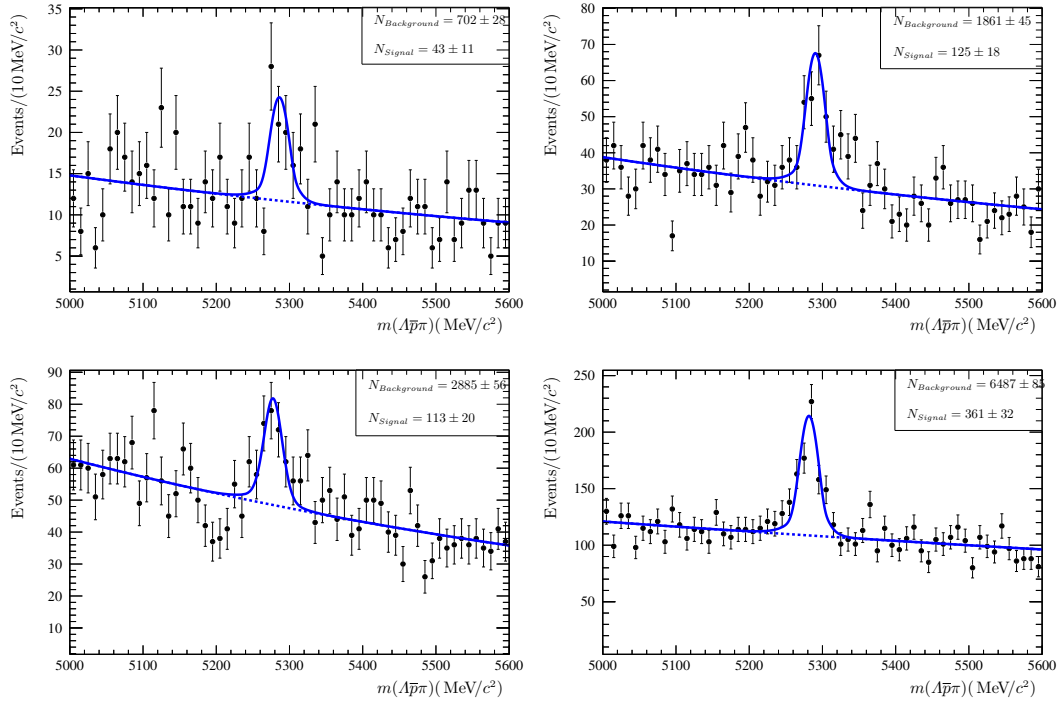


Figure 3.7: Distribution of the invariant  $m(\Lambda\bar{p}\pi)$  mass for the LL (left) and DD (right) sample for 2011 (top) and 2012 (bottom) after applying a loose MLP and proton PID selection as indicated in the text. The distributions are fitted with a Novosibirsk function and an exponential function. The signal and background yields are listed in the plots.

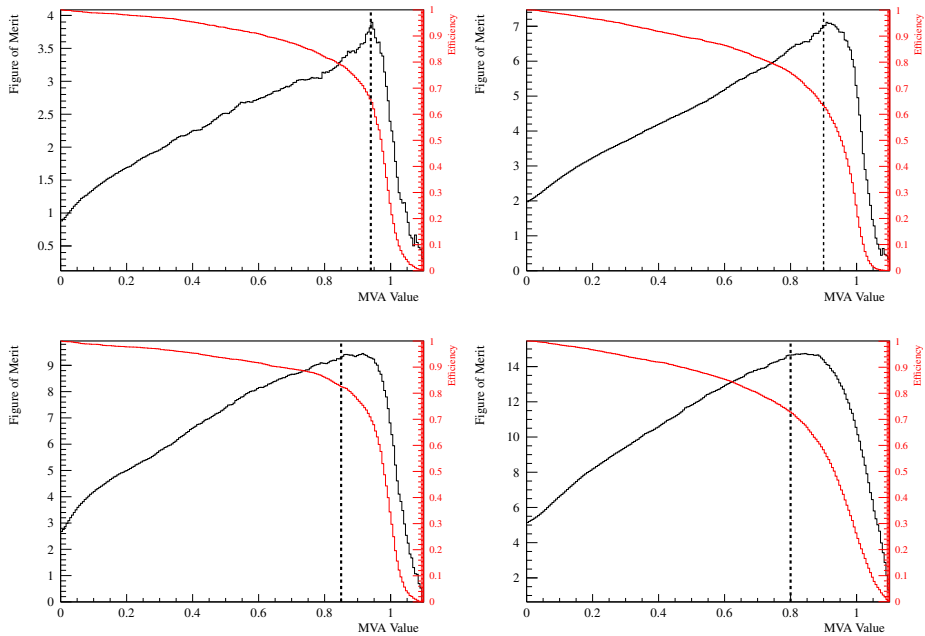


Figure 3.8: Figure of merit distributions for the LL (left) and DD selectors for 2011 (top) and 2012 (bottom). The selection cuts are indicated in the figures by the vertical lines.

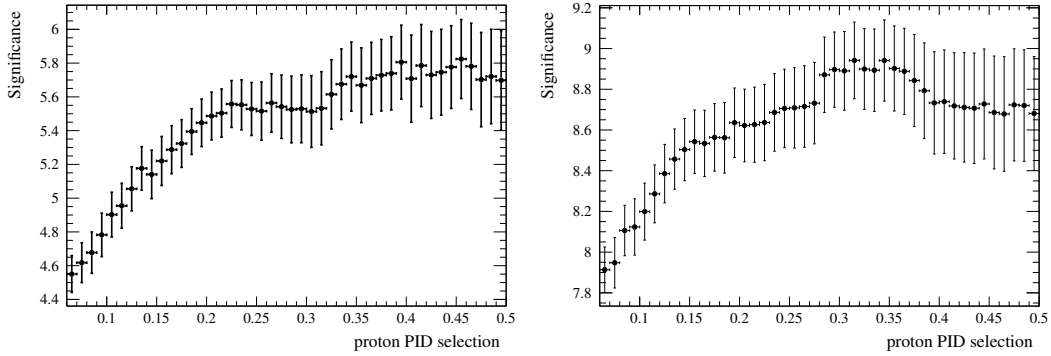


Figure 3.9: Distributions of the signal significance for a given proton PID selection. The left (right) plot shows the LL (DD) sample selection significance.

### 3.1.7 Particle Identification

A PID selection is applied to the bachelor proton and the bachelor meson. No PID cut is applied to the proton from the  $\Lambda$ ; indeed, as discussed in Sec. 3.2.4, no contamination from misidentified  $K^0_S$  mesons is observed. The Neural Net variables are used for the proton whereas the  $DLL_{K\pi}$  likelihood is used for the bachelor meson (*cf.* Sec. 2.4.3).

The protons are required to have

$$\text{NNPID}(p) > 0.3 \quad . \quad (3.10)$$

This selection is based on a study of the significance of the given selection. As figure of merit

$$\text{FoM} = \frac{\varepsilon_{\text{PID/MVA}} S_{\text{MVA}}}{\sqrt{\varepsilon_{\text{PID/MVA}} S_{\text{MVA}} + B_{\text{PID}}}} \quad (3.11)$$

is again chosen, where  $\varepsilon_{\text{PID/MVA}}$  is now the signal selection efficiency with respect to events passing the selection chain up to the MVA stage for a given proton PID selection based on the `PIDCalib` package [52], and  $S_{\text{MVA}}$  is the number of events expected for the MVA selection established in the previous section corrected for the PID efficiency for the loose proton selection. The number of background events is again determined by an exponential fit to the upper sideband and extrapolated into the signal region. The distribution of the selection significance is shown separately for the LL and DD samples in Fig. 3.9. The (common) PID selection is chosen at the beginning of the large plateau of the significances.

In the fitting stage of the analysis the PID selection efficiency is used to determine the individual cross-feeds of  $\bar{B}^0_{(s)} \rightarrow \Lambda \bar{p} h^+$ . In order to have statistically independent samples the samples are splitted according to a kaon PID of

$$DLL_{K\pi} = 1 \quad . \quad (3.12)$$

Bachelor mesons with  $DLL_{K\pi} \leq 1$  are put into the  $\Lambda \bar{p} \pi^+$  sample and mesons with  $DLL_{K\pi} > 1$  into the  $\Lambda \bar{p} K^+$  sample. This selection is chosen to allow both the  $\Lambda \bar{p} \pi^+$  and  $\Lambda \bar{p} K^+$  samples to have sufficient statistics.

### 3.1.8 Multiple Candidates

After applying the selection criteria introduced above, the remaining number of candidates per event is determined, and about 5% of all selected events contain more than one candidate. Multiple candidates per event can bias the efficiency determination due to the different track multiplicities between recorded and simulated data. A candidate is chosen (pseudo-)randomly among all candidates in an event, thereby avoiding potential biases. Each `DaVinci` subjob is configured using an independent seed in order to get reproducible results.

## 3.2 Background Studies

In the previous section the separation between signal and combinatorial background was described. As mentioned before, there are other sources of background especially related  $\bar{B}^0_{(s)}$  meson decays. These processes have similar decay topology and are not removed from the dataset by applying the selections described in sec. 3.1.

The non-combinatorial background is categorised into two types, the first being background via charm particles, in this case a  $\Lambda_c^+ \rightarrow \Lambda h^+$ ,  $h = \pi, K$ , and the second being other related charmless baryonic  $\bar{B}^0_{(s)}$  decays. The first can be removed by vetoing the invariant  $\Lambda\pi^+$  mass. This is discussed in Sec. 3.2.1. The characterisation of the remaining charmless backgrounds and of baryonic  $B$ -decays in general is challenging and complicated due to the limited knowledge of the various possible background modes. In this particular case, only the branching fraction of the mode  $\bar{B}^0 \rightarrow \Lambda\bar{p}\pi^+$  is known, the Belle collaboration having determined upper limits for ‘‘cousin modes’’, see discussion in Sec. 2.7.2. Cousin modes are decays which have similar characteristics. The first kind are decays of  $\bar{B}^0_s$  mesons into a kaon instead of the pion due to the  $\bar{s}$  being the spectator quark rather than than the  $\bar{d}$ . The decay is  $\bar{B}^0_s \rightarrow \Lambda\bar{p}K^+$  and is interesting by itself. Another source of background are decays with excited mesons or baryons such as  $B^0 \rightarrow \Lambda\bar{p}\rho^+$  with  $\rho^+ \rightarrow \pi^+\pi^0$ . These decays have very similar properties as the signal sample and are not completely suppressed by the selection and appear as broad contributions at smaller invariant masses. In the case of  $\Lambda$  baryon there is the special case of  $\Sigma^0 \rightarrow \Lambda\gamma$ . The mass difference between  $\Sigma^0$  and  $\Lambda$  is small [12],

$$\Delta m = m(\Sigma^0) - m(\Lambda) = (76.959 \pm 0.002) \text{ MeV}/c^2, \quad (3.13)$$

and the branching fraction is  $\mathcal{B}(\Sigma^0 \rightarrow \Lambda\gamma) = 100\%$  [12].

Therefore, modes such as  $\bar{B}^0_{(s)} \rightarrow \Sigma^0\bar{p}h^+$  peak very close to the signal decays. In this section, the relevant background modes are investigated and compared to the  $\bar{B}^0_{(s)} \rightarrow \Lambda\bar{p}h^+$  modes by discussing their influence on both the  $\bar{B}^0 \rightarrow \Lambda\bar{p}\pi^+$  and  $B^0_s \rightarrow \Lambda\bar{p}K^+$  modes. As for the recorded data each simulated sample is split into a pion and a kaon sample according to  $\text{DLL}_{K\pi} = 1$ . The selection discussed in the previous section is applied to all plots if not stated otherwise and the histograms shows are scaled according to the factors determined in Sec. 2.7.2.

### 3.2.1 Charm Veto Selection

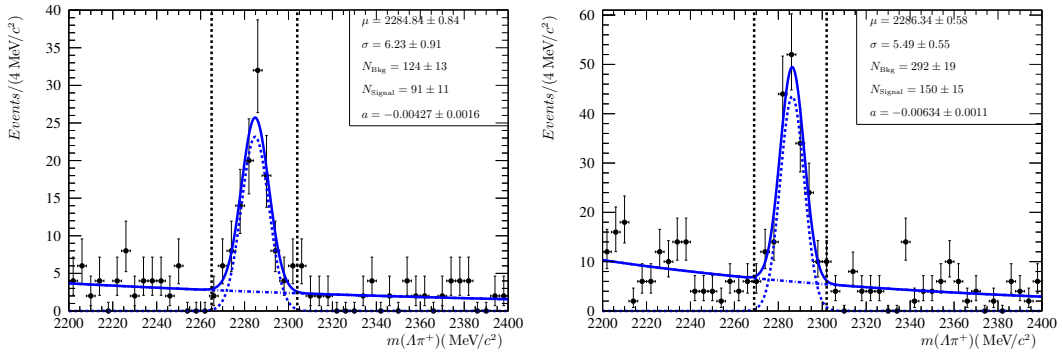


Figure 3.10: Distribution of  $m(\Lambda\pi^+)$  in  $\bar{B}^0 \rightarrow \Lambda\bar{p}\pi^+$  for (left) the LL and (right) DD samples after the stripping for the 2012 data set. The signal is described by a Gaussian distribution and the background by an exponential function. Candidates within  $3\sigma$  around the Gaussian mean value  $\mu$  are rejected.

After applying the selection introduced in the previous sections, decays with an identical final state and similar decay characteristics, *i.e.*  $b$  hadron decays into a  $\Lambda$ , an  $\bar{p}$ , and a charged pion or kaon, remain in the data. One kind of such decays are resonant decays like  $\bar{B}^0 \rightarrow \Lambda\bar{\Delta}^0$  with  $\bar{\Delta}^0 \rightarrow \bar{p}\pi^+$ . Here the  $\bar{p}\pi^+$  system is created through a resonant intermediate state, the  $\bar{\Delta}^0$  baryon. These are still of interest since the production mechanisms are identical



or very similar to the  $\bar{B}^0_{(s)} \rightarrow \Lambda \bar{p} h^+$  decays. Another kind of events, such as  $\bar{B}^0 \rightarrow \Lambda_c^+ \bar{p}$  with  $\Lambda_c^+ \rightarrow \Lambda \pi^+$ , also share the same final state as  $\bar{B}^0 \rightarrow \Lambda \bar{p} \pi^+$ , however, are mediated by a different mechanism, namely  $b \rightarrow c$  tree amplitudes. The  $\bar{B}^0 \rightarrow \Lambda_c^+ \bar{p}$  candidates are removed by rejecting  $\bar{B}^0 \rightarrow \Lambda \bar{p} \pi^+$  candidates whose  $m(\Lambda \pi^+)$  invariant mass is consistent with the  $\Lambda_c^+$  hypothesis. The invariant  $\Lambda \pi^+$  mass is shown in Fig. 3.10. There is a clear peak at the nominal  $\Lambda_c^+$  mass in the invariant  $\Lambda \pi^+$  mass distribution for both LL and DD samples. The  $\Lambda \pi^+$  invariant mass is fitted with a Gaussian function for the  $\Lambda_c^+$  signal and an exponential function for the background. Fig. 3.10 shows the results of the fit and  $\bar{B}^0 \rightarrow \Lambda \bar{p} \pi^+$  candidates with

$$\begin{aligned} m(\Lambda \pi^+) &\in [2265, 2305] \text{ MeV}/c^2 \\ m(\Lambda \pi^+) &\in [2269, 2302] \text{ MeV}/c^2 \end{aligned} \quad , \quad (3.14)$$

for the LL and DD samples, respectively, are rejected. This corresponds to three times the Gaussian width.

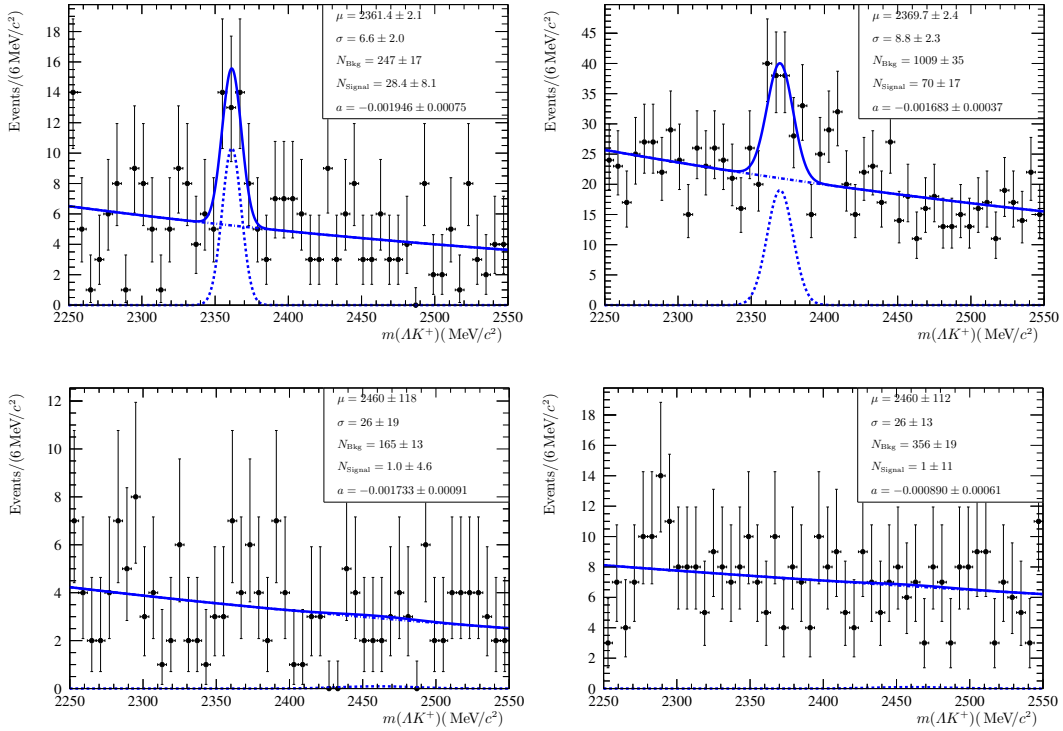


Figure 3.11: Distribution of  $m(\Lambda K^+)$  for the  $B_s^0 \rightarrow \Lambda \bar{p} K^+$  mode after the stripping before (top) and after (bottom) the kaon PID selection described in sec. 3.1.7 for the LL (left) and DD (right) sample. The datasets are each fitted with the sum of a Gaussian and an exponential; the parameters are listed in the plots. The bachelor PID selection removes  $\Lambda_c^+ \rightarrow \Lambda \pi^+$  candidates.

Due to pion-kaon misidentification  $\Lambda_c^+ \rightarrow \Lambda \pi^+$  can fake  $\bar{B}^0_s \rightarrow \Lambda \bar{p} K^+$  signal candidates as well. In Fig. 3.11 the invariant  $\Lambda K^+$  mass is shown. There is a peak corresponding to the  $\Lambda_c^+ \rightarrow \Lambda \pi^+$  decays with the pion being misidentified as a kaon. With the PID selection applied as described in Sec. 3.1.7 there are no  $\Lambda_c^+ \rightarrow \Lambda \pi^+$  events left in the invariant  $\Lambda K^+$  mass distribution. This is shown in Fig. 3.11 as well. Background from  $\bar{B}^0 \rightarrow \Lambda_c^+ \bar{p}$  with  $\Lambda_c^+ \rightarrow \Lambda K^+$  is Cabibbo suppressed with respect to  $\Lambda_c^+ \rightarrow \Lambda \pi^+$ . Due to the overall lower background in the kaon sample a signal for these events can be seen in the invariant  $m(\Lambda K^+)$  mass. Similar to the veto for  $\Lambda_c^+ \rightarrow \Lambda \pi^+$  decays, the distribution is fitted with a Gaussian and an exponential function and candidates within three times the width of the Gaussian distribution are rejected. The statistical uncertainty on the width of the Gaussian is large for LL sample, therefore, the LL veto is chosen to be identical with the DD veto, which is consistent with the veto on the  $\Lambda_c^+ \rightarrow \Lambda \pi^+$  decays. The fits are shown in Fig. 3.12 and candidates with

$$m(\Lambda K^+) \in [2270, 2307] \text{ MeV}/c^2 \quad (3.15)$$

are rejected.

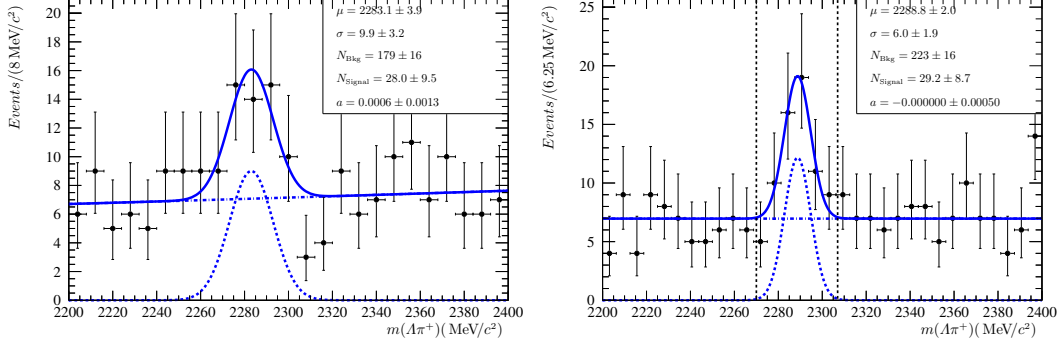


Figure 3.12: Distribution of  $m(AK^+)$  for  $B_s^0 \rightarrow \Lambda \bar{p} K^+$  candidates for the LL (left) and DD (right) samples after the stripping for the 2012 data set. The signal is described by a Gaussian distribution and the background by an exponential function. Candidates within  $3\sigma$  around the Gaussian mean value  $\mu$  of the DD fit are rejected. The DD veto is also applied to the LL sample.

Another source of background are  $B$  decays into a charmonium state such as  $B^0 \rightarrow J/\psi \pi^+ \pi^-$  with  $J/\psi \rightarrow p \bar{p}$ . The final state would be identical to  $\bar{B}^0 \rightarrow \Lambda \bar{p} \pi^+$  and again the production mechanism would be dominated by a  $b \rightarrow c$  tree amplitude. These modes, however, are suppressed due to the long lifetime of the  $\Lambda$  and no contribution of any charmonium states is found in the  $p \bar{p}$  invariant mass.

### 3.2.2 Background from Charged Particle Misidentification

The pion-kaon misidentification is expected to be a dominant source of peaking background for both  $\bar{B}^0 \rightarrow \Lambda \bar{p} \pi^+$  and  $\bar{B}_s^0 \rightarrow \Lambda \bar{p} K^+$ . Misidentifying a kaon as a pion leads to a shifted and asymmetric peak in the invariant  $\Lambda \bar{p} \pi$  mass distribution. The energy of the kaon is calculated using the pion mass hypothesis

$$E' = \sqrt{(m - \Delta m)^2 + \mathbf{p}^2} \quad , \quad (3.16)$$

$m$  being the kaon mass and  $\Delta m$  the mass difference between kaon and pion, and  $\mathbf{p}$  the kaon momentum. Due to the non-linear dispersion relation the effect of misidentification is not immediately evident. For low momenta the energy shift is dominated by the mass difference, for large momenta the shift becomes negligible. Since the track momenta at LHCb are large compared to  $\Delta m$  the peak values become similar. In the case of  $\bar{B}^0 \rightarrow \Lambda \bar{p} \pi^+$  and  $\bar{B}_s^0 \rightarrow \Lambda \bar{p} K^+$  the mass difference between  $\bar{B}^0$  and  $\bar{B}_s^0$  adds an additional shift. As a result, the  $\bar{B}^0 \rightarrow \Lambda \bar{p} \pi^+$  and misidentified  $\bar{B}_s^0 \rightarrow \Lambda \bar{p} K^+$  peaks have a large overlap.

In addition to these modes there are also the highly suppressed  $b \rightarrow d$  penguin amplitudes  $B^0 \rightarrow \Lambda \bar{p} K^+$  and  $\bar{B}_s^0 \rightarrow \Lambda \bar{p} \pi^+$  whose yields are negligible. Therefore, only the modes  $\bar{B}^0 \rightarrow \Lambda \bar{p} \pi^+$  and  $B_s^0 \rightarrow \Lambda \bar{p} K^+$  are considered as cross-feed to each other.

The distributions of fully selected  $\bar{B}^0 \rightarrow \Lambda \bar{p} \pi^+$  and  $B_s^0 \rightarrow \Lambda \bar{p} K^+$  simulated signal events reconstructed with the pion and kaon hypothesis, respectively, are presented in Fig. 3.13. The PID selection for the bachelor hadron suppresses the cross-feeds considerably, especially in case for the  $\bar{B}_s^0 \rightarrow \Lambda \bar{p} K^+$  mode under  $\pi$ -mass hypothesis. The contribution, however, remains sizable and needs to be accounted for. In order to distinguish these two decay channels the yields are determined in a simultaneous fit to both samples. The kaon-pion misidentification rates obtained with the PIDCalib package are used to determine the corresponding cross feeds. Thus both the  $\bar{B}^0 \rightarrow \Lambda \bar{p} \pi^+$  and  $\bar{B}_s^0 \rightarrow \Lambda \bar{p} K^+$  yields will be determined in a single fit.

Proton-pion and proton-kaon misidentification is also considered. The only relevant source is  $\Lambda_b^0 \rightarrow \Lambda p \bar{p}$ . In Fig. 3.13 the distribution of these events is shown using the pion and kaon hypothesis, respectively. The shape

of the  $\Lambda_b^0 \rightarrow \Lambda p \bar{p}$  candidates exhibits a long tail towards smaller  $\Lambda \bar{p} h$  invariant masses for both mass hypotheses overlapping with the signal peaks. The overall contribution from the proton misidentification, however, is found to be small and considering the expected small branching fraction and the production ratio for  $\Lambda_b^0$  baryons, this cross feed is assumed to be negligible.

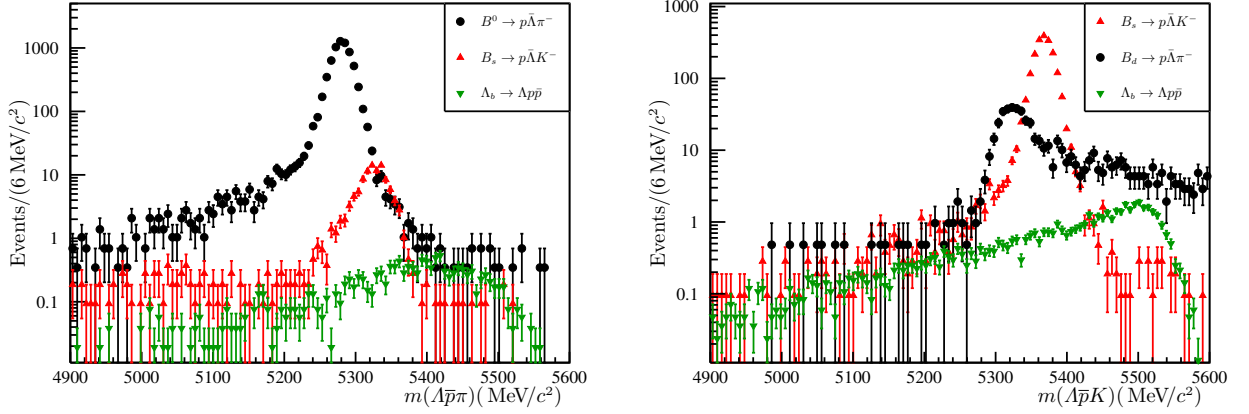


Figure 3.13: Comparison between  $\bar{B}^0 \rightarrow \Lambda \bar{p} \pi^+$  (black data points),  $\bar{B}_s^0 \rightarrow \Lambda \bar{p} K^+$  (red up triangles), and  $\Lambda_b^0 \rightarrow \Lambda p \bar{p}$  (green down triangles) MC simulated data reconstructed with the  $\pi$  mass hypothesis (left) and kaon hypothesis (right) for the (DD) 2012b sample. The integral of the histograms is scaled according to Table 2.1. The full selection has been applied to all samples.

### 3.2.3 Partially Reconstructed Backgrounds

Partially reconstructed background candidates are true  $\bar{B}_{(s)}^0$  decays with additional particles not being reconstructed. These can be non-resonant, *e.g.* decays such as  $B^- \rightarrow \Lambda \bar{p} \pi^+ \pi^-$ , or resonant, *e.g.*  $\bar{B}^0 \rightarrow \Sigma^0 \bar{p} \pi^+$  and  $\bar{B}^0 \rightarrow \Lambda \bar{p} \rho^+$ . Decays such as  $B^- \rightarrow \Lambda \bar{p} \pi^+ \pi^-$  are largely removed by the selection, the direction angle  $\theta_{\text{DIRA}}$  is particularly sensitive to such candidates. The additional pion may have an arbitrary momentum in the decay and this leads to larger values for  $\theta_{\text{DIRA}}$  which only uses  $\mathbf{p} = \mathbf{p}(\Lambda) + \mathbf{p}(\bar{p}) + \mathbf{p}(\pi^+)$ . In contrast, resonant decays are three-body decays. The momentum spectra of the missing particle depends on the mass of the intermediate particle. Resonances like  $K^*$  or  $\rho$  mesons are suppressed but not removed by the selection. Contributions from decays with  $\Sigma^0$  baryons decaying into  $\Sigma^0 \rightarrow \Lambda \gamma$ , the  $\gamma$  escaping detection and reconstruction, are expected to be only slightly suppressed due to the small mass difference. In addition, those modes are expected to leak into the signal region. Searches for related  $\Sigma^0$  modes have been conducted by the  $B$  factories such as  $\mathcal{B}(\bar{B}^0 \rightarrow \Sigma^0 \bar{p} \pi^+) < 3.8 \times 10^{-6}$  [22] and  $\mathcal{B}(\bar{B}^0 \rightarrow D^0 \Lambda \bar{\Sigma}^0 + \bar{B}^0 \rightarrow D^0 \Sigma^0 \bar{\Lambda}) < 3.1 \times 10^{-5}$  [53] and the limits are about the same size as the observed  $\Lambda$  modes,  $\mathcal{B}(\bar{B}^0 \rightarrow \Lambda \bar{p} \pi^+) = (3.14 \pm 0.29) \times 10^{-6}$  and  $\mathcal{B}(B^0 \rightarrow \bar{D}^0 \Lambda \bar{\Lambda}) = (1.00_{-0.26}^{+0.30}) \times 10^{-5}$  [12]. Therefore, it is not expected to measure these modes but a component describing these modes should be included in the fit model.

In Fig. 3.14 the distribution of  $\bar{B}^0 \rightarrow \Sigma^0 \bar{p} \pi^+$  MC simulated candidates in comparison with  $\bar{B}^0 \rightarrow \Lambda \bar{p} \pi^+$  and  $B_s^0 \rightarrow \Lambda \bar{p} K^+$  candidates is shown. The figures for the corresponding  $B_s^0$  decay mode,  $B_s^0 \rightarrow \Sigma^0 \bar{p} K^+$ , can be found in Fig. 3.14 as well. In contrast to the modes with a missing pion these modes peak very close to the signal and leak beneath the signal as well.

Despite their similar shapes the splitting into a pion and kaon sample allows both modes to be separated similar to the  $\bar{B}_{(s)}^0 \rightarrow \Lambda \bar{p} h^+$  modes.

The resonant four-body decays  $\bar{B}^0 \rightarrow \Lambda \bar{p} \rho^+$  and  $B_s^0 \rightarrow \Lambda \bar{p} K^{*+}$  are suppressed by the selection as expected. In Figure 3.15 the distributions for these two modes with respect to  $\bar{B}^0 \rightarrow \Lambda \bar{p} \pi^+$  and  $B_s^0 \rightarrow \Lambda \bar{p} K^+$  under pion and kaon mass hypothesis are shown. The overall contribution of these decays is small and is assumed to be negligible but an additional systematic uncertainty will be applied to take these contributions into account.

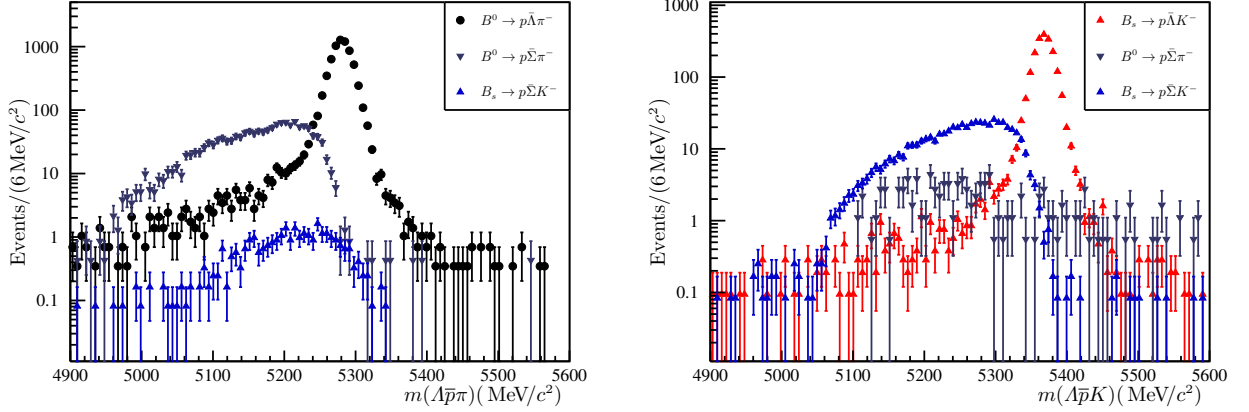


Figure 3.14: Comparison between  $\bar{B}^0 \rightarrow \Lambda \bar{p} \pi^+$  (black data points),  $\bar{B}_s^0 \rightarrow \Lambda \bar{p} K^+$  (red up triangles),  $\bar{B}^0 \rightarrow \Sigma^0 \bar{p} \pi^+$  (steel-grey down triangles), and  $\bar{B}_s^0 \rightarrow \Sigma^0 \bar{p} K^+$  (blue up triangles) MC simulated data reconstructed with the  $\pi$  mass hypothesis (left) and kaon hypothesis (right) for the (DD) 2012b sample. The integral of the histograms is scaled according to Table 2.1. The full selection has been applied to all samples.

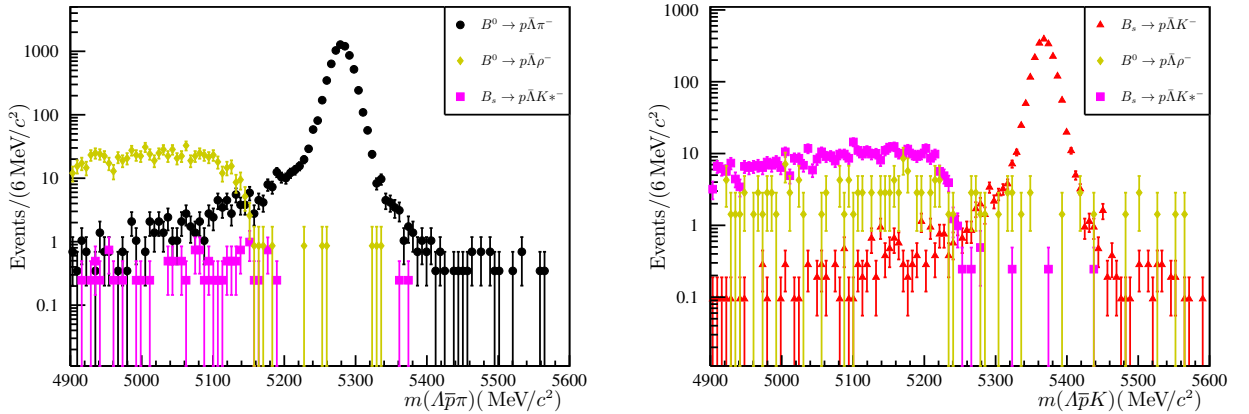


Figure 3.15: Comparison between  $\bar{B}^0 \rightarrow \Lambda \bar{p} \pi^+$  (black data points),  $\bar{B}_s^0 \rightarrow \Lambda \bar{p} K^+$  (red up triangles),  $\bar{B}^0 \rightarrow \Lambda \bar{p} \rho^+$  (khaki diamonds), and  $\bar{B}_s^0 \rightarrow \Lambda \bar{p} K^{*+}$  (magenta squares) MC simulated data reconstructed with the  $\pi$  mass hypothesis (left) and kaon hypothesis (right) for the (DD) 2012b sample. The integral of the histograms is scaled according to Table 2.1. The full selection has been applied to all samples.

### 3.2.4 Background from Decays Containing $K_S^0$ Mesons

The influence of proton-pion misidentification in the reconstruction and selection of the  $\Lambda$  baryon arising from  $K_S^0$  cross-feed is also investigated, since there is no PID requirement on the protons from the  $\Lambda$  decay. Related sources of background to the  $\bar{B}^0 \rightarrow \Lambda \bar{p} \pi^+$  spectrum could arise *e.g.* from  $\Lambda_b^0 \rightarrow K_S^0 p \pi^-$  decays.

In order to distinguish between the  $K_S^0$  and the  $\Lambda$  without PID information the Armenteros-Podolanski (AP) plot is exploited [36]. The plot makes use of the different decay kinematics of the  $K_S^0$  and  $\Lambda$  decays, the latter being

asymmetric due to the larger proton mass. One defines

$$p_T = p^+ \sin \phi^+ = p^- \sin \phi^- \quad \text{and} \quad (3.17)$$

$$\alpha = \frac{p_L^+ - p_L^-}{p_L^+ + p_L^-} \quad \text{with } p_L^\pm = p^\pm \cos \phi^\pm \quad ,$$

where  $p^\pm$  are the daughter momenta and  $\phi^\pm$  the angle between the daughter and  $V^0$  momenta in the laboratory frame. In Fig. 3.16 the AP plot for both  $\Lambda$  and  $K_S^0$  candidates from 2012 minimum bias events is shown. Minimum bias events are events with very loose trigger thresholds. The symmetry of the  $K_S^0$  decay and the two bands containing the  $\Lambda$  and  $\bar{\Lambda}$  candidates can be seen. Figure 3.17 shows the AP plot for  $\bar{B}^0 \rightarrow \Lambda \bar{p} \pi^+$  and  $B_s^0 \rightarrow \Lambda \bar{p} K^+$  events passing our full selection. No  $K_S^0$  candidates remain. The sharp edges compared to the distribution shown in Fig. 3.16 are due to the  $\Lambda$  mass constrain in the decay-tree fit.

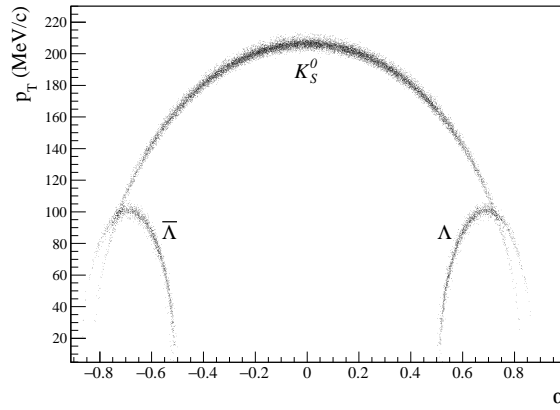


Figure 3.16: Armenteros-Podolanski plot for  $K_S^0$  and  $\Lambda$  candidates using minimum bias events from the 2012 data set.

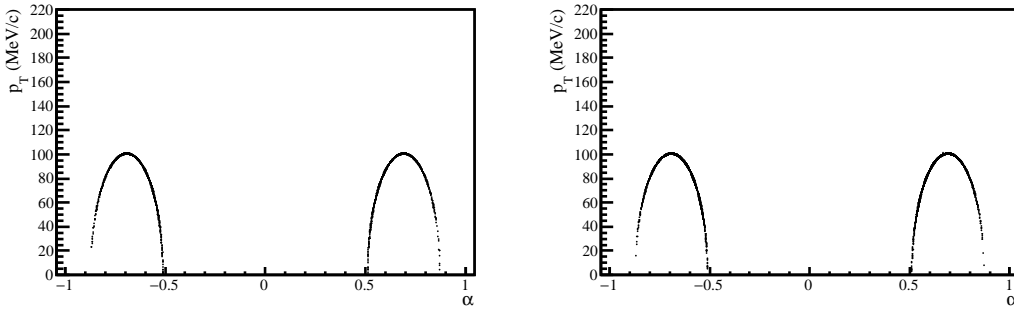


Figure 3.17: Armenteros-Podolanski plot for the  $\Lambda$  candidates after applying the selection as described in Sec. 3.1. There are no  $K_S^0$  present in the sample.

### 3.2.5 Summary of Background Contributions

In Figs. 3.18 and 3.19 the expected background contributions are stacked together with respect to the  $\bar{B}^0 \rightarrow \Lambda \bar{p} \pi^+$  and  $B_s^0 \rightarrow \Lambda \bar{p} K^+$  signal contributions using the scale factors listed in Tab. 2.1. For each mass hypothesis for the

bachelor meson the influence from partially reconstructed four-body decays with  $\rho$  or  $K^*$  mesons is expected to be negligible but additional four-body modes containing excited  $\Lambda$  or  $\Sigma^0$  baryons could contribute the overall number of background candidates. The  $\Sigma^0$  contributions are expected to be sizable, whereas crossfeed from misidentified  $\Lambda_b^0 \rightarrow \Lambda p \bar{p}$  decays is expected to be negligible.

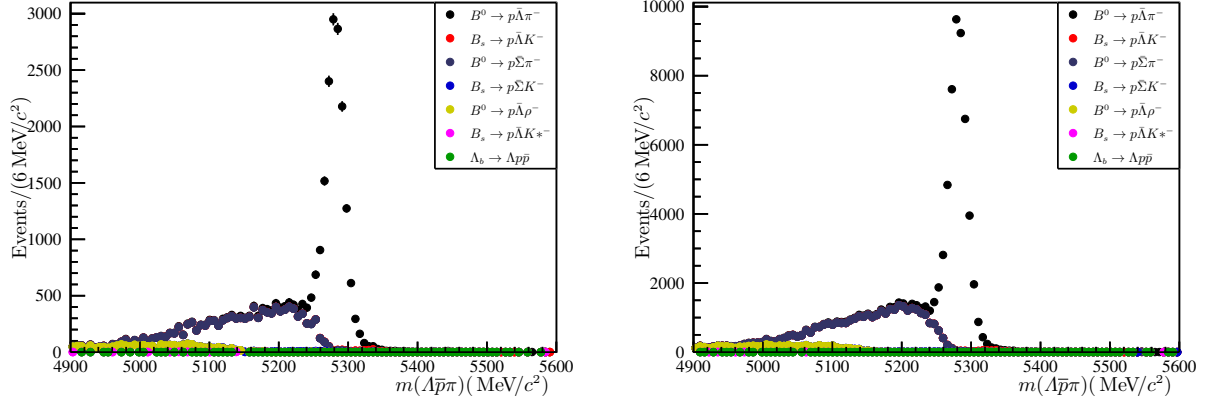


Figure 3.18: Plot of the invariant  $\Lambda \bar{p} \pi$  mass showing the expected background contributions as a stacked histogram with respect to the  $\bar{B}_s^0 \rightarrow \Lambda \bar{p} K^+$  mode. The left (right) plot shows the LL (DD) sample.

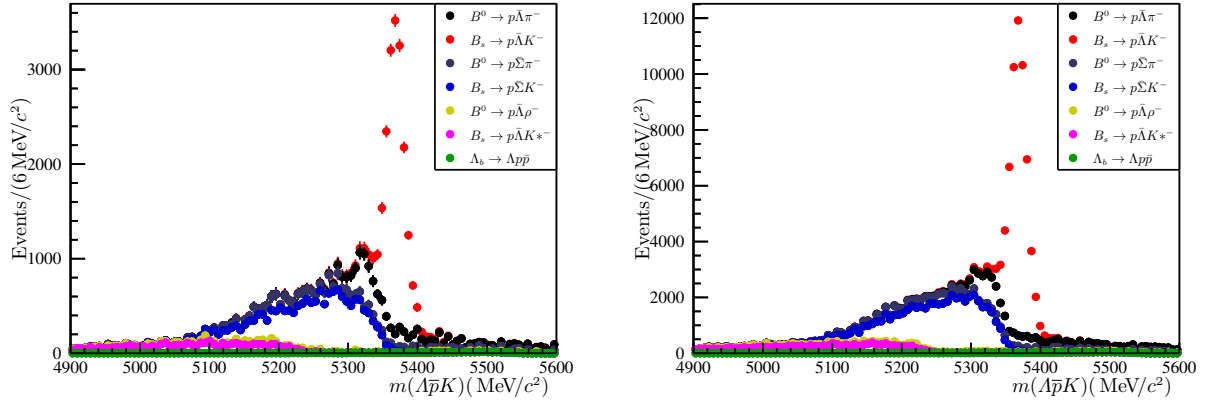


Figure 3.19: Plot of the invariant  $\Lambda \bar{p} K$  mass showing the expected background contributions as a stacked histogram with respect to the  $\bar{B}_s^0 \rightarrow \Lambda \bar{p} K^+$  mode. The left (right) plot shows the LL (DD) sample.

As a result of the background studies, the following components need to be included in the fit model, the  $\bar{B}^0_{(s)} \rightarrow \Lambda \bar{p} h^+$  signal modes and the  $\bar{B}^0_{(s)} \rightarrow \Sigma^0 \bar{p} h^+$  modes. The contribution from generic partially reconstructed four-body decays will be assessed as a systematic uncertainty. In addition the data-sample is split into a  $\pi$  and into a  $K$  sample. Both invariant mass spectra are fitted simultaneously in order to extract the number of the corresponding candidates.

### 3.3 Efficiency Calculations

This part of the analysis is concerned with the effects of an imperfect detector and an imperfect selection. An ideal detector would read out any event followed by an ideal selection, which would reject all background events while

keeping all signal events. Any realistic detector is not able to select all hits of a charged particle, neither is the reconstruction software able to find all tracks based on these hits. The read-out and network bandwidth forces restrictions on the amount of events that can be triggered. Background and signal events usually overlap in the selection variables as well. These factors all lead to a loss of candidates, *i.e.* not all signal events are detected and identified as such. The ratio between the number of actually selected candidates with respect to the initially produced number of candidates is referred to as efficiency. The overall efficiency can be written as a product of individual efficiencies dealing with singular effects<sup>4</sup>,

$$\varepsilon^{\text{tot}} = \varepsilon^{\text{gen}} \cdot \varepsilon^{\text{strip/gen}} \cdot \varepsilon^{\text{trig/strip}} \cdot \varepsilon^{\text{sel/trig}} \cdot \varepsilon^{\text{PID}} \quad , \quad (3.18)$$

the individual terms refer to:

- $\varepsilon^{\text{gen}}$  The generator efficiency determines how many decays take place in the detector volume in comparison to the full  $4\pi$  solid angle. This basically reflect the geometric acceptance determined by the active detector volume.
- $\varepsilon^{\text{strip/gen}}$  The stripping efficiency is determined relative to the generator efficiency, *i.e.* the number of events selected by the stripping line (*cf.* Sec. 3.1.2) with respect to the number of candidates moving into the detector volume.
- $\varepsilon^{\text{trig/strip}}$  The trigger efficiency is given by the ratio between candidates passing the trigger selection (*cf.* Sec. 3.1.1) and the number of candidates that have passed the stripping selection. This sequence seems unintuitive since any event needs to be triggered first before it can be used during the stripping, however, due to the workflow for handling simulated events, the stripping is applied before the trigger conditions.
- $\varepsilon^{\text{sel/trig}}$  The selection efficiency offers insight on how many signal events are rejected with respect to the trigger stage of the selection and includes the preselection (Sec. 3.1.5), the MVA selection (Sec. 3.1.6.4), and the charm veto (Sec. 3.2.1).
- $\varepsilon^{\text{PID}}$  The particle identification efficiency is calculated with respect to the selection efficiency  $\varepsilon^{\text{sel/trig}}$  and is the final step in the selection chain. In contrast to the other efficiencies both the acceptance and the rejection of a given particle hypotheses need to be taken into account, *i.e.* identifying a kaon as a kaon is as important to consider as misidentifying a kaon as a pion.

All efficiencies except the PID selection efficiency are determined using MC simulated signal events assuming a constant matrix element across the Dalitz plot. As described in Sec. 2.4.3, the PID performance in recorded and simulated data is different, therefore, the PID efficiency is determined using a data driven method based on different calibration samples compiled into the LHCb internal `PIDCalib` package.

Fortunately the measurement of both the relative branching fractions between the  $\bar{B}^0_{(s)} \rightarrow \Lambda\bar{p}h^+$  and  $\bar{B}^0_{(s)} \rightarrow \Sigma^0\bar{p}h^+$  modes and the measurement of the T violation asymmetry rely only on the ratios between the overall efficiencies. Similar to Eq. (3.18) the ratio between the  $\bar{B}^0_s \rightarrow \Lambda\bar{p}K^+$  and  $\bar{B}^0 \rightarrow \Lambda\bar{p}\pi^+$  efficiency is given by

$$\frac{\varepsilon^{\text{tot}}_{\bar{B}^0 \rightarrow \Lambda\bar{p}\pi^+}}{\varepsilon^{\text{tot}}_{\bar{B}^0_s \rightarrow \Lambda\bar{p}K^+}} = \frac{\varepsilon^{\text{gen}}_{\bar{B}^0 \rightarrow \Lambda\bar{p}\pi^+}}{\varepsilon^{\text{gen}}_{\bar{B}^0_s \rightarrow \Lambda\bar{p}K^+}} \cdot \frac{\varepsilon^{\text{strip/gen}}_{\bar{B}^0 \rightarrow \Lambda\bar{p}\pi^+}}{\varepsilon^{\text{strip/gen}}_{\bar{B}^0_s \rightarrow \Lambda\bar{p}K^+}} \cdot \frac{\varepsilon^{\text{trig/strip}}_{\bar{B}^0 \rightarrow \Lambda\bar{p}\pi^+}}{\varepsilon^{\text{trig/strip}}_{\bar{B}^0_s \rightarrow \Lambda\bar{p}K^+}} \cdot \frac{\varepsilon^{\text{sel/trig}}_{\bar{B}^0 \rightarrow \Lambda\bar{p}\pi^+}}{\varepsilon^{\text{sel/trig}}_{\bar{B}^0_s \rightarrow \Lambda\bar{p}K^+}} \cdot \frac{\varepsilon^{\text{PID}}_{\bar{B}^0 \rightarrow \Lambda\bar{p}\pi^+}}{\varepsilon^{\text{PID}}_{\bar{B}^0_s \rightarrow \Lambda\bar{p}K^+}} \quad . \quad (3.19)$$

A detailed listing of each individual contribution to the overall efficiency broken down into the three data taking periods for all relevant  $\bar{B}^0_{(s)} \rightarrow \Lambda\bar{p}h^+$  and  $\bar{B}^0_{(s)} \rightarrow \Sigma^0\bar{p}h^+$  modes can be found in Appendix F. For the following tables, the efficiency for 2012 is calculated averaging over the 2012a and 2012b periods according to their relative luminosities (*cf.* Eq. (2.4)). Table 3.5 lists the total efficiency given the correct bachelor meson hypotheses. In Table 3.6 the ratios between the total efficiencies relative to the  $\bar{B}^0 \rightarrow \Lambda\bar{p}\pi^+$  mode barring the PID efficiencies can be found. The ratios given in Tab. 3.6 are used in the fit allowing the application of physical constraints and are independent of the bachelor meson mass hypothesis. The PID selection efficiencies are included in the fit as well, but are incorporated separately from the selection efficiency ratios.

Finally it is necessary to point out that the efficiencies listed in this section are based on phase space MC simulated decays. The effect will be addressed in the following section.

<sup>4</sup>Other decompositions are of course viable. In the end it boils down to a practical choice given the details of the analysis at hand.

Table 3.5: Total selection efficiencies separated by data taking period and track reconstruction type.

Decay mode	Reco.	$\varepsilon_{\text{total}}(10^{-4})$ for correct mass hypothesis	
		2011	2012
$\bar{B}^0 \rightarrow \Lambda \bar{p} \pi^+$	LL	$1.03 \pm 0.03$	$1.22 \pm 0.03$
	DD	$2.92 \pm 0.05$	$3.44 \pm 0.04$
$B_s^0 \rightarrow \Lambda \bar{p} K^+$	LL	$1.15 \pm 0.04$	$1.35 \pm 0.03$
	DD	$3.45 \pm 0.06$	$4.01 \pm 0.05$
$\bar{B}^0 \rightarrow \Sigma^0 \bar{p} \pi^+$	LL	$0.90 \pm 0.07$	$1.02 \pm 0.04$
	DD	$2.46 \pm 0.11$	$3.05 \pm 0.07$
$\bar{B}_s^0 \rightarrow \Sigma^0 \bar{p} K^+$	LL	$0.95 \pm 0.05$	$1.14 \pm 0.04$
	DD	$2.91 \pm 0.09$	$3.46 \pm 0.06$

Table 3.6: Ratios of total selection efficiencies, with respect to the  $\bar{B}^0 \rightarrow \Lambda \bar{p} \pi^+$  selection efficiency, for all data taking periods and track reconstruction types.

Mode with respect to $\bar{B}^0 \rightarrow \Lambda \bar{p} \pi^+$	Efficiency ratio
$\delta_{\pi, \text{LL}, 11}^{\bar{B}_s^0 \rightarrow \Lambda \bar{p} K^+}$	$1.119 \pm 0.050$
$\delta_{\pi, \text{LL}, 12}^{\bar{B}_s^0 \rightarrow \Lambda \bar{p} K^+}$	$1.109 \pm 0.033$
$\delta_{\pi, \text{DD}, 11}^{\bar{B}_s^0 \rightarrow \Lambda \bar{p} K^+}$	$1.184 \pm 0.031$
$\delta_{\pi, \text{DD}, 12}^{\bar{B}_s^0 \rightarrow \Lambda \bar{p} K^+}$	$1.166 \pm 0.019$
$\delta_{\pi, \text{LL}, 11}^{\bar{B}^0 \rightarrow \Sigma^0 \bar{p} \pi^+}$	$0.877 \pm 0.073$
$\delta_{\pi, \text{LL}, 12}^{\bar{B}^0 \rightarrow \Sigma^0 \bar{p} \pi^+}$	$0.841 \pm 0.037$
$\delta_{\pi, \text{DD}, 11}^{\bar{B}^0 \rightarrow \Sigma^0 \bar{p} \pi^+}$	$0.843 \pm 0.042$
$\delta_{\pi, \text{DD}, 12}^{\bar{B}^0 \rightarrow \Sigma^0 \bar{p} \pi^+}$	$0.885 \pm 0.21$
$\delta_{\pi, \text{LL}, 11}^{\bar{B}_s^0 \rightarrow \Sigma^0 \bar{p} K^+}$	$0.920 \pm 0.059$
$\delta_{\pi, \text{LL}, 12}^{\bar{B}_s^0 \rightarrow \Sigma^0 \bar{p} K^+}$	$0.936 \pm 0.035$
$\delta_{\pi, \text{DD}, 11}^{\bar{B}_s^0 \rightarrow \Sigma^0 \bar{p} K^+}$	$0.997 \pm 0.037$
$\delta_{\pi, \text{DD}, 12}^{\bar{B}_s^0 \rightarrow \Sigma^0 \bar{p} K^+}$	$1.005 \pm 0.021$

### 3.4 Variance of the Efficiencies Across the Dalitz Plane

The overall efficiencies listed in Tab. 3.5 as well the ratios between the individual modes, *cf.* Tab. 3.6, are based on phase space simulated Events assuming a constant matrix element across the Dalitz plot. This is in stark contradiction with the observed results for the  $\bar{B}^0 \rightarrow \Lambda \bar{p} \pi^+$  decay mode, shown in Fig.3.20 for the projection upon the invariant  $\Lambda \bar{p}$  mass.

However, this is only problematic in case the efficiency varies largely across the Dalitz plane. It is therefore necessary to study the efficiency as a function of the Dalitz plot variables  $\varepsilon(m^2(\Lambda \bar{p}), m^2(\bar{p} h^+))$ . Due to data storage restrictions only events within the active detector volume are saved to disk. As a result the overall generated Dalitz plot is not accessible. This becomes problematic when a two dimensional binned efficiency correction is to be



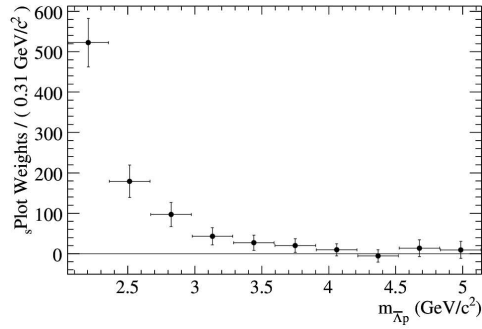


Figure 3.20: Background subtracted distribution of the invariant  $\Lambda\bar{p}$  mass for  $\bar{B}^0 \rightarrow \Lambda\bar{p}\pi^+$  candidates obtained by the *BABAR* collaboration [25].

applied, because the edges of the Dalitz plot do not fully overlap with all bins. This problem can be solved by applying a mass constraint on the  $\bar{B}^0$  mass as this leads to well defined edges for the reconstructed Dalitz plot as well. The generated Dalitz plot is calculated by hand using the generator efficiencies from Tab. F.1 and assuming a constant matrix element. The shape of the Dalitz plot is calculated using Eq. (1.61). The ratio between the reconstructed candidates passing the complete selection chain without the PID selection and the calculated number of events in each bin is taken as the efficiency. This procedure is done for both  $\bar{B}^0_{(s)} \rightarrow \Lambda\bar{p}h^+$  modes in 2011, 2012a, and 2012b as well as for LL and DD. The efficiency distribution for the 2012b DD  $\bar{B}^0 \rightarrow \Lambda\bar{p}\pi^+$  dataset is shown in Fig. 3.21. The efficiency maps for the remaining samples can be found in Appendix F.6. The efficiency is large for small  $m^2(\Lambda\bar{p})$  and large  $m^2(\bar{p}h^+)$ , but small for large values of  $m^2(\Lambda\bar{p})$  and small values of  $m^2(\bar{p}h^+)$ .

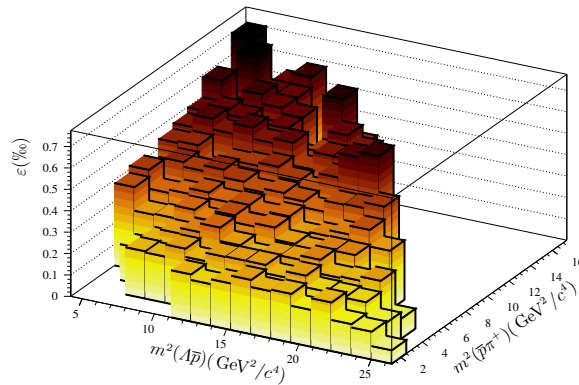


Figure 3.21: Plot of the efficiency as function of the two Dalitz plot variables  $\epsilon(m^2(\Lambda\bar{p}), m^2(\bar{p}h^+))$  for the  $\bar{B}^0 \rightarrow \Lambda\bar{p}\pi^+$  mode in 2012b DD.

### 3.5 Mass Fits

In general, analyses in the field of particle physics are counting experiments. This is basically also true for the determination of the T violation asymmetry to be determined in this analysis. Due to the complicated structure of the invariant  $\Lambda\bar{p}\pi$  mass it is difficult to simply count the number of signal candidates. In cases like this, the number of signal candidates is usually determined by a maximum likelihood fit to the data. The likelihood includes probability density functions (PDFs) for each physical contribution to the  $\Lambda\bar{p}h$  invariant masses. Over the course of

the next sections the overall fit strategy is introduced in detail followed by detailed listings of the PDFs used to describe the different physical components.

### 3.5.1 Fit Strategy

As explained earlier, the data is split per year, per bachelor particle hypothesis, and per track type of the reconstructed  $\Lambda$  daughters. An unbinned extended maximum likelihood fit is performed simultaneously on these eight sub-samples

- 2011 LL reconstructed with the pion mass hypothesis,
- 2011 LL reconstructed with the kaon mass hypothesis,
- 2011 DD reconstructed with the pion mass hypothesis,
- 2011 DD reconstructed with the kaon mass hypothesis,
- 2012 LL reconstructed with the pion mass hypothesis,
- 2012 LL reconstructed with the kaon mass hypothesis,
- 2012 DD reconstructed with the pion mass hypothesis,
- 2012 DD reconstructed with the kaon mass hypothesis.

Due to the expected limited statistics all spectra are described with a limited set of components:

- The two signal modes  $\bar{B}^0 \rightarrow \Lambda \bar{p} \pi^+$  and  $B_s^0 \rightarrow \Lambda \bar{p} K^+$ .
- One component for the contribution from each  $\Sigma^0$  baryon mode.
- Combinatorial background.

As was shown in the background summary (*cf.* 3.2.5) the contributions from  $\Lambda_b^0 \rightarrow \Lambda p \bar{p}$  and partially reconstructed decays can be neglected in the construction of the fit model.

All shape parameters are fixed to the values obtained from the signal MC simulation. The absolute momentum scale is different between the recorded and simulated data, which leads to a shift of the peak position of the invariant mass distributions. An additional parameter,  $\Delta m$ , is introduced to account for this effect. It is shared among all fit components and datasets. The different resolution between recorded and simulated data is treated as a systematic uncertainty using a different decay mode as a reference. A global scale factor for the width of the signal modes was prone to account for statistical fluctuations.

Several relations are shared among all datasets such as the ratio between the  $\bar{B}^0 \rightarrow \Lambda \bar{p} \pi^+$  and  $\bar{B}_s^0 \rightarrow \Lambda \bar{p} K^+$  and between the  $\bar{B}^0 \rightarrow \Sigma^0 \bar{p} \pi^+$  and  $\bar{B}^0 \rightarrow \Lambda \bar{p} \pi^+$  branching fractions. Naively one could expect, that

$$\frac{\mathcal{B}(\bar{B}^0 \rightarrow \Sigma^0 \bar{p} \pi^+)}{\mathcal{B}(\bar{B}^0 \rightarrow \Lambda \bar{p} \pi^+)} = \frac{\mathcal{B}(\bar{B}_s^0 \rightarrow \Sigma^0 \bar{p} K^+)}{\mathcal{B}(\bar{B}_s^0 \rightarrow \Lambda \bar{p} K^+)} \quad , \quad (3.20)$$

but due to the different isospin structure of  $\bar{B}^0$  and  $\bar{B}_s^0$  decays the ratios should be different. Since it is difficult to calculate the isospin relations between these two modes, each  $\Sigma^0$ -to- $\Lambda$  ratio is determined individually.

In addition to the physics derived constraints there are experimental effects, which can also be used to stabilise the complex fit model needed for this analysis. Due to the  $\Lambda$  baryon all modes have to be separated into a LL and a DD sample. As all decays share similar dynamics the ratio between the LL and DD samples should be the same, since the  $\Lambda$  baryon has similar properties. Differences in the individual efficiencies for selecting any candidate for the

different datasets are accounted for in the fit as well using Gaussian constraints. The individual fit functions are introduced in the following section.

The logarithmic likelihood for a given dataset can be expressed as

$$\begin{aligned} \log L = & - \left( N(\bar{B}^0 \rightarrow \Lambda\bar{p}\pi^+) + N(\bar{B}_s^0 \rightarrow \Lambda\bar{p}K^+) + N(\bar{B}^0 \rightarrow \Sigma^0\bar{p}\pi^+) + N(\bar{B}_s^0 \rightarrow \Sigma^0\bar{p}K^+) + N_{\text{Bkg}} \right) \\ & + \sum_j^N \log \left[ N(\bar{B}^0 \rightarrow \Lambda\bar{p}\pi^+) f_{\bar{B}^0 \rightarrow \Lambda\bar{p}\pi^+}(m_j(\Lambda\bar{p}h^+)|\vec{p}) + N(\bar{B}_s^0 \rightarrow \Lambda\bar{p}K^+) f_{\bar{B}_s^0 \rightarrow \Lambda\bar{p}K^+}(m_j(\Lambda\bar{p}h^+)|\vec{p}) \right. \\ & + N(\bar{B}^0 \rightarrow \Sigma^0\bar{p}\pi^+) f_{\bar{B}^0 \rightarrow \Sigma^0\bar{p}\pi^+}(m_j(\Lambda\bar{p}h^+)|\vec{p}) + N(\bar{B}_s^0 \rightarrow \Sigma^0\bar{p}K^+) f_{\bar{B}_s^0 \rightarrow \Sigma^0\bar{p}K^+}(m_j(\Lambda\bar{p}h^+)|\vec{p}) \\ & \left. + N_{\text{Bkg}} f_{\text{Bkg}}(m_j(\Lambda\bar{p}h^+)|\vec{p}) \right] \quad , \end{aligned} \quad (3.21)$$

where the  $N$  is the total number of candidates in a given datasample, the  $N(X)$  are the normalisations of the given individual PDFs  $f$ , that depend on the invariant  $\Lambda\bar{p}h^+$  mass and the parameters  $\vec{p}$ . The simplest approach to determine the number of signal events would now be to fit each of the eight datasets individually and to sum over all yields. However, in order to reduce the statistical uncertainties, the above mentioned constraints are applied. The PDFs remain unchanged but the yields are modified such as

$$\begin{aligned} N(\bar{B}^0 \rightarrow \Lambda\bar{p}\pi^+)_{\pi,\text{LL},12} &= \varepsilon_{\text{LL},12}^{\pi \rightarrow \pi} \times N(\bar{B}^0 \rightarrow \Lambda\bar{p}\pi^+) \\ N(\bar{B}^0 \rightarrow \Lambda\bar{p}\pi^+)_{K,\text{LL},12} &= \varepsilon_{\text{LL},12}^{\pi \rightarrow K} \times N(\bar{B}^0 \rightarrow \Lambda\bar{p}\pi^+) \quad , \end{aligned} \quad (3.22)$$

with  $N(\bar{B}^0 \rightarrow \Lambda\bar{p}\pi^+)$  being the  $\bar{B}^0 \rightarrow \Lambda\bar{p}\pi^+$  yield,  $N(\bar{B}^0 \rightarrow \Lambda\bar{p}\pi^+)_{h,\text{LL},12}$  the number of  $\bar{B}^0 \rightarrow \Lambda\bar{p}\pi^+$  candidates found for a given mass hypothesis of the bachelor meson for either the LL, DD, 2011, or 2012 dataset, respectively, and  $\varepsilon^{\pi \rightarrow h}$  the efficiency to identify a pion as either a pion or kaon. The number of produced  $\bar{B}^0 \rightarrow \Lambda\bar{p}\pi^+$  decays is independent of the PID selection, therefore, when taking the PID efficiencies into account, both equations should yield the same  $N(\bar{B}^0 \rightarrow \Lambda\bar{p}\pi^+)$  result, *i.e.*

$$\varepsilon_{\text{LL},12}^{\pi \rightarrow \pi} + \varepsilon_{\text{LL},12}^{\pi \rightarrow K} = 1 \quad . \quad (3.23)$$

The yields for the other modes can be expressed in a similar fashion, *i.e.* for the  $\bar{B}_s^0 \rightarrow \Lambda\bar{p}K^+$  yield,

$$\begin{aligned} N(\bar{B}_s^0 \rightarrow \Lambda\bar{p}K^+)_{\pi,\text{LL},12} &= \varepsilon_{\text{LL},12}^{K \rightarrow \pi} \times N(\bar{B}_s^0 \rightarrow \Lambda\bar{p}K^+) \\ N(\bar{B}_s^0 \rightarrow \Lambda\bar{p}K^+)_{K,\text{LL},12} &= \varepsilon_{\text{LL},12}^{K \rightarrow K} \times N(\bar{B}_s^0 \rightarrow \Lambda\bar{p}K^+) \quad , \end{aligned} \quad (3.24)$$

where  $N(\bar{B}_s^0 \rightarrow \Lambda\bar{p}K^+)_{h,\text{LL},12}$  is the number of  $\bar{B}_s^0 \rightarrow \Lambda\bar{p}K^+$  candidates in the respective dataset,  $\varepsilon^{K \rightarrow h}$  the efficiency to identify a kaon as either a pion or kaon, and  $N(\bar{B}_s^0 \rightarrow \Lambda\bar{p}K^+)$  the Number of  $\bar{B}_s^0 \rightarrow \Lambda\bar{p}K^+$  decays, which is related to the number of  $\bar{B}^0 \rightarrow \Lambda\bar{p}\pi^+$  decays by

$$\begin{aligned} N(\bar{B}_s^0 \rightarrow \Lambda\bar{p}K^+) &= r^{\bar{B}_s^0 \rightarrow \Lambda\bar{p}K^+} \times N(\bar{B}^0 \rightarrow \Lambda\bar{p}\pi^+) \\ &= \frac{f_d}{f_s} \frac{\mathcal{B}(\bar{B}_s^0 \rightarrow \Lambda\bar{p}K^+)}{\mathcal{B}(\bar{B}^0 \rightarrow \Lambda\bar{p}\pi^+)} \times N(\bar{B}^0 \rightarrow \Lambda\bar{p}\pi^+) \quad . \end{aligned} \quad (3.25)$$

Since LHCb is not suited to determine the absolute branching fractions of  $\bar{B}^0_{(s)}$  decays, the ratio between two branching fractions such as  $r^{\bar{B}_s^0 \rightarrow \Lambda\bar{p}K^+}$  is usually the relevant result. Eq. (3.25) holds only in case the overall selection and reconstruction efficiency is the same for the  $\bar{B}^0 \rightarrow \Lambda\bar{p}\pi^+$  and  $\bar{B}_s^0 \rightarrow \Lambda\bar{p}K^+$  decays. As was discussed in Sec. 3.3 the total efficiencies are similar but not identical, therefore, an additional term needs to be added of the form,

$$\begin{aligned} N(\bar{B}_s^0 \rightarrow \Lambda\bar{p}K^+) &= \frac{\varepsilon_{\bar{B}_s^0 \rightarrow \Lambda\bar{p}K^+}}{\varepsilon_{\bar{B}^0 \rightarrow \Lambda\bar{p}\pi^+}} \times r^{\bar{B}_s^0 \rightarrow \Lambda\bar{p}K^+} \times N(\bar{B}^0 \rightarrow \Lambda\bar{p}\pi^+) \\ &= \delta^{\bar{B}_s^0 \rightarrow \Lambda\bar{p}K^+} \times r^{\bar{B}_s^0 \rightarrow \Lambda\bar{p}K^+} \times N(\bar{B}^0 \rightarrow \Lambda\bar{p}\pi^+) \quad , \end{aligned} \quad (3.26)$$

where  $\varepsilon_{\bar{B}_s^0 \rightarrow \Lambda \bar{p} K^+}$  and  $\varepsilon_{\bar{B}^0 \rightarrow \Lambda \bar{p} \pi^+}$  are the total selection and reconstruction efficiencies. The efficiencies depend on the dataset, hence the factor  $\delta_{\bar{B}_s^0 \rightarrow \Lambda \bar{p} K^+}$  needs to be calculated for each sample independently. Using eq. (3.26) the  $\bar{B}_s^0 \rightarrow \Lambda \bar{p} K^+$  yields for the 2012 LL dataset can be written as

$$\begin{aligned} N(\bar{B}_s^0 \rightarrow \Lambda \bar{p} K^+)_{\pi, \text{LL}, 12} &= \delta_{\pi, \text{LL}, 12}^{\bar{B}_s^0 \rightarrow \Lambda \bar{p} K^+} \times \varepsilon_{\text{LL}, 12}^{K \rightarrow \pi} \times r_{\bar{B}_s^0 \rightarrow \Lambda \bar{p} K^+}^{\bar{B}_s^0} \times N(\bar{B}^0 \rightarrow \Lambda \bar{p} \pi^+) \\ N(\bar{B}_s^0 \rightarrow \Lambda \bar{p} K^+)_{K, \text{LL}, 12} &= \delta_{K, \text{LL}, 12}^{\bar{B}_s^0 \rightarrow \Lambda \bar{p} K^+} \times \varepsilon_{\text{LL}, 12}^{K \rightarrow K} \times r_{\bar{B}_s^0 \rightarrow \Lambda \bar{p} K^+}^{\bar{B}_s^0} \times N(\bar{B}^0 \rightarrow \Lambda \bar{p} \pi^+) \end{aligned} \quad (3.27)$$

The same arguments can be used to derive expressions for the other yields, which then read

$$\begin{aligned} N(\bar{B}^0 \rightarrow \Sigma^0 \bar{p} \pi^+)_{\pi, \text{LL}, 12} &= \delta_{\pi, \text{LL}, 12}^{\bar{B}^0 \rightarrow \Sigma^0 \bar{p} \pi^+} \times \varepsilon_{\text{LL}, 12}^{\pi \rightarrow \pi} \times r_{\bar{B}^0 \rightarrow \Sigma^0 \bar{p} \pi^+}^{\bar{B}^0} \times N(\bar{B}^0 \rightarrow \Lambda \bar{p} \pi^+) \\ N(\bar{B}^0 \rightarrow \Sigma^0 \bar{p} \pi^+)_{K, \text{LL}, 12} &= \delta_{K, \text{LL}, 12}^{\bar{B}^0 \rightarrow \Sigma^0 \bar{p} \pi^+} \times \varepsilon_{\text{LL}, 12}^{\pi \rightarrow K} \times r_{\bar{B}^0 \rightarrow \Sigma^0 \bar{p} \pi^+}^{\bar{B}^0} \times N(\bar{B}^0 \rightarrow \Lambda \bar{p} \pi^+) \end{aligned} \quad (3.28)$$

$$\begin{aligned} N(\bar{B}_s^0 \rightarrow \Sigma^0 \bar{p} K^+)_{\pi, \text{LL}, 12} &= \delta_{\pi, \text{LL}, 12}^{\bar{B}_s^0 \rightarrow \Sigma^0 \bar{p} K^+} \times \varepsilon_{\text{LL}, 12}^{K \rightarrow \pi} \times r_{\bar{B}_s^0 \rightarrow \Sigma^0 \bar{p} K^+}^{\bar{B}_s^0} \times N(\bar{B}^0 \rightarrow \Lambda \bar{p} \pi^+) \\ N(\bar{B}_s^0 \rightarrow \Sigma^0 \bar{p} K^+)_{K, \text{LL}, 12} &= \delta_{K, \text{LL}, 12}^{\bar{B}_s^0 \rightarrow \Sigma^0 \bar{p} K^+} \times \varepsilon_{\text{LL}, 12}^{K \rightarrow K} \times r_{\bar{B}_s^0 \rightarrow \Sigma^0 \bar{p} K^+}^{\bar{B}_s^0} \times N(\bar{B}^0 \rightarrow \Lambda \bar{p} \pi^+) \end{aligned} \quad (3.29)$$

As described in Sec. 3.3 the ratios of the efficiencies are determined with control samples (PID efficiency) and simulated events (stripping, trigger, and MVA selection).

So far only the LL case has been considered. As mentioned above, the ratio between LL and DD should be similar. In principal the ratio between LL and DD is an effect related to the overall efficiency, so using the information from the simulation allows us to write

$$\begin{aligned} N(\bar{B}^0 \rightarrow \Lambda \bar{p} \pi^+)_{\pi, \text{DD}, 12} &= \varepsilon_{\text{DD}, 12}^{\pi \rightarrow \pi} \times r_{\text{LL/DD}, 12}^{\text{MC}} \times N(\bar{B}^0 \rightarrow \Lambda \bar{p} \pi^+) \\ N(\bar{B}^0 \rightarrow \Lambda \bar{p} \pi^+)_{K, \text{DD}, 12} &= \varepsilon_{\text{DD}, 12}^{\pi \rightarrow K} \times r_{\text{LL/DD}, 12}^{\text{MC}} \times N(\bar{B}^0 \rightarrow \Lambda \bar{p} \pi^+) \end{aligned} \quad (3.30)$$

it is, however, not expected, that the simulated events correctly reproduce this ratio. It is therefore useful to write for the  $\bar{B}^0 \rightarrow \Lambda \bar{p} \pi^+$  DD yields

$$\begin{aligned} N(\bar{B}^0 \rightarrow \Lambda \bar{p} \pi^+)_{\pi, \text{DD}, 12} &= \varepsilon_{\text{DD}, 12}^{\pi \rightarrow \pi} \times r_{\text{LL/DD}, 12}^{\text{MC}} \times r_{12}^{\text{DD}} \times N(\bar{B}^0 \rightarrow \Lambda \bar{p} \pi^+) \\ N(\bar{B}^0 \rightarrow \Lambda \bar{p} \pi^+)_{K, \text{DD}, 12} &= \varepsilon_{\text{DD}, 12}^{\pi \rightarrow K} \times r_{\text{LL/DD}, 12}^{\text{MC}} \times r_{12}^{\text{DD}} \times N(\bar{B}^0 \rightarrow \Lambda \bar{p} \pi^+) \end{aligned} \quad (3.31)$$

with  $\varepsilon_{\text{DD}, 12}^{\pi \rightarrow h}$  again being the PID selection efficiencies,  $r_{\text{LL/DD}, 12}^{\text{MC}}$  the ratio between the number of LL and DD candidates predicted by the simulation, and  $N(\bar{B}^0 \rightarrow \Lambda \bar{p} \pi^+)$  remains the number of  $\bar{B}^0 \rightarrow \Lambda \bar{p} \pi^+$  events, however, only the number of LL  $\bar{B}^0 \rightarrow \Lambda \bar{p} \pi^+$  candidates. The additional factor  $r_{12}^{\text{DD}}$  accounts for differences between data and the simulation, but it is expected to be of the order of one. Due to major changes in the trigger configuration between 2011 and 2012, two independent ratios  $r_{11}^{\text{DD}}$  and  $r_{12}^{\text{DD}}$  are introduced. When defining the DD yields for the other modes, similar considerations have to be made. Naively one would simply write for the  $\bar{B}_s^0 \rightarrow \Lambda \bar{p} K^+$  DD yield

$$\begin{aligned} N(\bar{B}_s^0 \rightarrow \Lambda \bar{p} K^+)_{\pi, \text{DD}, 12} &= \delta_{\pi, \text{DD}, 12}^{\bar{B}_s^0 \rightarrow \Lambda \bar{p} K^+} \times \varepsilon_{\text{DD}, 12}^{K \rightarrow \pi} \times r_{12}^{\text{DD}} \times r_{\bar{B}_s^0 \rightarrow \Lambda \bar{p} K^+}^{\bar{B}_s^0} \times N(\bar{B}^0 \rightarrow \Lambda \bar{p} \pi^+) \\ N(\bar{B}_s^0 \rightarrow \Lambda \bar{p} K^+)_{K, \text{DD}, 12} &= \delta_{K, \text{DD}, 12}^{\bar{B}_s^0 \rightarrow \Lambda \bar{p} K^+} \times \varepsilon_{\text{DD}, 12}^{K \rightarrow K} \times r_{12}^{\text{DD}} \times r_{\bar{B}_s^0 \rightarrow \Lambda \bar{p} K^+}^{\bar{B}_s^0} \times N(\bar{B}^0 \rightarrow \Lambda \bar{p} \pi^+) \end{aligned} \quad (3.32)$$

but since the ratio  $r_{12}^{\text{DD}}$  is essentially an efficiency effect determined by the  $\bar{B}^0 \rightarrow \Lambda \bar{p} \pi^+$  decay it is necessary to take the predicted ratio between LL and DD from the simulation,  $r_{\text{LL/DD}, 12}^{\text{MC}}$ , into account as well, so that the  $\bar{B}_s^0 \rightarrow \Lambda \bar{p} K^+$  DD yields are defined as,

$$\begin{aligned} N(\bar{B}_s^0 \rightarrow \Lambda \bar{p} K^+)_{\pi, \text{DD}, 12} &= \delta_{\pi, \text{DD}, 12}^{\bar{B}_s^0 \rightarrow \Lambda \bar{p} K^+} \times \varepsilon_{\text{DD}, 12}^{K \rightarrow \pi} \times r_{\text{LL/DD}, 12}^{\text{MC}} \times r_{12}^{\text{DD}} \\ &\quad \times r_{\bar{B}_s^0 \rightarrow \Lambda \bar{p} K^+}^{\bar{B}_s^0} \times N(\bar{B}^0 \rightarrow \Lambda \bar{p} \pi^+) \\ N(\bar{B}_s^0 \rightarrow \Lambda \bar{p} K^+)_{K, \text{DD}, 12} &= \delta_{K, \text{DD}, 12}^{\bar{B}_s^0 \rightarrow \Lambda \bar{p} K^+} \times \varepsilon_{\text{DD}, 12}^{K \rightarrow K} \times r_{\text{LL/DD}, 12}^{\text{MC}} \times r_{12}^{\text{DD}} \\ &\quad \times r_{\bar{B}_s^0 \rightarrow \Lambda \bar{p} K^+}^{\bar{B}_s^0} \times N(\bar{B}^0 \rightarrow \Lambda \bar{p} \pi^+) \end{aligned} \quad (3.33)$$

Using the same arguments to derive the expressions for the  $\bar{B}^0 \rightarrow \Sigma^0 \bar{p} \pi^+$  yields,

$$\begin{aligned} N(\bar{B}^0 \rightarrow \Sigma^0 \bar{p} \pi^+)_{\pi, \text{DD}, 12} &= \delta_{\pi, \text{DD}, 12}^{\bar{B}^0 \rightarrow \Sigma^0 \bar{p} \pi^+} \times \varepsilon_{\text{DD}, 12}^{\pi \rightarrow \pi} \times r_{\text{LL}/\text{DD}, 12}^{\text{MC}} \times r_{12}^{\text{DD}} \\ &\quad \times r^{\bar{B}^0 \rightarrow \Sigma^0 \bar{p} \pi^+} \times N(\bar{B}^0 \rightarrow \Lambda \bar{p} \pi^+) \\ N(\bar{B}^0 \rightarrow \Sigma^0 \bar{p} \pi^+)_{K, \text{DD}, 12} &= \delta_{K, \text{DD}, 12}^{\bar{B}^0 \rightarrow \Sigma^0 \bar{p} \pi^+} \times \varepsilon_{\text{DD}, 12}^{\pi \rightarrow K} \times r_{\text{LL}/\text{DD}, 12}^{\text{MC}} \times r_{12}^{\text{DD}} \\ &\quad \times r^{\bar{B}^0 \rightarrow \Sigma^0 \bar{p} \pi^+} \times N(\bar{B}^0 \rightarrow \Lambda \bar{p} \pi^+) \quad , \end{aligned} \quad (3.34)$$

and for the  $\bar{B}_s^0 \rightarrow \Sigma^0 \bar{p} K^+$  yields,

$$\begin{aligned} N(\bar{B}_s^0 \rightarrow \Sigma^0 \bar{p} K^+)_{\pi, \text{LL}, 12} &= \delta_{\pi, \text{DD}, 12}^{\bar{B}_s^0 \rightarrow \Sigma^0 \bar{p} K^+} \times \varepsilon_{\text{DD}, 12}^{K \rightarrow \pi} \times r_{\text{LL}/\text{DD}, 12}^{\text{MC}} \times r_{12}^{\text{DD}} \\ &\quad \times r^{\bar{B}_s^0 \rightarrow \Sigma^0 \bar{p} K^+} \times N(\bar{B}^0 \rightarrow \Lambda \bar{p} \pi^+) \\ N(\bar{B}_s^0 \rightarrow \Sigma^0 \bar{p} K^+)_{K, \text{DD}, 12} &= \delta_{K, \text{DD}, 12}^{\bar{B}_s^0 \rightarrow \Sigma^0 \bar{p} K^+} \times \varepsilon_{\text{DD}, 12}^{K \rightarrow K} \times r_{\text{DD}/\text{DD}, 12}^{\text{MC}} \times r_{12}^{\text{DD}} \\ &\quad \times r^{\bar{B}_s^0 \rightarrow \Sigma^0 \bar{p} K^+} \times N(\bar{B}^0 \rightarrow \Lambda \bar{p} \pi^+) \quad . \end{aligned} \quad (3.35)$$

The whole process is repeated for the 2011 datasets sharing the same variables except  $r_{\text{LL}/\text{DD}, 12}^{\text{MC}}$  and  $r_{12}^{\text{DD}}$ , which are expected to differ between the years. The overall LL  $\bar{B}^0 \rightarrow \Lambda \bar{p} \pi^+$  yield is independent as well. The ratios between the  $\bar{B}^0_{(s)} \rightarrow \Lambda \bar{p} h^+$  and  $\bar{B}^0_{(s)} \rightarrow \Sigma^0 \bar{p} h^+$  modes are identical to the ratios found for the 2012 samples, but the ratios between the overall efficiencies are calculated using simulated data representing the 2011 conditions. Otherwise the constraints on the ratio would not be valid.

The yields of the combinatorial backgrounds are left independent throughout the samples, but the variables shared by the samples and components are determined simultaneously as mentioned above.

Finally, rather than fixing the efficiency related parameters, Gaussian constraints for these parameters are introduced using the uncertainties determined in Sec. 3.3. The uncertainties on the PID efficiencies are small compared to the uncertainties of the efficiency ratios and the expected overall statistical uncertainty due to the limited sample size of the data, therefore, the PID efficiencies are fixed rather than constrained during the fit to data.

Expanding Eq. (3.21) to all datasets the complete Likelihood can be expressed as

$$\begin{aligned} \log L &= \sum_t^{\text{LL}, \text{DD}} \sum_y^{11, 12} \sum_h^{\pi, K} \sum_i^{N_{t,y,h}} \log \left( \sum_X^{\text{Modes}} N_{t,y,h}(X) f_{t,h}^X(m(\Lambda \bar{p} h)_i | \vec{p}_{t,h}^X) - N_{\text{Bkg}} f_{\text{Bkg}}(m_i(\Lambda \bar{p} h^+) | \vec{p}_{\text{Bkg}}) \right) \\ &\quad - \sum_X^{\text{Modes}} N_{t,y,h}(X) - N_{\text{Bkg}} - \sum_t^{\text{LL}, \text{DD}} \sum_y^{11, 12} \sum_h^{\pi, K} \sum_X^{\text{Modes}} \frac{1}{2} \chi^2(\delta_{t,y,h}^X) - \sum_y^{11, 12} \chi^2(r_{\text{LL}/\text{DD}, y}^{\text{MC}}) \end{aligned} \quad (3.36)$$

being the sum of the logarithmic likelihoods for each sample, the mode index  $X$  iterates over the components listed before, namely

$$\text{Modes} = \{ \bar{B}^0 \rightarrow \Lambda \bar{p} \pi^+, \bar{B}_s^0 \rightarrow \Lambda \bar{p} K^+, \bar{B}^0 \rightarrow \Sigma^0 \bar{p} \pi^+, \bar{B}_s^0 \rightarrow \Sigma^0 \bar{p} K^+ \} \quad . \quad (3.37)$$

The remaining summations indicate sums of the LL and DD samples,  $t$ , the year of data taking,  $y$ , and the bachelor meson hypothesis,  $h$ . The number of events  $N_{t,y,h}$  depends on the given year,  $\Lambda$  daughter track type, and the meson hypothesis applied for the given sample. The normalisations introduced in Eqs. 3.22 to 3.35 are inserted as well.

### 3.5.2 Fit Components

In general the time dependence of a decay of a quantum mechanical state follows the exponential decay law, that is related by Fourier transformation to the Breit-Wigner function in the energy domain. The mean life time is related to the width of the Breit-Wigner function, which is known as the natural line shape and its width as the natural

line width of the state. As a result, the naive choice to describe the signal contribution should be a Breit-Wigner function, however, the shape of the peak in data is not just governed by its natural line shape but also by experimental uncertainties, such as the momentum resolution (*cf.* Sec. 2.3.2). The experimental uncertainties lead to a Gaussian line shape, so that in practical terms the line shape is given by a convolution of a Breit-Wigner and a Gaussian function. This, however, can be simplified in case the natural line width exceeds the experimental resolution or in case the experimental resolution is much larger than the natural line width. In the first case, a Breit-Wigner function should describe the data, and in the latter case a Gaussian distribution. For  $\bar{B}^0_{(s)}$  mesons, the latter case is true. The following notation is used for the Gaussian,

$$f_{\text{Gauss}}(m|\mu, \sigma) = \frac{1}{\sigma\sqrt{2\pi}} e^{-\frac{(m-\mu)^2}{2\sigma^2}}, \quad (3.38)$$

with  $\mu$  being the expected value of  $m$  and  $\sigma$  being the standard deviation.

In addition to the natural line shape and experimental resolution other effects also impact the shape of the signal distribution. The momentum resolution is a function of the momentum of the particle (*cf.* Fig. 2.14) and an overlap of these different Gaussian distributions can lead to a non-Gaussian behaviour. Another effect that influences the line shape is Bremsstrahlung of the final state particles. In case it is not correctly accounted for in the momentum measurement this effect will lead to a tail on the left hand side of the mass peak, *i.e.* towards smaller  $\Lambda\bar{p}h$  invariant masses. Both effects can be described by the Novosibirsk function [54],

$$f_{\text{Novo}}(m|\mu, \sigma, \alpha) = \exp\left[-\frac{1}{2}\left(\frac{\ln^2[1 + \Lambda\alpha(m - \mu)]}{\alpha^2} + \alpha^2\right)\right] \quad (3.39)$$

$$\Lambda = \frac{\sinh^{-1}(\alpha\sqrt{\ln 4})}{(\sigma\alpha\sqrt{\ln 4})},$$

with  $\mu$  being the peak value,  $\sigma$  the width, and  $\alpha$  determines the shape of the tail. In case of a vanishing tail parameter  $\alpha$  the Novosibirsk function behaves like a Gaussian. In comparison to the Crystal Ball function [55], which is widely used at LHCb, it is more stable in the fit due to the smaller set of parameters and by being a continuous function. This function is used to describe the  $\bar{B}^0 \rightarrow \Lambda\bar{p}\pi^+$  and  $\bar{B}^0_s \rightarrow \Lambda\bar{p}K^+$  decays in case of the correct mass hypothesis.

Decays reconstructed using an incorrect particle mass hypothesis or that are only partially reconstructed have a largely asymmetric distribution in the  $\Lambda\bar{p}h$  invariant mass. An example would be reconstructing the  $\bar{B}^0_s \rightarrow \Lambda\bar{p}K^+$  decay using the pion-mass hypothesis for the kaon or decays such as  $\bar{B}^0 \rightarrow \Lambda\bar{p}\pi^+\pi^0$  with the  $\pi^0$  not being reconstructed. In order to describe partially or largely asymmetric distributions a convolution of an Argus function [56] with a Gaussian is usually used. Due to numerical problems a different parametrisation is chosen, a product of an exponential and a Fermi-Dirac function given by

$$f_{\text{Fermi}}(m|m_0, T, a, \hat{N}) = \hat{N} \frac{e^{\delta am}}{e^{-\delta T(m_0 - m)} + 1}, \quad (3.40)$$

with  $T$  being the inverse reduced temperature,  $m_0$  the chemical potential,  $a$  the slope of the exponential, and  $\hat{N}$  the normalisation factor. The value of  $m_0$  determines the inflection point of the distribution and  $T$  its slope. The Fermi-Dirac distribution is constant except in the vicinity of the inflection point. The exponential is required to modify this behaviour. The additional parameter  $\delta$  is chosen to be  $\delta = \pm 1$  depending on whether it is necessary to describe an asymmetric behaviour towards smaller ( $\delta = +1$ ) or towards larger ( $\delta = -1$ )  $\Lambda\bar{p}h^+$  invariant masses.

The Fit functions are determined using the simulated events also used for the background studies. The candidates are matched to the simulated particles and the full selection is applied. The line shape depends indirectly on the PID selection since the PID depends directly on the momentum. Applying a PID selection rejects candidates depending on their momenta with different efficiencies warping the overall line shape. Therefore, the PID selections needs to be finalised before determining the fit functions. The same functions are used to describe the 2011 and 2012 data.

In order to match the fit as closely to data as possible, all fits are performed as unbinned extended maximum likelihood fits. In all figures shown in the next sections the units of the parameters are omitted. A collection of all shape parameters and function can be found in Appendix G.

### 3.5.2.1 Signal Modes

The line shape of the two signal components, *i.e.* the  $\bar{B}^0 \rightarrow \Lambda \bar{p} \pi^+$  and  $\bar{B}^0_s \rightarrow \Lambda \bar{p} K^+$  modes, are determined for four different samples, the LL and DD data need to be described by different functions, since the momentum resolution is worse for the  $\Lambda$  baryons reconstructed with DD tracks compared to LL  $\Lambda$  candidates. In addition to the shape for the correct mass hypothesis, the cross feed of each mode for the other bachelor mass hypothesis needs to be modeled.

The shape of the  $\bar{B}^0 \rightarrow \Lambda \bar{p} \pi^+$  decay is modeled by the sum of two Novosibirsk functions in case of the  $\pi$ -mass hypothesis. The distribution of  $\bar{B}^0 \rightarrow \Lambda \bar{p} \pi^+$  candidates reconstructed with the kaon-mass hypothesis is described by the sum a Gaussian and the modified Fermi-Dirac distribution (*cf.* Eq. 3.40). The fits are performed independently and the results of the fits are shown in Fig. 3.22.

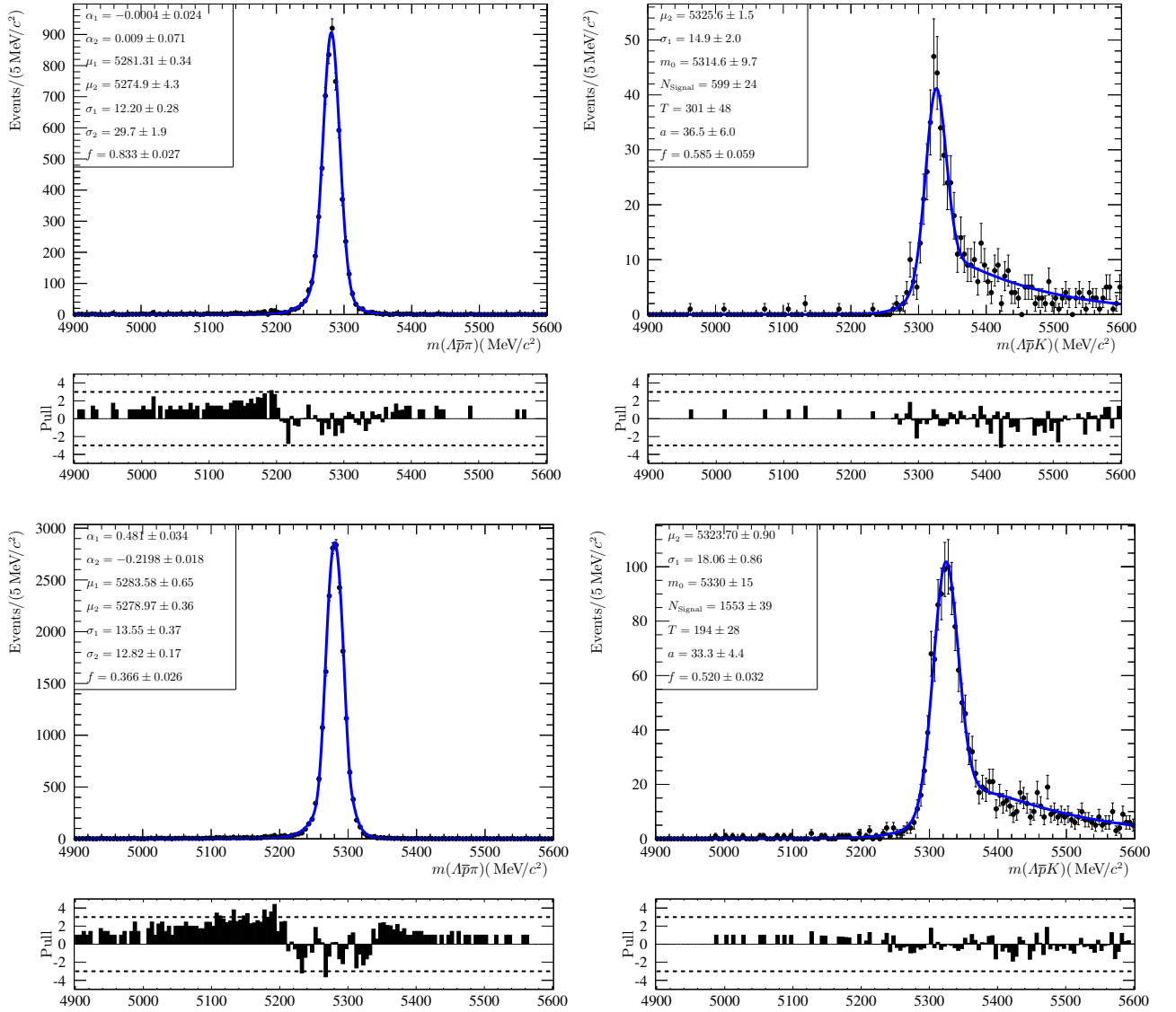


Figure 3.22: Fit model for the  $\bar{B}^0 \rightarrow \Lambda \bar{p} \pi^+$  signal mode, reconstructed with the pion hypothesis (left) and with the kaon hypothesis (right) for the LL sample (top) and the DD sample (bottom).

The distributions of the  $\bar{B}_s^0 \rightarrow \Lambda \bar{p} K^+$  are described analogously. Under the kaon mass hypothesis, the  $\Lambda \bar{p} K$  invariant mass is described by the sum two Novosibirsk functions and under the pion-mass hypothesis as the sum of a Gaussian and the modified Fermi-Dirac distribution. As with the  $\bar{B}^0 \rightarrow \Lambda \bar{p} \pi^+$  fits, all fits are performed independent of each other. The results are shown in Fig. 3.23.

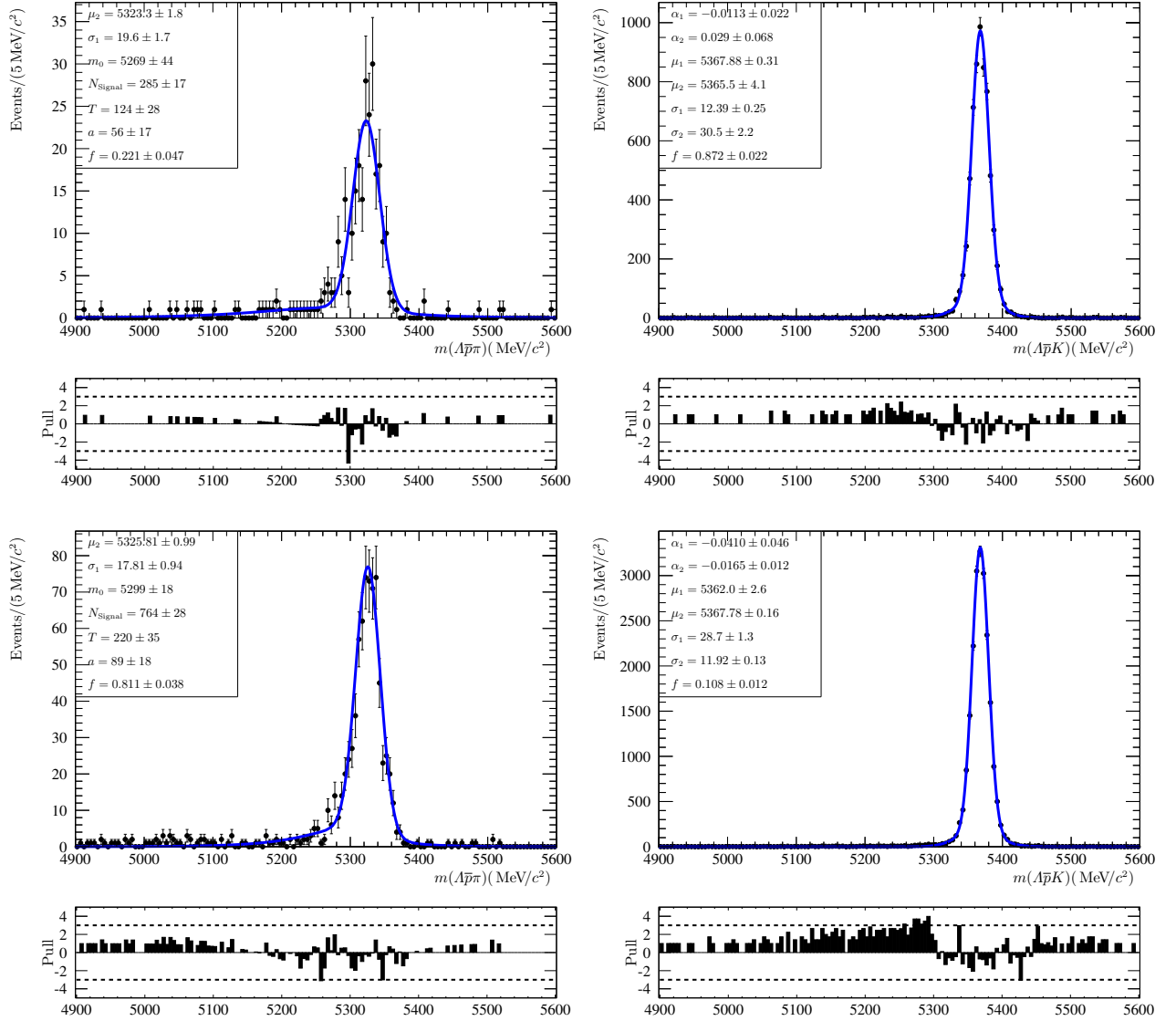


Figure 3.23: Fit model for the  $B_s^0 \rightarrow \Lambda \bar{p} K^+$  signal mode, reconstructed with the pion hypothesis (left) and with the kaon hypothesis (right) for the LL sample (top) and the DD sample (bottom).



### 3.5.2.2 Peaking Background

As discussed in Sec. 3.2.3, the possible contributions from  $\bar{B}^0_{(s)} \rightarrow \Sigma^0 \bar{p} h^+$  decays need to be taken into account in the fit model. The line shapes for  $\bar{B}^0 \rightarrow \Sigma^0 \bar{p} \pi^+$  and  $\bar{B}^0_s \rightarrow \Sigma^0 \bar{p} K^+$  are quite similar for each mass hypothesis (*cf.* Figs. 3.14) but similar to the cross feed between the signal contributions the PID selection suppresses the kaon contribution to the  $\Lambda \bar{p} \pi$  invariant mass distribution and vice versa. This allows to statistically disentangle the two  $\Sigma^0$  contributions.

The  $\bar{B}^0 \rightarrow \Sigma^0 \bar{p} \pi^+$  line shape is modeled by a modified Fermi-Dirac distribution except for the DD sample under  $\pi$  mass hypothesis, which is described by a sum of a Novosibirsk and a Gaussian function. The fit results are shown in Fig. 3.24.

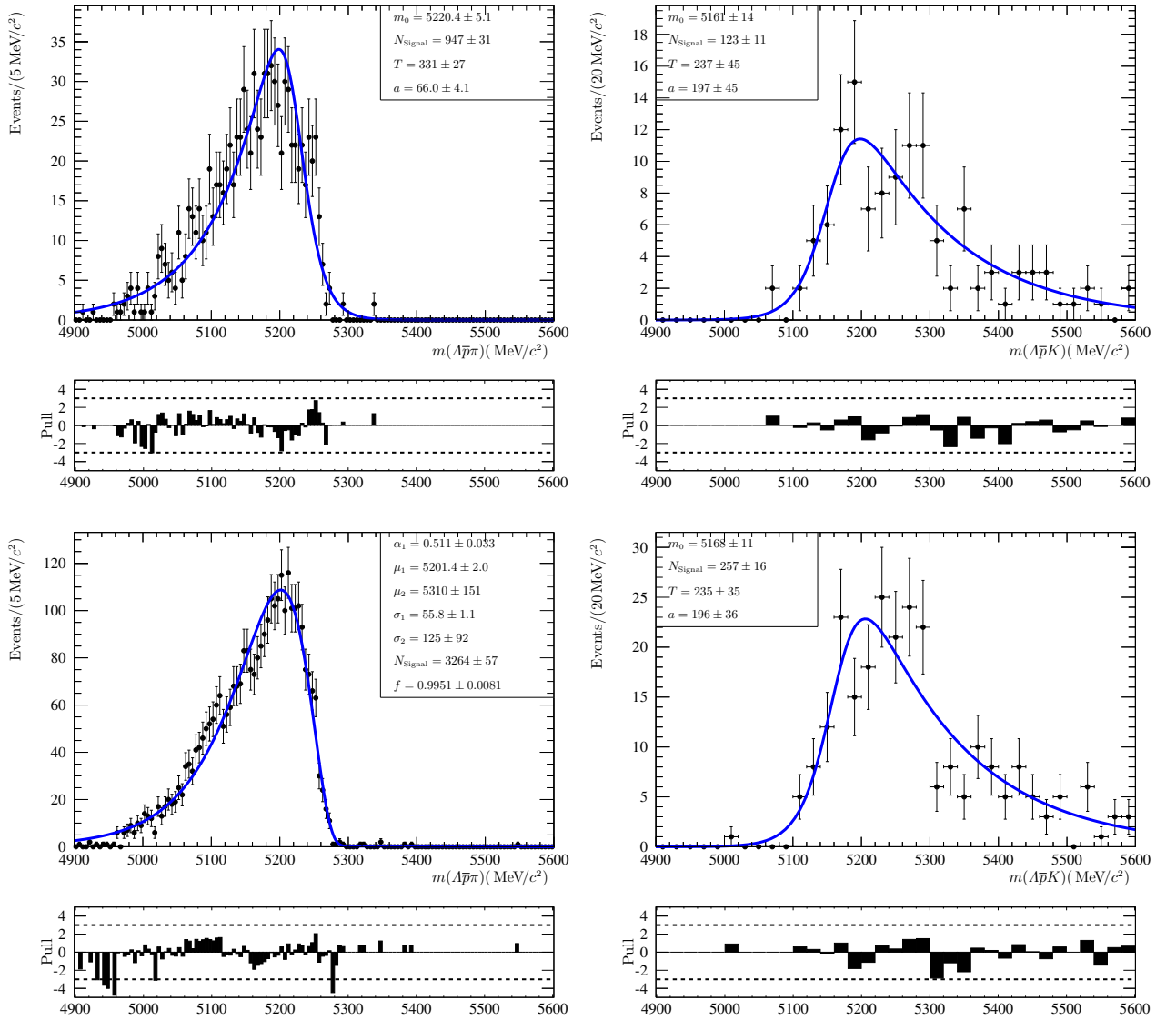


Figure 3.24: Fit model for the mode  $\bar{B}^0 \rightarrow \Sigma^0 \bar{p} h^+$ , reconstructed with the pion hypothesis (left) and with the kaon hypothesis (right) for the LL sample (top) and the DD sample (bottom).

The  $\Lambda \bar{p} h$  invariant mass distribution for  $\bar{B}^0_s \rightarrow \Sigma^0 \bar{p} K^+$  candidates is modeled by a modified Fermi-Dirac distribution

for the case, that the kaon is reconstructed as a pion and by a sum of a Novosibirsk a Fermi-Dirac distribution for the LL case under kaon hypothesis. The corresponding DD sample is described by a sum of two Novosibirsk functions. The fits to the simulated data samples are shown in Fig. 3.25.

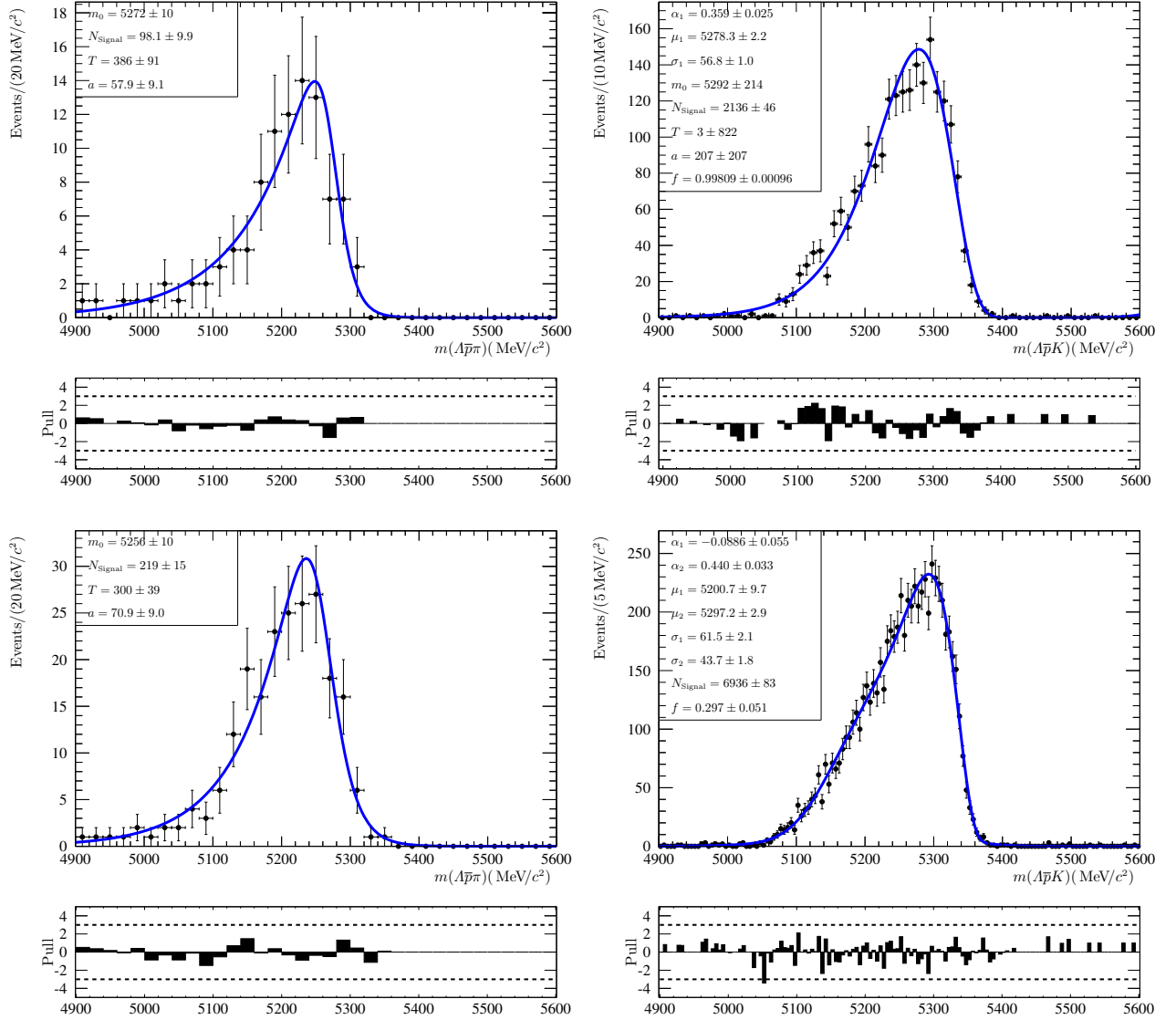


Figure 3.25: Fit model for the mode  $\bar{B}_s^0 \rightarrow \Sigma^0 \bar{p} K^+$ , reconstructed with the pion hypothesis (left) and with the kaon hypothesis (right) for the LL sample (top) and the DD sample (bottom).

Again, all fits are performed independent of each other, the units of the fit parameters are omitted.

### 3.5.2.3 Combinatorial Background

Combinatorial background from random  $p\bar{\Lambda}h^-$  combinations is described by an exponential function for both bachelor meson hypotheses. All shape parameter are left floating in the data fit and all exponential functions are determined independent of each other.

### 3.5.3 Fit Summary

To conclude, the fit models for both  $\Lambda\bar{p}\pi^+$  and  $\Lambda\bar{p}K^+$  spectra are listed in Tables 3.7 and 3.8. The 2011 and 2012 datasets are fitted simultaneously.

The floating parameters in the fit are listed in Table 3.9. All shape parameters are fixed to the values presented in the previous sections. A mass shift parameter, shared among the  $\bar{B}^0 \rightarrow \Lambda\bar{p}\pi^+$ ,  $\bar{B}_s^0 \rightarrow \Lambda\bar{p}K^+$ ,  $\bar{B}^0 \rightarrow \Sigma^0\bar{p}\pi^+$ , and  $\bar{B}_s^0 \rightarrow \Sigma^0\bar{p}K^+$  modes is allowed in the fit for both bachelor meson hypotheses and the  $\Lambda$  reconstruction types. No global scale factor for the signal resolutions is applied in order to avoid being dominated by statistical fluctuations. Furthermore, many modes overlap in the signal region and allowing for free scaling factor for the width could bias the overall fit. This discrepancy between recorded and simulated data is addressed as a systematic uncertainty instead. Several physical constraints are applied.

The ratio between the  $\bar{B}^0 \rightarrow \Lambda\bar{p}\pi^+$  and  $\bar{B}_s^0 \rightarrow \Lambda\bar{p}K^+$  decays is a physical quantity determined by the branching fractions. Therefore, the ratio should be constant throughout all data samples, and is constrained to be so. The same argument is true for the ratio between the  $\bar{B}^0_{(s)} \rightarrow \Sigma^0\bar{p}h^+$  modes with respect to the corresponding  $\bar{B}^0_{(s)} \rightarrow \Lambda\bar{p}h^+$  modes, and these ratios are constrained as well.

Table 3.7: Summary of the fit model describing the  $\Lambda\bar{p}\pi$  invariant mass spectra.

Mode	Sample	Fit function
$\bar{B}^0 \rightarrow \Lambda\bar{p}\pi^+$	LL DD	Sum of two Novosibirsk functions
$\bar{B}_s^0 \rightarrow \Lambda\bar{p}K^+$	LL DD	Sum of a Gaussian and modified Fermi function
$\bar{B}^0 \rightarrow \Sigma^0\bar{p}\pi^+$	LL DD	Modified Fermi function Sum of a Gaussian and Novosibirsk function
$\bar{B}_s^0 \rightarrow \Sigma^0\bar{p}K^+$	LL DD	Modified Fermi function
Combinatorial	LL DD	Exponential function

Table 3.8: Summary of the fit model describing the  $\Lambda\bar{p}K$  invariant mass spectra.

Mode	Sample	Fit function
$\bar{B}^0 \rightarrow \Lambda\bar{p}\pi^+$	LL DD	Sum of a Gaussian and a modified Fermi function
$\bar{B}_s^0 \rightarrow \Lambda\bar{p}K^+$	LL DD	Sum of two Novosibirsk functions
$\bar{B}^0 \rightarrow \Sigma^0\bar{p}\pi^+$	LL DD	Modified Fermi function
$\bar{B}_s^0 \rightarrow \Sigma^0\bar{p}K^+$	LL DD	Sum of a Novosibirsk and a modified Fermi function Sum of two Novosibirsk functions
Combinatorial	LL DD	Exponential function

All modes share similar  $\Lambda$  characteristics. The ratio between the number of LL and DD candidates is dominated by the  $\Lambda$  baryon decay. Due to the similar kinematics between the  $\bar{B}^0_{(s)} \rightarrow \Lambda\bar{p}h^+$  and  $\bar{B}^0_{(s)} \rightarrow \Sigma^0\bar{p}h^+$  modes the

ratio between LL and DD should be compatible with respect to the limited statistics. Due to the different trigger configuration in 2011 and 2012 this ratio should be dependant in the data period. The ratios are constrained for all 2011 data sets and all 2012 data sets.

Finally, the cross-feed contributions of  $\bar{B}_s^0 \rightarrow \Lambda\bar{p}K^+$  and  $\bar{B}_s^0 \rightarrow \Sigma^0\bar{p}K^+$  modes to the pion sample are constrained to be consistent with the expectations calculated using the PID calibration samples with respect to the number of  $\bar{B}_s^0 \rightarrow \Lambda\bar{p}K^+$  and  $\bar{B}_s^0 \rightarrow \Sigma^0\bar{p}K^+$  candidates determined in the kaon sample. The cross-feed of the  $\bar{B}^0 \rightarrow \Lambda\bar{p}\pi^+$  and  $\bar{B}^0 \rightarrow \Sigma^0\bar{p}\pi^+$  modes to the kaon sample are constrained in the same way.

Table 3.9: Free parameters determined in the simultaneous fit. The index  $y$  indicates the years 2011 and 2012, the index  $h$  the bachelor hypotheses pion or kaon, and  $t$  the LL or DD configuration.

Parameter	Description
$N_y^{\text{LL}}(\bar{B}^0 \rightarrow \Lambda\bar{p}\pi^+)$	Number of LL $\bar{B}^0 \rightarrow \Lambda\bar{p}\pi^+$ candidates
$r_{y,\bar{B}_s^0 \rightarrow \Lambda\bar{p}K^+}$	Ratio between the $\bar{B}_s^0 \rightarrow \Lambda\bar{p}K^+$ and $\bar{B}^0 \rightarrow \Lambda\bar{p}\pi^+$ candidates
$r_y^{\text{DD}}$	Correction factor for the MC ratio between the LL and DD yields
$r_{y,\bar{B}^0 \rightarrow \Sigma^0\bar{p}\pi^+}$	Ratio between the $\bar{B}^0 \rightarrow \Sigma^0\bar{p}\pi^+$ and $\bar{B}^0 \rightarrow \Lambda\bar{p}\pi^+$ yields
$r_{y,\bar{B}_s^0 \rightarrow \Sigma^0\bar{p}K^+}$	Ratio between the $\bar{B}_s^0 \rightarrow \Sigma^0\bar{p}K^+$ and $\bar{B}_s^0 \rightarrow \Lambda\bar{p}K^+$ yields
$\Delta m$	Mass shift shared among the $\bar{B}_{(s)}^0 \rightarrow \Lambda\bar{p}h^+$ and $\bar{B}_{(s)}^0 \rightarrow \Sigma^0\bar{p}h^+$ modes
$N_{y,h,t}^{\text{Bkg}}$	Number of combinatorial background events
$a_{y,h,t}^{\text{Bkg}}$	Slope of the exponential function for the combinatorial background

The ratios between the overall selection efficiencies need to be included in the fit as well, otherwise the physical constraints are not valid. The uncertainty on these ratios is often not negligible, thus they are included as Gaussian constraints to the overall fit, and are listed in Tab. 3.10 and are based on phase space simulated events.

Table 3.10: Parameters with a Gaussian constraint applied. The parameters are constraint according to their values listed in the second column. The variables are introduced in detail in Sec. 3.5.1.

Constraint parameter	Gaussian constraint	Description
$r_{\text{LL/DD},11}^{\text{MC}}$ $r_{\text{LL/DD},12}^{\text{MC}}$	$0.354 \pm 0.007$ $0.332 \pm 0.009$	MC prediction for the ratio between LL and DD events
$\delta_{\pi,\text{LL},11}^{\bar{B}_s^0 \rightarrow \Lambda\bar{p}K^+}$ $\delta_{\pi,\text{LL},12}^{\bar{B}_s^0 \rightarrow \Lambda\bar{p}K^+}$ $\delta_{\pi,\text{DD},11}^{\bar{B}_s^0 \rightarrow \Lambda\bar{p}K^+}$ $\delta_{\pi,\text{DD},12}^{\bar{B}_s^0 \rightarrow \Lambda\bar{p}K^+}$	$1.051 \pm 0.047$ $1.059 \pm 0.032$ $1.110 \pm 0.029$ $1.109 \pm 0.018$	Ratio between the overall selection efficiencies between $\bar{B}_s^0 \rightarrow \Lambda\bar{p}K^+$ and $\bar{B}^0 \rightarrow \Lambda\bar{p}\pi^+$ for 2011, 2012, LL, and DD samples; the PID selection is excluded
$\delta_{\pi,\text{LL},11}^{\bar{B}^0 \rightarrow \Sigma^0\bar{p}K^+}$ $\delta_{\pi,\text{LL},12}^{\bar{B}^0 \rightarrow \Sigma^0\bar{p}K^+}$ $\delta_{\pi,\text{DD},11}^{\bar{B}^0 \rightarrow \Sigma^0\bar{p}K^+}$ $\delta_{\pi,\text{DD},12}^{\bar{B}^0 \rightarrow \Sigma^0\bar{p}K^+}$	$0.857 \pm 0.055$ $0.887 \pm 0.034$ $0.922 \pm 0.034$ $0.945 \pm 0.020$	Ratio between the overall selection efficiencies between $\bar{B}_s^0 \rightarrow \Sigma^0\bar{p}K^+$ and $\bar{B}^0 \rightarrow \Lambda\bar{p}\pi^+$ for 2011, 2012, LL, and DD samples; the PID selection is excluded
$\delta_{\pi,\text{LL},11}^{\bar{B}^0 \rightarrow \Sigma^0\bar{p}\pi^+}$ $\delta_{\pi,\text{LL},12}^{\bar{B}^0 \rightarrow \Sigma^0\bar{p}\pi^+}$ $\delta_{\pi,\text{DD},11}^{\bar{B}^0 \rightarrow \Sigma^0\bar{p}\pi^+}$ $\delta_{\pi,\text{DD},12}^{\bar{B}^0 \rightarrow \Sigma^0\bar{p}\pi^+}$	$0.872 \pm 0.073$ $0.837 \pm 0.037$ $0.840 \pm 0.042$ $0.882 \pm 0.210$	Ratio between the overall selection efficiencies between $\bar{B}^0 \rightarrow \Sigma^0\bar{p}\pi^+$ and $\bar{B}^0 \rightarrow \Lambda\bar{p}\pi^+$ for 2011, 2012, LL, and DD samples; the PID selection is excluded



## Chapter 4

# Calculation of $\mathcal{B}(\bar{B}_s^0 \rightarrow \Lambda\bar{p}K^+)$ and $\mathcal{A}_T$

### 4.1 Dalitz Plots for $\bar{B}_{(s)}^0 \rightarrow \Lambda\bar{p}h^+$ Decays and Efficiency Recalculation

The efficiencies listed in Section 3.3 are based on phase space simulated events. In order to check this assumption it is necessary to investigate the data Dalitz plots before running the global fit on the Run-I data.

The general structure of the  $\bar{B}_{(s)}^0 \rightarrow \Lambda\bar{p}h^+$  decays was introduced in Sec. 1.4. For the recorded data the Dalitz plot is not directly accessible since the background component needs to be subtracted in order to get the signal distribution. There are several statistical methods to achieve this such as performing the nominal fit in each bin of the Dalitz plot, with the advantage of being independent of different background shapes in different bins across the Dalitz plot, but it is limited by the available statistics since the fit needs to converge in each bin limiting the resolution of the Dalitz Plot. Another method is to use  $_s$ Plot weights [57], also known as  $_s$ Weights, in which the covariance matrix of a global fit is used to calculate a weight for each event with respect to different event classes, in this case  $\bar{B}^0 \rightarrow \Lambda\bar{p}\pi^+$ ,  $\bar{B}_s^0 \rightarrow \Lambda\bar{p}K^+$ ,  $\bar{B}^0 \rightarrow \Sigma^0\bar{p}\pi^+$ ,  $\bar{B}_s^0 \rightarrow \Sigma^0\bar{p}K^+$ , and combinatorial background. The global fit is done in a variable suitable to separate these classes, in this case the  $m(\Lambda\bar{p}\pi)$  and  $m(\Lambda\bar{p}K)$  invariant masses. It is important to note, that the only free parameters are the normalisations for the event classes, all shape parameters need to be fixed. In addition to that, no constraints should be applied in order to get the correct covariance matrix. Finally, the variable in which the weights are calculated needs to be uncorrelated with the variables one is interested in, which in this case are the invariant two body daughter masses. Due to these limitations the global fit described previously cannot be applied and the weights are determined in each dataset individually rather than in the simultaneous fit. However, the overall Dalitz plot for the  $\bar{B}_{(s)}^0 \rightarrow \Lambda\bar{p}h^+$  modes is accessible as a sum of the individual Dalitz plots. The content for a bin with the width  $\Delta x$  and its uncertainty are determined by

$$n = \sum_j^{\text{datasets}} \sum_{x \in \text{Bin}(x \pm \frac{\Delta x}{2})} w_i(x) \quad \text{and} \quad u_n = \sqrt{\sum_i^{\text{datasets}} \sum_{x \in \text{Bin}(x \pm \frac{\Delta x}{2})} w_i^2}, \quad (4.1)$$

where dataset denotes the year, the LL/DD splitting, and the bachelor meson mass hypothesis. It is necessary to point out that the sum of the weights must yield the fit result for the normalisation.

On the left hand side of Figure 4.1 the  $\bar{B}^0 \rightarrow \Lambda\bar{p}\pi^+$  Dalitz plot is shown. The Dalitz plot is dominated by an enhancement in the invariant  $\Lambda\bar{p}$  mass squared, which is consistent with previous studies and the theoretical predictions, *cf.* Fig. 1.5. No additional structures appear in  $m^2(\Lambda\bar{p})$  or the two squared invariant baryon meson masses. The enhancement itself is not evenly distributed along the  $m^2(\bar{p}\pi^+)$  axis. This hints to an additional internal structure. Explanations for the enhancement have included, among others, baryonium states. Depending on its structure this could lead to a non-trivial angular distribution for the  $\Lambda\bar{p}$  pair.

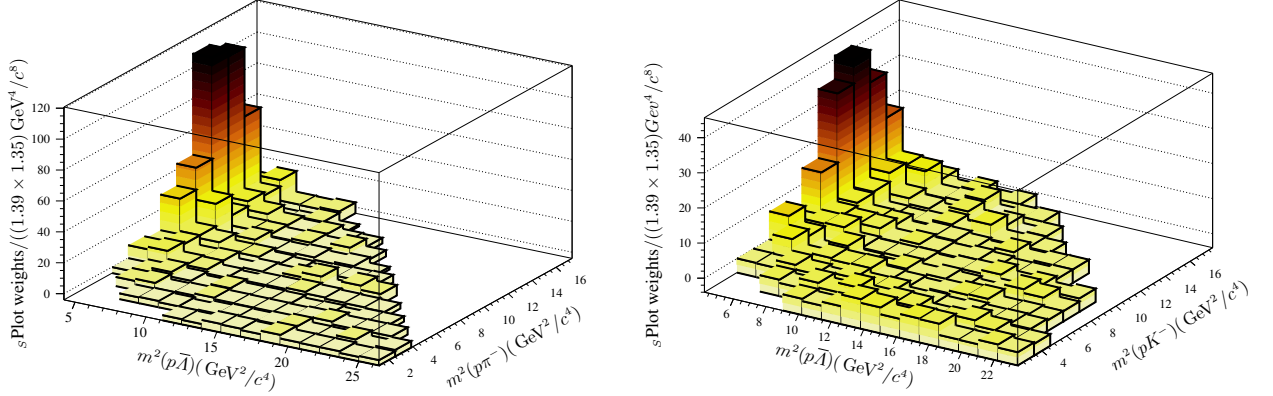


Figure 4.1: Dalitz plot for the  $\bar{B}^0 \rightarrow \Lambda\bar{p}\pi^+$  and  $\bar{B}_s^0 \rightarrow \Lambda\bar{p}K^+$  decay modes. The bin contents are given by the sum of the  $_s$ Plot weights extracted from the fits to the  $m(\Lambda\bar{p}h)$  invariant mass for each data sample. The only structure visible is a pronounced enhancement at the  $m(\Lambda\bar{p})$  threshold. There are no hints for additional resonances in the  $m(\bar{p}h^+)$  or  $m(\Lambda h^+)$  invariant masses.

The right hand side of Figure 4.1 shows the  $\bar{B}_s^0 \rightarrow \Lambda\bar{p}K^+$  Dalitz plot. The enhancement near the  $\Lambda\bar{p}$  threshold can be clearly seen as well. It is, however broader along the  $m^2(\bar{p}K^+)$  axis compared to the enhancement seen in  $\bar{B}^0 \rightarrow \Lambda\bar{p}\pi^+$ . As for the  $\bar{B}^0 \rightarrow \Lambda\bar{p}\pi^+$  mode, no additional structures are found in the Dalitz plot, neither in  $m^2(\bar{p}K^+)$  nor in  $m^2(\Lambda K^+)$ .

The Dalitz plots found in data are in stark contrast to the phase space model used in the simulation (*cf.* Fig. 2.16). The fit strategy introduced in Sec. 3.5 makes use of the selection efficiencies in order to constrain the signal yields across different data sets each with a different set of conditions. In Section 3.4 the total selection efficiency was shown as a function of the two Dalitz variables and it became obvious that the selection efficiency varies and is considerably larger for small  $m^2(\Lambda\bar{p})$  and large  $m^2(\bar{p}\pi^+)$  masses. Using these efficiencies only leads to an unbiased result in case of a flat data Dalitz plot. This is not the case and the average efficiencies need to be recalculated using the information obtained from the  $_s$ Plots.

The new average efficiencies are calculated as follows,

$$\bar{\varepsilon} = \frac{\sum_i^k n_i}{\sum_i^k \varepsilon_i}, \quad (4.2)$$

with  $n_i$  being the sum of the  $_s$ Weights and  $\varepsilon_i$  the efficiency in the  $i$ th bin. The total number of bins  $k$  depends on the statistical uncertainty of the overall yield and the individual efficiencies. If  $k$  is too large the recalculated efficiency is dominated by statistical fluctuations, if  $k$  is too small it is not possible to be sensitive to structures at small scales. Due to the Dalitz structure of the  $\bar{B}^0_{(s)} \rightarrow \Lambda\bar{p}h^+$  modes an asymmetrical binning in  $m^2(\Lambda\bar{p})$  is chosen making use of two small bins to take the narrow enhancement into account and a large bin for the remaining phase space. The fluctuations in the  $_s$ Weights and the efficiencies are large across the full two dimensional plane and in order to avoid being dominated by statistical fluctuations, a one dimensional correction is applied integrating over  $m^2(\bar{p}h^+)$  using  $k = 3$ . The efficiencies and the yields are treated in the Poisson approximation. The background contribution to each bin is still sizeable so that a multinomial approach might underestimate the statistical uncertainties. The efficiencies are very small and in this case the Poisson approximation is valid. In Table 4.1 both the sum of the  $_s$ Weights and the efficiency for each bin are listed for  $\bar{B}^0 \rightarrow \Lambda\bar{p}\pi^+$  and  $\bar{B}_s^0 \rightarrow \Lambda\bar{p}K^+$  and the resulting average efficiencies are listed as well. It should be noted, that two different efficiencies are listed,  $\bar{\varepsilon}_{\bar{B}^0_{(s)} \rightarrow \Lambda\bar{p}h^+}$  is calculated using all three bins whereas  $\bar{\varepsilon}_{\bar{B}^0_{(s)} \rightarrow \Lambda\bar{p}h^+}^{\text{Enh}}$  only takes the first two bins into account, *i.e.* the enhancement region. The first is used in the  $\bar{B}_s^0 \rightarrow \Lambda\bar{p}K^+$  branching fraction measurement, the latter for the time reversal asymmetry measurement.

Table 4.1: Efficiencies and  $_S$ Weighted signal events for the three bins of the invariant  $\Lambda \bar{p}$  mass used to determine the data driven average efficiency. The 2012 efficiencies are determined as the luminosity weighted sum of the 2012a and 2012b efficiencies. The new average efficiencies  $\bar{\epsilon}$  are shown as well. The ‘‘Enh’’ denotes that only the first two bins are considered in the calculation.

2011 LL sample				
$m^2(\Lambda \bar{p})$ bin in $(\text{GeV}/c^2)^2$	Sum of $_S$ Weights		Efficiency in %	
	$\bar{B}^0 \rightarrow \Lambda \bar{p} \pi^+$	$\bar{B}^0_s \rightarrow \Lambda \bar{p} K^+$	$\bar{B}^0 \rightarrow \Lambda \bar{p} \pi^+$	$\bar{B}^0_s \rightarrow \Lambda \bar{p} K^+$
$[(m_p + m_\Lambda)^2, 6.9)$	$29.4 \pm 7.0$	$12.3 \pm 3.9$	$0.120 \pm 0.006$	$0.139 \pm 0.006$
$[6.9, 12.3)$	$0.7 \pm 2.3$	$1.6 \pm 2.0$	$0.117 \pm 0.004$	$0.128 \pm 0.004$
$[12.3, (m_B - m_h)]$	$-1.5 \pm 1.5$	$0.5 \pm 2.1$	$0.095 \pm 0.003$	$0.109 \pm 0.003$
$\bar{\epsilon}_{\bar{B}^0 \rightarrow \Lambda \bar{p} \pi^+}^{\text{Enh}} = (0.120 \pm 0.006)\%$		$\bar{\epsilon}_{\bar{B}^0_s \rightarrow \Lambda \bar{p} K^+}^{\text{Enh}} = (0.138 \pm 0.005)\%$		
$\bar{\epsilon}_{\bar{B}^0 \rightarrow \Lambda \bar{p} \pi^+} = (0.121 \pm 0.007)\%$		$\bar{\epsilon}_{\bar{B}^0_s \rightarrow \Lambda \bar{p} K^+} = (0.136 \pm 0.007)\%$		
2011 DD sample				
$m^2(\Lambda \bar{p})$ bin in $(\text{GeV}/c^2)^2$	Sum of $_S$ Weights		Efficiency in %	
	$\bar{B}^0 \rightarrow \Lambda \bar{p} \pi^+$	$\bar{B}^0_s \rightarrow \Lambda \bar{p} K^+$	$\bar{B}^0 \rightarrow \Lambda \bar{p} \pi^+$	$\bar{B}^0_s \rightarrow \Lambda \bar{p} K^+$
$[(m_p + m_\Lambda)^2, 6.9)$	$84.4 \pm 11.6$	$40.8 \pm 7.3$	$0.409 \pm 0.010$	$0.454 \pm 0.012$
$[6.9, 12.3)$	$7.5 \pm 7.0$	$10.1 \pm 4.0$	$0.335 \pm 0.006$	$0.400 \pm 0.007$
$[12.3, (m_B - m_h)]$	$4.2 \pm 5.6$	$3.7 \pm 3.2$	$0.229 \pm 0.004$	$0.280 \pm 0.005$
$\bar{\epsilon}_{\bar{B}^0 \rightarrow \Lambda \bar{p} \pi^+}^{\text{Enh}} = (0.402 \pm 0.011)\%$		$\bar{\epsilon}_{\bar{B}^0_s \rightarrow \Lambda \bar{p} K^+}^{\text{Enh}} = (0.442 \pm 0.010)\%$		
$\bar{\epsilon}_{\bar{B}^0 \rightarrow \Lambda \bar{p} \pi^+} = (0.389 \pm 0.018)\%$		$\bar{\epsilon}_{\bar{B}^0_s \rightarrow \Lambda \bar{p} K^+} = (0.425 \pm 0.016)\%$		
2012 LL sample				
$m^2(\Lambda \bar{p})$ bin in $(\text{GeV}/c^2)^2$	Sum of $_S$ Weights		Efficiency in %	
	$\bar{B}^0 \rightarrow \Lambda \bar{p} \pi^+$	$\bar{B}^0_s \rightarrow \Lambda \bar{p} K^+$	$\bar{B}^0 \rightarrow \Lambda \bar{p} \pi^+$	$\bar{B}^0_s \rightarrow \Lambda \bar{p} K^+$
$[(m_p + m_\Lambda)^2, 6.9)$	$84.6 \pm 13.0$	$38.3 \pm 7.6$	$0.133 \pm 0.004$	$0.178 \pm 0.006$
$[6.9, 12.3)$	$9.3 \pm 7.1$	$10.2 \pm 4.7$	$0.1299 \pm 0.0025$	$0.159 \pm 0.004$
$[12.3, (m_B - m_h)]$	$5.5 \pm 6.9$	$14.1 \pm 5.2$	$0.1129 \pm 0.0019$	$0.157 \pm 0.003$
$\bar{\epsilon}_{\bar{B}^0 \rightarrow \Lambda \bar{p} \pi^+}^{\text{Enh}} = (0.133 \pm 0.004)\%$		$\bar{\epsilon}_{\bar{B}^0_s \rightarrow \Lambda \bar{p} K^+}^{\text{Enh}} = (0.174 \pm 0.005)\%$		
$\bar{\epsilon}_{\bar{B}^0 \rightarrow \Lambda \bar{p} \pi^+} = (0.131 \pm 0.004)\%$		$\bar{\epsilon}_{\bar{B}^0_s \rightarrow \Lambda \bar{p} K^+} = (0.169 \pm 0.004)\%$		
2012 DD sample				
$m^2(\Lambda \bar{p})$ bin in $(\text{GeV}/c^2)^2$	Sum of $_S$ Weights		Efficiency in %	
	$\bar{B}^0 \rightarrow \Lambda \bar{p} \pi^+$	$\bar{B}^0_s \rightarrow \Lambda \bar{p} K^+$	$\bar{B}^0 \rightarrow \Lambda \bar{p} \pi^+$	$\bar{B}^0_s \rightarrow \Lambda \bar{p} K^+$
$[(m_p + m_\Lambda)^2, 6.9)$	$268.6 \pm 22.9$	$108.6 \pm 12.8$	$0.463 \pm 0.006$	$0.593 \pm 0.011$
$[6.9, 12.3)$	$51.9 \pm 13.8$	$15.7 \pm 6.4$	$0.403 \pm 0.004$	$0.513 \pm 0.006$
$[12.3, (m_B - m_h)]$	$27.2 \pm 10.9$	$-0.7 \pm 5.6$	$0.282 \pm 0.003$	$0.428 \pm 0.005$
$\bar{\epsilon}_{\bar{B}^0 \rightarrow \Lambda \bar{p} \pi^+}^{\text{Enh}} = (0.452 \pm 0.005)\%$		$\bar{\epsilon}_{\bar{B}^0_s \rightarrow \Lambda \bar{p} K^+}^{\text{Enh}} = (0.581 \pm 0.010)\%$		
$\bar{\epsilon}_{\bar{B}^0 \rightarrow \Lambda \bar{p} \pi^+} = (0.432 \pm 0.009)\%$		$\bar{\epsilon}_{\bar{B}^0_s \rightarrow \Lambda \bar{p} K^+} = (0.569 \pm 0.029)\%$		

In order to increase the statistical precision for the measurement of the time reversal invariance in the  $\bar{B}^0 \rightarrow \Lambda \bar{p} \pi^+$  decay mode, it is sensible to limit the fit to the enhancement. The signal to background ratio is considerably larger in the enhancement region compared to the remainder of the Dalitz plot since the combinatorial background is uniformly distributed. As a result the T violation measurement is done for  $\bar{B}^0 \rightarrow \Lambda \bar{p} \pi^+$  candidates with  $m^2(\Lambda \bar{p}) < 12.3(\text{GeV}/c^2)^2$  and the average efficiencies for the enhancement region are employed in the asymmetry fit.

The treatment of the  $\bar{B}^0_{(s)} \rightarrow \Sigma^0 \bar{p} h^+$  modes is more complicated. No data Dalitz plot is accessible due to the lack



of statistics and the missing photon. Applying the method used for the  $\bar{B}^0_{(s)} \rightarrow \Lambda \bar{p} h^+$  modes would be prone to statistical fluctuations and due to the missing photon no unambiguous Dalitz plot can be defined. Since the ratio between the  $\bar{B}^0_{(s)} \rightarrow \Lambda \bar{p} h^+$  and  $\bar{B}^0_{(s)} \rightarrow \Sigma^0 \bar{p} h^+$  branching fraction is not of particular interest for this analysis a workaround can be applied assuming a similar behaviour for the  $\Sigma^0$  modes with respect to the invariant baryon antibaryon mass. The assumption made here is, that all  $\bar{B}^0_{(s)} \rightarrow \Sigma^0 \bar{p} h^+$  candidates would fall in the interval of  $[(m_p + m_\Lambda)^2, 6.9]$ . The efficiency would be calculated as such

$$\bar{\varepsilon}(\bar{B}^0_{(s)} \rightarrow \Sigma^0 \bar{p} h^+) = \frac{N_{\text{Reco}}}{N_{\text{Gen}}} \Bigg|_{m(\Lambda \bar{p})^2 \in [(m_p + m_\Lambda)^2, 6.9] (\text{GeV}/c^2)^2} . \quad (4.3)$$

The number of reconstructed events from the phase space simulated events  $N_{\text{Reco}}$  can be determined, but it is problematic to calculate the number of generated events fulfilling that condition due to the loss of generator information. The statistical significance on both  $\bar{B}^0_{(s)} \rightarrow \Sigma^0 \bar{p} h^+$  modes is below  $3\sigma$  and it was decided not to put the effort into a dedicated calculation of the  $\bar{B}^0_{(s)} \rightarrow \Sigma^0 \bar{p} h^+$  Dalitz plots. The missing information in the generated Dalitz plot, however, can be absorbed into the fit parameter  $r^{\bar{B}^0_{(s)} \rightarrow \Sigma^0 \bar{p} h^+}$ . Starting from Eq. (3.28) omitting the sample indices one finds

$$\begin{aligned} N(\bar{B}^0_{(s)} \rightarrow \Sigma^0 \bar{p} h^+) &= \frac{\bar{\varepsilon}_{\bar{B}^0_{(s)} \rightarrow \Sigma^0 \bar{p} h^+}}{\bar{\varepsilon}_{\bar{B}^0_{(s)} \rightarrow \Lambda \bar{p} h^+}} \times \varepsilon^{\pi \rightarrow h} \times r^{\bar{B}^0_{(s)} \rightarrow \Sigma^0 \bar{p} h^+} \times N(\bar{B}^0_{(s)} \rightarrow \Lambda \bar{p} h^+) \\ &= \frac{N_{\text{Reco}}^{\bar{B}^0_{(s)} \rightarrow \Sigma^0 \bar{p} h^+}}{N_{\text{Gen}}^{\bar{B}^0_{(s)} \rightarrow \Sigma^0 \bar{p} h^+}} \times \frac{1}{\bar{\varepsilon}_{\bar{B}^0_{(s)} \rightarrow \Lambda \bar{p} h^+}} \times \varepsilon^{\pi \rightarrow h} \times r^{\bar{B}^0_{(s)} \rightarrow \Sigma^0 \bar{p} h^+} \times N(\bar{B}^0_{(s)} \rightarrow \Lambda \bar{p} h^+) \\ &= \frac{N_{\text{Reco}}^{\bar{B}^0_{(s)} \rightarrow \Sigma^0 \bar{p} h^+}}{\bar{\varepsilon}_{\bar{B}^0_{(s)} \rightarrow \Lambda \bar{p} h^+}} \times \frac{r^{\bar{B}^0_{(s)} \rightarrow \Sigma^0 \bar{p} h^+}}{N_{\text{Gen}}^{\bar{B}^0_{(s)} \rightarrow \Sigma^0 \bar{p} h^+}} \times \varepsilon^{\pi \rightarrow h} \times N(\bar{B}^0_{(s)} \rightarrow \Lambda \bar{p} h^+) , \end{aligned} \quad (4.4)$$

and using the following redefinitions

$$\tilde{\delta}^{\bar{B}^0_{(s)} \rightarrow \Sigma^0 \bar{p} h^+} = \frac{N_{\text{Reco}}^{\bar{B}^0_{(s)} \rightarrow \Sigma^0 \bar{p} h^+}}{\bar{\varepsilon}_{\bar{B}^0_{(s)} \rightarrow \Lambda \bar{p} h^+}} \quad \text{and} \quad \tilde{r}^{\bar{B}^0_{(s)} \rightarrow \Sigma^0 \bar{p} h^+} = \frac{r^{\bar{B}^0_{(s)} \rightarrow \Sigma^0 \bar{p} h^+}}{N_{\text{Gen}}^{\bar{B}^0_{(s)} \rightarrow \Sigma^0 \bar{p} h^+}} \quad (4.5)$$

leads to the same normalisation as before, the variables just have a different meaning now, especially  $r^{\bar{B}^0_{(s)} \rightarrow \Sigma^0 \bar{p} h^+}$ , which loses its physical meaning. Another remark has to be made, that  $\tilde{r}^{\bar{B}^0_{(s)} \rightarrow \Sigma^0 \bar{p} h^+}$  is not constant over the 2011 and 2012 data sets, however, one finds

$$\begin{aligned} \tilde{r}_{11}^{\bar{B}^0_{(s)} \rightarrow \Sigma^0 \bar{p} h^+} &= \frac{r^{\bar{B}^0_{(s)} \rightarrow \Sigma^0 \bar{p} h^+}}{N_{\text{Gen},11}^{\bar{B}^0_{(s)} \rightarrow \Sigma^0 \bar{p} h^+}} \\ &= \frac{r^{\bar{B}^0_{(s)} \rightarrow \Sigma^0 \bar{p} h^+}}{N_{\text{Gen},11}^{\bar{B}^0_{(s)} \rightarrow \Sigma^0 \bar{p} h^+}} \times \frac{N_{\text{Gen},12}^{\bar{B}^0_{(s)} \rightarrow \Sigma^0 \bar{p} h^+}}{N_{\text{Gen},12}^{\bar{B}^0_{(s)} \rightarrow \Sigma^0 \bar{p} h^+}} = \frac{r^{\bar{B}^0_{(s)} \rightarrow \Sigma^0 \bar{p} h^+}}{N_{\text{Gen},12}^{\bar{B}^0_{(s)} \rightarrow \Sigma^0 \bar{p} h^+}} \times \frac{N_{\text{Gen},12}^{\bar{B}^0_{(s)} \rightarrow \Sigma^0 \bar{p} h^+}}{N_{\text{Gen},11}^{\bar{B}^0_{(s)} \rightarrow \Sigma^0 \bar{p} h^+}} , \end{aligned} \quad (4.6)$$

with  $N_{\text{Gen},\{11,12\}}^{\bar{B}^0_{(s)} \rightarrow \Sigma^0 \bar{p} h^+}$  being the number of generated events for  $m^2(\Lambda \bar{p}) \in [(m_p + m_\Lambda)^2, 6.9]$ . The efficiency of this selection on the generated events is identical for 2011 and 2012, so that the ratio is given by the overall ratio of generated events between 2011 and 2012. Taking this constant into account for the normalisation for the 2011  $\bar{B}^0_{(s)} \rightarrow \Sigma^0 \bar{p} h^+$  PDFs allows the nominal fit to be applied just to the enhancement region without further modifications or assumptions. These changes are also valid for the branching fraction fit, the assumptions for the efficiency are absorbed into the global  $r^{\bar{B}^0_{(s)} \rightarrow \Sigma^0 \bar{p} h^+}$ . The recalculated ratios between the efficiencies for  $\bar{B}^0 \rightarrow \Lambda \bar{p} \pi^+$  and  $\bar{B}_s^0 \rightarrow \Lambda \bar{p} K^+$ , as well as the ratios between the  $\bar{B}^0 \rightarrow \Lambda \bar{p} \pi^+$  efficiency and the found  $\bar{B}^0_{(s)} \rightarrow \Sigma^0 \bar{p} h^+$  candidates are listed in Tab. 4.2 and again enter the global fit for the  $\bar{B}_s^0 \rightarrow \Lambda \bar{p} K^+$  branching fraction as well as for the  $\mathcal{A}_T$  determination as Gaussian constraints.

Table 4.2: Ratio between the average efficiencies for the  $\bar{B}^0_{(s)} \rightarrow \Lambda\bar{p}h^+$  modes and the ratio between the number of found  $\bar{B}^0_{(s)} \rightarrow \Sigma^0\bar{p}h^+$  events in the enhancement region and the recalculated average efficiency of  $\bar{B}^0 \rightarrow \Lambda\bar{p}\pi^+$  for each data set as well as the ratio between LL and DD for the  $\bar{B}^0 \rightarrow \Lambda\bar{p}\pi^+$  mode for 2011 and 2012.

Ratio	2011 LL	2011 DD	2012 LL	2012 DD
$\delta^{\bar{B}^0_s \rightarrow \Lambda\bar{p}K^+}$	$1.15 \pm 0.07$	$1.10 \pm 0.04$	$1.31 \pm 0.05$	$1.285 \pm 0.26$
$\delta^{\bar{B}^0 \rightarrow \Sigma^0\bar{p}\pi^+} \times 10^{-3}$	$2116.7 \pm 169.8$	$1900.5 \pm 86.2$	$3706.8 \pm 200.7$	$3588.5 \pm 97.5$
$\delta^{\bar{B}^0_s \rightarrow \Sigma^0\bar{p}K^+} \times 10^{-3}$	$4975.0 \pm 321.5$	$4534.8 \pm 163.3$	$11187.9 \pm 444.2$	$9643.8 \pm 210.3$
$r_{LL/DD}^{MC}$	$0.298 \pm 0.017$		$0.294 \pm 0.009$	

The global fit as introduced in Sec. 3.5.3 is now applied to the Run-I data using the new efficiency and one finds

$$N_{11}^{LL}(\bar{B}^0 \rightarrow \Lambda\bar{p}\pi^+) = 42.3^{+9.2}_{-6.9} \quad (4.7)$$

$$N_{12}^{LL}(\bar{B}^0 \rightarrow \Lambda\bar{p}\pi^+) = 148.7^{+16.9}_{-15.1} \quad (4.8)$$

$$r_{11}^{DD} = 1.07^{+0.25}_{-0.23} \quad (4.9)$$

$$r_{12}^{DD} = 0.71^{+0.10}_{-0.09} \quad (4.10)$$

$$r^{\bar{B}^0_s \rightarrow \Lambda\bar{p}K^+} = 0.392^{+0.044}_{-0.040} \quad (4.11)$$

corresponding to the following overall yields

$$N(\bar{B}^0 \rightarrow \Lambda\bar{p}\pi^+) = 684.1 \pm 41.6 \quad (4.12)$$

$$N(\bar{B}^0_s \rightarrow \Lambda\bar{p}K^+) = 268.0 \pm 23.3 \quad (4.13)$$

Since the modified ratios for the  $\bar{B}^0_{(s)} \rightarrow \Sigma^0\bar{p}h^+$  modes lost their physical meaning, no yields are listed here. Similarly a list containing all other fit variables can be found in Appendix H.1. In Fig. 4.2 the fit to the data is shown. The fit for the enhancement only can be seen in Fig. 4.3 and its results are listed in Appendix H.1. The improvement in the signal-to-background ratio is obvious especially for the 2012 DD pion sample. The individual yields calculated from the global fit for each sample are listed in Tab. 4.3. It should be pointed out, that these yields are not yet corrected for the PID efficiencies hence the difference to the results listed above.

Table 4.3: Yields for the  $\bar{B}^0_{(s)} \rightarrow \Lambda\bar{p}h^+$  and  $\bar{B}^0_{(s)} \rightarrow \Sigma^0\bar{p}h^+$  modes for the individual data samples calculated using the global PDF. A full list of the parameters can be found in Appendix H.1.

Decay mode	Reco.	2011 Yields		2012 Yields	
		$m(\Lambda\bar{p}\pi)$	$m(\Lambda\bar{p}K)$	$m(\Lambda\bar{p}\pi)$	$m(\Lambda\bar{p}K)$
$\bar{B}^0 \rightarrow \Lambda\bar{p}\pi^+$	LL	$31.0 \pm 5.9$	$3.5 \pm 0.7$	$111.5 \pm 12.1$	$11.4 \pm 1.3$
	DD	$104.2 \pm 11.0$	$12.0 \pm 1.3$	$262.6 \pm 21.2$	$26.5 \pm 2.1$
$B^0_s \rightarrow \Lambda\bar{p}K^+$	LL	$0.67 \pm 0.14$	$14.4 \pm 3.0$	$3.0 \pm 0.4$	$59.4 \pm 7.3$
	DD	$2.06 \pm 0.26$	$48.9 \pm 6.1$	$6.1 \pm 0.6$	$136.7 \pm 12.9$
$\bar{B}^0 \rightarrow \Sigma^0\bar{p}\pi^+$	LL	$3.6 \pm 3.2$	$0.4 \pm 0.4$	$12.0 \pm 10.5$	$1.2 \pm 1.1$
	DD	$11.5 \pm 10.3$	$1.3 \pm 1.2$	$28.2 \pm 25.1$	$2.9 \pm 2.5$
$\bar{B}^0_s \rightarrow \Sigma^0\bar{p}K^+$	LL	$0.2 \pm 0.1$	$4.9 \pm 2.1$	$1.1 \pm 0.4$	$20.8 \pm 8.2$
	DD	$0.67 \pm 0.26$	$15.9 \pm 6.1$	$2.0 \pm 0.7$	$43.4 \pm 16.1$

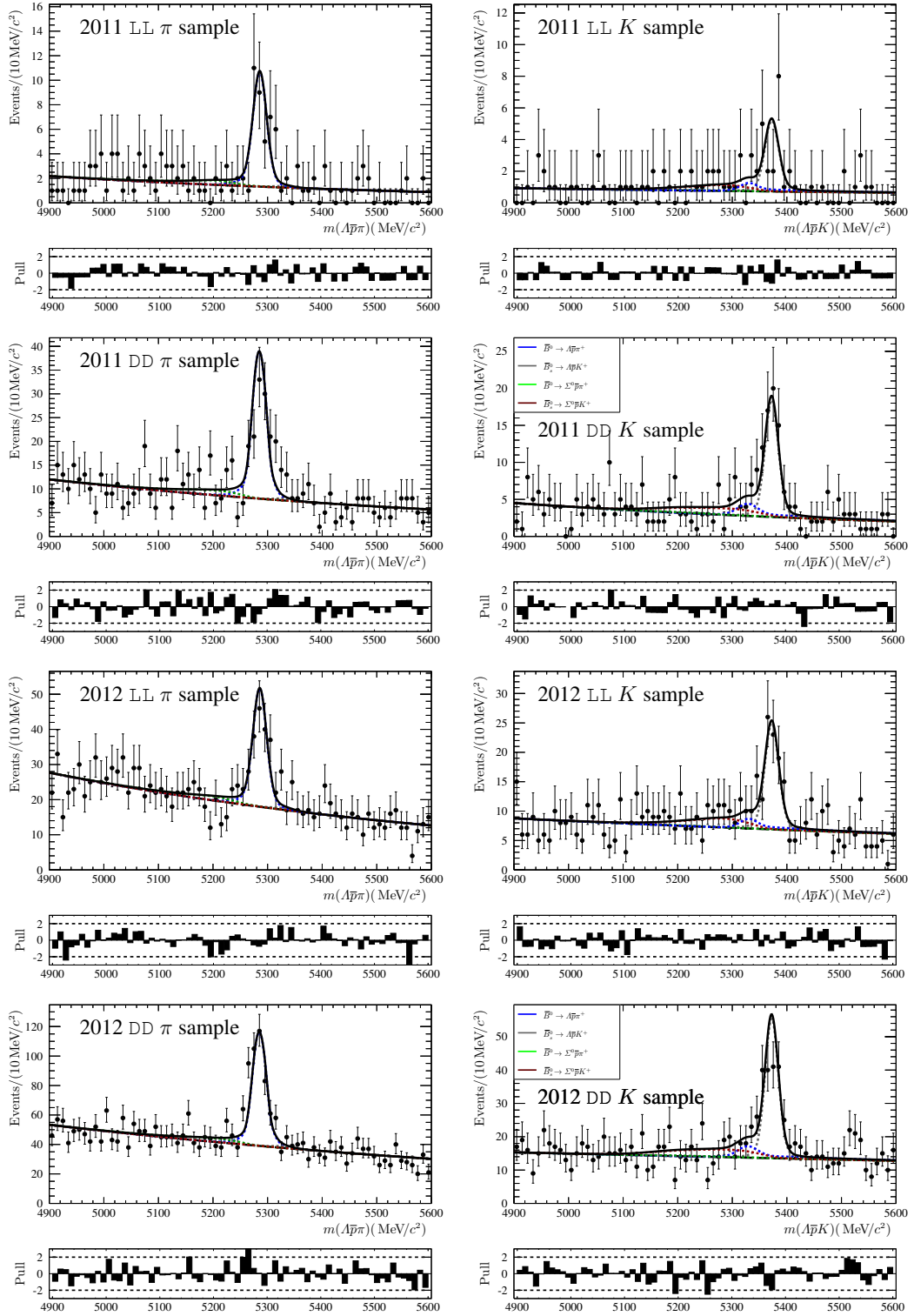


Figure 4.2: Results for global fit using the Dalitz plot corrected average efficiencies. The black points represent the data in the individual sample indicated in the plots. The  $\bar{B}_s^0 \rightarrow \Lambda \bar{p} \pi^+$  contribution is shown in blue,  $\bar{B}_s^0 \rightarrow \Lambda \bar{p} K^+$  in grey,  $\bar{B}_s^0 \rightarrow \Sigma^0 \bar{p} \pi^+$  in green, and  $\bar{B}_s^0 \rightarrow \Sigma^0 \bar{p} K^+$  in brown. The sum of all components is shown in black.

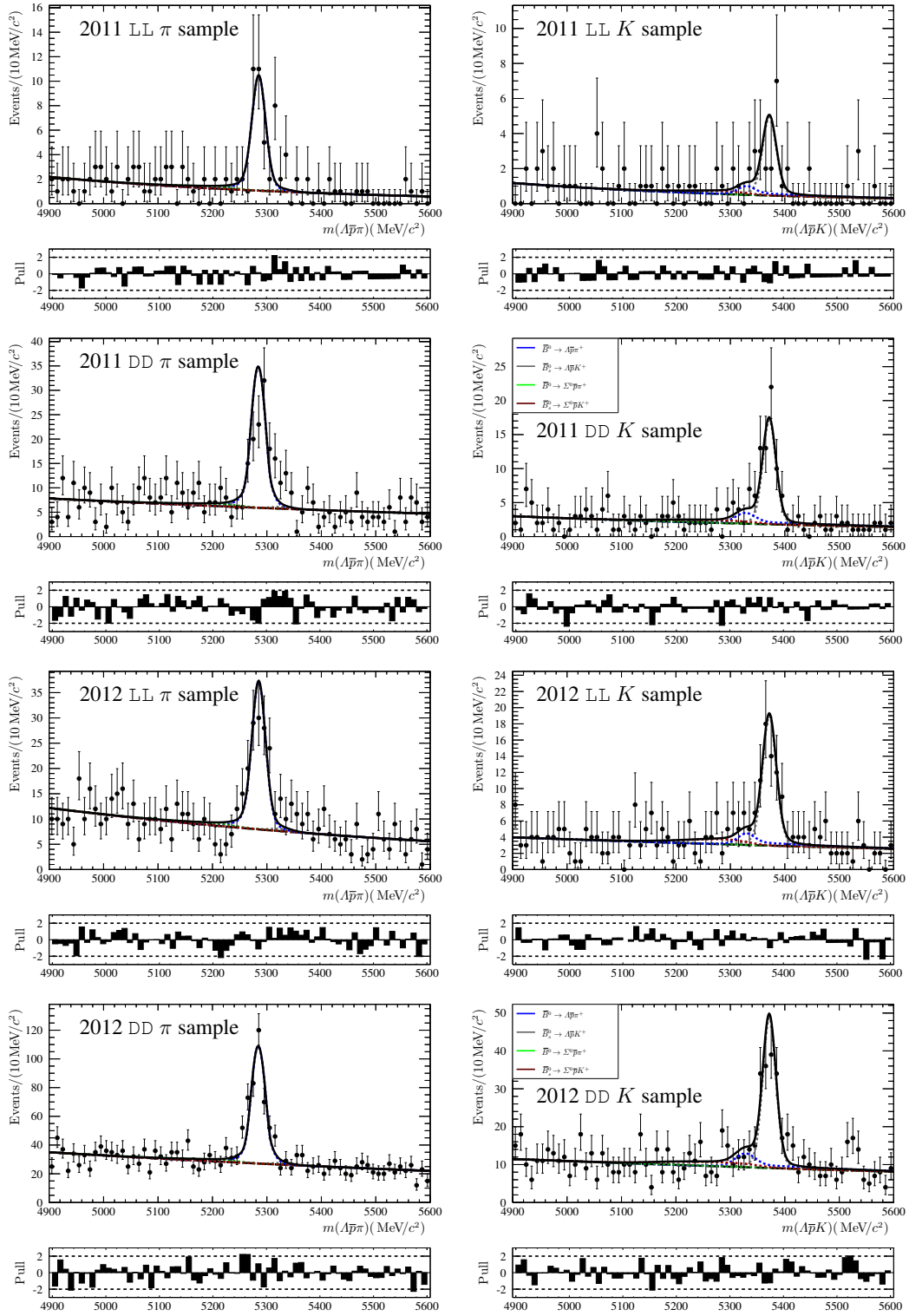


Figure 4.3: Results for global fit for  $m^2(\Lambda \bar{p}) < 12.3 (\text{GeV}/c^2)^2$  using the Dalitz plot corrected average efficiencies. The black points represent the data in the individual sample indicated in the plots. The  $\bar{B}^0 \rightarrow \Lambda \bar{p} \pi^+$  contribution is shown in blue,  $\bar{B}_s^0 \rightarrow \Lambda \bar{p} K^+$  in grey,  $\bar{B}^0 \rightarrow \Sigma^0 \bar{p} \pi^+$  in green, and  $\bar{B}_s^0 \rightarrow \Sigma^0 \bar{p} K^+$  in brown. The sum of all components is shown in black.

## 4.2 Branching Fraction of the Decays $\bar{B}_s^0 \rightarrow \Lambda \bar{p} K^+$ and $\bar{B}_s^0 \rightarrow \bar{\Lambda} p K^-$

As mentioned earlier, up to now, no baryonic  $B_s^0$  decays have been observed either by the  $B$ -factories nor by LHCb. The fit in Fig. 4.2 shows clear peaks in several subsamples at the nominal  $B_s^0$  mass and the fit finds  $N(\bar{B}_s^0 \rightarrow \Lambda \bar{p} K^+) = 268.0 \pm 23.3$  candidates in the run-I data. This is an observation of the  $\bar{B}_s^0 \rightarrow \Lambda \bar{p} K^+$  decay. Assuming that the ratio between the likelihoods with and without the  $\bar{B}_s^0 \rightarrow \Lambda \bar{p} K^+$  signal hypothesis behaves like a  $\chi^2$  distribution with one degree of freedom, the significance is calculated by

$$S = \sqrt{-2 \log(L_0/L_{\text{Sig}})} = 17.2 \quad , \quad (4.14)$$

which corresponds to 17.2 Gaussian standard deviations. Therefore, the first observation of these baryonic  $\bar{B}_s^0$  decays can be claimed by LHCb.

For the calculation of the  $\bar{B}_s^0 \rightarrow \Lambda \bar{p} K^+$  branching fraction additional input is needed. Basically the branching fraction  $\mathcal{B}$  of a decay chain like  $\bar{B}_s^0 \rightarrow \Lambda \bar{p} K^+$  and  $\Lambda \rightarrow p \pi^-$  is calculated as a product branching fraction, because the  $\bar{B}_s^0$  decay and the daughter decay are independent,

$$\mathcal{B}(\bar{B}_s^0 \rightarrow \Lambda \bar{p} K^+) \times \mathcal{B}(\Lambda \rightarrow p \pi^-) = \frac{N_{\text{Sig}}}{\varepsilon N_{\bar{B}_s^0}} \quad , \quad (4.15)$$

where  $\varepsilon$  is the overall efficiency,  $N_{\text{Sig}}$  is the Number of signal events selected for the given decay chain, and  $N_{\bar{B}_s^0}$  represents the total number of  $\bar{B}_s^0$  mesons produced during the Run-I. Since the selection includes the charge conjugated decay  $B_s^0 \rightarrow \Lambda \bar{p} K^+$  as well, the branching fraction is calculated by

$$\mathcal{B}(\bar{B}_s^0 \rightarrow \Lambda \bar{p} K^+) \times \mathcal{B}(\Lambda \rightarrow p \pi^-) = \frac{N_{\text{Sig}}}{\varepsilon(N_{B_s^0} + N_{\bar{B}_s^0})} \quad . \quad (4.16)$$

It is, however, very difficult to estimate the absolute number of  $\bar{B}_s^0$  mesons produced during the first run of the LHC. Using the knowledge of the integrated luminosity, the  $b\bar{b}$  cross section, and the fragmentation probabilities the number of  $\bar{B}_s^0$  mesons is given by

$$(N_{B_s^0} + N_{\bar{B}_s^0}) = \int \mathcal{L} dt \times \sigma_{b\bar{b}} \times 2 \times f_s \quad , \quad (4.17)$$

where  $\int \mathcal{L} dt$  is the integrated luminosity,  $\sigma_{b\bar{b}}$  is the  $b\bar{b}$  cross section, the factor 2 accounts for the production of both the  $b$  and the  $\bar{b}$ , and  $f_s$  represents the  $b$  hadronisation probability to the  $\bar{B}_s^0$  meson. Each of these measured parameters contributes with its uncertainty to the overall uncertainty of the number of  $\bar{B}_s^0$  mesons, the hadronisation probability  $f_s$  is only known relative to  $f_d$ . Therefore, it is not useful to measure absolute branching fractions at LHCb but to search for a suitable normalisation decay mode, which shares a lot of similarities with the signal decay and whose branching fraction is already known. In the case of the  $\bar{B}_s^0 \rightarrow \Lambda \bar{p} K^+$  decay, the ideal normalisation mode is  $\bar{B}^0 \rightarrow \Lambda \bar{p} \pi^+$  since it is already included in the analysis, the only difference being the PID selection and differences between the kaon and pion reconstruction. As was shown in Sec. 3.3 and 4.1 the overall selection efficiency for both decay modes is very similar and the ratio between their efficiencies is already accounted for in the final fit. In practical terms, the  $\bar{B}_s^0 \rightarrow \Lambda \bar{p} K^+$  branching fraction is calculated relative to that of the  $\bar{B}^0 \rightarrow \Lambda \bar{p} \pi^+$  normalisation channel, taking into account that only a sum of the two  $B_s^0$  decays  $\bar{B}_s^0 \rightarrow \Lambda \bar{p} K^+$  and  $\bar{B}_s^0 \rightarrow \bar{\Lambda} p K^-$  can be measured, extracted from

$$\mathcal{B}(\bar{B}_s^0 \rightarrow \Lambda \bar{p} K^+) + \mathcal{B}(\bar{B}_s^0 \rightarrow \bar{\Lambda} p K^-) = \frac{f_d}{f_s} \times \frac{N(\bar{B}_s^0 \rightarrow \Lambda \bar{p} K^+) + N(\bar{B}_s^0 \rightarrow \bar{\Lambda} p K^-)}{N(\bar{B}^0 \rightarrow \Lambda \bar{p} \pi^+)} \times \frac{\varepsilon_{\bar{B}^0 \rightarrow \Lambda \bar{p} \pi^+}}{\varepsilon_{\bar{B}_s^0 \rightarrow \Lambda \bar{p} K^+}} \times \mathcal{B}(\bar{B}^0 \rightarrow \Lambda \bar{p} \pi^+) \quad , \quad (4.18)$$

where  $f_q$  represents the  $b$  hadronisation probability to the relevant hadron and  $\varepsilon$  contains the product of all efficiencies for the signal daughters to be in the LHCb acceptance, for triggering, reconstruction, stripping, and final selection. The  $\Lambda$  branching fraction cancels in the ratio as does the number of  $B^0$  and  $B_s^0$  mesons, which are replaced by the

corresponding hadronisation probabilities. The ratio  $f_s/f_d$  is known and the latest  $f_s/f_d$  combination from LHCb is used here,  $f_s/f_d = 0.259 \pm 0.015$  [44]. The term

$$\frac{N(\bar{B}_s^0 \rightarrow \Lambda \bar{p} K^+ + \bar{B}_s^0 \rightarrow \bar{\Lambda} p K^-)}{N(\bar{B}^0 \rightarrow \Lambda \bar{p} \pi^+)} \times \frac{\varepsilon_{\bar{B}^0 \rightarrow \Lambda \bar{p} \pi^+}}{\varepsilon_{\bar{B}_s^0 \rightarrow \Lambda \bar{p} K^+}} \quad (4.19)$$

is already accounted for in the fit, thus the  $\bar{B}_s^0 \rightarrow \Lambda \bar{p} K^+$  branching fraction is given by

$$\mathcal{B}(\bar{B}_s^0 \rightarrow \Lambda \bar{p} K^+) + \mathcal{B}(\bar{B}_s^0 \rightarrow \bar{\Lambda} p K^-) = \frac{f_d}{f_s} \times r^{\bar{B}_s^0 \rightarrow \Lambda \bar{p} K^+} \times \mathcal{B}(\bar{B}^0 \rightarrow \Lambda \bar{p} \pi^+) \quad (4.20)$$

Since no dedicated flavour tagging is applied only the sum of the  $\bar{B}_s^0 \rightarrow \Lambda \bar{p} K^+$  and  $\bar{B}_s^0 \rightarrow \bar{\Lambda} p K^-$  branching fraction can be measured. Using  $\mathcal{B}(\bar{B}^0 \rightarrow \Lambda \bar{p} \pi^+) = (3.14 \pm 0.29) \times 10^{-6}$  [12] the branching fraction is determined to be

$$\mathcal{B}(\bar{B}_s^0 \rightarrow \Lambda \bar{p} K^+) + \mathcal{B}(\bar{B}_s^0 \rightarrow \bar{\Lambda} p K^-) = (4.75_{-0.49}^{+0.53} \pm 0.44(\mathcal{B}(\bar{B}^0 \rightarrow \Lambda \bar{p} \pi^+))) \times 10^{-6} \quad (4.21)$$

where the uncertainty is statistical and based on the  $\bar{B}^0 \rightarrow \Lambda \bar{p} \pi^+$  branching fraction only. Another advantage of choosing the  $\bar{B}^0 \rightarrow \Lambda \bar{p} \pi^+$  as normalisation mode is, that a lot of systematic uncertainties cancel in the ratio. The dominating source of systematic uncertainty is expected to be the fit model, especially the contributions from the  $\Sigma^0$  and partially reconstructed modes. An additional systematic uncertainty is based on the limited knowledge of the true line shape, which is taken from the simulation. But as both  $\bar{B}^0 \rightarrow \Lambda \bar{p} \pi^+$  and  $\bar{B}_s^0 \rightarrow \Lambda \bar{p} K^+$  line shapes are similar, the effect should be relatively small. The systematic uncertainties are studied in detail in Section 4.5

### 4.3 Time Reversal Asymmetry $\mathcal{A}_T$ Determination

In the previous section the fit to whole Run-I data was shown, *cf.* Fig. 4.2, using data driven average efficiencies taking the Dalitz plot structure into account. For the  $\mathcal{A}_T$  measurement the data need to be split into four independent samples depending on the  $B^0$  hadron flavour and on the sign of the triple product. Three different asymmetries need to be calculated as follows,

$$A_T = \frac{N_{(\mathcal{O}>0)}^{\bar{B}^0 \rightarrow \Lambda \bar{p} \pi^+} - N_{(\mathcal{O}<0)}^{\bar{B}^0 \rightarrow \Lambda \bar{p} \pi^+}}{N_{(\mathcal{O}>0)}^{\bar{B}^0 \rightarrow \Lambda \bar{p} \pi^+} + N_{(\mathcal{O}<0)}^{\bar{B}^0 \rightarrow \Lambda \bar{p} \pi^+}} \quad (4.22)$$

$$\bar{A}_T = \frac{N_{(\mathcal{O}>0)}^{B^0 \rightarrow \bar{\Lambda} p \pi^-} - N_{(\mathcal{O}<0)}^{B^0 \rightarrow \bar{\Lambda} p \pi^-}}{N_{(\mathcal{O}>0)}^{B^0 \rightarrow \bar{\Lambda} p \pi^-} + N_{(\mathcal{O}<0)}^{B^0 \rightarrow \bar{\Lambda} p \pi^-}} \quad (4.23)$$

$$\mathcal{A}_T = 1/2(A_T - \bar{A}_T) \quad (4.24)$$

where  $A_T$  is defined as the asymmetry between the number of  $\bar{B}^0 \rightarrow \Lambda \bar{p} \pi^+$  candidates with a positive sign of the triple product and the number of candidates with a negative sign,  $\bar{A}_T$  is the asymmetry for the  $B^0 \rightarrow \bar{\Lambda} p \pi^-$  events, and  $\mathcal{A}_T$  is half the difference between the asymmetries. The triple product  $\mathcal{O}$  is given by

$$\mathcal{O} = \mathbf{s}_\Lambda \cdot (\mathbf{p}_\Lambda \times \mathbf{p}_{\pi^+}) \quad (4.25)$$

and was introduced in Sec. 1.2.4.

Instead of determining the number of candidates for each sub sample independently, all samples are fit simultaneously and the time reversal asymmetry is calculated in the fit making use of the complete covariance matrix taking into account correlations as well. In order to achieve this, in each sample, the individual yields for  $\bar{B}^0 \rightarrow \Lambda \bar{p} \pi^+$  are expressed in terms of the parameters of the asymmetry. Using Equations (4.22), (4.23), and (4.24) the yields take

the form

$$N_{\text{LL},11,(\mathcal{O}>0)}^{\bar{B}^0 \rightarrow \Lambda \bar{p} \pi^+} = N_{\text{LL},11,(\mathcal{O}<0)}^{\bar{B}^0 \rightarrow \Lambda \bar{p} \pi^+} \frac{A_T + 1}{1 - A_T} \quad (4.26)$$

$$N_{\text{DD},11,(\mathcal{O}>0)}^{\bar{B}^0 \rightarrow \Lambda \bar{p} \pi^+} = r_{11}^{\text{DD}} \times r_{\text{LL/DD},11}^{\text{MC}} \times N_{\text{LL},11,(\mathcal{O}<0)}^{\bar{B}^0 \rightarrow \Lambda \bar{p} \pi^+} \frac{A_T + 1}{1 - A_T} \quad (4.27)$$

$$N_{\text{LL},12,(\mathcal{O}>0)}^{\bar{B}^0 \rightarrow \Lambda \bar{p} \pi^+} = N_{\text{LL},12,(\mathcal{O}<0)}^{\bar{B}^0 \rightarrow \Lambda \bar{p} \pi^+} \frac{A_T + 1}{1 - A_T} \quad (4.28)$$

$$N_{\text{DD},12,(\mathcal{O}>0)}^{\bar{B}^0 \rightarrow \Lambda \bar{p} \pi^+} = r_{12}^{\text{DD}} \times r_{\text{LL/DD},12}^{\text{MC}} \times N_{\text{LL},12,(\mathcal{O}<0)}^{\bar{B}^0 \rightarrow \Lambda \bar{p} \pi^+} \frac{A_T + 1}{1 - A_T} \quad , \quad (4.29)$$

for the  $\bar{B}^0 \rightarrow \Lambda \bar{p} \pi^+$  components and

$$N_{\text{LL},11,(\mathcal{O}>0)}^{B^0 \rightarrow \bar{\Lambda} p \pi^-} = N_{\text{LL},11,(\mathcal{O}<0)}^{B^0 \rightarrow \bar{\Lambda} p \pi^-} \frac{(A_T - 2\mathcal{A}_T) + 1}{1 - (A_T - 2\mathcal{A}_T)} \quad (4.30)$$

$$N_{\text{DD},11,(\mathcal{O}>0)}^{B^0 \rightarrow \bar{\Lambda} p \pi^-} = r_{11}^{\text{DD}} \times r_{\text{LL/DD},11}^{\text{MC}} \times N_{\text{LL},11,(\mathcal{O}<0)}^{B^0 \rightarrow \bar{\Lambda} p \pi^-} \frac{(A_T - 2\mathcal{A}_T) + 1}{1 - (A_T - 2\mathcal{A}_T)} \quad (4.31)$$

$$N_{\text{LL},12,(\mathcal{O}>0)}^{B^0 \rightarrow \bar{\Lambda} p \pi^-} = N_{\text{LL},12,(\mathcal{O}<0)}^{B^0 \rightarrow \bar{\Lambda} p \pi^-} \frac{(A_T - 2\mathcal{A}_T) + 1}{1 - (A_T - 2\mathcal{A}_T)} \quad (4.32)$$

$$N_{\text{DD},12,(\mathcal{O}>0)}^{B^0 \rightarrow \bar{\Lambda} p \pi^-} = r_{12}^{\text{DD}} \times r_{\text{LL/DD},12}^{\text{MC}} \times N_{\text{LL},12,(\mathcal{O}<0)}^{B^0 \rightarrow \bar{\Lambda} p \pi^-} \frac{(A_T - 2\mathcal{A}_T) + 1}{1 - (A_T - 2\mathcal{A}_T)} \quad (4.33)$$

for the  $B^0 \rightarrow \bar{\Lambda} p \pi^-$  components. The  $N_{\text{LL},11,(\mathcal{O} \leq 0)}^{\bar{B}^0 \rightarrow \Lambda \bar{p} \pi^+}$  denotes the over all  $\bar{B}^0 \rightarrow \Lambda \bar{p} \pi^+$  yield in the sample with  $\mathcal{O} \leq 0$  for a given year or  $\Lambda$  configuration. The yields for  $\mathcal{O} < 0$  are independent, but the yields for  $\mathcal{O} > 0$  are connected via the asymmetries to the yields for  $\mathcal{O} < 0$ . All other yields are determined independently in each sample to allow for a different behaviour with respect to the triple product. This approach increases the statistical uncertainty but leads to no additional model dependent systematic uncertainties.

### 4.3.1 Correction Factors for the Time Reversal Asymmetry

The asymmetries listed in the previous chapter reflect an unrealistic scenario in which there are no diluting effects. There are two major effects diluting the overall asymmetry. The first effect is driven by the detector, whereas the second is driven by the assumptions made in order to determine the  $\Lambda$  spin, which is not directly ccessible to the LHCb experiment.

In Fig. 4.4(a) the triple product is shown schematically. In case the angle between two of its vectors is very small the value of the triple product is also small, but more importantly, the uncertainty on the sign of the triple product is larger. The distribution of the values of the triple product for the generated particles is shown in Fig. 4.4(b) and it is centred around zero. Due to the non-zero angular resolution it might happen, that the reconstructed triple product switches its sign with respect to its true value. This effect was studied using simulated events, comparing the sign of the triple products before (*cf.* Fig. 4.4(b)) and after the reconstruction. Since only the sign is important rather than its value, it is checked how often the sign flips following the reconstruction. The effect is found to be small and it should be noted, that only the enhancement region is checked, since the triple product is evaluated in that part of the three body phase space. The probabilities to flip the sign during the reconstruction are listed in Tab. 4.4.

Table 4.4: Probability  $\mathcal{P}_{\text{Flip}}$  for flipping the sign of the triple product due to the angular resolution.

	2011 LL	2011 DD	2012 LL	2012 DD
$\mathcal{P}_{\text{Flip}}$ in %	$4.12 \pm 0.13$	$15.54 \pm 0.08$	$3.5 \pm 0.07$	$13.3 \pm 0.04$

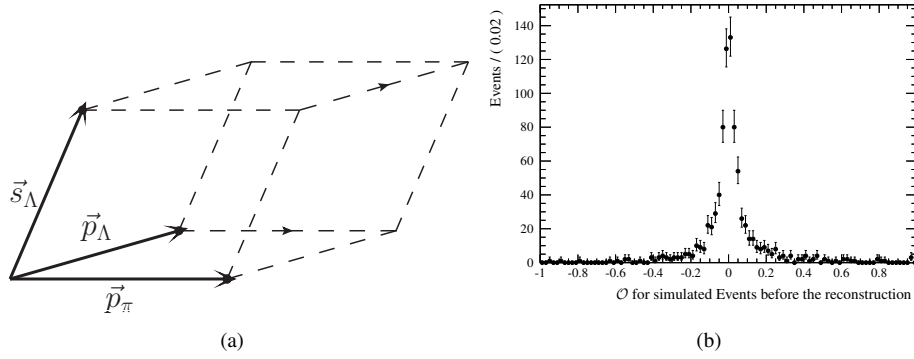


Figure 4.4: Illustration of the triple product employed to determine the time reversal violation in the  $\bar{B}^0 \rightarrow \Lambda \bar{p} \pi^+$  decay (a) and distribution of the triple product for simulated  $\bar{B}^0 \rightarrow \Lambda \bar{p} \pi^+$  decays before the reconstruction (b).

The probability  $\mathcal{P}_{\text{Flip}}$  to flip the sign is treated as a dilution factor  $D_{\text{Flip}}$ . A dilution factor is an effect that reduces the amplitude of the asymmetry, which for the sign flip is given by

$$D_{\text{Flip}} = 1 - 2\mathcal{P}_{\text{Flip}} \quad . \quad (4.34)$$

Another, more pronounced dilution effect results from the  $\Lambda$  spin estimation. As was explained in Sec. 1.3 the direction of the proton in the  $\Lambda$  rest frame is taken as the direction of the  $\Lambda$  spin and it is then boosted into the  $B^0$  rest frame. It was shown in Sec. 1.3, that this approach leads to an additional dilution since the expectation value of the angle between the proton momentum and the  $\Lambda$  spin is given by

$$\langle \cos \theta \rangle = +\frac{\alpha}{3} \quad , \quad (4.35)$$

with the decay parameter  $\alpha$ , which in case of maximal parity violation in the  $\Lambda$  decay would take the value of one, so even for this extreme case, the dilution would be one in three. The measured values for  $\alpha$  are given as [12]

$$\begin{aligned} \alpha(\Lambda \rightarrow p\pi^-) &= +0.642 \pm 0.013 \\ \alpha(\bar{\Lambda} \rightarrow \bar{p}\pi^+) &= -0.71 \pm 0.08 \quad . \end{aligned} \quad (4.36)$$

The decay parameters for  $\Lambda$  and  $\bar{\Lambda}$  overlap within their uncertainties and the  $\alpha$  with the smaller uncertainty is used in the fit. In doing so it is assumed that CP is conserved in the  $\Lambda$  decay. The uncertainty on  $\alpha$  is treated as an external systematic uncertainty. In contrast to  $\mathcal{P}_{\text{Flip}}$  entering the dilution  $D_{\text{Flip}}$ , the value for  $\langle \cos \theta \rangle$  is already a dilution factor, therefore one finds

$$D_{\Lambda\text{-spin}} = \frac{\alpha}{3} = 0.214 \quad . \quad (4.37)$$

The overall dilution is given by

$$D_T = D_{\text{Flip}} D_{\Lambda\text{-spin}} = (1 - 2\mathcal{P}_{\text{Flip}}) \frac{\alpha}{3} \quad . \quad (4.38)$$

The dilution factors can be included in the overall fit by modifying the individual yields. Instead of the physical asymmetries, the fit yields so called raw asymmetries, defined as

$$A_{\text{raw}} = D_T A_T \quad (4.39)$$

$$\bar{A}_{\text{raw}} = \bar{D}_T \bar{A}_T \quad , \quad (4.40)$$



note that the dilution factor need not be identical for the  $\bar{B}^0 \rightarrow \Lambda \bar{p} \pi^+$  and  $B^0 \rightarrow \bar{\Lambda} p \pi^-$  decays, for example the decay parameter for the  $\bar{\Lambda}$  is different than for the  $\Lambda$  baryon, but assuming CP conservation in the  $\Lambda$  decay leads to  $D_T = \bar{D}_T$ .

The fit is modified to take these effects into account by multiplying the asymmetries with the corresponding dilution factors and then extract the physical asymmetries. The fit employed in this analysis is flexible enough to allow for an individual dilution factor for each sample, which is necessary given the different values of  $D_{\text{Flip}}$ . But before including the correction to the asymmetry it is useful to determine the raw asymmetries themselves in order to get an impression of the overall statistical sensitivity of the analysis. The raw asymmetries derived from the fit are

$$A_{\text{raw}} = (-0.3_{-7.8}^{+7.8})\% \quad (4.41)$$

$$\bar{A}_{\text{raw}} = (-3.3_{-8.2}^{+8.2})\% \quad (4.42)$$

$$\mathcal{A}_{\text{raw}} = (1.5_{-5.7}^{+5.7})\% \quad , \quad (4.43)$$

the uncertainties being statistical only. The theoretical prediction for  $\mathcal{A}_T$  is about 10 percent and in case of no dilution factors entering the determination of the physical asymmetries the analysis should be able to establish a time reversal violation at the  $1 \dots 2\sigma$  in case  $\mathcal{A}_T \sim 10\%$ , which is remarkable given the limited statistics. Due to the large dilution coming from the assumptions made for the  $\Lambda$  spin the uncertainty increases considerably, for the full fit including both dilution factors the physical asymmetries are found to be

$$A_T = (-1.0_{-37.2}^{+37.2})\% \quad (4.44)$$

$$\bar{A}_T = (-16.2_{-39.1}^{+39.1})\% \quad (4.45)$$

$$\mathcal{A}_T = (7.6_{-27.0}^{+27.0})\% \quad , \quad (4.46)$$

again the uncertainties being statistical only. Within the large uncertainty the central value for  $\mathcal{A}_{\text{raw}}$  is in agreement with both the theoretical prediction as well as the no time reversal violation hypothesis. Furthermore, the sign of the asymmetry cannot be determined unambiguously either. The results of the full asymmetry fit including all dilution factors is shown in Figs. 4.5, 4.6, 4.7, and 4.8 for the  $\bar{B}^0 \rightarrow \Lambda \bar{p} \pi^+$  sample with  $\mathcal{O} > 0$ ,  $\bar{B}^0 \rightarrow \Lambda \bar{p} \pi^+$  sample with  $\mathcal{O} < 0$ ,  $B^0 \rightarrow \bar{\Lambda} p \pi^-$  sample with  $\mathcal{O} > 0$ , and  $B^0 \rightarrow \bar{\Lambda} p \pi^-$  sample with  $\mathcal{O} < 0$ , respectively. The final values for all fit parameters can be found in Appendix H.3.

## 4.4 Systematic uncertainties for $\mathcal{A}_T$

The results listed in the previous section contain only the statistical uncertainties. This section is centred around the systematic uncertainties for the time reversal asymmetry and relative  $\bar{B}_s^0 \rightarrow \Lambda \bar{p} K^+$  branching fraction measurement. Several sources of systematic uncertainties need to be considered, fortunately in the asymmetry measurement many sources cancel, especially due to the fact, that the result is based on the difference between two asymmetries. The same is also true for the relative branching fraction measurement. The following sources have been investigated:

**Fit model:** The overall fit model is very complex containing a lot of components, many cross-sample constraints and it is considered to be the largest source of systematic effects on the  $\mathcal{A}_T$  measurement. Several individual factors need to be considered, the influence of the four body decays appearing at smaller  $\Lambda \bar{p} h$  invariant masses, the  $\Sigma^0$  modes and the assumptions made on its dynamic structure, and differences between the simulated line shape and the line shape in the recorded data.

**Selection:** In this analysis two distinctive selections are applied, the PID and candidate selection. The kaon/pion particle identification enters the fit as a crucial component allowing the separation of the different  $\bar{B}^0$  and  $\bar{B}_s^0$  modes. Although the method of extracting the efficiencies is data driven, differences in the coverage between the signal modes and the calibration sample might lead to a systematic effect. The same is true for the proton identification. The remaining selection is based on a multivariate approach using simulated data as input for the signal sample. Differences between the input variables for simulated and recorded events need to be investigated since the relative efficiencies are used in the fit as well. Finally, effects of the trigger and tracking should be investigated as well at least for differences between the  $\bar{B}^0$  and  $\bar{B}_s^0$  modes.

$\Lambda$  decay constant: The uncertainty of  $\Lambda$  decay constant is at the 2% level for the  $\Lambda$  and at the 11% level for  $\bar{\Lambda}$ . This uncertainty will be considered as an external uncertainty. The assumption of CP conservation in the  $\Lambda$  decay will also be checked and its influence on the T asymmetry measurement will be evaluated as well.

#### 4.4.1 Fit model

The overall fit to the invariant  $\Lambda\bar{p}h$  masses contains a lot of components compared to the available statistical precision. This section evaluates the systematic uncertainties based on the fit model.

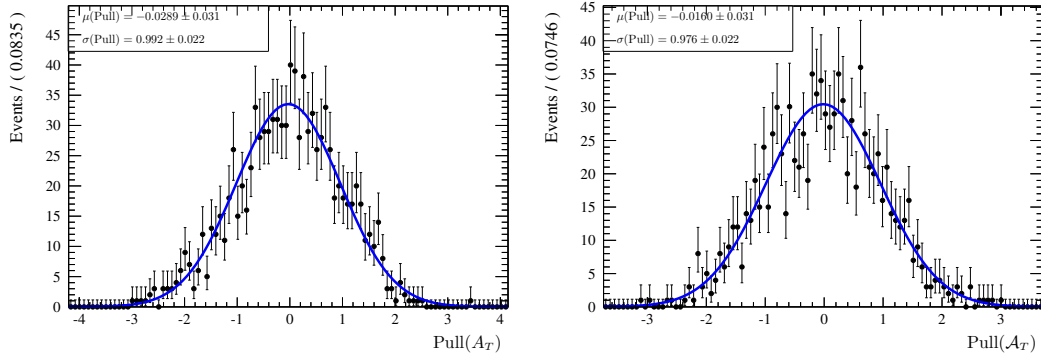


Figure 4.9: Distribution of Pulls for the Time reversal asymmetry measurement for a thousand toy experiments using the results for the nominal fit. The plot in the left hand side shows the Pull plot for  $\mathcal{A}_T$  and on the right hand side the Pull plot for  $\mathcal{A}_T$  is shown. Both distribution agree with a standard normal distribution within the statistical uncertainty, hence no bias is detected.

Before investigating the individual contributions to the systematic uncertainties for the fit model, it is useful to perform toy experiment studies to check whether the complex fit converges consistently and reproduces the fit results listed in Sec. 4.3.1. For that reason a thousand toy experiments are generated according to the nominal fit results and the overall fit function. Each toy set is generated according to a Poisson distribution for each variable and is fitted afterwards. The fit results can now be compared to the nominal values used in the toy generation using the pull distribution defined for a variable  $x$  as

$$\text{Pull} = \frac{x^{\text{Fit}} - x^{\text{Gen}}}{\sigma^{\text{Fit}}}, \quad (4.47)$$

where  $x^{\text{Fit}}$  is the fit value,  $\sigma^{\text{Fit}}$  the uncertainty of  $x^{\text{Fit}}$ , and  $x^{\text{Gen}}$  the nominal value for each toy sample, respectively. Ideally, the pull distribution follows a normal distribution, in case the fit is unbiased, *i.e.* its mean value is zero and its standard deviation is one. In Fig. 4.9 the pull distribution for the relevant variables for the  $\mathcal{A}_T$  measurement are shown, the asymmetry for the  $\bar{B}^0$  samples,  $\mathcal{A}_T$ , and the difference between the  $\bar{B}^0$  and  $B^0$  asymmetry,  $\mathcal{A}_T$ . Both are compatible with the expectation from an unbiased fit, therefore, no corrections due to a biased fit need to be applied.

The true composition of the lower mass sideband is unknown, many different  $\bar{B}^0$  and  $\bar{B}_s^0$  decays contribute apart from the  $\Sigma^0$  decays or the studied  $\bar{B}^0 \rightarrow \Lambda\bar{p}\rho^+$  and  $\bar{B}_s^0 \rightarrow \Lambda\bar{p}K^{*+}$  decays, neither of which has been observed and there are no available limits on these modes. Including a component for these four body modes based on the  $\bar{B}^0 \rightarrow \Lambda\bar{p}\rho^+$  and  $\bar{B}_s^0 \rightarrow \Lambda\bar{p}K^{*+}$  decays has been included in the fit, the yields, however, were compatible with zero in the fit to the data. In order to evaluate the influence of these modes on the T asymmetry measurement, the range of the fit is changed. Instead of using the full range of  $m(\Lambda\bar{p}h) \in [4900, 5600]$  MeV/ $c^2$  the fit is repeated using a smaller range of  $m(\Lambda\bar{p}h) \in [5100, 5600]$  MeV/ $c^2$ .

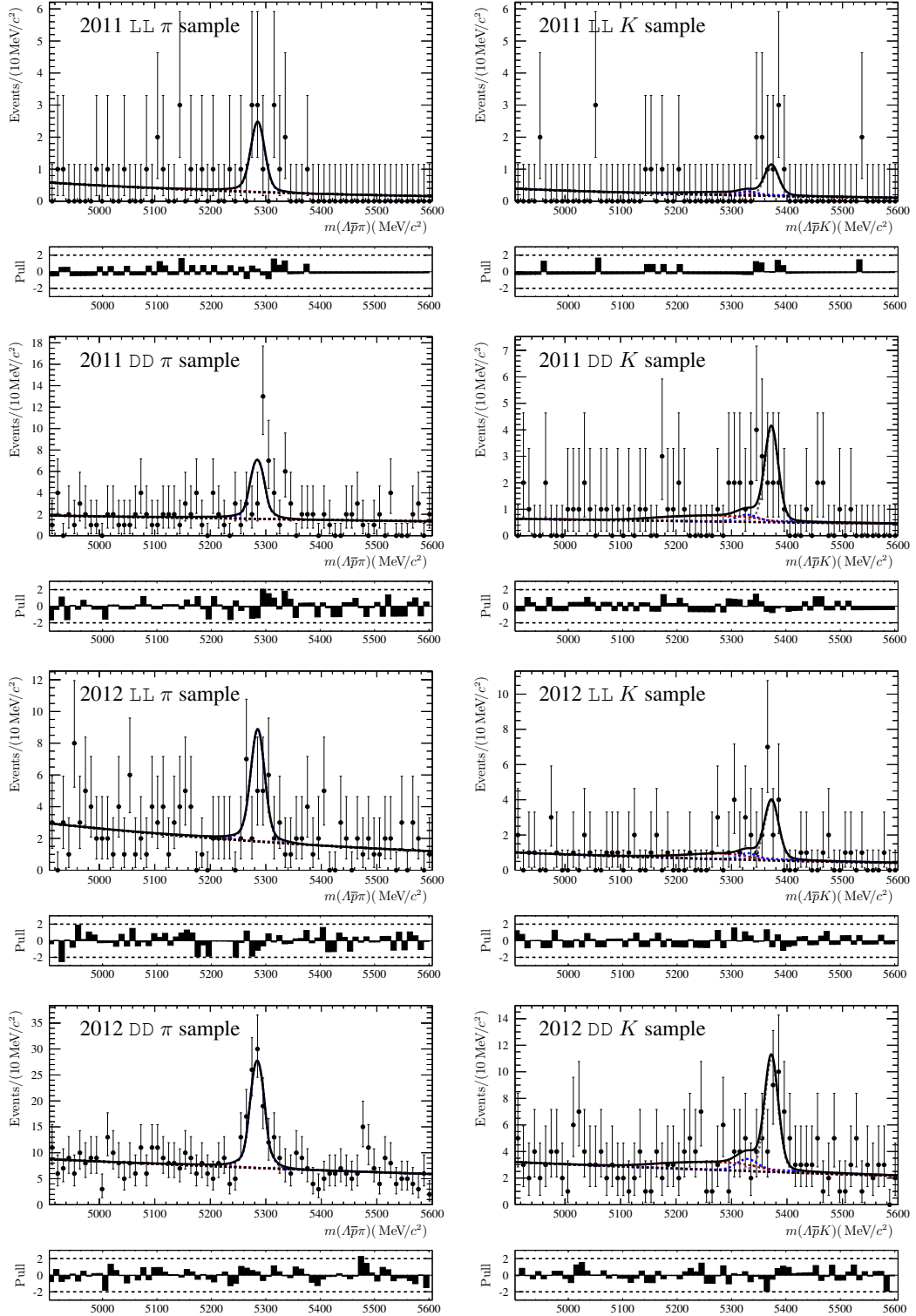


Figure 4.5: Fit results for the full asymmetry fit for the  $\mathcal{O} > 0$  and  $\bar{B}^0 \rightarrow \Lambda \bar{p} \pi^+$  samples. The graphical representation is identical to Fig. 4.3. The samples are denoted in the plots.

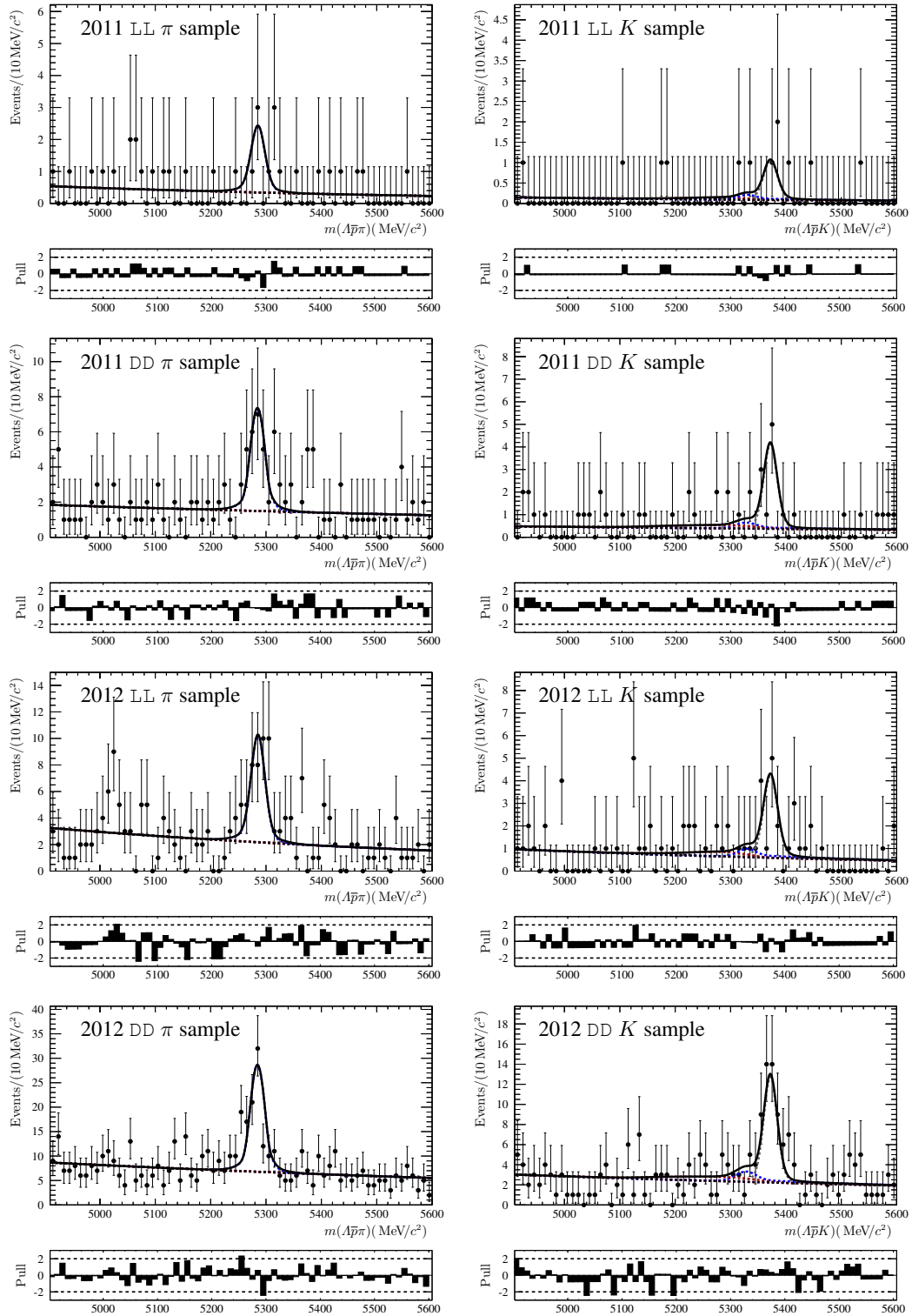


Figure 4.6: Fit results for the full asymmetry fit for the  $\mathcal{O} < 0$  and  $\bar{B}^0 \rightarrow A\bar{p}\pi^+$  samples. The graphical representation is identical to Fig. 4.3. The samples are denoted in the plots.

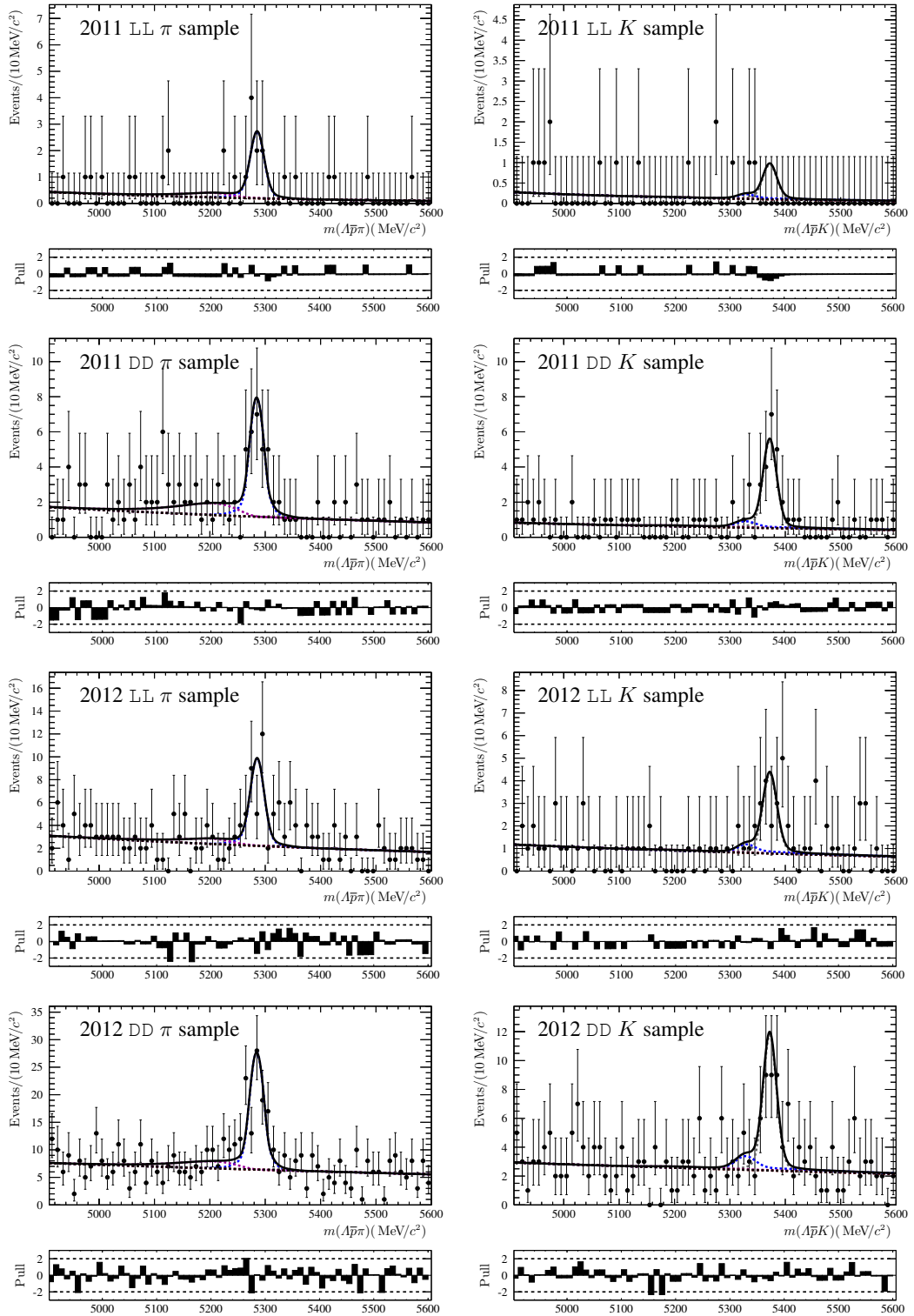


Figure 4.7: Fit results for the full asymmetry fit for the  $O > 0$  and  $B^0 \rightarrow \bar{\Lambda} p \pi^-$  samples. The graphical representation is identical to Fig. 4.3. The samples are denoted in the plots.

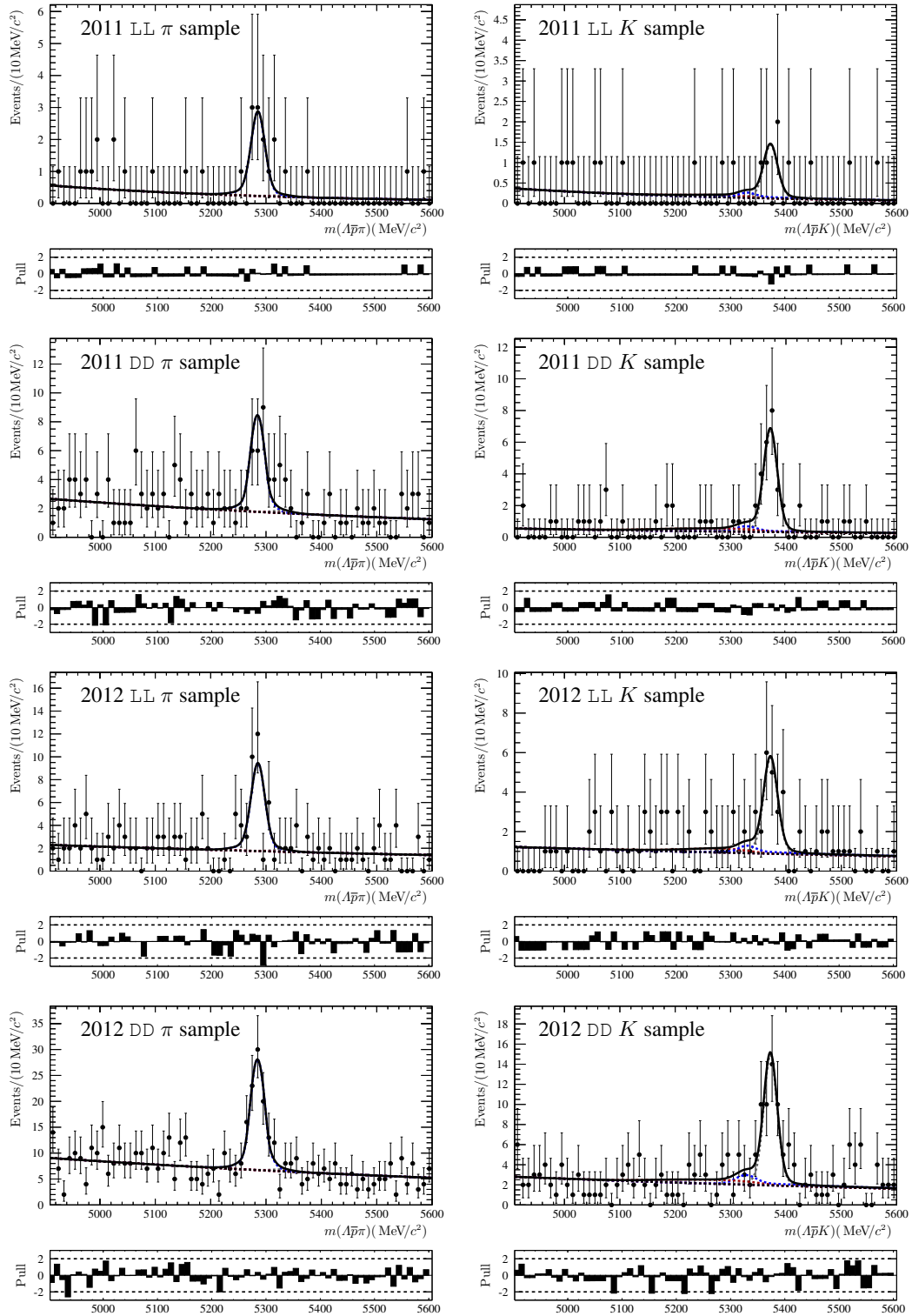


Figure 4.8: Fit results for the full asymmetry fit for the  $\mathcal{O} < 0$  and  $B^0 \rightarrow \bar{\Lambda} p \pi^-$  samples. The graphical representation is identical to Fig. 4.3. The samples are denoted in the plots.

The fit result for the asymmetry using the updated fit range and the difference with respect to the nominal fit is

$$\mathcal{A}_T = (7.3^{+28.0}_{-28.0})\% \quad (4.48)$$

$$\Delta\mathcal{A}_T = 0.3\% \quad , \quad (4.49)$$

the statistical uncertainty on the difference is neglected since the same candidates are used. The difference of  $\Delta\mathcal{A}_T = 0.3\%$  is included as systematic uncertainty based on the fit model.

As was described in Sec. 4.1 it is assumed that the  $\bar{B}^0_{(s)} \rightarrow \Sigma^0 \bar{p} h^+$  decay modes have a similar dynamic distribution as the  $\bar{B}^0_{(s)} \rightarrow \Lambda \bar{p} h^+$  modes. The systematic effect of this assumption is tested by using the overall phase space efficiencies (cf. Sec. 3.3). The new asymmetry  $\mathcal{A}_T$  and the difference to the nominal number is given by

$$\mathcal{A}_T = (7.7^{+27.0}_{-27.0})\% \quad (4.50)$$

$$\Delta\mathcal{A}_T = 0.1\% \quad , \quad (4.51)$$

omitting the statistical uncertainty, and the difference of  $\Delta\mathcal{A}_T = 0.1\%$  is assigned as a contribution to the overall systematic uncertainty for the fit model.

The individual line shapes for the  $\bar{B}^0_{(s)} \rightarrow \Lambda \bar{p} h^+$  modes are determined using simulated events and are fixed in the fit to data. In general, the simulation underestimates the mass resolution. While measuring the relative branching ratios for  $B^+ \rightarrow p \bar{p} h^+$  A. Hicheur *et al.* [50] determined the width of the  $B^+ \rightarrow p \bar{p} K^+$  line shape in recorded and simulated events. The width in data was 16.7% larger compared to the simulation. This factor is applied for the  $\bar{B}^0_{(s)} \rightarrow \Lambda \bar{p} h^+$  modes in the nominal fit, the  $\bar{B}^0_{(s)} \rightarrow \Sigma^0 \bar{p} h^+$  distributions in contrast are broad and no scaling factor is applied. The resulting asymmetry and difference to the nominal fit given by

$$\mathcal{A}_T = (8.6^{+26.3}_{-26.3})\% \quad (4.52)$$

$$\Delta\mathcal{A}_T = 1.0\% \quad , \quad (4.53)$$

the statistical uncertainty on the difference is neglected since the same candidates are used. The difference of  $\Delta\mathcal{A}_T = 1.1\%$  is used to determine systematic uncertainty for the fit model.

The overall systematic uncertainty due to the fit model is given by summing the individual contributions in quadrature and is found to be

$$\Delta\mathcal{A}_T^{\text{Fit}} = 1.1\% \quad . \quad (4.54)$$

## 4.4.2 Selection

There are several steps in the selection chain that need to be investigated as sources for systematic uncertainties, one being the PID selection.

The PID selection efficiency enters the fit in two ways. First the proton selection efficiency is used in the overall constraints and the pion and kaon (mis-)identification is exploited to constrain the  $\bar{B}^0_{(s)} \rightarrow \Lambda \bar{p} h^+$  cross feeds. Due to the finite size of the calibration samples provided for the PIDCalib package and problems with the  $p$ - $\eta$  coverage for the proton samples it is necessary to investigate any systematic effects. This is done by choosing a different binning in order to extract the efficiency for the given selection. The efficiencies for the kaons and pions are stable compared to the previous binning, the proton efficiency drops by several percent, the drop, however, is almost equal among all modes, so the effect on the asymmetry is expected to be small and it is estimated by running the full fit using the new efficiencies and the difference is used as an estimate for the systematic uncertainty, one finds

$$\mathcal{A}_T = (7.7^{+27.0}_{-27.0})\% \quad (4.55)$$

$$\Delta\mathcal{A}_T = 0.1\% \quad .$$

In addition to that it is recommended to assign an additional relative uncertainty of 0.1% due to the  $s$ Plot formalism applied to the kaon and pion calibrations samples. Summing both effects in quadrature one finds for the systematic uncertainty based in the PID

$$\Delta\mathcal{A}_T^{\text{PID}} = 0.1\% \quad . \quad (4.56)$$

The multivariate analysis uses simulated events as source for the signal class. Several input variables require good knowledge of the  $\bar{B}^0$  and  $B_s^0$  production processes. Especially the pseudorapidity and transverse momentum of the  $B$  mesons depend on these models but also derived variables such lifetimes. Furthermore, variables such as the impact parameters depend on the correct simulation of the detector. It is necessary to check, whether the response function for the neural nets matches between the simulation and the recorded data. This is done by comparing the response of simulated signal events with  $s$ Weighted data events. The resulting behaviour is shown in Fig. 4.10. Except for the 2011 DD sample the agreement between the simulation and the data is very good. Nevertheless, only the ratio of events before and after the selection is of importance here. Since this is good for 2011 DD as well, no systematic effects can be found. In addition to that, the selection is mostly based on topological variables. Systematic effects would be expected to cause the sign of the triple product to flip and it was shown in Sec. 4.3.1 that these effects are expected to be small compared to dilution effects based on the  $\Lambda$  spin determination.

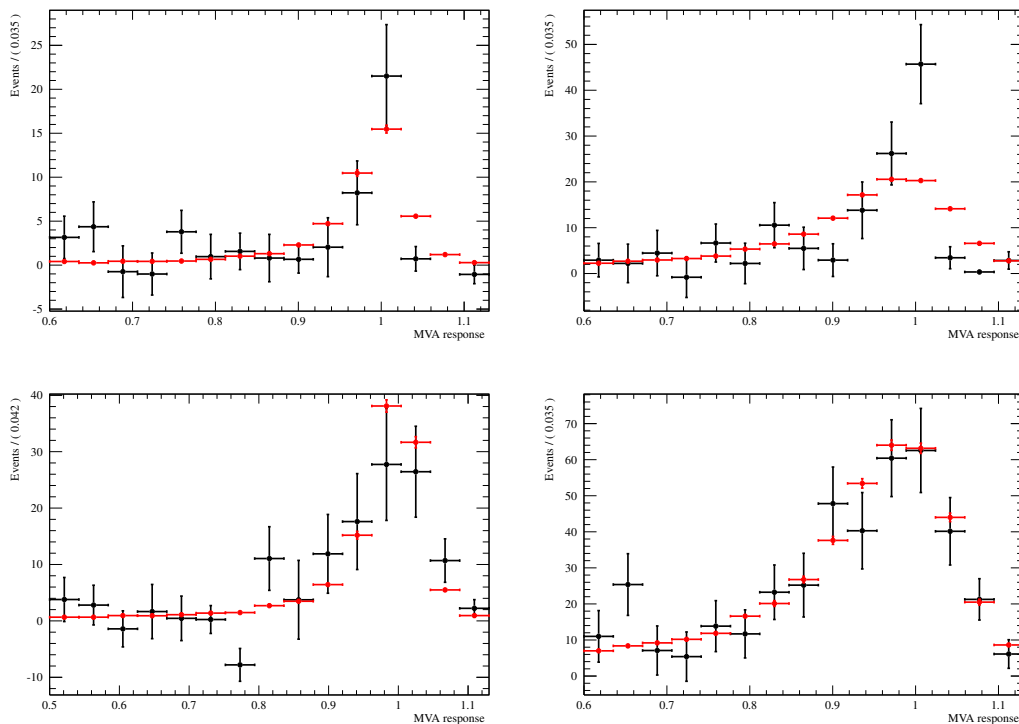


Figure 4.10: Comparison between the MVA response for simulated signal candidates (red data points) and background subtracted candidates in recorded data (black data points). The background subtraction is performed using the  $s$ Plot technique. The histograms are scaled to have the same integral. The top (bottom) row shows the plots for the 2011 (2012) samples, the LL (DD) sample on the left (right) hand side. Except for the 2011 DD sample the agreement is good.

Effects based on the deviation from the simulation based on a constant matrix element are accounted for in the statistical uncertainty, as the uncertainty on the recalculated efficiency is included as a Gaussian constraint. The trigger efficiency is not expected to be constant across the Dalitz plot, but this effect is included in the overall efficiency and therefore in the overall statistical uncertainty. Additional differences between data and the simulation



may arise to misalignment effects not correctly reproduced by the simulation. Here, the angular measurement is important since it may change the sign of the triple product. As was shown in Sec. 4.3.1 the predicted effect from the simulation is at the per mille level. Even a discrepancy by a factor of two between data and simulation would have a smaller effect than the uncertainty on the  $\Lambda$  decay constant. Therefore, no uncertainty due this effect is assigned.

#### 4.4.3 $\Lambda$ Decay and $\Lambda$ Decay Constant

The uncertainty on the  $\Lambda$  decay constant is given by [12]

$$\frac{\Delta\alpha(\Lambda \rightarrow p\pi^-)}{\alpha(\Lambda \rightarrow p\pi^-)} = 2.0\% \quad , \quad (4.57)$$

and it is mitigated as an external systematic uncertainty on the time reversal asymmetry. The systematic uncertainty on  $\mathcal{A}_T$  is given as

$$\Delta\mathcal{A}_T^A = 0.15\% \quad . \quad (4.58)$$

So far it is assumed, that CP is conserved in the  $\Lambda$  decay and the decay parameter for the  $\Lambda$  is used for  $\bar{\Lambda}$  decay as well since its uncertainty is smaller. This is in agreement with the experimental observation, and the predictions from the Standard Model. Still it is interesting to allow for CP violation in the  $\Lambda$  decay by using the different decay parameters for the  $\Lambda$  and the  $\bar{\Lambda}$ . In order to account for the effect, the asymmetries are modified

$$A_{\text{raw}} = D_T A_T = (1 - 2\mathcal{P}_{\text{Flip}}) \frac{\alpha(\Lambda)}{3} \quad (4.59)$$

$$\bar{A}_{\text{raw}} = \bar{D}_T \bar{A}_T = (1 - 2\mathcal{P}_{\text{Flip}}) \frac{\alpha(\bar{\Lambda})}{3} \quad , \quad (4.60)$$

and the fit is rerun with this configuration, one finds

$$A_T^{\text{CPV}} = (-1.2^{+37.3}_{-37.1})\% \quad (4.61)$$

$$\bar{A}_T^{\text{CPV}} = (-9.9^{+23.6}_{-23.6})\% \quad (4.62)$$

$$\mathcal{A}_T^{\text{CPV}} = (4.3^{+22.1}_{-22.0})\% \quad , \quad (4.63)$$

which is slightly smaller compared to the asymmetry assuming CP conservation. This based on the smaller dilution due to the larger  $\alpha$  for the  $\bar{\Lambda}$ . The uncertainty on the  $\bar{\Lambda}$  decay constant is considerably larger [12],

$$\frac{\Delta\alpha(\bar{\Lambda} \rightarrow \bar{p}\pi^+)}{\alpha(\bar{\Lambda} \rightarrow \bar{p}\pi^+)} = 11.3\% \quad , \quad (4.64)$$

and the overall systematic uncertainty due to the decay parameters is

$$\Delta\mathcal{A}_T^{A\text{CPV}} = 0.5\% \quad . \quad (4.65)$$

The total systematic uncertainty calculated by summing the individual uncertainties in quadrature assuming no correlation between the individual sources is given by

$$\begin{aligned} \Delta\mathcal{A}_T &= 1.1\% \\ \Delta\mathcal{A}_T^{\text{CPV}} &= 1.2\% \quad , \end{aligned} \quad (4.66)$$

the first uncertainty is based on assuming CP conservation for the  $\Lambda$  decay, the second allows for CP violation in the  $\Lambda$  decay. In Table 4.5 the relative systematic uncertainties are listed.

## 4.5 Systematic Uncertainties for the $\bar{B}_s^0 \rightarrow \Lambda\bar{p}K^+$ Branching Fraction

The systematic uncertainties on the branching fraction measurement are quite similar to the uncertainties for  $\mathcal{A}_T$ . In the end, the  $\bar{B}_s^0 \rightarrow \Lambda\bar{p}K^+$  branching fraction is extracted from the ratio relative to  $\bar{B}^0 \rightarrow \Lambda\bar{p}\pi^+$ .

The relevant uncertainties are :

**Fit model:** The overall fit determines the ratio between the  $\bar{B}_s^0 \rightarrow \Lambda\bar{p}K^+$  and  $\bar{B}_s^0 \rightarrow \Lambda\bar{p}K^-$  modes and  $\bar{B}^0 \rightarrow \Lambda\bar{p}\pi^+$ . Similar to the  $\mathcal{A}_T$  measurement the relevant sources are due the limited knowledge of the composition of the lower  $m(\Lambda\bar{p}h)$  invariant mass sideband and the line shapes for the  $\bar{B}^0_{(s)} \rightarrow \Lambda\bar{p}h^+$  decays. Both sources are treated similarly to the  $\mathcal{A}_T$  measurement, the fit is performed in different ranges and with the width scaling from  $B^+ \rightarrow p\bar{p}K^+$ , respectively.

**Selection:** Again the fit uses constraints on the relative branching fractions thus makes use of the selection and PID efficiencies. These effects are investigated separately.

**Hadronisation factor:** The  $\bar{B}_s^0 \rightarrow \Lambda\bar{p}K^+$  branching fraction is measured with respect to the  $\bar{B}^0$  mode  $\bar{B}^0 \rightarrow \Lambda\bar{p}\pi^+$ . Since the hadronisation probabilities are different from  $\bar{B}^0$  and  $\bar{B}_s^0$  the ratio  $f_s/f_d$  is treated as an external systematic uncertainty on the  $\bar{B}_s^0 \rightarrow \Lambda\bar{p}K^+$  branching fraction.

**Branching fraction for  $\bar{B}^0 \rightarrow \Lambda\bar{p}\pi^+$ :** Since the  $\bar{B}_s^0 \rightarrow \Lambda\bar{p}K^+$  branching fraction is determined relative to  $\bar{B}^0 \rightarrow \Lambda\bar{p}\pi^+$  the limited knowledge on  $\mathcal{B}(\bar{B}^0 \rightarrow \Lambda\bar{p}\pi^+)$  is accounted for in the systematic uncertainty.

### 4.5.1 Fit Model

As for the time reversal asymmetry fit, it is useful to perform toy studies in order to check the stability of the overall fit. In Fig. 4.11 the pull distribution for the ratio between the  $\bar{B}^0 \rightarrow \Lambda\bar{p}\pi^+$  and  $\bar{B}_s^0 \rightarrow \Lambda\bar{p}K^+$  branching fractions is shown, as before the mean value and standard deviation agree with a normal distribution signalling an unbiased fit.

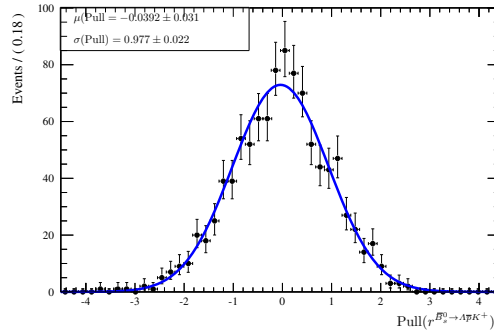


Figure 4.11: Pull distribution for ratio between the  $\bar{B}^0 \rightarrow \Lambda\bar{p}\pi^+$  and  $\bar{B}_s^0 \rightarrow \Lambda\bar{p}K^+$  branching fraction for one thousand toy experiments using the nominal fit results.

The uncertainties due to the limited knowledge of the four body modes is accounted for by performing the fit using the reduced interval of  $m(\Lambda\bar{p}h) \in [5100, 5600] \text{ MeV}/c^2$ . Using the new result for  $r^{\bar{B}_s^0 \rightarrow \Lambda\bar{p}K^+}$  the relative deviation from the nominal value is taken as a systematic uncertainty, one finds

$$\frac{\Delta r^{\bar{B}_s^0 \rightarrow \Lambda\bar{p}K^+}}{r^{\bar{B}_s^0 \rightarrow \Lambda\bar{p}K^+}} = 2\% \quad . \quad (4.67)$$

The uncertainty due to the assumptions on the  $\bar{B}^0_{(s)} \rightarrow \Sigma^0 \bar{p} h^+$  Dalitz plot distribution is treated similar to the uncertainty on  $\mathcal{A}_T$ , the fit is performed using the efficiencies calculated from the phase space simulated events. The relative deviation between the updated  $r^{\bar{B}_s^0 \rightarrow \Lambda \bar{p} K^+}$  and the nominal fit value is taken as the systematic uncertainty,

$$\frac{\Delta r^{\bar{B}_s^0 \rightarrow \Lambda \bar{p} K^+}}{r^{\bar{B}_s^0 \rightarrow \Lambda \bar{p} K^+}} = 1\% \quad . \quad (4.68)$$

For the time reversal asymmetry the main systematic uncertainty was due to the imperfect knowledge of the line shape. Again using the the 16% difference between the recorded data and the simulation based on the  $B^+ \rightarrow p \bar{p} K^+$  analysis the new ratio  $r^{\bar{B}_s^0 \rightarrow \Lambda \bar{p} K^+}$  is determined and the deviation from the nominal value taken as a relative systematic uncertainty. One finds

$$\frac{\Delta r^{\bar{B}_s^0 \rightarrow \Lambda \bar{p} K^+}}{r^{\bar{B}_s^0 \rightarrow \Lambda \bar{p} K^+}} = 2.5\% \quad . \quad (4.69)$$

Summing all uncertainties in quadrature the total relative systematic uncertainty based on the fit model is given as

$$\frac{\Delta r^{\bar{B}_s^0 \rightarrow \Lambda \bar{p} K^+}}{r^{\bar{B}_s^0 \rightarrow \Lambda \bar{p} K^+}} = 3.4\% \quad . \quad (4.70)$$

## 4.5.2 Selection

The systematic uncertainty for the PID selection follows the same line as for  $\mathcal{A}_T$ . The PID efficiencies are calculated using a different binning, the relative change in  $r^{\bar{B}_s^0 \rightarrow \Lambda \bar{p} K^+}$  is taken as the systematic uncertainty.

Rerunning the fit using the modified PID efficiencies one finds,

$$\frac{\Delta r^{\bar{B}_s^0 \rightarrow \Lambda \bar{p} K^+}}{r^{\bar{B}_s^0 \rightarrow \Lambda \bar{p} K^+}} = 1.3\% \quad . \quad (4.71)$$

Another source of systematic uncertainty is based on the remaining selections and most effects cancel. In Fig. 4.10 the comparison between background subtracted signal in data and truth matched simulated events shows good agreement between the multivariate selectors in data and the simulation save for the 2011 DD sample, however, the efficiency for the selection is identical within the statistical uncertainty. Therefore, the simulation describes the input variables reasonably well and no additional systematic uncertainty is applied.

The largest difference between the efficiencies for  $\bar{B}_s^0 \rightarrow \Lambda \bar{p} K^+$  and  $\bar{B}^0 \rightarrow \Lambda \bar{p} \pi^+$  modes is the trigger efficiency. Neglecting small differences between these two modes based on the different masses of the  $B^0$  and  $B_s^0$  meson as well the larger kaon mass, the trigger efficiencies for each mode should be identical within the uncertainty. Taking into account the different relative luminosities for each sample the average maximum difference in the trigger efficiencies is 4.3% and half this value, 2.2%, is taken as a systematic uncertainty.

The total relative systematic uncertainty is determined by adding both contributions in quadrature,

$$\frac{\Delta r^{\bar{B}_s^0 \rightarrow \Lambda \bar{p} K^+}}{r^{\bar{B}_s^0 \rightarrow \Lambda \bar{p} K^+}} = 2.6\% \quad . \quad (4.72)$$

## 4.5.3 External Systematic Uncertainties

As mentioned before, the hadronisation probabilities for  $\bar{B}^0$  and  $\bar{B}_s^0$  mesons need to be taken into account in order to determine the relative branching fraction. The ratio  $f_s/f_d$  was determined by the LHCb experiment averaging over hadronic and semi-leptonic modes to be [44]

$$\frac{f_s}{f_d} = 0.259 \pm 0.015 \quad . \quad (4.73)$$

The relative systematic uncertainty of 5.8% is taken as a systematic uncertainty. The branching fraction for  $\bar{B}^0 \rightarrow \Lambda \bar{p} \pi^+$  is taken from the PDG averaging previous *BABAR* and *BELLE* measurements

$$\mathcal{B}(\bar{B}^0 \rightarrow \Lambda \bar{p} \pi^+) = (3.14 \pm 0.29) \times 10^{-6} \quad . \quad (4.74)$$

Its relative uncertainty of 9.2% is taken as a systematic uncertainty. Fortunately, the uncertainty on the  $\Lambda$  branching fraction cancels in the ratio as both decays are reconstructed using the identical  $\Lambda$  decay into a proton and a pion. Since these two uncertainties dominate and are not related to the measurements provided by this analysis, these are listed as separate systematic uncertainties.

In Table 4.5 the relative systematic uncertainties are summarised.

Table 4.5: Summary of the relative systematic uncertainties for the  $\mathcal{A}_T$ , the  $\mathcal{A}_T^{\text{CPV}}$ , and the relative branching fraction measurement.

Uncertainty origin	Value (%)		
	$\mathcal{A}_T$	$\mathcal{A}_T^{\text{CPV}}$	$\mathcal{B}(\bar{B}_s^0 \rightarrow \Lambda \bar{p} K^+)$
Fit Model	14.7%		3.4%
Selection	1.3%		2.6%
$\Lambda$ decay constant	2.0%	6.7%	–
Hadronisation factor	–		5.8%
Branching fraction of $\bar{B}^0 \rightarrow \Lambda \bar{p} \pi^+$	–		9.2%
Total	14.7%	16.0%	11.7%



# Chapter 5

## Results and Conclusion

The initial goal of this analysis was the measurement of the time reversal violating asymmetry  $\mathcal{A}_T$  using the triple product

$$\mathcal{O} = \mathbf{s}_\Lambda \cdot (\mathbf{p}_\Lambda \times \mathbf{p}_{\pi^+}) \quad (5.1)$$

and the following asymmetries

$$A_T = \frac{N_{(\mathcal{O}>0)}^{\bar{B}^0 \rightarrow \Lambda \bar{p} \pi^+} - N_{(\mathcal{O}<0)}^{\bar{B}^0 \rightarrow \Lambda \bar{p} \pi^+}}{N_{(\mathcal{O}>0)}^{\bar{B}^0 \rightarrow \Lambda \bar{p} \pi^+} + N_{(\mathcal{O}<0)}^{\bar{B}^0 \rightarrow \Lambda \bar{p} \pi^+}} \quad (5.2)$$

$$\bar{A}_T = \frac{N_{(\mathcal{O}>0)}^{B^0 \rightarrow \bar{\Lambda} p \pi^-} - N_{(\mathcal{O}<0)}^{B^0 \rightarrow \bar{\Lambda} p \pi^-}}{N_{(\mathcal{O}>0)}^{B^0 \rightarrow \bar{\Lambda} p \pi^-} + N_{(\mathcal{O}<0)}^{B^0 \rightarrow \bar{\Lambda} p \pi^-}} \quad (5.3)$$

$$\mathcal{A}_T = 1/2(\mathcal{A}_T - \bar{\mathcal{A}}_T) \quad (5.4)$$

The asymmetries are calculated independently for  $\bar{B}^0 \rightarrow \Lambda \bar{p} \pi^+$  and  $B^0 \rightarrow \bar{\Lambda} p \pi^-$  and finally subtracted and in doing so CP conserving effects due to final state interaction cancel. The whole analysis was proposed by C. Q. Geng and Y. K. Hsiao [2]. The asymmetries have been determined in a simultaneous unbinned extended maximum likelihood fit to the data taken in 2011 and 2012, a combined sample of  $3 \text{ fb}^{-1}$ , as well two different  $\Lambda$  configurations based on whether the  $\Lambda$  decays inside (LL) or outside (DD) the Vertex Locator.

There are three main results to report, the first two are the asymmetries for  $\bar{B}^0 \rightarrow \Lambda \bar{p} \pi^+$  assuming CP conservation and CP violation in the  $\Lambda$  decay. The third result is the first observation of the baryonic  $\bar{B}_s^0$  decay  $\bar{B}_s^0 \rightarrow \Lambda \bar{p} K^+$ .

For the CP conserving asymmetry  $\mathcal{A}_T$  ones finds

$$\mathcal{A}_T = (7.6 \pm 27.0 \text{ (stat)} \pm 1.1 \text{ (syst)})\% \quad (5.5)$$

Allowing for CP violation in the  $\Lambda$  decay the asymmetry is determined to be

$$\mathcal{A}_T^{\text{CPV}} = (4.3_{-22.0}^{+22.1} \text{ (stat)} \pm 1.2 \text{ (syst)})\% \quad (5.6)$$

The decays  $\bar{B}_s^0 \rightarrow \Lambda \bar{p} K^+$  and  $\bar{B}_s^0 \rightarrow \bar{\Lambda} p K^-$  are observed for the first time and their combined statistical significance corresponds to 17.2 Gaussian standard deviations.

The branching fraction for the sum of  $\bar{B}_s^0 \rightarrow \Lambda \bar{p} K^+$  and  $\bar{B}_s^0 \rightarrow \bar{\Lambda} p K^-$  is measured to be

$$\mathcal{B}(\bar{B}_s^0 \rightarrow \Lambda \bar{p} K^+) + \mathcal{B}(\bar{B}_s^0 \rightarrow \bar{\Lambda} p K^-) = \left[ 4.75_{-0.49}^{+0.53} \text{ (stat)} \pm 0.20 \text{ (syst)} \pm 0.28(f_s/f_d) \pm 0.44(\mathcal{B}) \right] \times 10^{-6} \quad (5.7)$$

For each result the first uncertainty is statistical and the second systematic, further additional external uncertainties are labelled accordingly. In addition to these results, the Dalitz plot for  $\bar{B}^0 \rightarrow \Lambda \bar{p} \pi^+$  and  $\bar{B}_s^0 \rightarrow \Lambda \bar{p} K^+$  has been studied and shows the familiar behaviour with a pronounced enhancement at threshold in the invariant baryon antibaryon mass. Each result will be discussed in the following sections.

## 5.1 Asymmetries $\mathcal{A}_T$ and $\mathcal{A}_T^{\text{CPV}}$

The theoretical prediction for asymmetry  $\mathcal{A}_T$  is given by C. Q. Geng and Y. K. Hsiao [2] to be

$$\mathcal{A}_T \in [10.2, 10.4]\% \quad (5.8)$$

assuming different strong phases between the interfering Feynman diagrams. The experimental results are compatible with the prediction, but due to the limited statistics and large dilution factor based on the determination of the  $\Lambda$  spin the significance of the measurement is small. The theoretical prediction can neither be excluded nor confirmed, the asymmetry is compatible with the no T violation hypothesis. Furthermore, the sign of the asymmetry cannot be determined either. As can be seen by the difference between  $\mathcal{A}_T$  and  $\mathcal{A}_T^{\text{CPV}}$  the dilution due to the  $\Lambda$  spin ambiguity is the main limitation of the analysis. The statistical precision of the raw asymmetry, *i.e.* neglecting dilution effects, was found to be  $\mathcal{A}_{\text{raw}} = (1.5 \pm 5.7)\%$ .

Previous analyses using the triple product technique in search for CP violation used different triple products containing only momentum vectors. Using a triple product containing the spin of one daughter particle has the advantage, that  $\mathcal{A}_T$  is even with respect to parity and only changes sign with respect to T. Baryonic  $B_{(s)}^0$  decays allow using the spin rather than just the momentum and define a triple product only sensitive to T, however, the inability to determine the spin vector of a fermion negates the advantage. Due to the large dilution factor the available number of candidates needs to be increased by an order of magnitude to allow a significant measurement. Experimentally, the reconstruction of the  $\Lambda$  baryon at LHCb imposes further restrictions since the detection efficiency is small. Unfortunately, decays such as  $B^+ \rightarrow p\bar{p}K^+$  are not suited for this kind of triple product either, because the spin of the proton cannot be determined. Studying  $B$  decays to  $\Lambda_c^+$  might prove more successful, the overall branching fraction for decays such as  $B^- \rightarrow \Lambda_c^+ \bar{p}\pi^-$  is two orders of magnitude larger compared to charmless modes such as  $\bar{B}^0 \rightarrow \Lambda \bar{p}\pi^+$  with  $\mathcal{B}(B^- \rightarrow \Lambda_c^+ \bar{p}\pi^-) = (2.8 \pm 0.8) \times 10^{-4}$  [12] and the detection efficiency is larger at LHCb due to the shorter lifetime of the  $\Lambda_c^+$  baryon. The downside of using  $\Lambda_c^+$  baryons is, that there is no well known two body decay mode with a large branching fraction such as  $\Lambda \rightarrow p\pi^-$ . The decay mode  $\Lambda_c^+ \rightarrow \Lambda\pi^+$  with  $\mathcal{B}(\Lambda_c^+ \rightarrow \Lambda\pi^+) = (1.07 \pm 0.28)\%$  [12] suffers from similar experimental issues due to the  $\Lambda$  in the decay chain, but the decay parameter for  $\Lambda_c^+ \rightarrow \Lambda\pi^+$  is close to one  $\alpha(\Lambda_c^+ \rightarrow \Lambda\pi^+) = -0.91 \pm 0.15$  [12] decreasing the dilution factor. Unfortunately, taking all these effects into account the statistical precision will again be the limiting factor, the small  $\Lambda_c^+ \rightarrow \Lambda\pi^+$  branching fraction almost negates the overall larger branching fraction of  $B^- \rightarrow \Lambda_c^+ \bar{p}\pi^-$  with respect to  $\bar{B}^0 \rightarrow \Lambda \bar{p}\pi^+$ . The uncertainty on  $\alpha(\Lambda_c^+ \rightarrow \Lambda\pi^+)$  is also large compared to the  $\Lambda$  decay constant, whose uncertainty is a large contributor to the overall systematic uncertainty. Finally, decays with  $b \rightarrow c$  transitions, such as  $B^- \rightarrow \Lambda_c^+ \bar{p}\pi^-$ , are not very interesting since the CP or T violation appearing in such tree decays is expected to be negligible.

To conclude on the results for  $\mathcal{A}_T$  and  $\mathcal{A}_T^{\text{CPV}}$ , this analysis is mainly a feasibility study to check the approach of using a triple product containing a spin vector compared to using momentum vectors only, repeating this analysis using the Run-I and Run-II data collected by LHCb during the next years seems unreasonable, as the available number of recorded  $B$  mesons will not increase by an order of magnitude and there has been no major revision of the  $V^0$  reconstruction before the start of Run-II. It will be interesting to see the  $V^0$  reconstruction efficiency of the BELLE2 experiment and the actual luminosity that will be achieved. Maybe the BELLE2 experiment will be more suited to doing this kind of analysis.

## 5.2 Observation of the Baryonic $B_s^0$ Decay $\bar{B}_s^0 \rightarrow \Lambda \bar{p} K^+$

The field of baryonic  $\bar{B}_s^0$  decays is still an unexplored field of study. For the  $\bar{B}^0$  and  $B^\pm$  mesons a number of baryonic decays have been observed. This is mainly due to the experimental constraints of the second generation  $B$  factories BABAR and BELLE operating at the  $\Upsilon(4S)$  resonance, which is not heavy enough to decay into  $B_s^0$  mesons. The BELLE experiment has a small sample of  $\Upsilon(5S)$  data. The  $\Upsilon(5S)$  resonance decays include  $B_s^0$  mesons. The BELLE collaboration has found evidence for a baryonic  $B_s^0$  decay [58] namely  $B_s^0 \rightarrow \bar{\Lambda}_c^- \Lambda \pi^+$ . A charmless

baryonic  $B_s^0$  decay has not been observed yet. The decays  $\bar{B}_s^0 \rightarrow \Lambda \bar{p} K^+$  and  $\bar{B}_s^0 \rightarrow \bar{\Lambda} p K^-$  are observed in this analysis with a significance of 17.2 Gaussian standard deviations.

At first glance the  $B_s^0$  decay  $\bar{B}_s^0 \rightarrow \Lambda \bar{p} K^+$  should be the analogue to  $\bar{B}^0 \rightarrow \Lambda \bar{p} \pi^+$  but as was shown in Sec. 1.2.2 this is not the case. There are several different amplitudes contributing with different strong phases and the expectation, that the only difference between the two decays was the spectator quark is invalidated. The difference between these two modes goes even further. Due to the  $s$  quark in the  $B_s^0$  meson in combination with an  $\bar{s}$  quark produced in either the penguin loop or the  $b \rightarrow u W^-$  decay it is possible to create either a  $\Lambda$  baryon or a  $\bar{\Lambda}$  antibaryon while the second  $\bar{s}$  or  $s$  quark is part of the kaon. This implies that both the  $B_s^0$  and the  $\bar{B}_s^0$  can decay into the identical final state  $\Lambda \bar{p} K$ . Such an effect does not occur for the  $\bar{B}^0 \rightarrow \Lambda \bar{p} \pi^+$  decay. In this analysis the flavour of the  $\bar{B}_s^0$  meson, *i.e.* whether it is a  $B_s^0$  or  $\bar{B}_s^0$ , was not tagged, but for future studies with enhanced statistics it should be possible to do a time dependent CP violation measurement. Since the weak phase difference of  $b \rightarrow s$  penguin decays interfering with  $b \rightarrow u$  tree amplitudes is given by the CKM angle  $\gamma$  a large direct CP violation could occur depending on the strong phase differences. But as for further studies for  $\mathcal{A}_T$  this will be difficult to achieve with the Run-I and Run-II data only. Typically the tagging efficiency at LHCb is about 7% which combined with the lower number of  $\bar{B}_s^0$  meson available and the low  $\Lambda$  reconstruction efficiency will severely limit the statistical precision. A time dependent measurement would be further diluted by the decay resolution. A time integrated measurement is an alternative but yields its own problems. The time dependent CP violation is separated into two terms, a sine term containing the mixing between the  $B_s^0$  and  $\bar{B}_s^0$  and a cosine term determined by the direct CP violation. The mixing is determined by the small angle  $\beta_s$ , therefore, the contribution of the sine term should be rather small and the asymmetry should be dominated by the cosine term. A time integrated measurement would integrate over the sine term and in case of a coherent initial state, the sine term would vanish. Unfortunately, the  $B_s^0$  and  $\bar{B}_s^0$  mesons at LHCb are not produced in a coherent state, thus a time integrated measurement will always measure the mixture of the sine and cosine term.

In contrast to the measurement of  $\mathcal{A}_T$  the time dependent CP asymmetry measurement is probably not feasible for the BELLE2 experiment. First, its main focus will be running at the  $\Upsilon(4S)$  resonance rather than the  $\Upsilon(5S)$  resonance and therefore the available statistics will be limited as well. Furthermore, the  $\Upsilon(5S)$  does not decay exclusively into a  $B_s^0$ - $\bar{B}_s^0$  pair further limiting the statistics at hand and the  $B_s^0$  and  $\bar{B}_s^0$  mesons are not necessarily in a coherent state, so a time integrated measurement will again measure both the sine and cosine term. In general, the tagging efficiency at the  $e^+e^-B$  factories was larger than it is at LHCb, but the performance of the new BELLE2 detector and the reconstruction software are yet unknown as well.

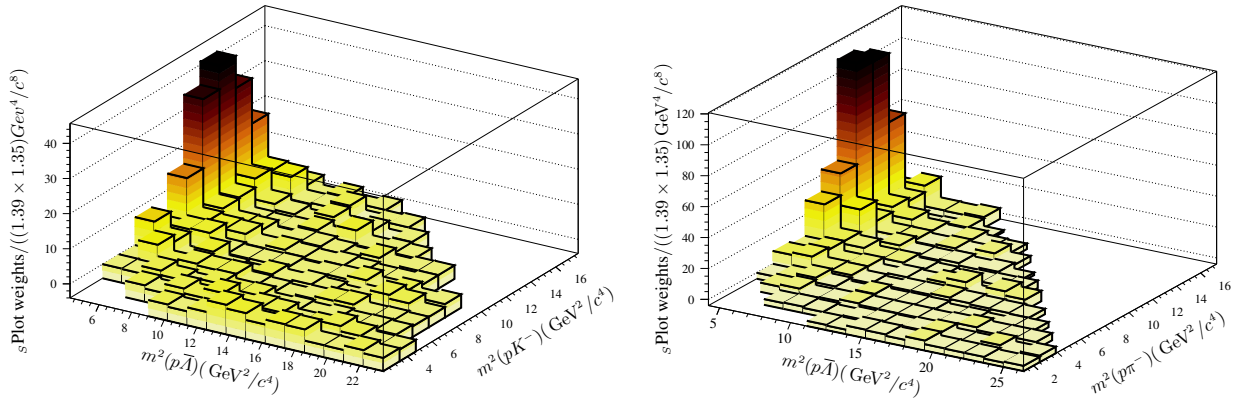


Figure 5.1: Dalitz plot for the  $\bar{B}_s^0 \rightarrow \Lambda \bar{p} K^+$  (left plot) and  $\bar{B}_s^0 \rightarrow \Lambda \bar{p} \pi^+$  (right plot) decay modes. The bin contents are given by the sum of the  $s$ Plot weights extracted from the fits to the  $m(\Lambda \bar{p} h)$  invariant mass for each data sample. The only structure visible is a pronounced enhancement at the  $m(p\Lambda)$  threshold.

Apart from the observation of these two  $\bar{B}_s^0$  decays the Dalitz plot has been studied, although a full amplitude



analysis is not feasible given the limited statistics, the structures become apparent. In Fig.5.1 the Dalitz plots for both the  $\bar{B}_s^0 \rightarrow \Lambda\bar{p}K^+$  and  $\bar{B}^0 \rightarrow \Lambda\bar{p}\pi^+$  are shown again. While the structures look similar there are slight differences. While the width of the enhancement with respect to the  $m^2(\Lambda\bar{p})$  invariant mass is similar, the  $\bar{B}_s^0 \rightarrow \Lambda\bar{p}K^+$  enhancement is broader with respect to the  $m^2(\bar{p}K^+)$  invariant mass compared to the  $\bar{B}^0 \rightarrow \Lambda\bar{p}\pi^+$  mode. The latter is almost exclusively limited to the upper left corner of the Dalitz plot indicating an asymmetry in the decay dynamics. Coming back to the Feynman diagrams and the fragmentation picture, the pronounced threshold enhancement in the  $m^2(\Lambda\bar{p})$  invariant mass favours the meson pole hypothesis. There are no structures visible in any baryon meson invariant mass combination disfavouring the baryon pole description of baryonic  $B$  decays.

Another advantage of having such a pronounced enhancement in both decay modes is a simplification of a CP asymmetry measurement. Three body decays usually necessitate a full amplitude analysis across the Dalitz plot in order to determine a CP asymmetry, because different regions of the Dalitz plot may show different interference effects between the CP eigenstates. The enhancement in  $\bar{B}_s^0 \rightarrow \Lambda\bar{p}K^+$  and  $\bar{B}^0 \rightarrow \Lambda\bar{p}\pi^+$  allows these decays to be treated as pseudo two body decays similar to decays such as  $B \rightarrow J/\psi K_s^0$ . The enhancement hereby takes the role of the  $J/\psi$ . Once the quantum numbers of the enhancement are determined, the CP asymmetry can be extracted without having to model the whole Dalitz plot. The BES collaboration observed an enhancement in  $J/\psi \rightarrow \gamma p\bar{p}$  and measured the quantum numbers of this resonance to be consistent with both  $J^{PC} = 0^{-+}$  and  $J^{PC} = 0^{++}$  [59]. A similar determination is beyond the scope of this analysis but once these numbers are known, the CP eigenvalues of the decays can be determined as well.

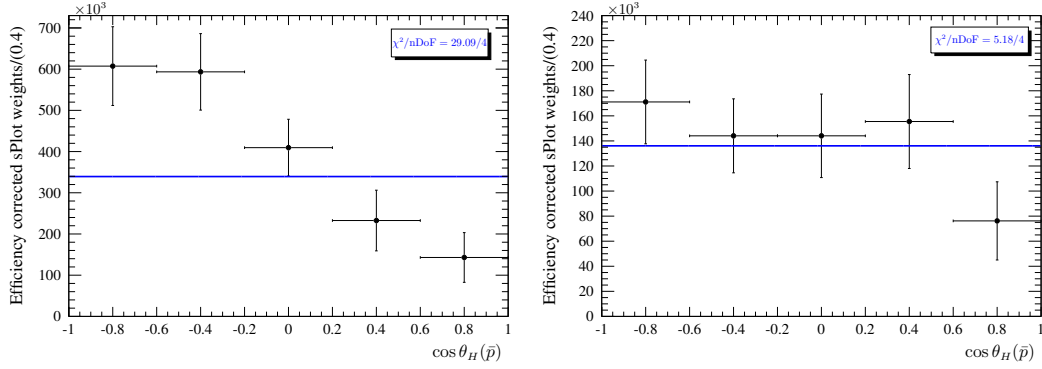


Figure 5.2: Distribution of the proton helicity angle for efficiency corrected and background subtracted  $\bar{B}^0 \rightarrow \Lambda\bar{p}\pi^+$  (left) and  $\bar{B}_s^0 \rightarrow \Lambda\bar{p}K^+$  (right) candidates for  $m^2(\Lambda\bar{p}) \in [(m_p + m_\Lambda)^2, 6.9](\text{GeV}/c^2)^2$ . Each distribution was fitted with a constant (blue curve) corresponding to the spin-0 hypothesis for the threshold enhancement. The  $\chi^2/\text{nDoF}$  is listed in the plots. The data disfavour the spin-0 hypothesis for the  $\bar{B}^0 \rightarrow \Lambda\bar{p}\pi^+$  mode, the  $\bar{B}_s^0 \rightarrow \Lambda\bar{p}K^+$  mode is compatible with the spin-0 hypothesis.

The angular quantum numbers of the threshold enhancement can be determined through the helicity angle  $\theta_H$  of one of its daughters. Here, the angle between the  $\bar{p}$  and the  $\bar{B}_{(s)}^0$  meson is calculated in the rest frame of the  $\Lambda\bar{p}$  system. In order to measure the angular distribution only for the enhancement region, the invariant  $m(\Lambda\bar{p})$  mass squared is restricted to  $m^2(\Lambda\bar{p}) \in [(m_p + m_\Lambda)^2, 6.9](\text{GeV}/c^2)^2$ . The  $s$ Plot weights determined in the extraction of the Dalitz plots are used here (*cf.* Sec. 4.1). It was shown, that the efficiency is not flat across the Dalitz plot and, therefore, not flat in the helicity angle as well. In a similar approach to the one described in Sec. 4.1 the efficiency is determined in five bins of the helicity angle and the  $s$ Plot weights are corrected with these efficiencies. In Fig. 5.2 the results for both the  $\bar{B}^0 \rightarrow \Lambda\bar{p}\pi^+$  (left) and  $\bar{B}_s^0 \rightarrow \Lambda\bar{p}K^+$  (right) can be found. The distribution for the proton helicity angle for  $\bar{B}^0 \rightarrow \Lambda\bar{p}\pi^+$  is compatible with the previous BELLE measurement shown in Fig. 5.3 and exhibits a strong asymmetry, which is not yet understood by theory [60]. Naively, one would expect the angular distribution for a pole to be flat, since the dominant poles have zero angular momentum. The proton helicity angle distribution was fit assuming a constant distribution and the  $\chi^2/\text{nDoF}$  is 29.09/4 indicating a bad fit. The asymmetry in the angular distribution for  $\bar{B}_s^0 \rightarrow \Lambda\bar{p}K^+$  is less pronounced and the a  $\chi^2/\text{nDoF}$  of 5.18/4 shows good a agreement with the hypothesis of no angular momentum.

Apart from measuring the angular quantum numbers for the threshold enhancement, the helicity analysis can be

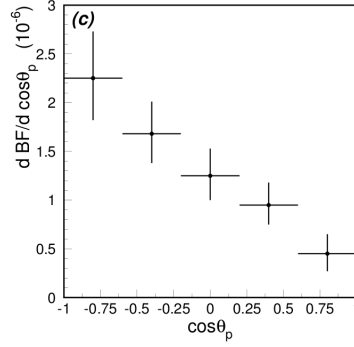


Figure 5.3: Distribution of the proton helicity angle over the differential branching fraction obtained by the BELLE collaboration [24].

applied to measure the polarisation of the  $\Lambda$  hyperon on the  $B_{(s)}^0$  decay. Here, the angular distribution for the proton from the  $\Lambda$  decay is measured with respect to the  $\bar{B}^0$  or, alternatively, the  $\Lambda \bar{p}$  system each determined in the  $\Lambda$  rest frame. The angular distribution for the proton is given by

$$I(\theta) = 1 + \alpha P \cos \theta \quad , \quad (5.9)$$

which is similar to the distribution employed to determine the T reversal asymmetry, the difference being, rather than measuring the spin of a single  $\Lambda$ , the statistical average is analysed. The polarisation  $P$  is an indication, how often the  $\Lambda$  spins have similar orientations. For fully polarised  $\Lambda$  baryons,  $P = 1$ , all spins have the same orientation in space, for unpolarised  $\Lambda$  hyperons,  $P = 0$ , the spins are distributed uniformly canceling each other. The  $\cos \theta_H$  distributions for the  $\Lambda$  proton can be found in Fig. 5.4, on the left side for the  $\bar{B}^0 \rightarrow \Lambda \bar{p} \pi^+$  mode and on the right hand side for  $\bar{B}_s^0 \rightarrow \Lambda \bar{p} K^+$ . The black (blue) data points show the  $\cos \theta_H$  distribution calculated with respect to the  $\Lambda \bar{p}$  ( $\bar{B}^0$ ) system. The polarisation is determined by a  $\chi^2$  fit to the  $\cos \theta_H$ . Within the uncertainties the  $\Lambda$  polarisation is identical with respect to both systems of reference, the fit results are given in Tab.5.1. In order to improve the statistical sensitivity the polarisation is determined averaging over  $\Lambda$  and  $\bar{\Lambda}$  assuming equal polarisation by measuring  $\alpha P$  instead of  $P$ . In the  $\bar{B}^0 \rightarrow \Lambda \bar{p} \pi^+$  decay, the  $\Lambda$  baryons are partly polarised whereas the  $\Lambda$  hyperons are unpolarised in the  $\bar{B}_s^0 \rightarrow \Lambda \bar{p} K^+$  decay.

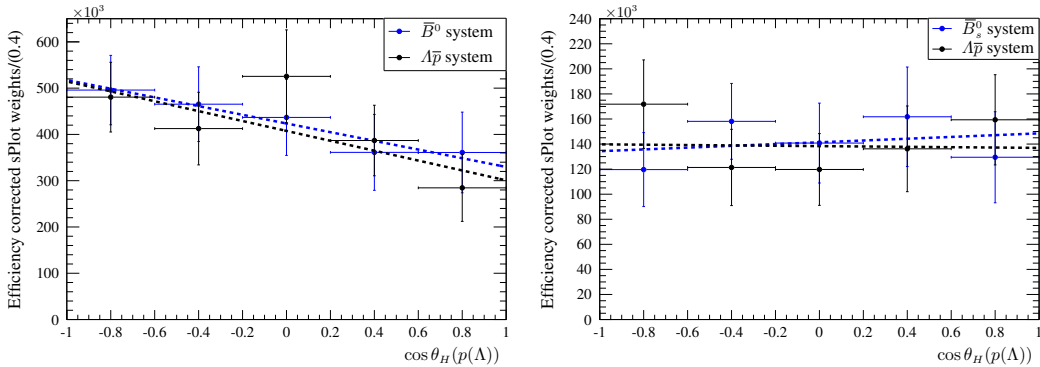


Figure 5.4: Distribution of the proton helicity angle for the proton from the  $\Lambda$  with respect to the  $\Lambda \bar{p}$  system (black data points) and the  $\Lambda \bar{p} \pi$  system (blue data points) for efficiency corrected and background subtracted data for the  $\bar{B}^0 \rightarrow \Lambda \bar{p} \pi^+$  (left) and  $\bar{B}_s^0 \rightarrow \Lambda \bar{p} K^+$  (right) candidates for  $m^2(\Lambda \bar{p}) \in [(m_p + m_\Lambda)^2, 6.9](\text{GeV}/c^2)^2$ . The fit function for the  $\Lambda$  polarity is indicated by the dashed lines coloured according to the system of reference.

The polarisation of the  $\Lambda$  baryons can help understanding the underlying structure of these baryonic  $\bar{B}_{(s)}^0$  decays. The  $\Lambda$  baryons are bound states of three quarks in an  $s$  wave state, the  $u$  and  $d$  quark forming a spin singlet.

Table 5.1: Fit results for the polarisation fit for the  $\bar{B}^0 \rightarrow \Lambda \bar{p} \pi^+$  and  $\bar{B}_s^0 \rightarrow \Lambda \bar{p} K^+$  decays for both axis of reference, the  $\Lambda$ -antiproton system and the  $\bar{B}_{(s)}^0$  system, respectively.

Axis of reference	$\alpha P(\bar{B}^0 \rightarrow \Lambda \bar{p} \pi^+)$	$\alpha P(\bar{B}_s^0 \rightarrow \Lambda \bar{p} K^+)$
$\Lambda\text{-}\bar{p}$	$-0.26 \pm 0.15$	$-0.01 \pm 0.20$
$\bar{B}_{(s)}^0$	$-0.22 \pm 0.15$	$0.05 \pm 0.19$

Therefore, the  $\Lambda$  spin is entirely given by the  $s$  quark spin in the static quark model. After a boost into a moving frame of reference, the  $\Lambda$  helicity is determined by the  $s$  quark helicity. Measuring the handedness of the  $\Lambda$  allows to determine the chirality of the  $s$  quark in the weak interaction.

In the  $\bar{B}^0 \rightarrow \Lambda \bar{p} \pi^+$  decay, the  $s$  quark can be produced either in the  $b \rightarrow s$  penguin or through a  $W$  boson in the  $b \rightarrow u$  amplitude. In the first case, the  $s$  quark carries over the momentum of the decaying  $b$  quark and is, therefore, dominant left handed. In the fragmentation of the  $\Lambda$  baryon, the  $s$  is the leading quark, therefore, the  $\Lambda$  baryons should be polarised. In case of a  $b \rightarrow u$  tree amplitude, the momentum of the  $s$  quark is small compared to the  $b$  quark and thus not dominant left handed. As a result, the  $\Lambda$  should be less polarised in comparison. Applying these thoughts to the decays at hand, the  $\bar{B}_s^0 \rightarrow \Lambda \bar{p} K^+$  and  $\bar{B}_s^0 \rightarrow \bar{\Lambda} p K^-$  decays should be dominated by the  $b \rightarrow u$  tree and  $W$  exchange diagrams. The  $\bar{B}^0 \rightarrow \Lambda \bar{p} \pi^+$  decay mode should have mixed contributions from the penguin and tree decay amplitudes.

The chirality argument should lead to a dependence of the  $\Lambda$  polarisation on the  $\Lambda$  energy in the  $\bar{B}^0$  rest frame. For large  $\Lambda$  energies the  $\Lambda$  should be highly polarised due to the  $s$  quark chirality [61]. In case the  $s$  quark has a large boost in the  $b$  rest frame it is predominant left handed, therefore, the  $\Lambda$  polarisation is large. For small boosts the polarisation should vanish. In Fig. 5.5 the dependence of the  $\Lambda$  polarisation on the  $\Lambda$  energy in the  $\bar{B}^0$  rest frame is shown for a previous *BABAR* measurement [25], this analysis, and the theoretical prediction [61]. The results agree well with the theoretical prediction, but cannot exclude the hypothesis of unpolarised  $\Lambda$  hyperons due to the large uncertainties.

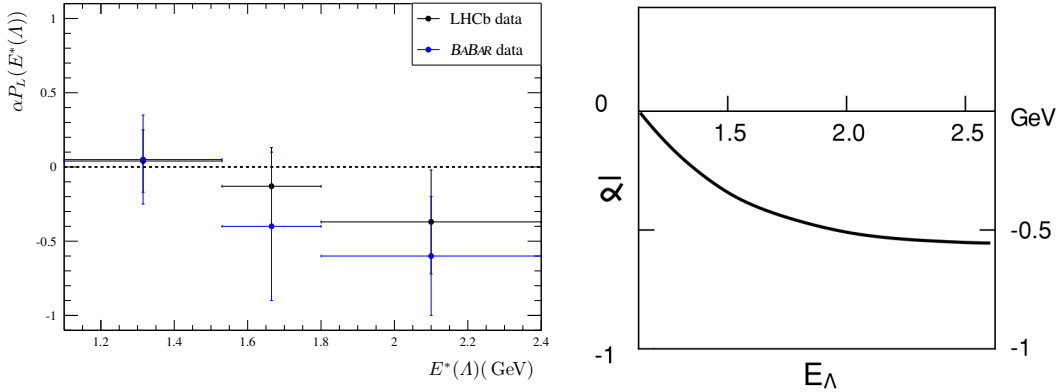


Figure 5.5: Distribution of  $\alpha P$  as a function of  $\Lambda$  energy in the  $\bar{B}^0$  rest frame. The left plot shows the LHCb data in black and the *BABAR* results in blue [25]. The predicted relation for  $\alpha P(E^*(\Lambda))$  is shown on the right hand side [61].

To conclude this section, one can learn a lot about the decay dynamics of baryonic  $B$  decays by studying the various angular distributions. In order to receive conclusive measurements, the statistical uncertainty needs to be reduced. This makes this an interesting field of study for the upcoming *BELLE2* experiment and future runs of the LHC. Concerning LHCb, however, improvements to the  $\Lambda$  detection efficiency are necessary to allow conclusive measurements.

# List of Figures

1.1	Feynman diagrams for the Standard Model process $b \rightarrow su\bar{u}$ and the diagrams in the reduced theory assuming $q^2 \ll m_W^2$ . The subscript $L$ denotes, that the vector currents are left-handed following the Fermi theory of the weak interaction. The Operators $\mathcal{O}_i$ denote the interactions in the effective low energy regime. . . . .	7
1.2	Leading order diagrams for the $\bar{B}^0 \rightarrow \Lambda\bar{p}\pi^+$ decay. Gluon lines are omitted. The amplitudes are proportional to $V_{ub}V_{us}^*$ (a,b,c,d) and $V_{tb}V_{ts}^*$ (e,f). . . . .	8
1.3	Leading order diagrams for the $\bar{B}_s^0 \rightarrow \Lambda\bar{p}K^+$ decay. Gluon lines are omitted. The amplitudes are proportional to $V_{ub}V_{us}^*$ (a,b,d,e) and $V_{tb}V_{ts}^*$ (c). . . . .	9
1.4	Leading order diagrams for the $\bar{B}_s^0 \rightarrow \bar{\Lambda}pK^-$ decay. Gluon lines are omitted. The amplitudes are proportional to $V_{ub}V_{us}^*$ (a,b,d,e) and $V_{tb}V_{ts}^*$ (c). . . . .	10
1.5	Dependence of the branching fraction for $\bar{B}^0 \rightarrow \Lambda\bar{p}\pi^+$ and $\bar{B}^0 \rightarrow \Sigma^0\bar{p}\pi^+$ on the invariant baryon antibaryon mass. The left plot shows the prediction from [16] for different number of colours, The dashed, solid, and dot-dashed lines correspond to $N_c = 2, 3, \infty$ , respectively. The right plot shows two extreme cases for the dependence calculated in [23] overlaid with the BELLE data from [22]. . . . .	11
1.6	Decay of a $b$ quark into a $u$ quark by emission of a $W$ boson (a), and the time reversed process (b). The diagram in (c) shows the $b \rightarrow s$ penguin decay and (d) its time reversed process. . . . .	12
1.7	Dependence of the branching fraction for $\bar{B}^0 \rightarrow \Lambda\bar{p}\pi^+$ and $\bar{B}^0 \rightarrow \Sigma^0\bar{p}\pi^+$ on the CKM angle $\gamma$ , here noted as $\phi_3$ [16]. The current value of $\gamma$ is $\gamma = 73.2_{-7.0}^{+6.3^\circ}$ [7]. The notation is the same as in Fig. 1.5. . . . .	13
1.8	Illustration of the $\Lambda$ rest frame, $\sigma$ being the $\Lambda$ spin $p$ the proton momentum. . . . .	15
1.9	Shape of the kinematically allowed Dalitz plot for the $\bar{B}^0 \rightarrow \Lambda\bar{p}\pi^+$ decay. The edges of the Dalitz plot are determined by the $B$ mass and the individual daughter masses. . . . .	16
2.1	Layout of the LHC accelerator complex. The layout shows the four major experiments. The energy of the protons is ramped up through several smaller accelerators. Additional experiments also receive their protons from these. . . . .	18
2.2	(a) Distribution of the average number of visible interactions (top) and the instantaneous luminosity over Run I at the LHCb interaction point. The dotted lines show the design values. (b) Integrated luminosity of the LHCb experiment taken during the Run I of the LHC. . . . .	18
2.3	Schematic representation of the LHCb detector. The coordinate system is indicated. . . . .	19
2.5	Layout of the two VELO halves and the individual modules in the $x$ - $z$ plane [31]. . . . .	20
2.4	Layout of the VELO modules in the $x$ - $y$ plane in the closed state [33]. . . . .	20

2.6	The VELO hit resolution as a function of the pitch between the silicon strips for the R sensors. Results are shown for two angle ranges and a single-hit binary system [32]. . . . .	21
2.7	Layout of the planar tracking stations (left). Arrangement of the IT around the beam pipe covering the more active central region [31]. . . . .	21
2.8	Drift-time distribution for the modules closest to the beam for three different bunch crossing rates (left). Drift time versus distance (right). The dotted lines indicate the centre and the edge of the wire, corresponding to a drift-time of 0 ns and 36 ns, respectively [31]. . . . .	22
2.9	Layout of the RICH detectors, on the left hand side the RICH1 and on the right hand side the RICH2 [31]. . . . .	23
2.10	Lateral segmentation for the SPD, PS, and ECAL (left) and the HCAL (right). A quarter of the detector front face is shown and the dimensions are given for the ECAL and HCAL [31]. . . . .	23
2.11	Layout of the muon system [31]. . . . .	24
2.12	Layout of the LHCb magnet (left); $z$ dependence of the magnetic field (right) [31]. . . . .	25
2.13	Illustration of the various track types, the $z$ coordinate position is also indicated [32]. . . . .	25
2.14	Mass (left) and momentum (right) resolution for $J/\psi \rightarrow \mu^+ \mu^-$ decays. The momentum resolution is about 5% for momenta below 20 GeV/ $c$ and about 8% for momenta about 100 GeV/ $c$ . . . . .	27
2.15	Reconstructed Cherenkov angle for isolated tracks as a function of the track momentum for the $C_4F_{10}$ radiator [32]. . . . .	28
2.16	Dalitz plot for the $\bar{B}^0 \rightarrow \Lambda \bar{p} \pi^+$ decay mode assuming a constant matrix element across the Dalitz plane before the application of the DecProdCut. . . . .	32
3.1	Distribution of $m(\Lambda \pi^+ \pi^-)$ (left) using the $\pi$ mass hypothesis and using the correct mass hypotheses (right) for the $\bar{B}^0 \rightarrow \Lambda \bar{p} \pi^+$ (black data points) and $B_s^0 \rightarrow \Lambda \bar{p} K^+$ (blue data points) modes. The data shown in both plots are simulated events only. . . . .	39
3.2	Correlations among the MVA input variables for the 2012 LL signal (top) and background (bottom) sample. . . . .	42
3.3	Exemplary network layout similar to the one used in the analysis [51]. . . . .	43
3.4	Comparison between the log IP( $\Lambda$ ) before (left) and after (right) the uniform transformation. The blue histogram represent the signal sample and the red histogram the background sample. . . . .	44
3.5	ROC curve (left) and comparison between the test and training sample (right) obtained for, from top to bottom, the 2011 LL, 2011 DD, 2012 LL, and 2012 DD data samples. . . . .	45
3.6	Comparison between the MVA-response for the two 2012 periods for LL (left) and the DD (right) sample. The red (black) histogram represent the pre-(post-)June trigger conditions. . . . .	46
3.7	Distribution of the invariant $m(\Lambda \bar{p} \pi)$ mass for the LL (left) and DD (right) sample for 2011 (top) and 2012 (bottom) after applying a loose MLP and proton PID selection as indicated in the text. The distributions are fitted with a Novosibirsk function and an exponential function. The signal and background yields are listed in the plots. . . . .	47
3.8	Figure of merit distributions for the LL (left) and DD selectors for 2011 (top) and 2012 (bottom). The selection cuts are indicated in the figures by the vertical lines. . . . .	47
3.9	Distributions of the signal significance for a given proton PID selection. The left (right) plot shows the LL (DD) sample selection significance. . . . .	48

- 3.10 Distribution of  $m(\Lambda\pi^+)$  in  $\bar{B}^0 \rightarrow \Lambda\bar{p}\pi^+$  for (left) the LL and (right) DD samples after the stripping for the 2012 data set. The signal is described by a Gaussian distribution and the background by an exponential function. Candidates within  $3\sigma$  around the Gaussian mean value  $\mu$  are rejected. . . . . 49
- 3.11 Distribution of  $m(\Lambda K^+)$  for the  $B_s^0 \rightarrow \Lambda\bar{p}K^+$  mode after the stripping before (top) and after (bottom) the kaon PID selection described in sec. 3.1.7 for the LL (left) and DD (right) sample. The datasets are each fitted with the sum of a Gaussian and an exponential; the parameters are listed in the plots. The bachelor PID selection removes  $\Lambda_c^+ \rightarrow \Lambda\pi^+$  candidates. . . . . 50
- 3.12 Distribution of  $m(\Lambda K^+)$  for  $B_s^0 \rightarrow \Lambda\bar{p}K^+$  candidates for the LL (left) and DD (right) samples after the stripping for the 2012 data set. The signal is described by a Gaussian distribution and the background by an exponential function. Candidates within  $3\sigma$  around the Gaussian mean value  $\mu$  of the DD fit are rejected. The DD veto is also applied to the LL sample. . . . . 51
- 3.13 Comparison between  $\bar{B}^0 \rightarrow \Lambda\bar{p}\pi^+$  (black data points),  $\bar{B}_s^0 \rightarrow \Lambda\bar{p}K^+$  (red up triangles), and  $\Lambda_b^0 \rightarrow \Lambda p\bar{p}$  (green down triangles) MC simulated data reconstructed with the  $\pi$  mass hypothesis (left) and kaon hypothesis (right) for the (DD) 2012b sample. The integral of the histograms is scaled according to Table 2.1. The full selection has been applied to all samples. . . . . 52
- 3.14 Comparison between  $\bar{B}^0 \rightarrow \Lambda\bar{p}\pi^+$  (black data points),  $\bar{B}_s^0 \rightarrow \Lambda\bar{p}K^+$  (red up triangles),  $\bar{B}^0 \rightarrow \Sigma^0\bar{p}\pi^+$  (steel-grey down triangles), and  $\bar{B}_s^0 \rightarrow \Sigma^0\bar{p}K^+$  (blue up triangles) MC simulated data reconstructed with the  $\pi$  mass hypothesis (left) and kaon hypothesis (right) for the (DD) 2012b sample. The integral of the histograms is scaled according to Table 2.1. The full selection has been applied to all samples. . . . . 53
- 3.15 Comparison between  $\bar{B}^0 \rightarrow \Lambda\bar{p}\pi^+$  (black data points),  $\bar{B}_s^0 \rightarrow \Lambda\bar{p}K^+$  (red up triangles),  $\bar{B}^0 \rightarrow \Lambda\bar{p}\rho^+$  (khaki diamonds), and  $\bar{B}_s^0 \rightarrow \Lambda\bar{p}K^{*+}$  (magenta squares) MC simulated data reconstructed with the  $\pi$  mass hypothesis (left) and kaon hypothesis (right) for the (DD) 2012b sample. The integral of the histograms is scaled according to Table 2.1. The full selection has been applied to all samples. . . . . 53
- 3.16 Armenteros-Podolanski plot for  $K_s^0$  and  $\Lambda$  candidates using minimum bias events from the 2012 data set. . . . . 54
- 3.17 Armenteros-Podolanski plot for the  $\Lambda$  candidates after applying the selection as described in Sec. 3.1. There are no  $K_s^0$  present in the sample. . . . . 54
- 3.18 Plot of the invariant  $\Lambda\bar{p}\pi$  mass showing the expected background contributions as a stacked histogram with respect to the  $\bar{B}_s^0 \rightarrow \Lambda\bar{p}K^+$  mode. The left (right) plot shows the LL (DD) sample. . . . . 55
- 3.19 Plot of the invariant  $\Lambda\bar{p}K$  mass showing the expected background contributions as a stacked histogram with respect to the  $\bar{B}_s^0 \rightarrow \Lambda\bar{p}K^+$  mode. The left (right) plot shows the LL (DD) sample. . . . . 55
- 3.20 Background subtracted distribution of the invariant  $\Lambda\bar{p}$  mass for  $\bar{B}^0 \rightarrow \Lambda\bar{p}\pi^+$  candidates obtained by the BABAR collaboration [25]. . . . . 58
- 3.21 Plot of the efficiency as function of the two Dalitz plot variables  $\varepsilon(m^2(\Lambda\bar{p}), m^2(\bar{p}h^+))$  for the  $\bar{B}^0 \rightarrow \Lambda\bar{p}\pi^+$  mode in 2012b DD. . . . . 58
- 3.22 Fit model for the  $\bar{B}^0 \rightarrow \Lambda\bar{p}\pi^+$  signal mode, reconstructed with the pion hypothesis (left) and with the kaon hypothesis (right) for the LL sample (top) and the DD sample (bottom). . . . . 64
- 3.23 Fit model for the  $B_s^0 \rightarrow \Lambda\bar{p}K^+$  signal mode, reconstructed with the pion hypothesis (left) and with the kaon hypothesis (right) for the LL sample (top) and the DD sample (bottom). . . . . 65
- 3.24 Fit model for the mode  $\bar{B}^0 \rightarrow \Sigma^0\bar{p}\pi^+$ , reconstructed with the pion hypothesis (left) and with the kaon hypothesis (right) for the LL sample (top) and the DD sample (bottom). . . . . 66
- 3.25 Fit model for the mode  $\bar{B}_s^0 \rightarrow \Sigma^0\bar{p}K^+$ , reconstructed with the pion hypothesis (left) and with the kaon hypothesis (right) for the LL sample (top) and the DD sample (bottom). . . . . 67

- 4.1 Dalitz plot for the  $\bar{B}^0 \rightarrow \Lambda\bar{p}\pi^+$  and  $\bar{B}_s^0 \rightarrow \Lambda\bar{p}K^+$  decay modes. The bin contents are given by the sum of the  $s$ Plot weights extracted from the fits to the  $m(\Lambda\bar{p}h)$  invariant mass for each data sample. The only structure visible is a pronounced enhancement at the  $m(\Lambda\bar{p})$  threshold. There are no hints for additional resonances in the  $m(\bar{p}h^+)$  or  $m(\Lambda h^+)$  invariant masses. . . . . 72
- 4.2 Results for global fit using the Dalitz plot corrected average efficiencies. The black points represent the data in the individual sample indicated in the plots. The  $\bar{B}^0 \rightarrow \Lambda\bar{p}\pi^+$  contribution is shown in blue,  $\bar{B}_s^0 \rightarrow \Lambda\bar{p}K^+$  in grey,  $\bar{B}^0 \rightarrow \Sigma^0\bar{p}\pi^+$  in green, and  $\bar{B}_s^0 \rightarrow \Sigma^0\bar{p}K^+$  in brown. The sum of all components is shown in black. . . . . 76
- 4.3 Results for global fit for  $m^2(\Lambda\bar{p}) < 12.3(\text{GeV}/c^2)^2$  using the Dalitz plot corrected average efficiencies. The black points represent the data in the individual sample indicated in the plots. The  $\bar{B}^0 \rightarrow \Lambda\bar{p}\pi^+$  contribution is shown in blue,  $\bar{B}_s^0 \rightarrow \Lambda\bar{p}K^+$  in grey,  $\bar{B}^0 \rightarrow \Sigma^0\bar{p}\pi^+$  in green, and  $\bar{B}_s^0 \rightarrow \Sigma^0\bar{p}K^+$  in brown. The sum of all components is shown in black. . . . . 77
- 4.4 Illustration of the triple product employed to determine the time reversal violation in the  $\bar{B}^0 \rightarrow \Lambda\bar{p}\pi^+$  decay (a) and distribution of the triple product for simulated  $\bar{B}^0 \rightarrow \Lambda\bar{p}\pi^+$  decays before the reconstruction (b). . . . . 81
- 4.9 Distribution of Pulls for the Time reversal asymmetry measurement for a thousand toy experiments using the results for the nominal fit. The plot in the left hand side shows the Pull plot for  $\mathcal{A}_T$  and on the right hand side the `PULL` plot for  $\mathcal{A}_T$  is shown. Both distribution agree with a standard normal distribution within the statistical uncertainty, hence no bias is detected. . . . . 83
- 4.5 Fit results for the full asymmetry fit for the  $\mathcal{O} > 0$  and  $\bar{B}^0 \rightarrow \Lambda\bar{p}\pi^+$  samples. The graphical representation is identical to Fig. 4.3. The samples are denoted in the plots. . . . . 84
- 4.6 Fit results for the full asymmetry fit for the  $\mathcal{O} < 0$  and  $\bar{B}^0 \rightarrow \Lambda\bar{p}\pi^+$  samples. The graphical representation is identical to Fig. 4.3. The samples are denoted in the plots. . . . . 85
- 4.7 Fit results for the full asymmetry fit for the  $\mathcal{O} > 0$  and  $B^0 \rightarrow \bar{\Lambda}p\pi^-$  samples. The graphical representation is identical to Fig. 4.3. The samples are denoted in the plots. . . . . 86
- 4.8 Fit results for the full asymmetry fit for the  $\mathcal{O} < 0$  and  $B^0 \rightarrow \bar{\Lambda}p\pi^-$  samples. The graphical representation is identical to Fig. 4.3. The samples are denoted in the plots. . . . . 87
- 4.10 Comparison between the MVA response for simulated signal candidates (red data points) and background subtracted candidates in recorded data (black data points). The background subtraction is performed using the  $s$ Plot technique. The histograms are scaled to have the same integral. The top (bottom) row shows the plots for the 2011 (2012) samples, the LL (DD) sample on the left (right) hand side. Except for the 2011 DD sample the agreement is good. . . . . 89
- 4.11 Pull distribution for ratio between the  $\bar{B}^0 \rightarrow \Lambda\bar{p}\pi^+$  and  $\bar{B}_s^0 \rightarrow \Lambda\bar{p}K^+$  branching fraction for one thousand toy experiments using the nominal fit results. . . . . 91
- 5.1 Dalitz plot for the  $\bar{B}_s^0 \rightarrow \Lambda\bar{p}K^+$  (left plot) and  $\bar{B}^0 \rightarrow \Lambda\bar{p}\pi^+$  (right plot) decay modes. The bin contents are given by the sum of the  $s$ Plot weights extracted from the fits to the  $m(\Lambda\bar{p}h)$  invariant mass for each data sample. The only structure visible is a pronounced enhancement at the  $m(p\bar{\Lambda})$  threshold. . . . . 97
- 5.2 Distribution of the proton helicity angle for efficiency corrected and background subtracted  $\bar{B}^0 \rightarrow \Lambda\bar{p}\pi^+$  (left) and  $\bar{B}_s^0 \rightarrow \Lambda\bar{p}K^+$  (right) candidates for  $m^2(\Lambda\bar{p}) \in [(m_p + m_\Lambda)^2, 6.9](\text{GeV}/c^2)^2$ . Each distribution was fitted with a constant (blue curve) corresponding to the spin-0 hypothesis for the threshold enhancement. The  $\chi^2/\text{nDoF}$  is listed in the plots. The data disfavour the spin-0 hypothesis for the  $\bar{B}^0 \rightarrow \Lambda\bar{p}\pi^+$  mode, the  $\bar{B}_s^0 \rightarrow \Lambda\bar{p}K^+$  mode is compatible with the spin-0 hypothesis. . . . . 98

5.3	Distribution of the proton helicity angle over the differential branching fraction obtained by the BELLE collaboration [24]. . . . .	99
5.4	Distribution of the proton helicity angle for the proton from the $\Lambda$ with respect to the $\Lambda\bar{p}$ system (black data points) and the $\Lambda\bar{p}\pi$ system (blue data points) for efficiency corrected and background subtracted data for the $\bar{B}^0 \rightarrow \Lambda\bar{p}\pi^+$ (left) and $\bar{B}_s^0 \rightarrow \Lambda\bar{p}K^+$ (right) candidates for $m^2(\Lambda\bar{p}) \in [(m_p + m_\Lambda)^2, 6.9](\text{GeV}/c^2)^2$ . The fit function for the $\Lambda$ polarity is indicated by the dashed lines coloured according to the system of reference. . . . .	99
5.5	Distribution of $\alpha P$ as a function of $\Lambda$ energy in the $\bar{B}^0$ rest frame. The left plot shows the LHCb data in black and the BABAR results in blue [25]. The predicted relation for $\alpha P(E^*(\Lambda))$ is shown on the right hand side [61]. . . . .	100
B.1	Input variables for the training for the 2011 period for the LL sample. The blue data points are signal, the red data points background. . . . .	112
B.2	Input variables for the training for the 2011 period for the LL sample. The blue data points are signal, the red data points background. . . . .	113
B.3	Input variables for the training for the 2011 period for the LL sample. The blue data points are signal, the red data points background. . . . .	114
B.4	Input variables and output of the training for the 2011 period for the LL sample. The blue data points are signal, the red data points background. . . . .	115
B.5	Input variables for the training for the 2011 period for the DD sample. The blue data points are signal, the red data points background. . . . .	116
B.6	Input variables for the training for the 2011 period for the DD sample. The blue data points are signal, the red data points background. . . . .	117
B.7	Input variables for the training for the 2011 period for the DD sample. The blue data points are signal, the red data points background. . . . .	118
B.8	Input variables and output of the training for the 2011 period for the DD sample. The blue data points are signal, the red data points background. . . . .	119
B.9	Input variables for the training for the 2012 period for the LL sample. The blue data points are signal, the red data points background. . . . .	120
B.10	Input variables for the training for the 2012 period for the LL sample. The blue data points are signal, the red data points background. . . . .	121
B.11	Input variables for the training for the 2012 period for the LL sample. The blue data points are signal, the red data points background. . . . .	122
B.12	Input variables and output of the training for the 2012 period for the LL sample. The blue data points are signal, the red data points background. . . . .	123
B.13	Input variables for the training for the 2012 period for the DD sample. The blue data points are signal, the red data points background. . . . .	124
B.14	Input variables for the training for the 2012 period for the DD sample. The blue data points are signal, the red data points background. . . . .	125
B.15	Input variables for the training for the 2012 period for the DD sample. The blue data points are signal, the red data points background. . . . .	126
B.16	Input variables and output of the training for the 2012 period for the DD sample. The blue data points are signal, the red data points background. . . . .	127



C.1	MVA input variables for the two 2012 data-taking periods for the LL sample – set 1. The red (black) points represent the pre-(post-)June trigger conditions. . . . .	130
C.2	MVA input variables for the two 2012 data-taking periods for the LL sample – set 2. The red (black) points represent the pre-(post-)June trigger conditions. . . . .	131
C.3	MVA input variables for the two 2012 data-taking periods for the LL sample – set 3. The red (black) points represent the pre-(post-)June trigger conditions. . . . .	132
C.4	MVA input variables for the two 2012 data-taking periods for the LL sample – set 4. The red (black) points represent the pre-(post-)June trigger conditions. . . . .	133
C.5	MVA input variables for the two 2012 data-taking periods for the DD sample – set 1. The red (black) points represent the pre-(post-)June trigger conditions. . . . .	134
C.6	MVA input variables for the two 2012 data-taking periods for the DD sample – set 2. The red (black) points represent the pre-(post-)June trigger conditions. . . . .	135
C.7	MVA input variables for the two 2012 data-taking periods for the DD sample – set 3. The red (black) points represent the pre-(post-)June trigger conditions. . . . .	136
C.8	MVA input variables for the two 2012 data-taking periods for the DD sample – set 4. The red (black) points represent the pre-(post-)June trigger conditions. . . . .	137
E.1	Correlations between the input variables for the 2011 LL signal sample. . . . .	141
E.2	Correlations between the input variables for the 2011 LL background sample. . . . .	142
E.3	Correlations between the input variables for the 2011 DD signal sample. . . . .	142
E.4	Correlations between the input variables for the 2011 DD background sample. . . . .	143
E.5	Correlations between the input variables for the 2012 DD signal sample. . . . .	143
E.6	Correlations between the input variables for the 2012 DD background sample. . . . .	144
F.1	Plot of the efficiency as function of the two Dalitz plot variables $\varepsilon(m^2(\Lambda\bar{p}), m^2(\bar{p}h^+))$ for the $\bar{B}^0 \rightarrow \Lambda\bar{p}\pi^+$ mode in 2011 LL (left) and DD(right). . . . .	150
F.2	Plot of the efficiency as function of the two Dalitz plot variables $\varepsilon(m^2(\Lambda\bar{p}), m^2(\bar{p}h^+))$ for the $\bar{B}^0 \rightarrow \Lambda\bar{p}\pi^+$ mode in 2012a LL (left) and DD(right). . . . .	151
F.3	Plot of the efficiency as function of the two Dalitz plot variables $\varepsilon(m^2(\Lambda\bar{p}), m^2(\bar{p}h^+))$ for the $\bar{B}^0 \rightarrow \Lambda\bar{p}\pi^+$ mode in 2012b LL (left) and DD(right). . . . .	151
F.4	Plot of the efficiency as function of the two Dalitz plot variables $\varepsilon(m^2(\Lambda\bar{p}), m^2(\bar{p}h^+))$ for the $\bar{B}_s^0 \rightarrow \Lambda\bar{p}K^+$ mode in 2011 LL (left) and DD(right). . . . .	151
F.5	Plot of the efficiency as function of the two Dalitz plot variables $\varepsilon(m^2(\Lambda\bar{p}), m^2(\bar{p}h^+))$ for the $\bar{B}_s^0 \rightarrow \Lambda\bar{p}K^+$ mode in 2012a LL (left) and DD(right). . . . .	152
F.6	Plot of the efficiency as function of the two Dalitz plot variables $\varepsilon(m^2(\Lambda\bar{p}), m^2(\bar{p}h^+))$ for the $\bar{B}_s^0 \rightarrow \Lambda\bar{p}K^+$ mode in 2012b LL (left) and DD(right). . . . .	152

# Appendices



# Appendix A

## Study of Trigger Lines

It is interesting to study the contribution to the overall trigger efficiencies coming from the individual lines at all trigger levels. Such a study is here performed for the standard lines typically employed as trigger requirements on hadronic  $B$  decays.

The tables below show the various contributions separately for LL and DD samples of the  $\bar{B}^0 \rightarrow A\bar{p}\pi^+$  signal decay mode. Very similar numbers are obtained for the  $B_s^0 \rightarrow A\bar{p}K^+$  mode; they are not shown as they are redundant.

As explained in Sec. 3.1.1, the `BodySimple` trigger lines are only used in the 2011 data selection. They are hence omitted in the studies on the 2012b sample. The results are the following for the 2012b LL and DD samples, respectively:

```
=====
eff_{L0/strip}          = ( 44.97 +/- 0.39 ) %    ( 12985 out of 28874 )
                        L0HadronTos = ( 24.51 +/- 0.29 ) %    ( 7078 out of 28874 )
                        L0GlobalTis = ( 29.07 +/- 0.32 ) %    ( 8393 out of 28874 )
-----
eff_{HLT1/L0}          = ( 73.62 +/- 0.75 ) %    ( 9560 out of 12985 )
                        Hlt1TrackAllL0Tos = ( 73.62 +/- 0.75 ) %    ( 9560 out of 12985 )
-----
eff_{HLT2/HLT1}       = ( 69.75 +/- 0.85 ) %    ( 6668 out of 9560 )
                        Hlt2Topo2BodyBBDTTos = ( 61.23 +/- 0.80 ) %    ( 5854 out of 9560 )
                        Hlt2Topo3BodyBBDTTos = ( 50.59 +/- 0.73 ) %    ( 4836 out of 9560 )
                        Hlt2Topo4BodyBBDTTos = ( 15.84 +/- 0.41 ) %    ( 1514 out of 9560 )
=====
eff_{trig/strip}      = ( 23.09 +/- 0.28 ) %    ( 6668 out of 28874 )
=====

=====
eff_{L0/strip}          = ( 45.59 +/- 0.20 ) %    ( 50912 out of 111681 )
                        L0HadronTos = ( 27.11 +/- 0.16 ) %    ( 30276 out of 111681 )
                        L0GlobalTis = ( 27.66 +/- 0.16 ) %    ( 30890 out of 111681 )
-----
eff_{HLT1/L0}          = ( 64.46 +/- 0.36 ) %    ( 32819 out of 50912 )
                        Hlt1TrackAllL0Tos = ( 64.46 +/- 0.36 ) %    ( 32819 out of 50912 )
-----
eff_{HLT2/HLT1}       = ( 65.86 +/- 0.45 ) %    ( 21616 out of 32819 )
                        Hlt2Topo2BodyBBDTTos = ( 57.71 +/- 0.42 ) %    ( 18941 out of 32819 )
                        Hlt2Topo3BodyBBDTTos = ( 37.41 +/- 0.34 ) %    ( 12278 out of 32819 )
                        Hlt2Topo4BodyBBDTTos = ( 0.00 +/- 0.00 ) %    ( 0 out of 32819 )
=====
eff_{trig/strip}      = ( 19.36 +/- 0.13 ) %    ( 21616 out of 111681 )
=====
```

The results are the following for the 2011 LL and DD samples, respectively:

```

=====
eff_{L0/strip}                = ( 47.31 +/- 0.51 ) %    ( 8523 out of 18014 )
                                L0HadronTos = ( 27.35 +/- 0.39 ) %    ( 4927 out of 18014 )
                                L0GlobalTis = ( 29.84 +/- 0.41 ) %    ( 5375 out of 18014 )
-----
eff_{HLT1/L0}                 = ( 71.72 +/- 0.92 ) %    ( 6113 out of 8523 )
                                Hlt1TrackAllL0Tos = ( 71.72 +/- 0.92 ) %    ( 6113 out of 8523 )
-----
eff_{HLT2/HLT1}              = ( 61.41 +/- 1.00 ) %    ( 3754 out of 6113 )
                                Hlt2Topo2BodyBBDTTos = ( 55.01 +/- 0.95 ) %    ( 3363 out of 6113 )
                                Hlt2Topo3BodyBBDTTos = ( 36.09 +/- 0.77 ) %    ( 2206 out of 6113 )
                                Hlt2Topo4BodyBBDTTos = ( 13.43 +/- 0.47 ) %    ( 821 out of 6113 )
                                Hlt2Topo2BodySimpleTos = ( 36.10 +/- 0.77 ) %    ( 2207 out of 6113 )
                                Hlt2Topo3BodySimpleTos = ( 21.25 +/- 0.59 ) %    ( 1299 out of 6113 )
                                Hlt2Topo4BodySimpleTos = ( 8.80 +/- 0.38 ) %    ( 538 out of 6113 )
-----
eff_{trig/strip}             = ( 20.84 +/- 0.34 ) %    ( 3754 out of 18014 )
=====

=====
eff_{L0/strip}                = ( 49.18 +/- 0.28 ) %    ( 31265 out of 63570 )
                                L0HadronTos = ( 30.04 +/- 0.22 ) %    ( 19099 out of 63570 )
                                L0GlobalTis = ( 29.52 +/- 0.22 ) %    ( 18767 out of 63570 )
-----
eff_{HLT1/L0}                 = ( 63.82 +/- 0.45 ) %    ( 19954 out of 31265 )
                                Hlt1TrackAllL0Tos = ( 63.82 +/- 0.45 ) %    ( 19954 out of 31265 )
-----
eff_{HLT2/HLT1}              = ( 52.44 +/- 0.51 ) %    ( 10464 out of 19954 )
                                Hlt2Topo2BodyBBDTTos = ( 51.58 +/- 0.51 ) %    ( 10293 out of 19954 )
                                Hlt2Topo3BodyBBDTTos = ( 0.18 +/- 0.03 ) %    ( 36 out of 19954 )
                                Hlt2Topo4BodyBBDTTos = ( 0.00 +/- 0.00 ) %    ( 0 out of 19954 )
                                Hlt2Topo2BodySimpleTos = ( 31.77 +/- 0.40 ) %    ( 6339 out of 19954 )
                                Hlt2Topo3BodySimpleTos = ( 0.10 +/- 0.02 ) %    ( 20 out of 19954 )
                                Hlt2Topo4BodySimpleTos = ( 0.00 +/- 0.00 ) %    ( 0 out of 19954 )
-----
eff_{trig/strip}             = ( 16.46 +/- 0.16 ) %    ( 10464 out of 63570 )
=====

```

It is clear that all trigger lines are relevant apart from the HLT2 Topo4Body lines when it comes to selecting DD signal candidates. For consistency the selection is nevertheless kept the same throughout, as it is believed that this does not introduce any non-negligible systematic uncertainty.

## **Appendix B**

# **Distribution of the MVA Input Variables for the Individual Data Samples**

## B.1 MVA Training for the 2011 LL Data

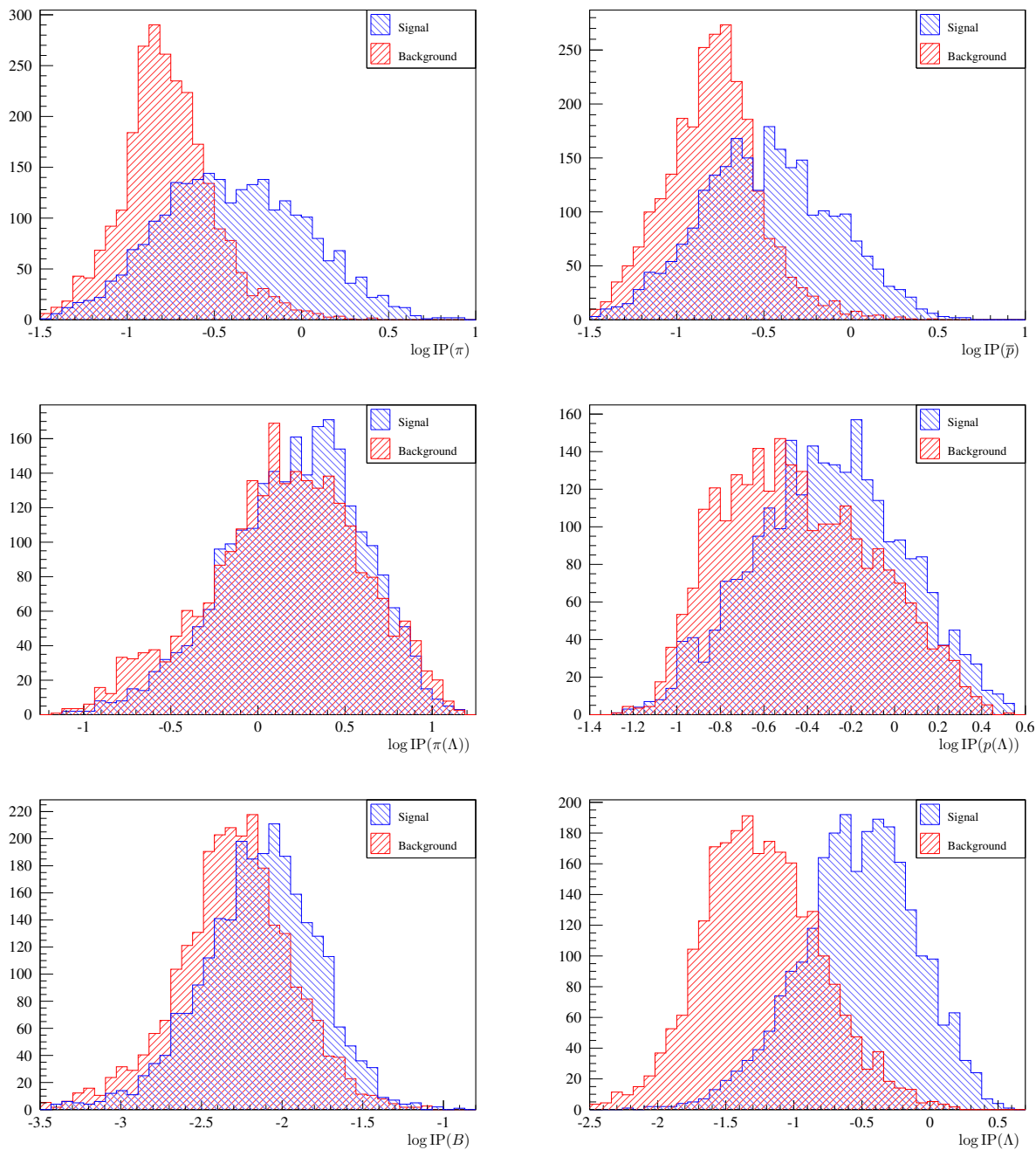


Figure B.1: Input variables for the training for the 2011 period for the LL sample. The blue data points are signal, the red data points background.

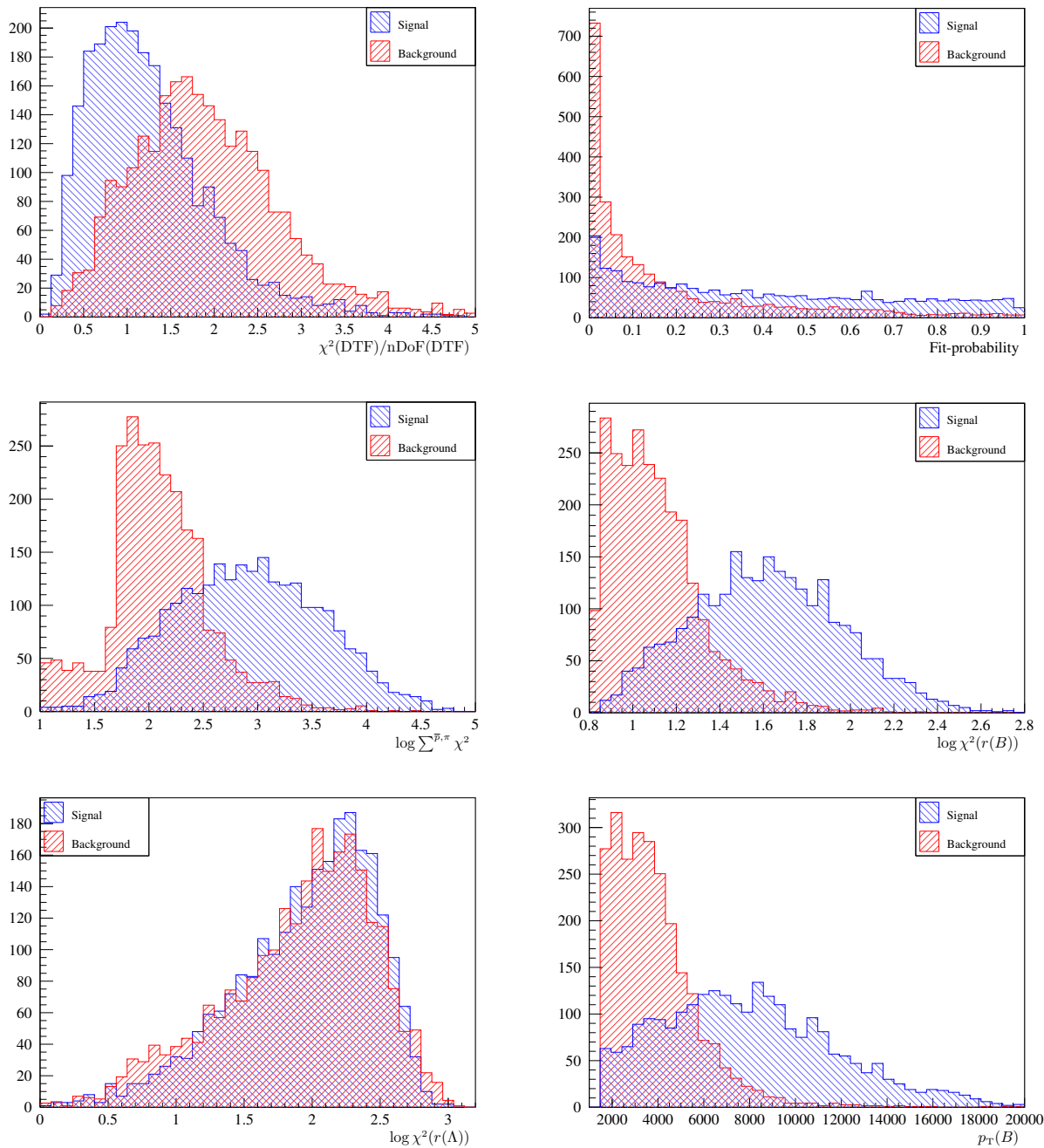


Figure B.2: Input variables for the training for the 2011 period for the LL sample. The blue data points are signal, the red data points background.



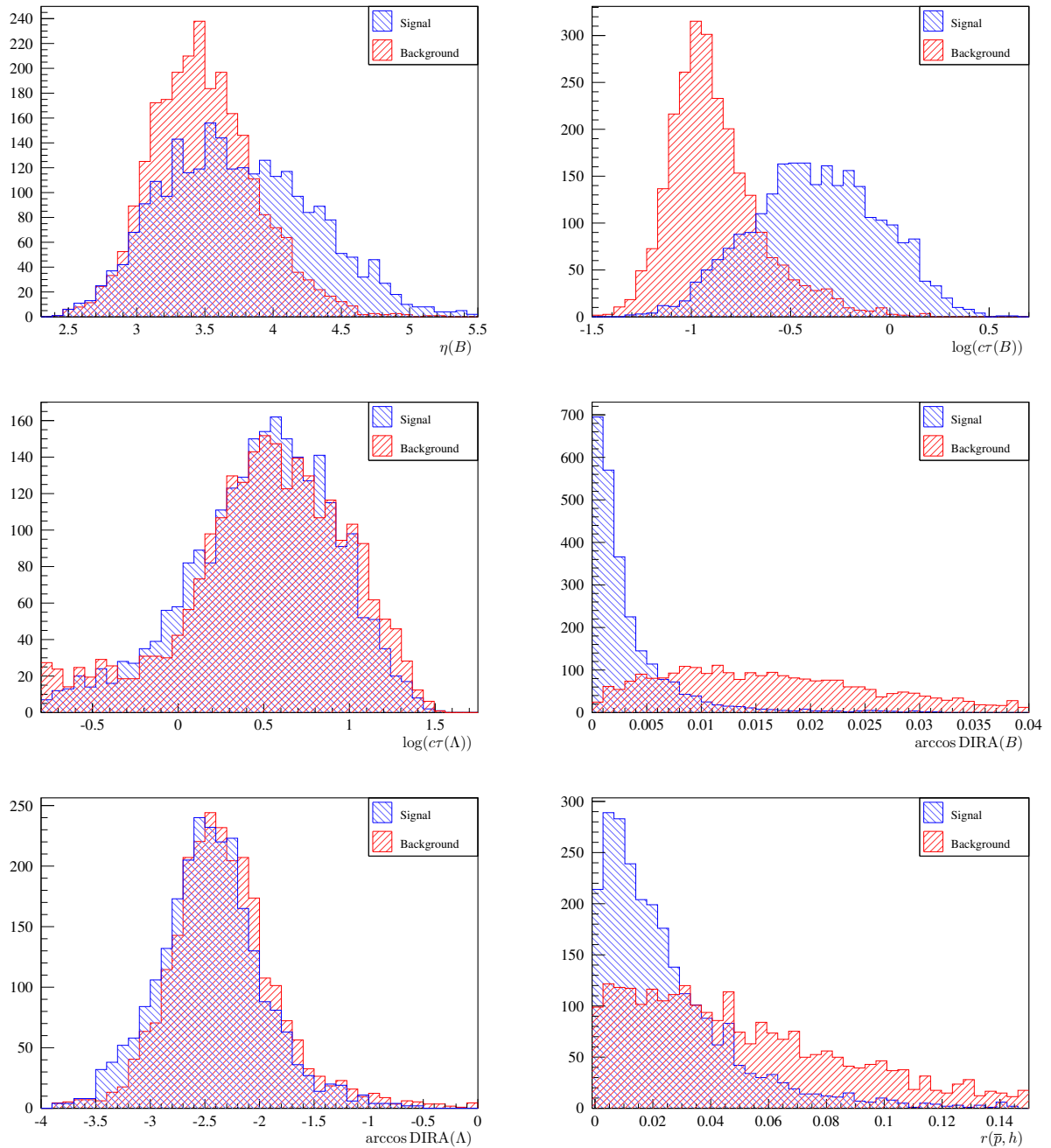


Figure B.3: Input variables for the training for the 2011 period for the LL sample. The blue data points are signal, the red data points background.

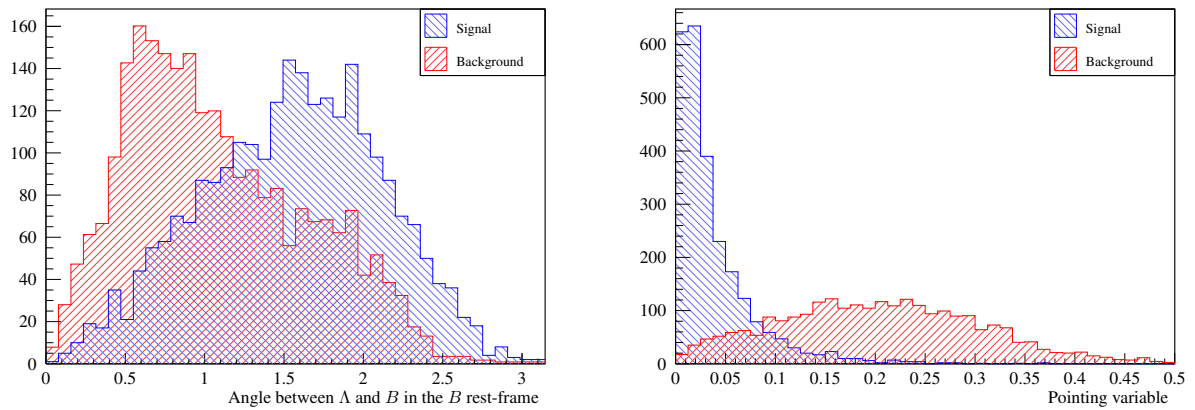


Figure B.4: Input variables and output of the training for the 2011 period for the  $LL$  sample. The blue data points are signal, the red data points background.

## B.2 MVA Training for the 2011 DD Data

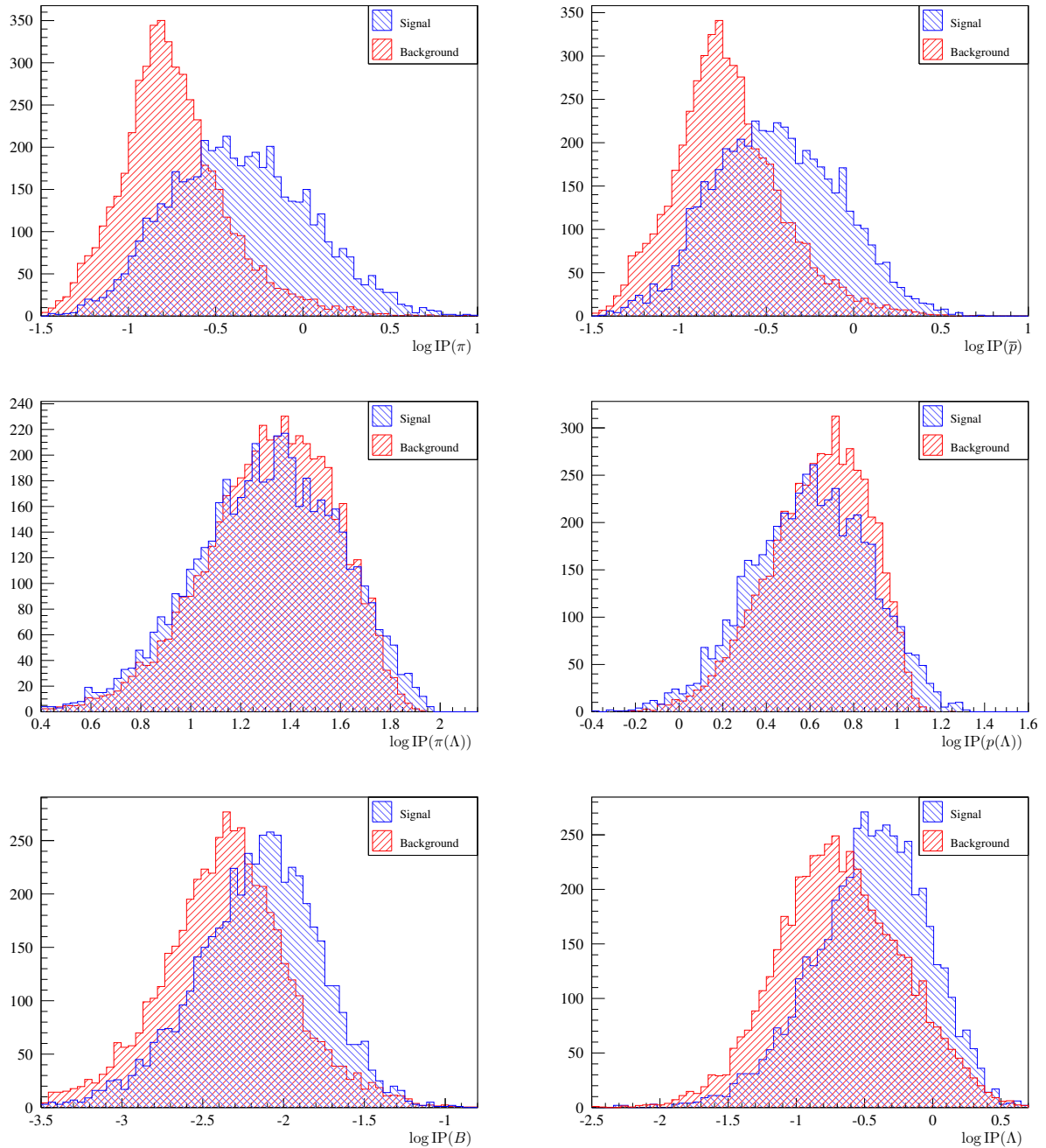


Figure B.5: Input variables for the training for the 2011 period for the DD sample. The blue data points are signal, the red data points background.

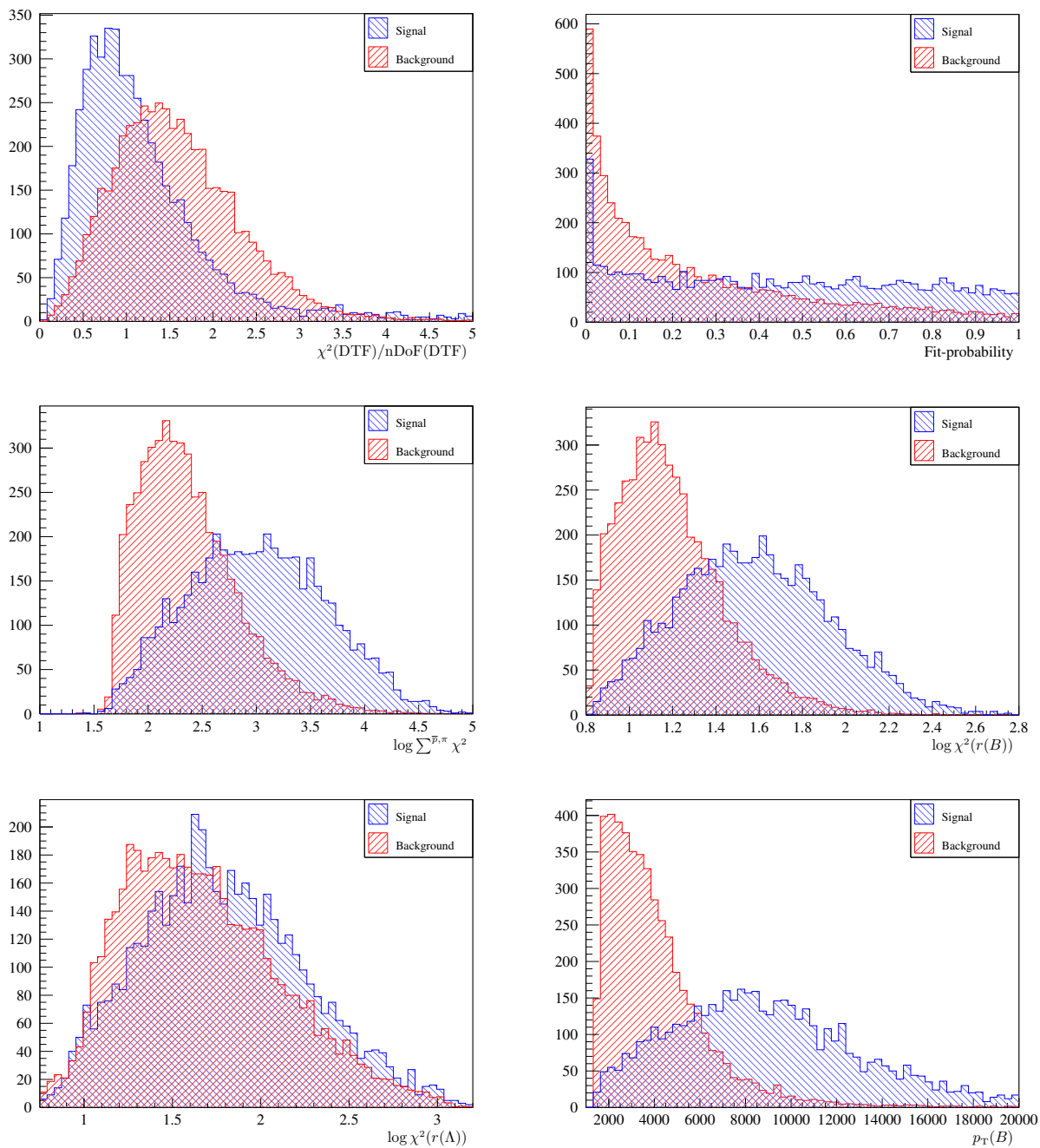


Figure B.6: Input variables for the training for the 2011 period for the DD sample. The blue data points are signal, the red data points background.

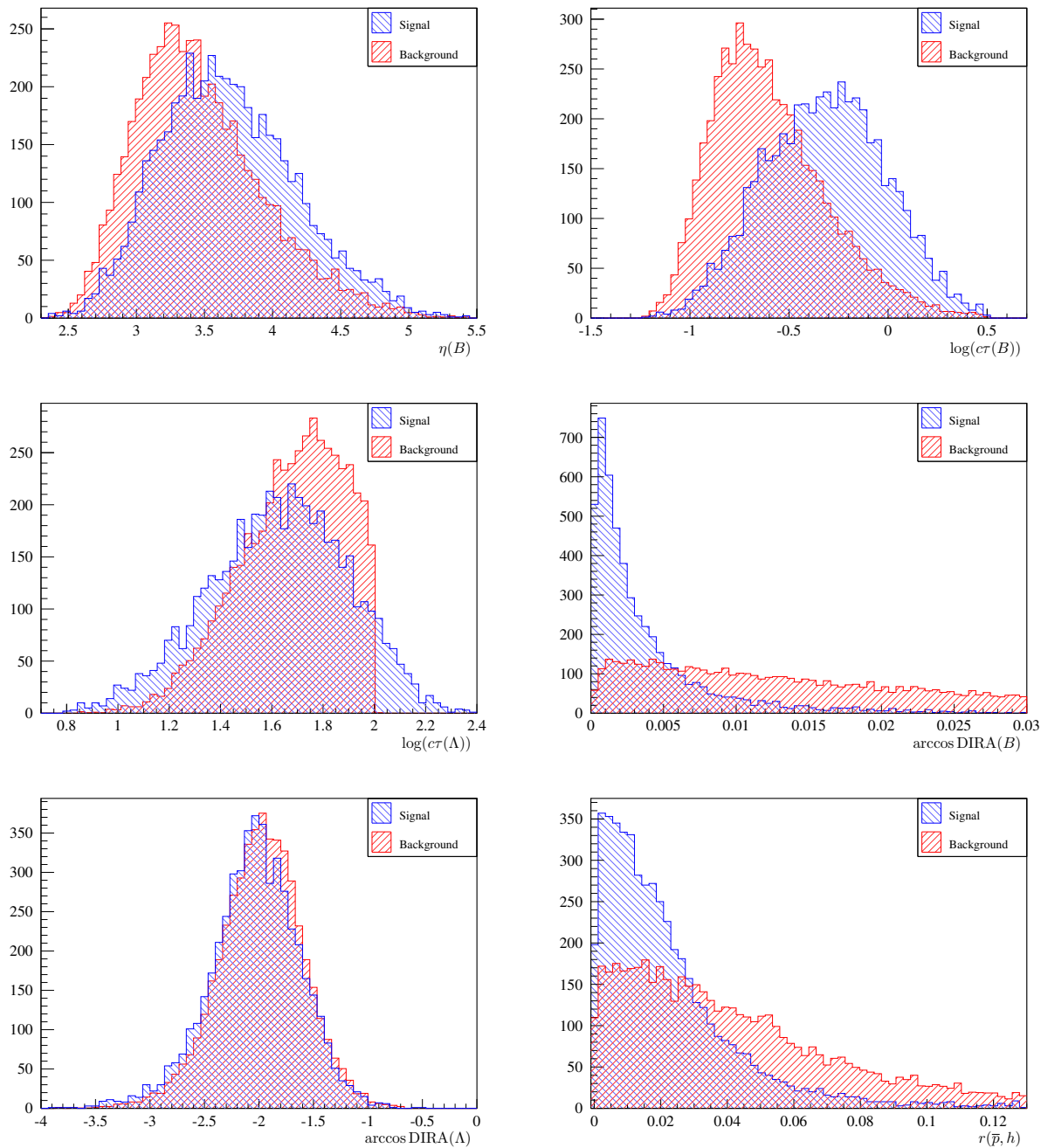


Figure B.7: Input variables for the training for the 2011 period for the DD sample. The blue data points are signal, the red data points background.

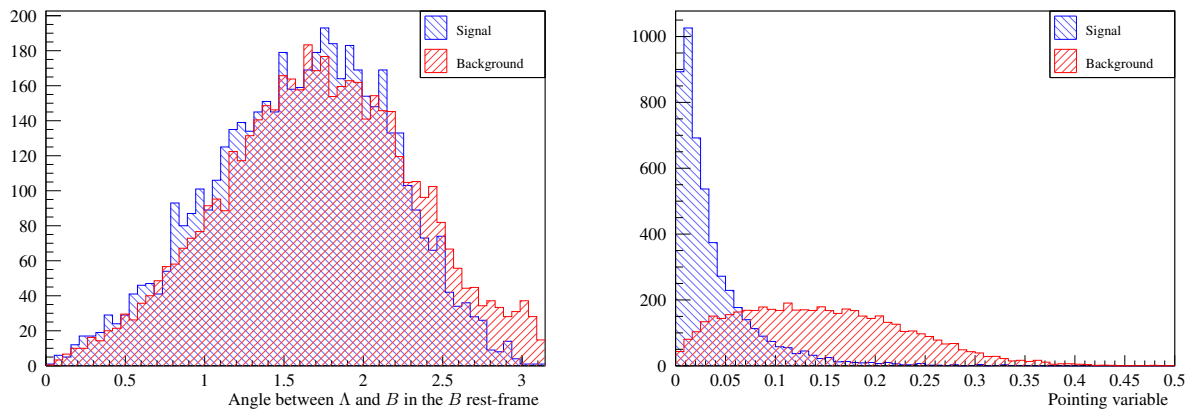


Figure B.8: Input variables and output of the training for the 2011 period for the DD sample. The blue data points are signal, the red data points background.

### B.3 MVA Training for the 2012 LL Data

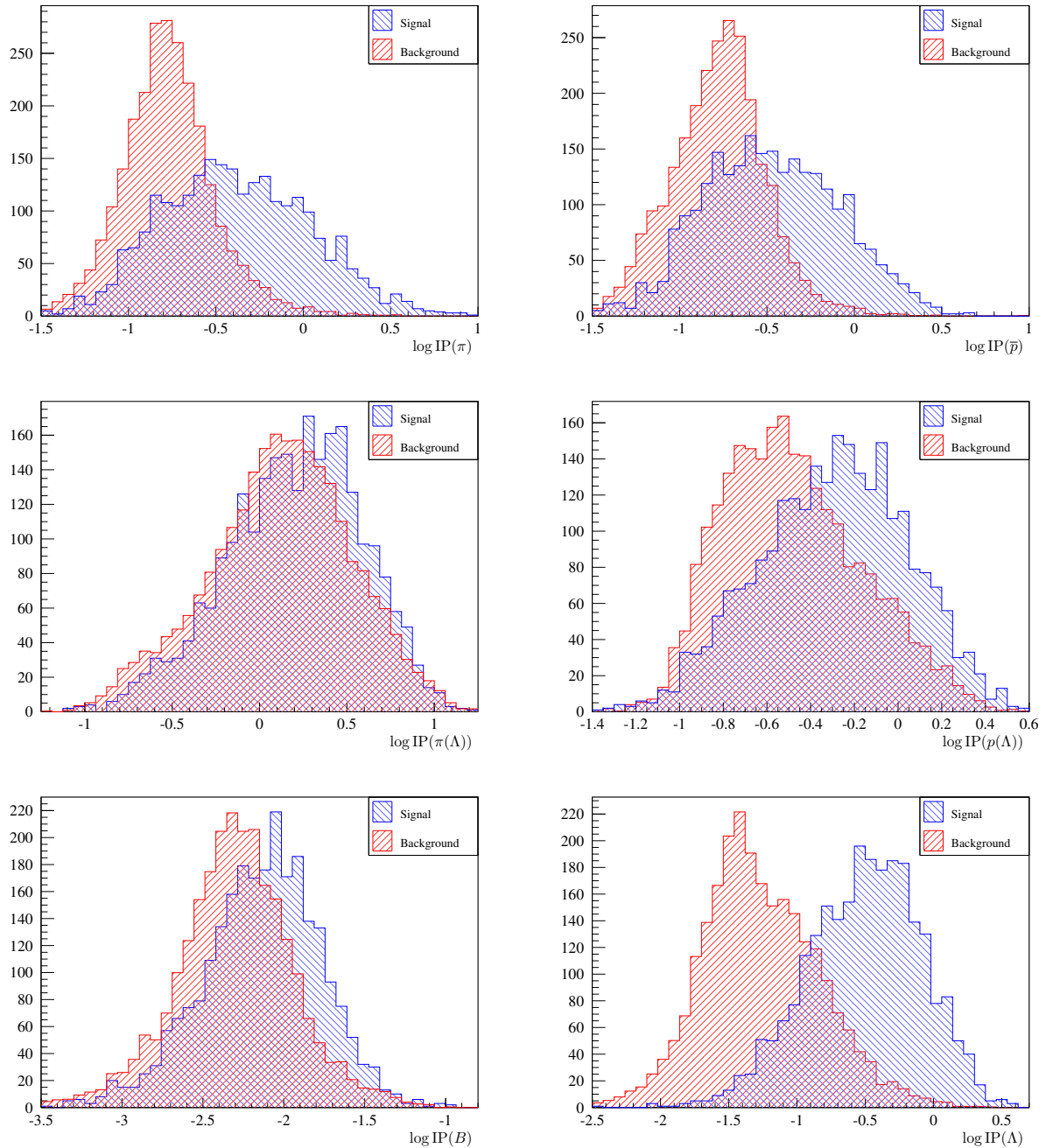


Figure B.9: Input variables for the training for the 2012 period for the LL sample. The blue data points are signal, the red data points background.

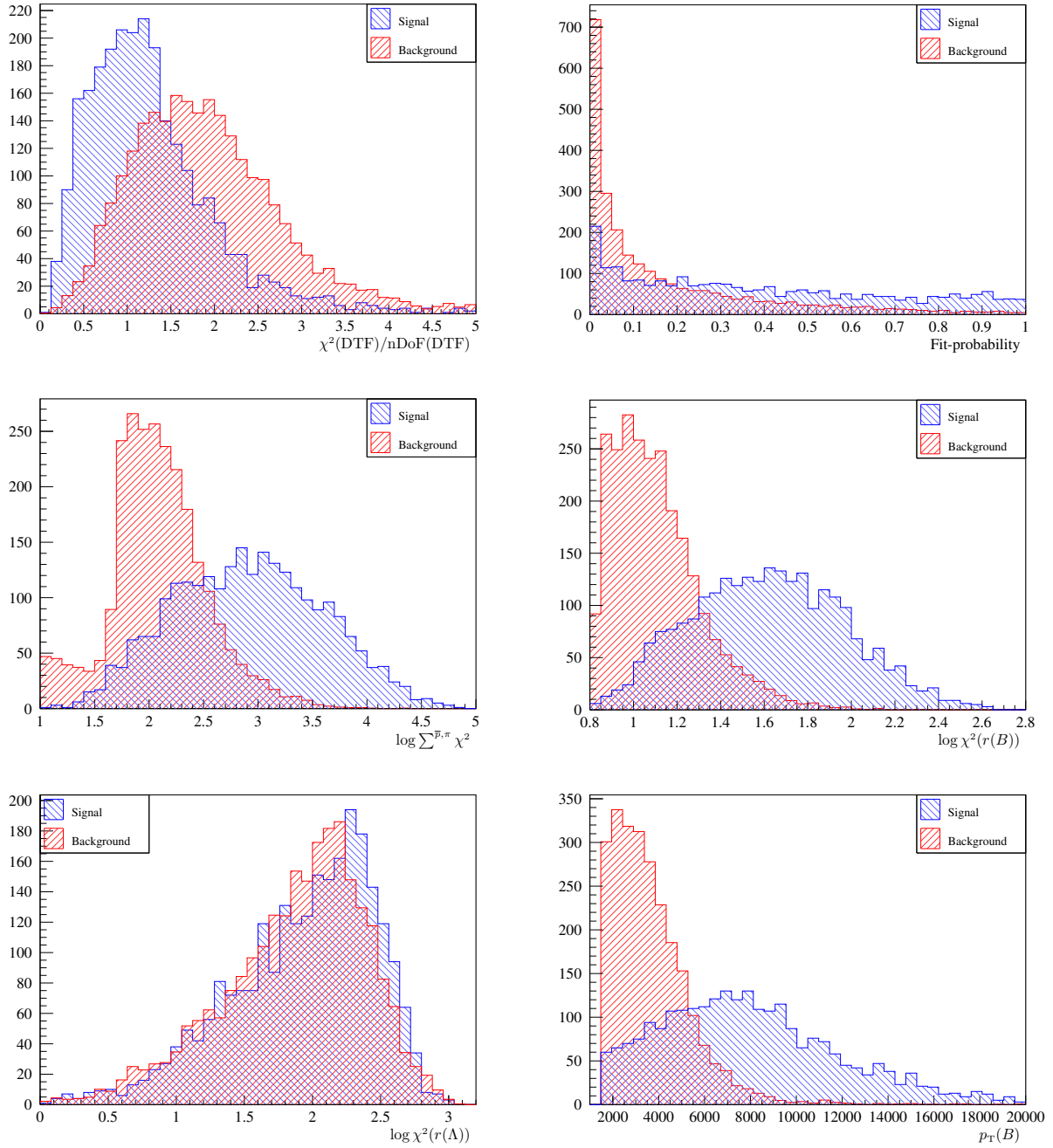


Figure B.10: Input variables for the training for the 2012 period for the LL sample. The blue data points are signal, the red data points background.



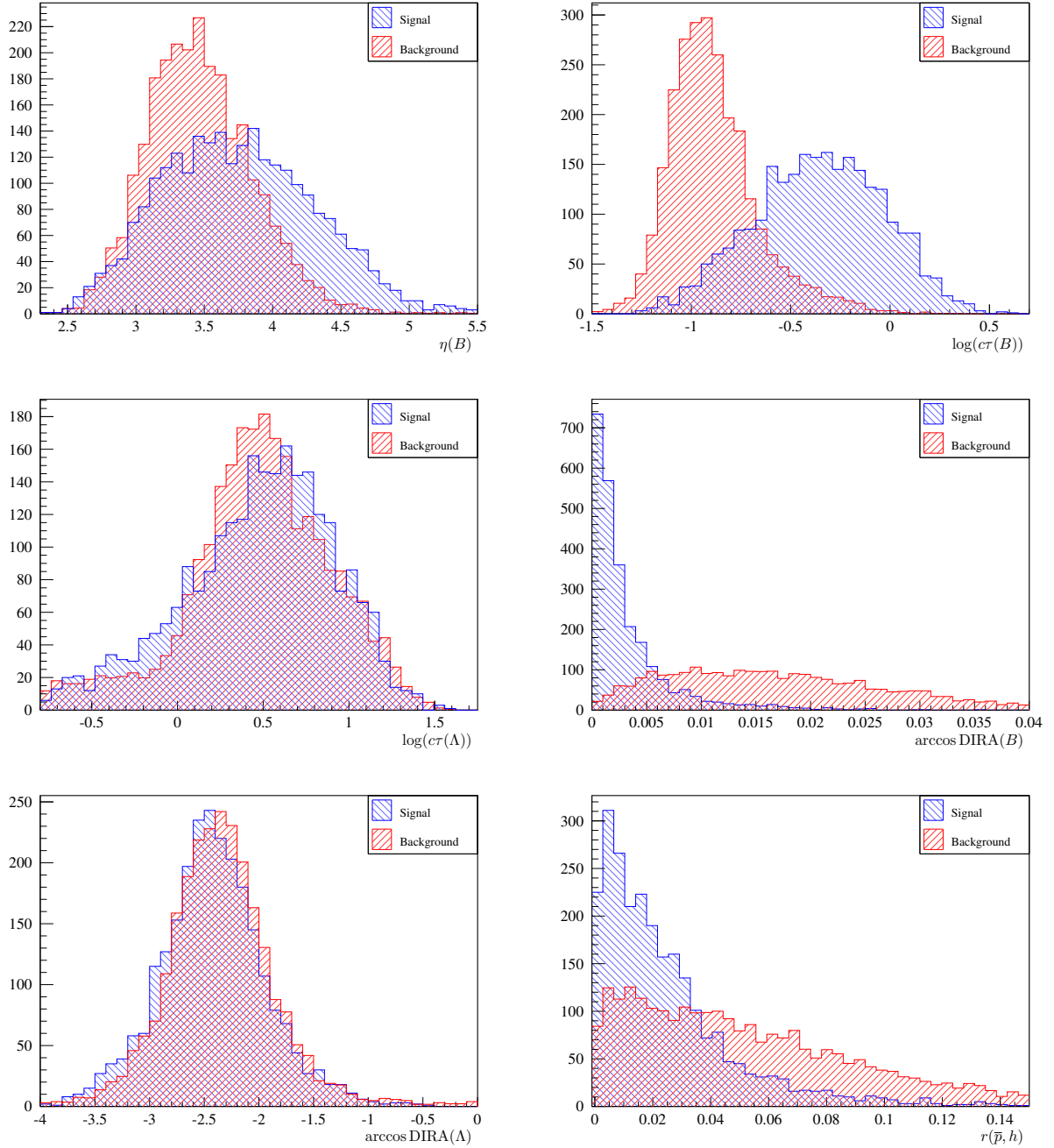


Figure B.11: Input variables for the training for the 2012 period for the LL sample. The blue data points are signal, the red data points background.

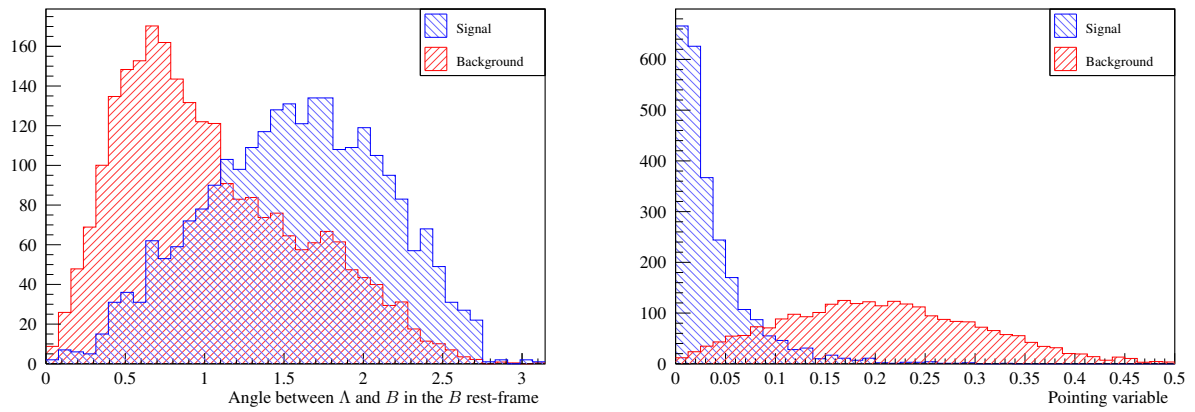


Figure B.12: Input variables and output of the training for the 2012 period for the  $LL$  sample. The blue data points are signal, the red data points background.

## B.4 MVA Training for the 2012 DD Data

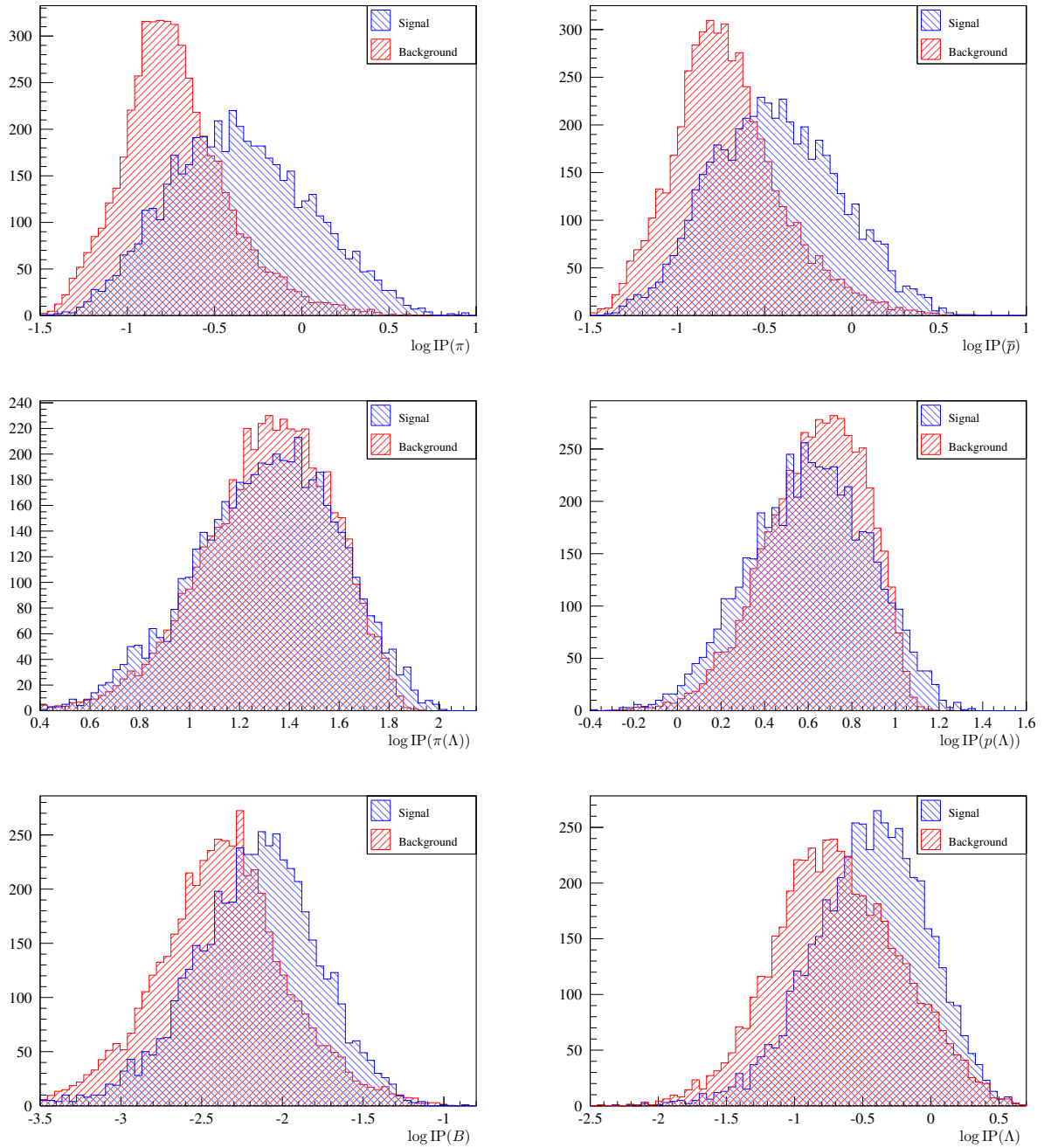


Figure B.13: Input variables for the training for the 2012 period for the DD sample. The blue data points are signal, the red data points background.

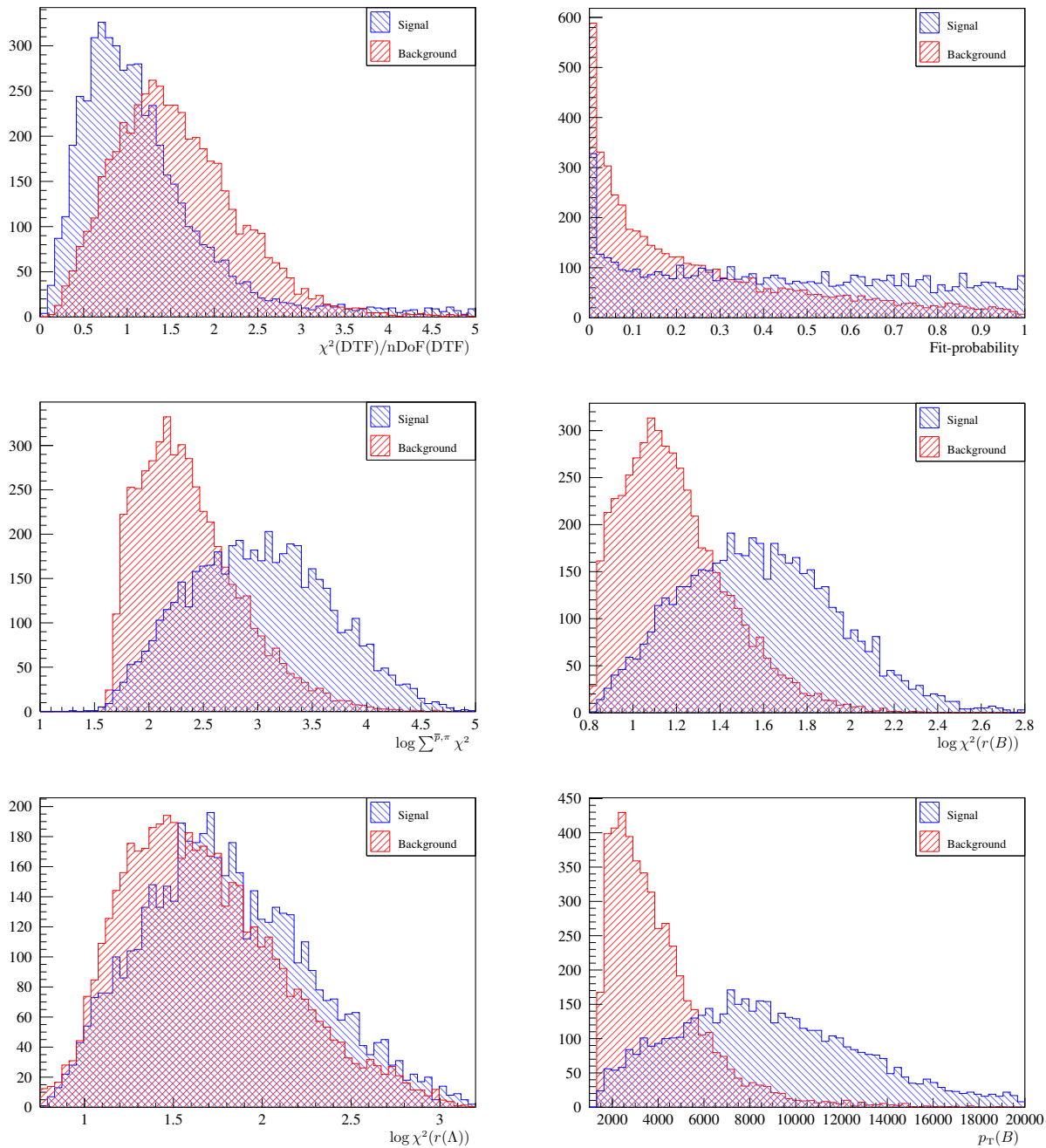
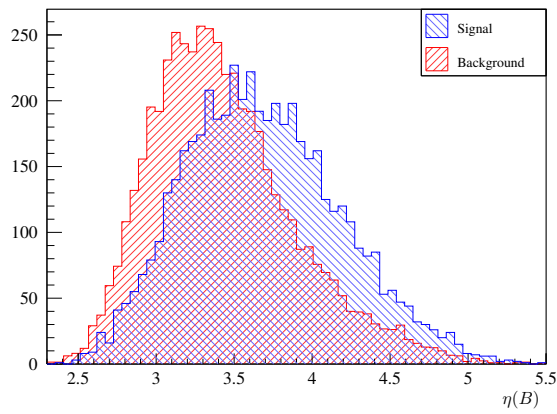
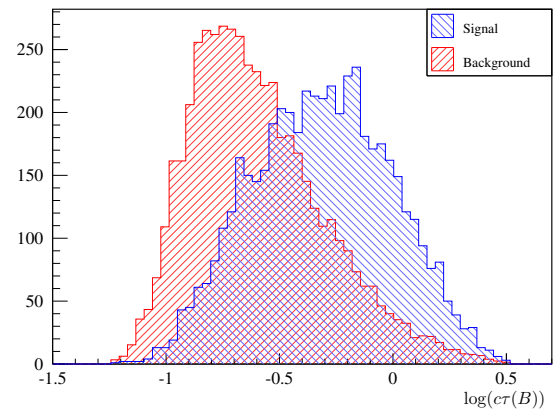


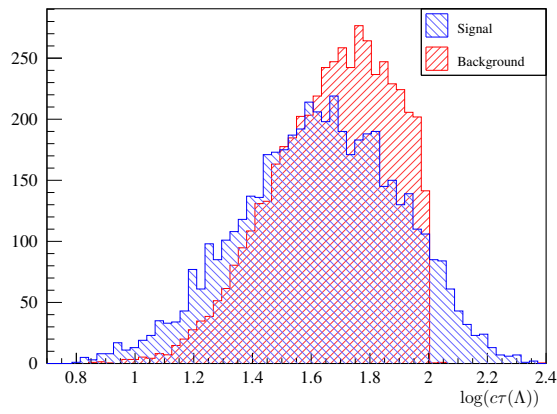
Figure B.14: Input variables for the training for the 2012 period for the DD sample. The blue data points are signal, the red data points background.



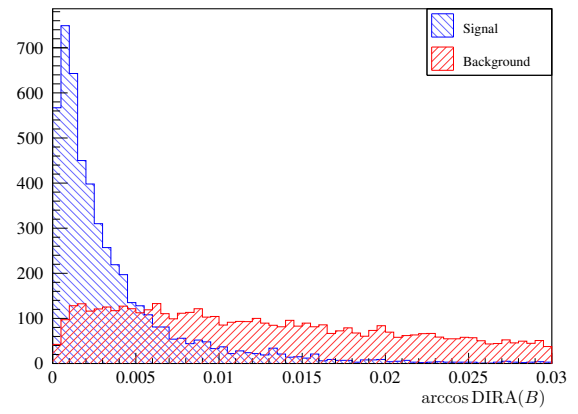
(a)



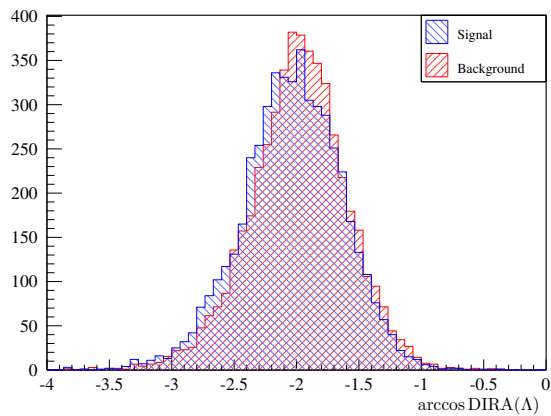
(b)



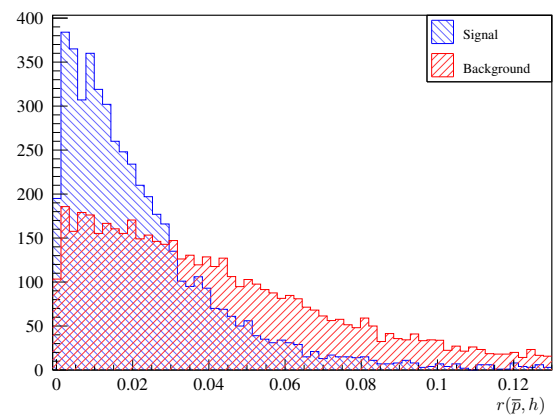
(c)



(d)



(e)



(f)

Figure B.15: Input variables for the training for the 2012 period for the  $DD$  sample. The blue data points are signal, the red data points background.

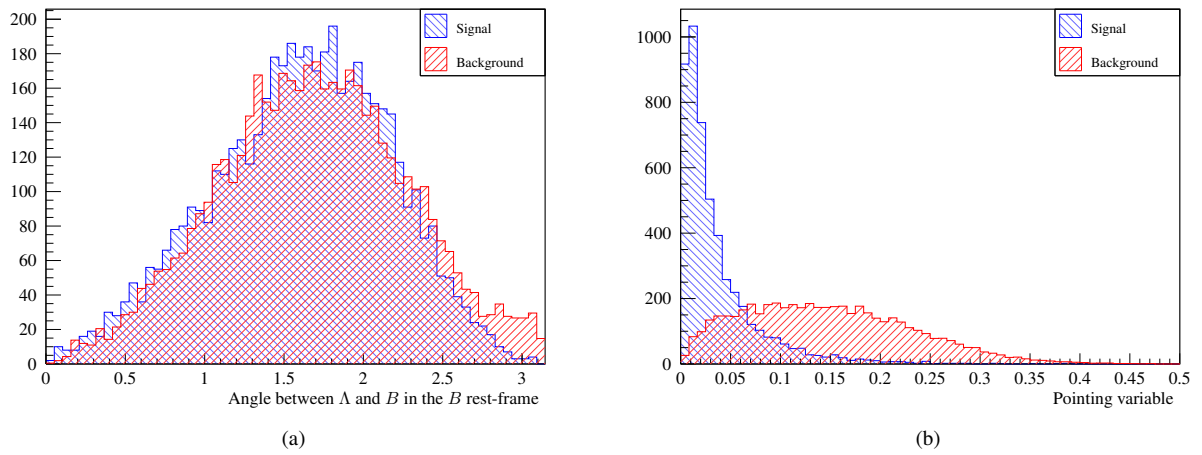


Figure B.16: Input variables and output of the training for the 2012 period for the DD sample. The blue data points are signal, the red data points background.



## Appendix C

# Effect of the Trigger Configuration in 2012

During the June technical stop significant changes to the trigger were implemented increasing the performance for  $V^0$  particles significantly. The influence of the new trigger configuration on the input variables was checked comparing their distributions in the pre-June and post-June configurations, see Figs. C.1 to C.4 and C.5 to C.8 for the `Long` and `Down` sample, respectively. All pre-June and post-June distributions are found to be in rather good agreement, meaning no significant deviations are observed for any variable. Hence it was decided not to split the data sample in two disjoint sub-samples for 2012 for the purposes of the event selection.



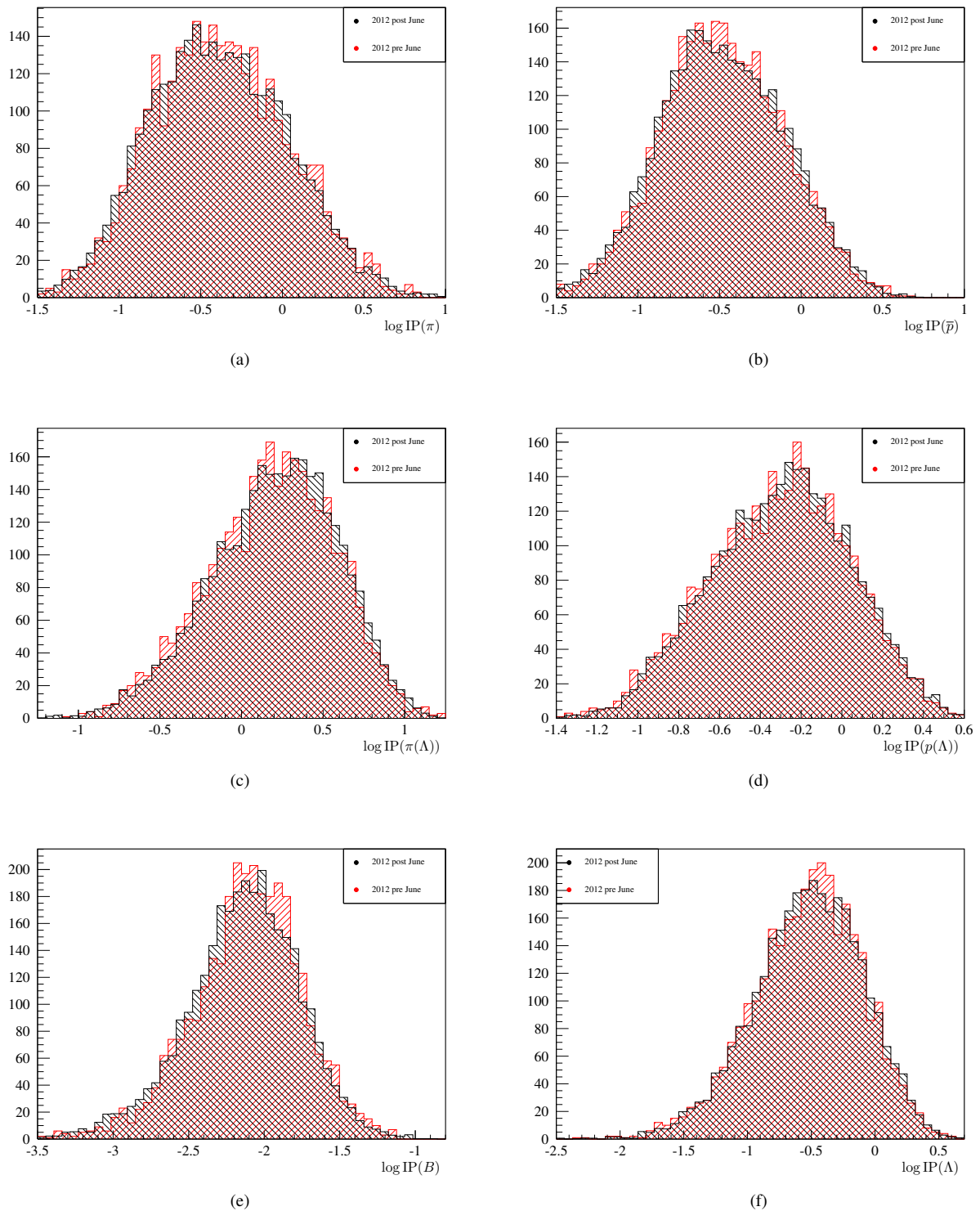
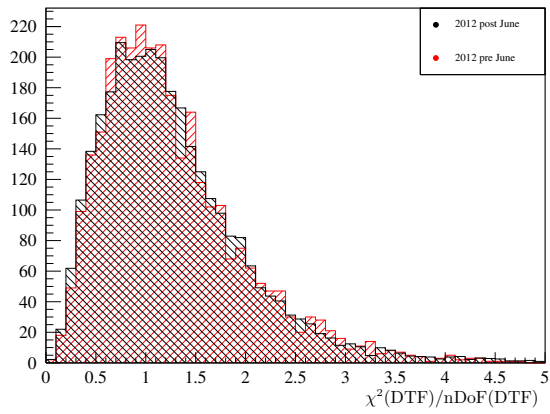
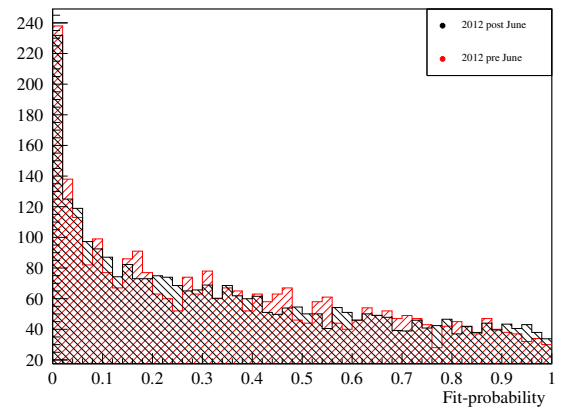


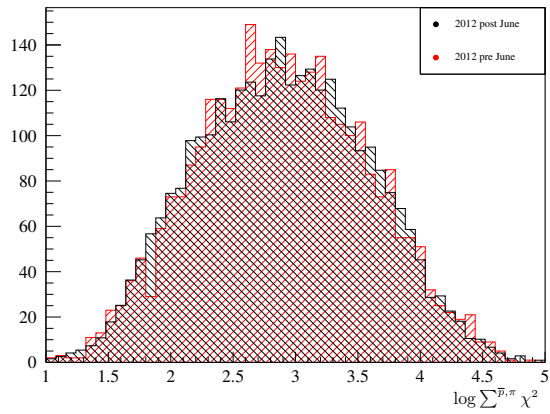
Figure C.1: MVA input variables for the two 2012 data-taking periods for the  $LL$  sample – set 1. The red (black) points represent the pre-(post-)June trigger conditions.



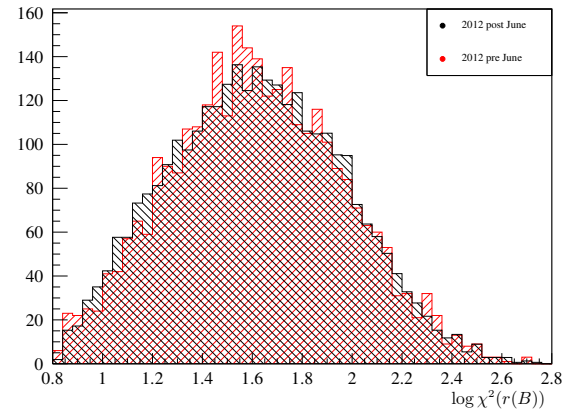
(a)



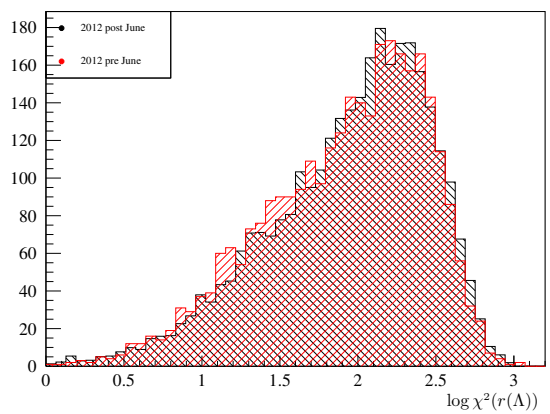
(b)



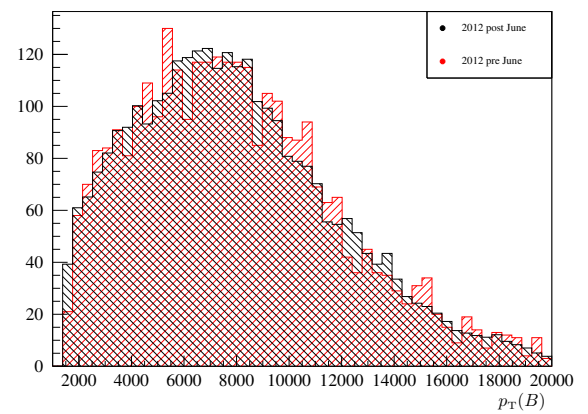
(c)



(d)

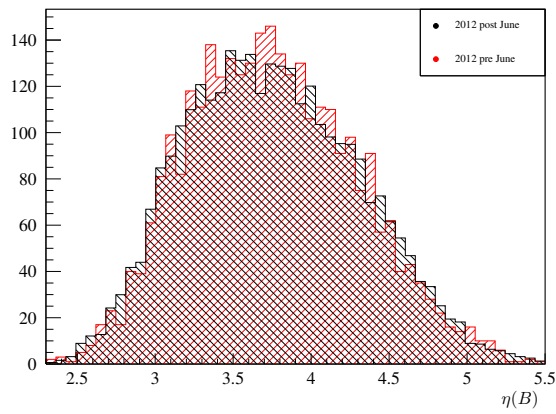


(e)

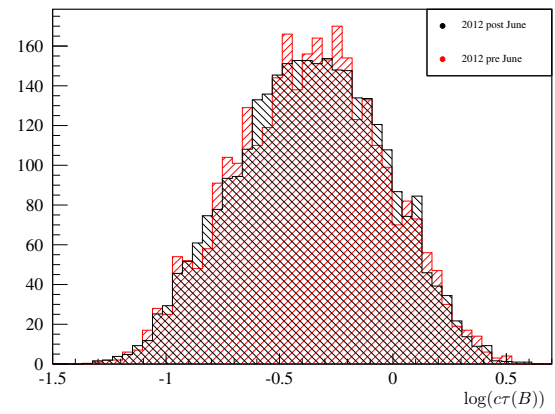


(f)

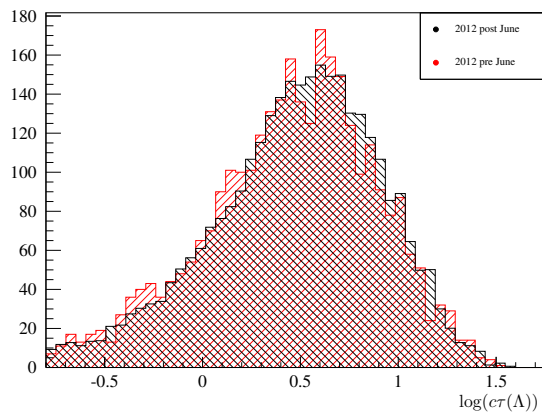
Figure C.2: MVA input variables for the two 2012 data-taking periods for the LL sample – set 2. The red (black) points represent the pre-(post-)June trigger conditions.



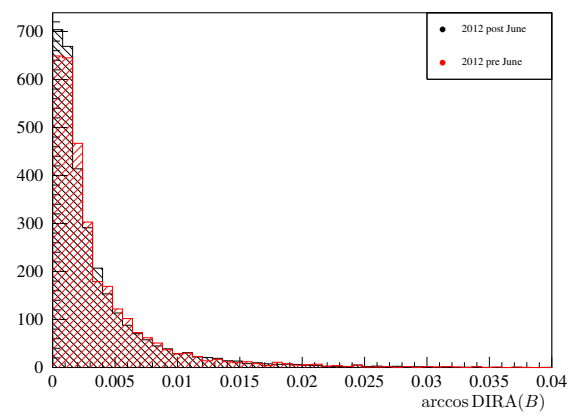
(a)



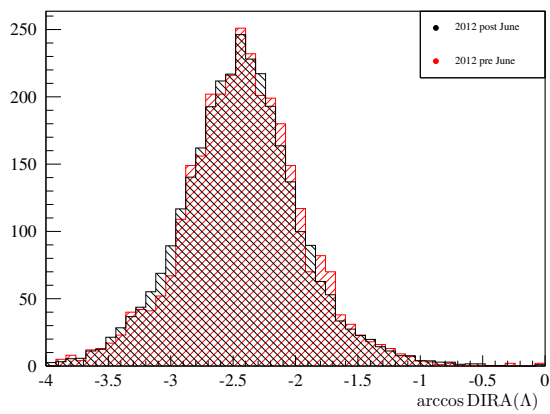
(b)



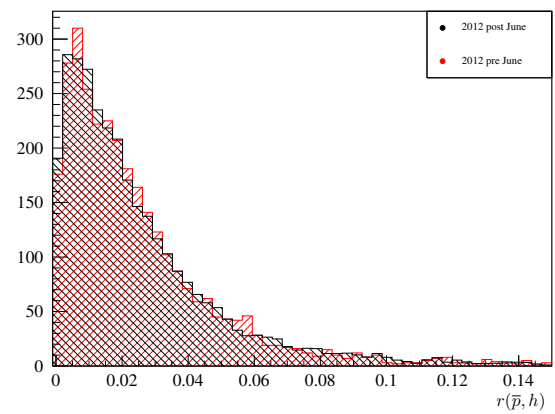
(c)



(d)



(e)



(f)

Figure C.3: MVA input variables for the two 2012 data-taking periods for the  $LL$  sample – set 3. The red (black) points represent the pre-(post-)June trigger conditions.

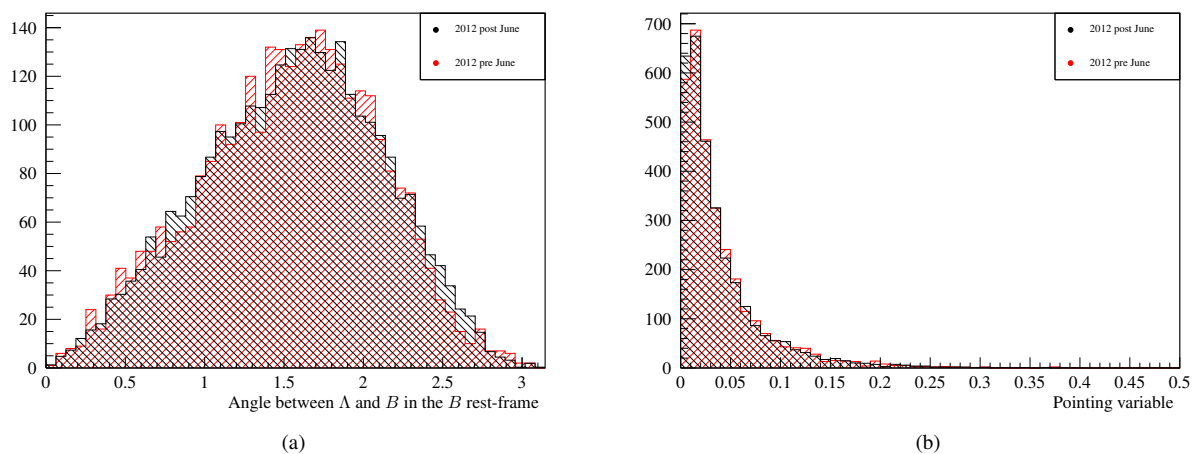


Figure C.4: MVA input variables for the two 2012 data-taking periods for the LL sample – set 4. The red (black) points represent the pre-(post-)June trigger conditions.

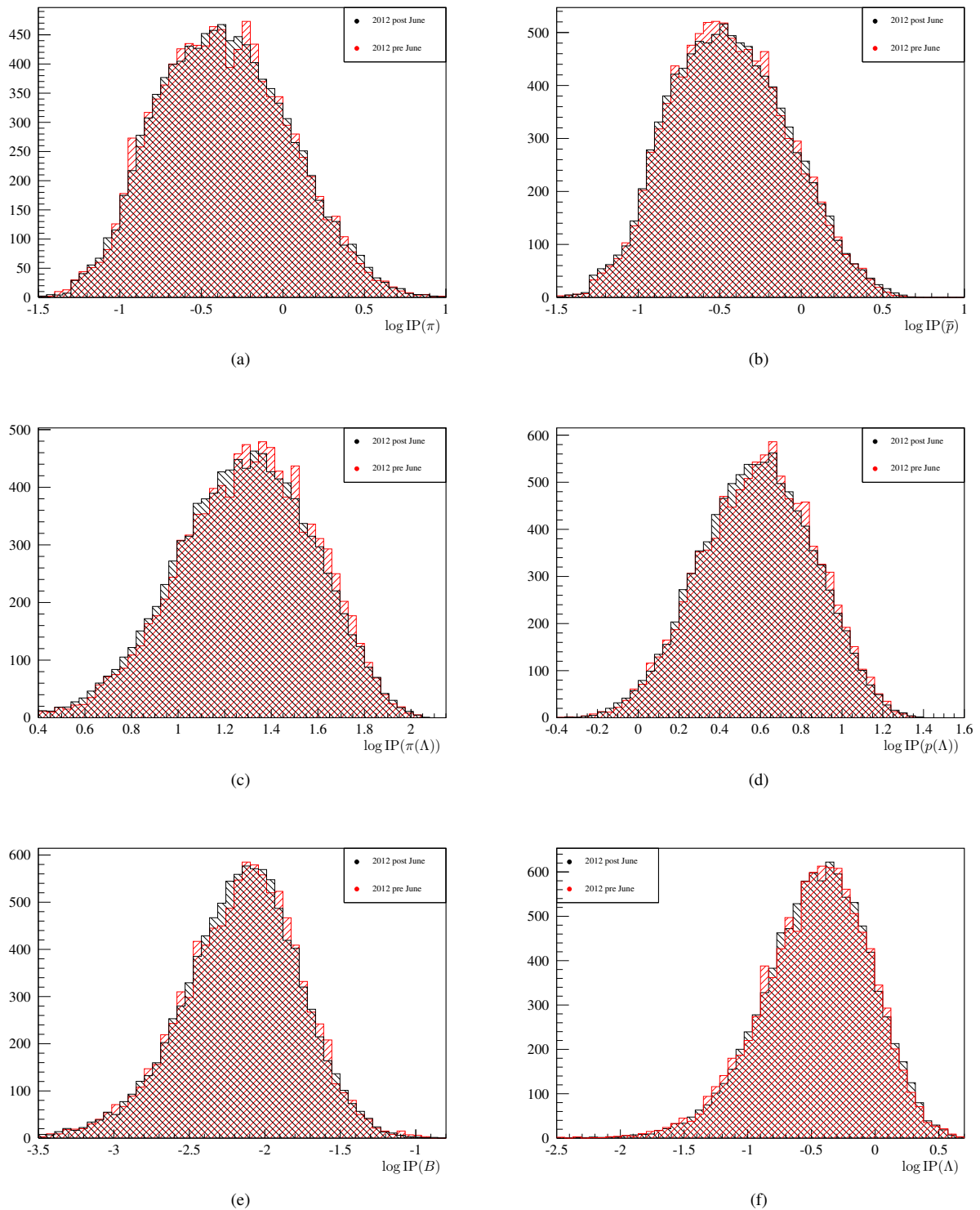
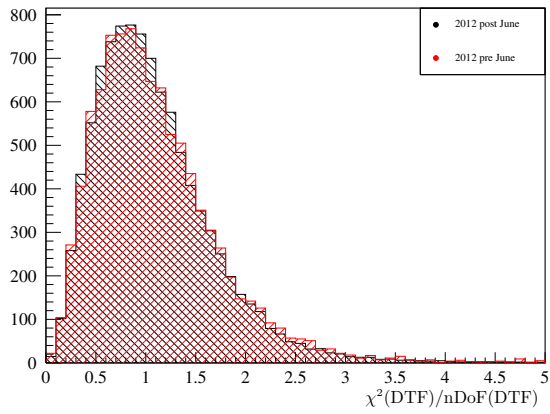
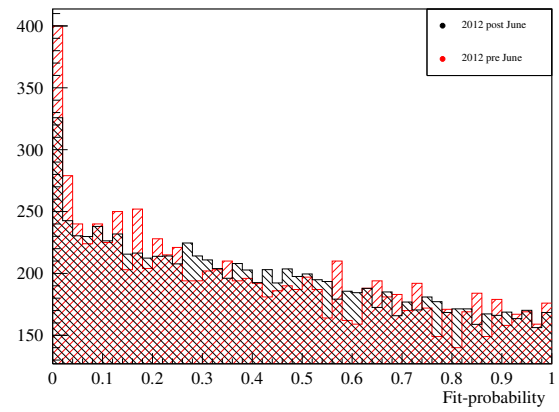


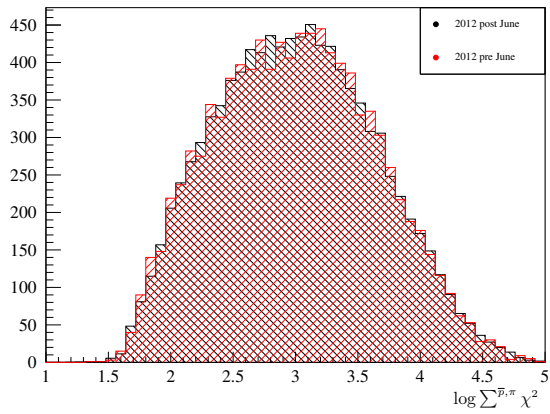
Figure C.5: MVA input variables for the two 2012 data-taking periods for the DD sample – set 1. The red (black) points represent the pre-(post-)June trigger conditions.



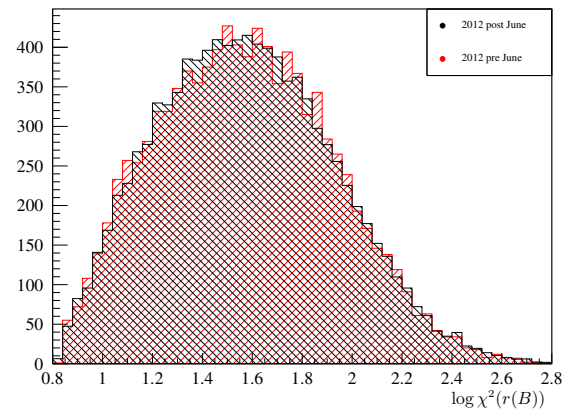
(a)



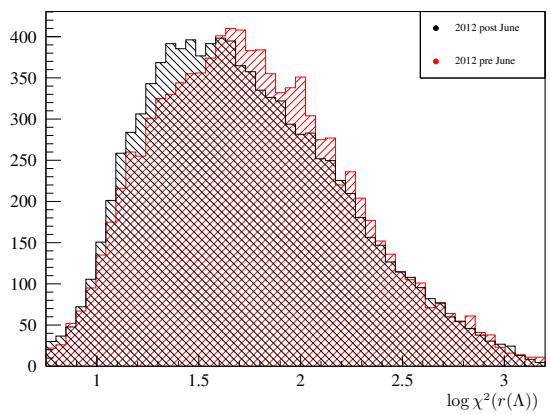
(b)



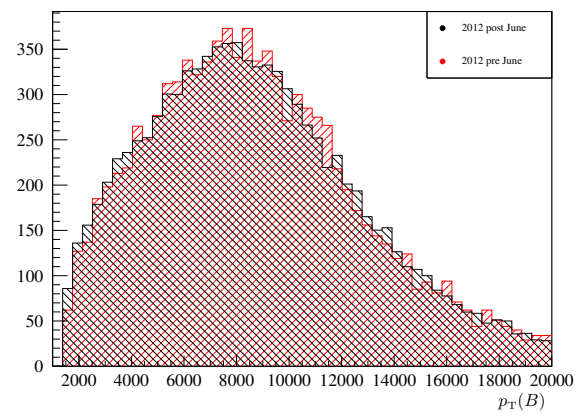
(c)



(d)



(e)



(f)

Figure C.6: MVA input variables for the two 2012 data-taking periods for the DD sample – set 2. The red (black) points represent the pre-(post-)June trigger conditions.

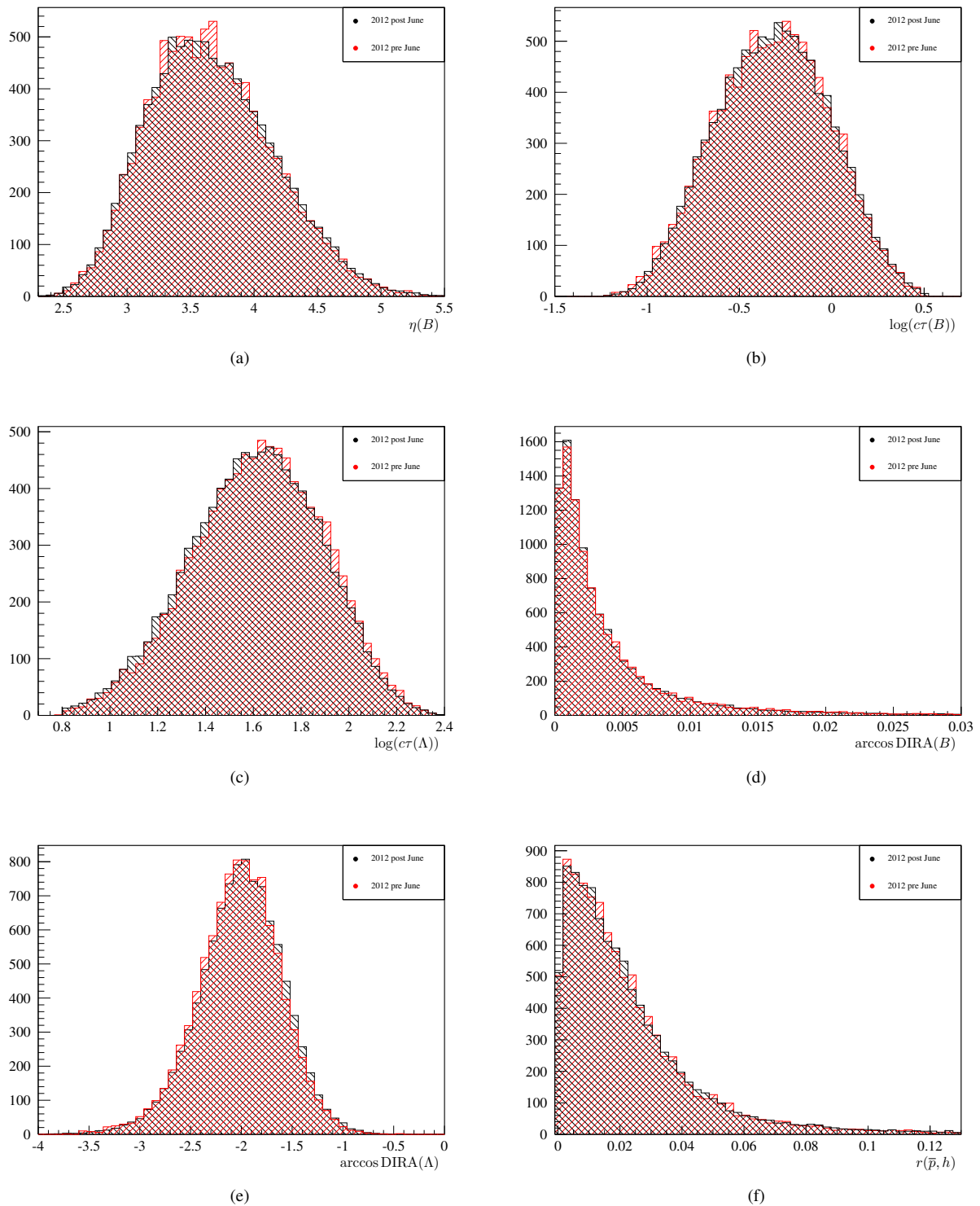


Figure C.7: MVA input variables for the two 2012 data-taking periods for the DD sample – set 3. The red (black) points represent the pre-(post-)June trigger conditions.



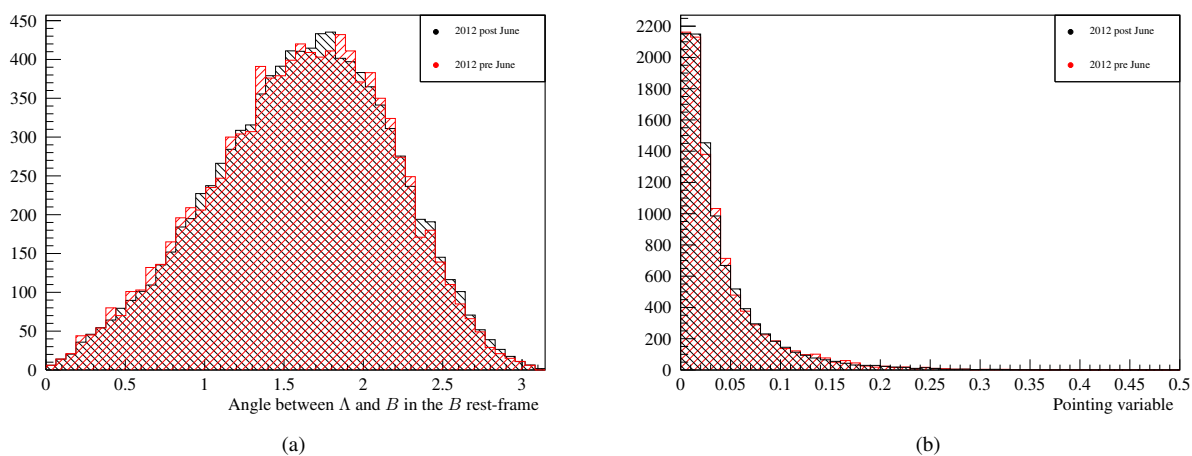


Figure C.8: MVA input variables for the two 2012 data-taking periods for the DD sample – set 4. The red (black) points represent the pre-(post-)June trigger conditions.





## Appendix D

# Hadronisation Fractions

The hadronisation fractions  $f_q$  represent the  $b$  hadronisation probabilities to the possible  $b$ -flavoured final states. In this analysis all  $f_q$  values have been taken or determined from LHCb measurements [44, 45] assuming isospin symmetry, namely  $f_u/f_d = 1$ . They are collected in Tab. D.1. The values given in the table have been used to determine expected signal and background yields, and to assess relative background contributions.

Table D.1: Hadronisation fractions used in the analysis. The quoted  $f_{\Lambda_b^0}/(f_u + f_d)$  result was obtained assuming an average  $p_T$  of 10 GeV/ $c$ .

Measured quantity	Experimental result
$f_u/f_d$	1 (assumed)
$f_s/f_d$	$0.259 \pm 0.015$ [44]
$f_{\Lambda_b^0}/(f_u + f_d)$	$(0.404 \pm 0.110) \times [1 - (0.31 \pm 0.05)]$ [45]
$f_q$	Used value
$f_d$	0.350
$f_u$	0.350
$f_s$	0.092
$f_{\Lambda_b^0}$	0.198



# Appendix E

## Correlation between the MVA Input Variables

The correlations of the MVA input variables in signal and background were presented in Section 3.1.6.1 for the 2012 LL sample for the sake of argumentation. For completeness the correlation tables for the remaining samples are here, see Figures E.1 to E.6.

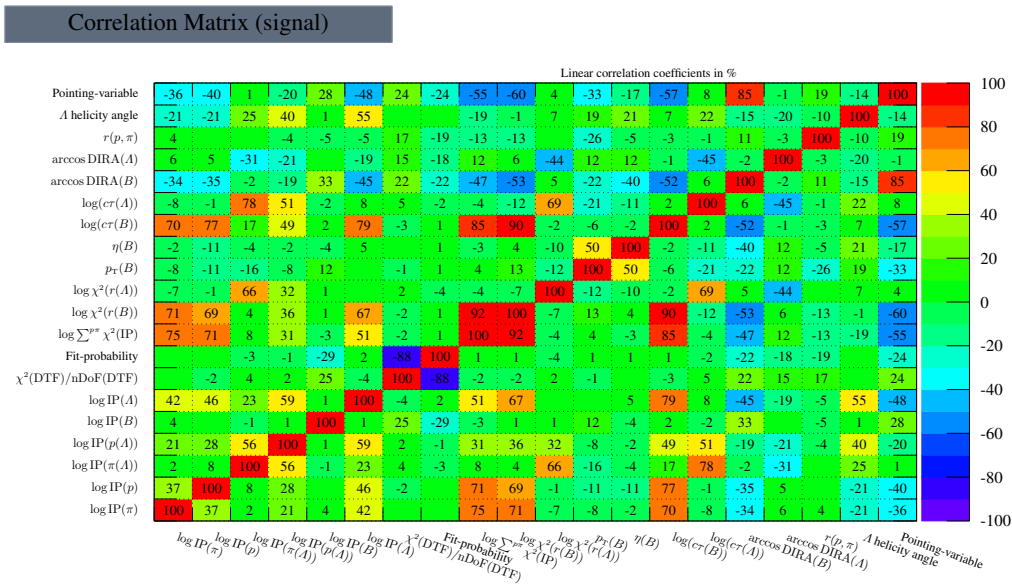


Figure E.1: Correlations between the input variables for the 2011 LL signal sample.

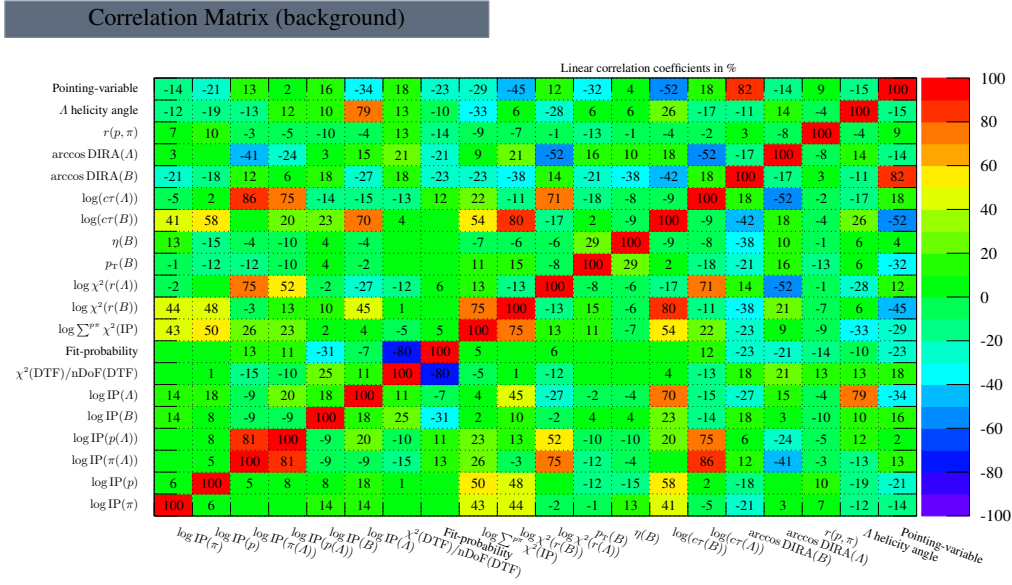


Figure E.2: Correlations between the input variables for the 2011 LL background sample.

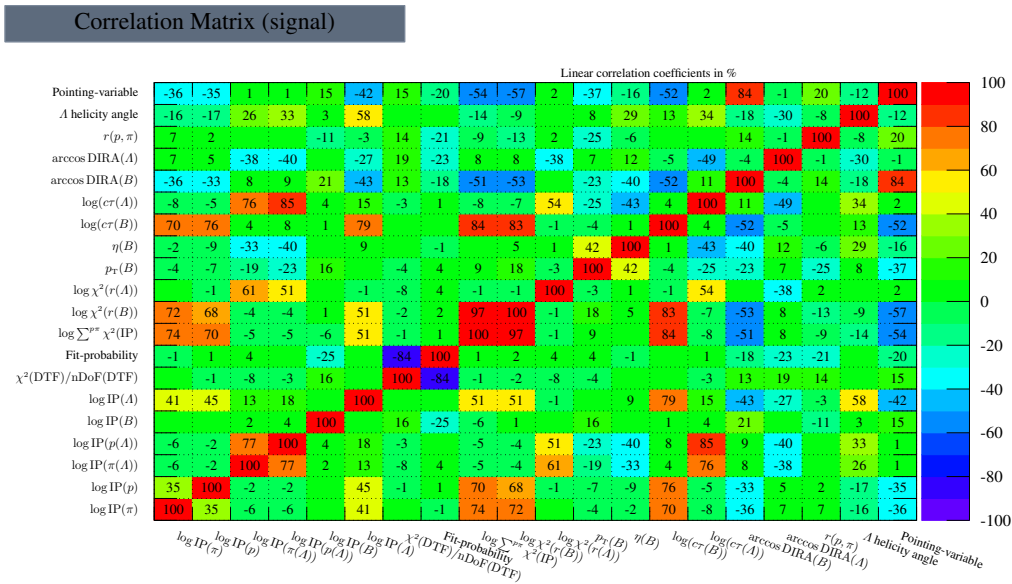


Figure E.3: Correlations between the input variables for the 2011 DD signal sample.

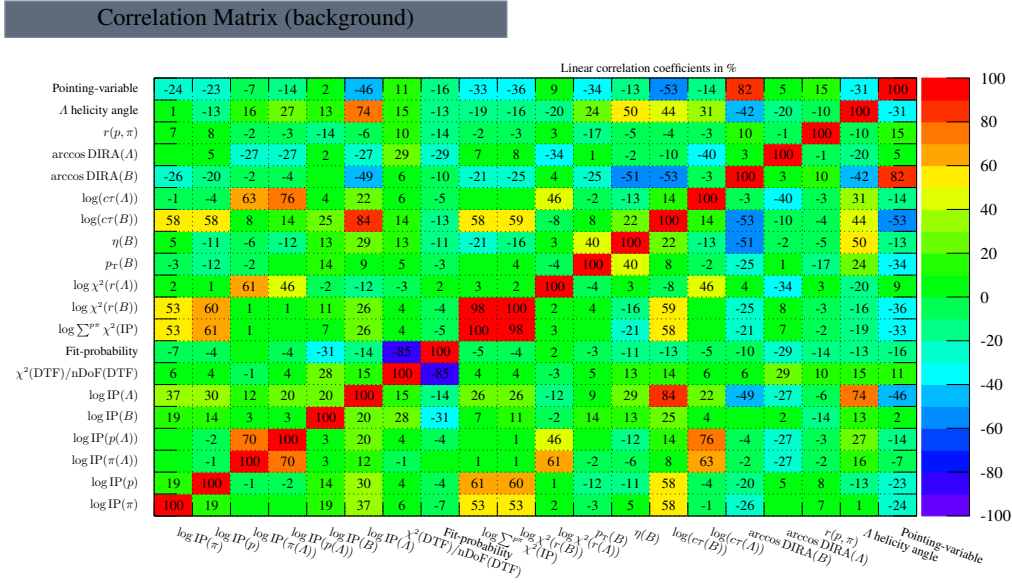


Figure E.4: Correlations between the input variables for the 2011 DD background sample.

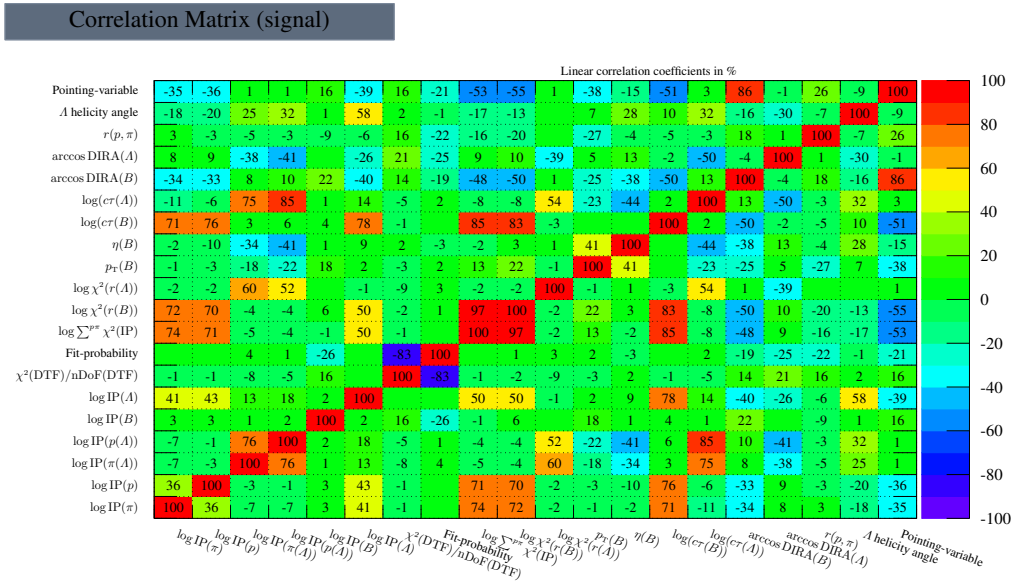


Figure E.5: Correlations between the input variables for the 2012 DD signal sample.

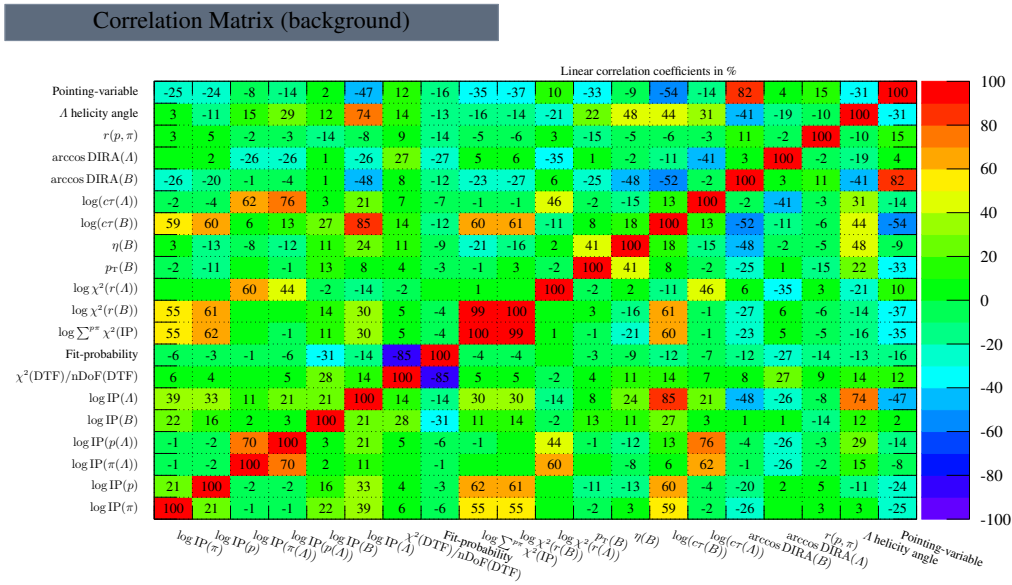


Figure E.6: Correlations between the input variables for the 2012 DD background sample.

# Appendix F

## Breakdown of the Selection Efficiencies

### F.1 Generator Efficiencies

The generator-level efficiencies for all daughters to satisfy  $10 < \theta < 400$  mrad – averaged over the magnet up and down samples – for both  $\bar{B}^0_{(s)} \rightarrow \Lambda \bar{p} h^+$  signal modes are collected in Table F.1. As expected all numbers are rather similar, slightly higher for the  $B^0_s$  mode and for 2012 compared with 2011.

Table F.1: Generator-level efficiencies obtained on the MC samples for both years.

Decay mode	$\varepsilon_{\text{gen}}(\%)$	
	2011	2012
$\bar{B}^0 \rightarrow \Lambda \bar{p} \pi^+$	$21.28 \pm 0.03$	$21.52 \pm 0.03$
$B^0_s \rightarrow \Lambda \bar{p} K^+$	$22.01 \pm 0.05$	$22.37 \pm 0.05$
$\bar{B}^0 \rightarrow \Sigma^0 \bar{p} \pi^+$	$21.13 \pm 0.06$	$21.54 \pm 0.05$
$\bar{B}^0_s \rightarrow \Sigma^0 \bar{p} K^+$	$22.14 \pm 0.05$	$22.35 \pm 0.04$



## F.2 Stripping Efficiencies

Table F.2 summarises the (combined) reconstruction and stripping selection efficiencies obtained from MC for all relevant decay modes separately according to the year and the  $\Lambda$ -daughter reconstruction type. These efficiencies also incorporate the reconstruction efficiencies for all final-state particles. All quoted numbers are again weighted averages over the magnet up and down samples.

Table F.2: Reconstruction and stripping selection efficiencies relative to the generation level, obtained on the MC samples, for both track reconstruction types and years.

Decay mode	Reco.	$\varepsilon_{\text{strip/gen}} (\%)$	
		2011	2012
$\bar{B}^0 \rightarrow \Lambda \bar{p} \pi^+$	LL	$4.42 \pm 0.03$	$3.60 \pm 0.02$
	DD	$15.59 \pm 0.06$	$13.94 \pm 0.04$
$B_s^0 \rightarrow \Lambda \bar{p} K^+$	LL	$4.26 \pm 0.03$	$3.61 \pm 0.02$
	DD	$15.77 \pm 0.06$	$14.62 \pm 0.04$
$\bar{B}^0 \rightarrow \Sigma^0 \bar{p} \pi^+$	LL	$3.99 \pm 0.07$	$2.43 \pm 0.04$
	DD	$14.06 \pm 0.14$	$9.62 \pm 0.07$
$\bar{B}_s^0 \rightarrow \Sigma^0 \bar{p} K^+$	LL	$3.82 \pm 0.05$	$3.19 \pm 0.03$
	DD	$14.1 \pm 0.1$	$13.10 \pm 0.07$

### F.3 Trigger Efficiencies

The trigger efficiencies are calculated on MC with respect to stripped events, but prior to the application of the MVA and PID requirements. All results are collected in Tables F.3 to F.5, which present the numbers independently for each data taking period. The efficiencies per trigger level also also detailed. The “overall” trigger efficiencies are the product of the three per-level efficiencies. As expected, the overall efficiencies for the DD candidates are lower than the corresponding efficiencies for the LL candidates.

Table F.3: Trigger efficiencies obtained on the MC samples for 2011. Refer to the text for details.

Decay mode	Reco.	$\varepsilon_{L0/strip}(\%)$	$\varepsilon_{HLT1/L0}(\%)$	$\varepsilon_{HLT2/HLT1}(\%)$	$\varepsilon_{trig/strip}(\%)$
$\bar{B}^0 \rightarrow \Lambda \bar{p} \pi^+$	LL	$47.31 \pm 0.62$	$71.72 \pm 1.20$	$61.41 \pm 1.27$	$20.84 \pm 0.37$
	DD	$49.18 \pm 0.34$	$63.82 \pm 0.58$	$52.44 \pm 0.63$	$16.46 \pm 0.17$
$B_s^0 \rightarrow \Lambda \bar{p} K^+$	LL	$47.29 \pm 0.64$	$73.69 \pm 1.25$	$64.11 \pm 1.33$	$22.34 \pm 0.40$
	DD	$48.56 \pm 0.34$	$66.16 \pm 0.59$	$54.73 \pm 0.64$	$17.58 \pm 0.18$
$\bar{B}^0 \rightarrow \Sigma^0 \bar{p} \pi^+$	LL	$48.20 \pm 1.52$	$71.60 \pm 2.86$	$58.38 \pm 2.93$	$20.15 \pm 0.88$
	DD	$48.64 \pm 0.41$	$63.47 \pm 1.40$	$51.16 \pm 1.52$	$15.64 \pm 0.41$
$\bar{B}_s^0 \rightarrow \Sigma^0 \bar{p} K^+$	LL	$46.51 \pm 1.07$	$72.50 \pm 2.13$	$61.58 \pm 2.23$	$20.76 \pm 0.65$
	DD	$48.02 \pm 0.57$	$65.78 \pm 1.02$	$55.52 \pm 1.12$	$17.54 \pm 0.31$

Table F.4: Trigger efficiencies obtained on the MC samples for 2012a. Refer to the text for details.

Decay mode	Reco.	$\varepsilon_{L0/strip}(\%)$	$\varepsilon_{HLT1/L0}(\%)$	$\varepsilon_{HLT2/HLT1}(\%)$	$\varepsilon_{trig/strip}(\%)$
$\bar{B}^0 \rightarrow \Lambda \bar{p} \pi^+$	LL	$47.86 \pm 0.97$	$66.30 \pm 1.75$	$78.26 \pm 2.41$	$24.83 \pm 0.64$
	DD	$48.95 \pm 0.49$	$58.62 \pm 0.79$	$54.83 \pm 0.98$	$15.74 \pm 0.24$
$B_s^0 \rightarrow \Lambda \bar{p} K^+$	LL	$48.12 \pm 0.87$	$67.10 \pm 1.61$	$79.35 \pm 2.31$	$25.62 \pm 0.62$
	DD	$49.17 \pm 0.48$	$59.11 \pm 0.77$	$55.62 \pm 0.96$	$16.16 \pm 0.23$

Table F.5: Trigger efficiencies obtained on the MC samples for 2012b. Refer to the text for details.

Decay mode	Reco.	$\varepsilon_{L0/strip}(\%)$	$\varepsilon_{HLT1/L0}(\%)$	$\varepsilon_{HLT2/HLT1}(\%)$	$\varepsilon_{trig/strip}(\%)$
$\bar{B}^0 \rightarrow \Lambda \bar{p} \pi^+$	LL	$44.97 \pm 0.48$	$73.62 \pm 0.99$	$69.75 \pm 1.11$	$23.09 \pm 0.31$
	DD	$45.59 \pm 0.24$	$64.46 \pm 0.46$	$65.86 \pm 0.58$	$19.36 \pm 0.14$
$B_s^0 \rightarrow \Lambda \bar{p} K^+$	LL	$44.32 \pm 0.47$	$74.51 \pm 1.01$	$71.55 \pm 1.13$	$23.63 \pm 0.32$
	DD	$44.87 \pm 0.24$	$65.81 \pm 0.46$	$67.62 \pm 0.57$	$19.97 \pm 0.14$
$\bar{B}^0 \rightarrow \Sigma^0 \bar{p} \pi^+$	LL	$43.59 \pm 1.12$	$71.70 \pm 2.38$	$66.54 \pm 2.66$	$20.80 \pm 0.71$
	DD	$45.10 \pm 0.57$	$63.36 \pm 1.08$	$64.20 \pm 1.36$	$18.35 \pm 0.33$
$\bar{B}_s^0 \rightarrow \Sigma^0 \bar{p} K^+$	LL	$44.55 \pm 0.81$	$73.56 \pm 1.74$	$70.57 \pm 1.97$	$22.61 \pm 0.54$
	DD	$44.17 \pm 0.40$	$65.30 \pm 0.78$	$66.48 \pm 0.98$	$19.18 \pm 0.24$

## F.4 Selection Efficiencies

The selection efficiencies, Table F.6, are calculated on MC with respect to stripped and triggered events. They take into account the efficiencies for the candidates to pass the preselection cuts, the veto requirements, and the actual MVA selection. The table also shows the efficiencies for stripped-only events.

Table F.6: Selection efficiencies obtained on the MC samples, for both track reconstruction types and years.

Decay mode	Reco.	$\epsilon_{\text{sel}/\text{trig}}(\%)$			$\epsilon_{\text{sel}/\text{strip}}(\%)$		
		2011	2012a	2012b	2011	2012a	2012b
$\bar{B}^0 \rightarrow \Lambda \bar{p} \pi^+$	LL	$73.63 \pm 1.85$	$87.3 \pm 3.0$	$89.49 \pm 1.59$	$15.34 \pm 0.31$	$21.67 \pm 0.59$	$20.67 \pm 0.29$
	DD	$74.54 \pm 1.12$	$85.0 \pm 0.83$	$83.09 \pm 0.84$	$12.27 \pm 0.15$	$13.38 \pm 0.22$	$16.08 \pm 0.13$
$B_s^0 \rightarrow \Lambda \bar{p} K^+$	LL	$72.43 \pm 1.81$	$86.7 \pm 2.9$	$88.42 \pm 1.56$	$16.18 \pm 0.33$	$20.87 \pm 0.71$	$20.89 \pm 0.29$
	DD	$74.04 \pm 1.07$	$84.3 \pm 1.9$	$81.89 \pm 0.79$	$13.02 \pm 0.15$	$13.12 \pm 0.21$	$16.35 \pm 0.13$
$\bar{B}^0 \rightarrow \Sigma^0 \bar{p} \pi^+$	LL	$73.52 \pm 4.51$	--	$87.31 \pm 3.97$	$14.81 \pm 0.74$	--	$18.16 \pm 0.65$
	DD	$73.06 \pm 2.72$	--	$80.92 \pm 2.01$	$11.43 \pm 0.34$	--	$14.85 \pm 0.29$
$\bar{B}_s^0 \rightarrow \Sigma^0 \bar{p} K^+$	LL	$70.83 \pm 3.13$	--	$85.37 \pm 2.69$	$14.71 \pm 0.33$	--	$19.30 \pm 0.49$
	DD	$68.91 \pm 1.74$	--	$79.32 \pm 1.37$	$12.08 \pm 0.15$	--	$15.21 \pm 0.21$

## F.5 PID Efficiencies

PID selection criteria are applied to the bachelor meson of the  $\Lambda\bar{p}h^+$  candidates as well as to the proton originating from the  $B$  candidate. There is no PID selection applied to the  $\Lambda$  daughters, therefore the efficiencies listed in Tables F.7 and F.8 apply to both the LL and the DD samples. The former (latter) table gives the efficiencies of the bachelor (proton) meson PID selection.

The standard configuration of the `PIDCalib` package is chosen in order to determine the kaon and pion efficiencies; for the protons a mixture of the  $\Lambda$  and  $\Lambda_c^+$  samples is used, *i.e.* `P_IncLc as PIDCalib` option. The default binning schemes are employed but the efficiencies are determined depending on the momentum and pseudorapidity of the hadrons. The proton selection efficiency is determined using version 3 of the MC tuning.

Table F.7: PID efficiencies of the bachelor meson to be identified as a pion or a kaon for both years. The values and their uncertainties are determined by the `PIDCalib` package. The proton PID efficiency is not included.

Decay mode	Reco.	2011 $\varepsilon_{\text{PID}}(\%)$		2012 $\varepsilon_{\text{PID}}(\%)$	
		$\varepsilon_{h \rightarrow \pi}$	$\varepsilon_{h \rightarrow K}$	$\varepsilon_{h \rightarrow \pi}$	$\varepsilon_{h \rightarrow K}$
$\bar{B}^0 \rightarrow \Lambda\bar{p}\pi^+$	LL	$89.619 \pm 0.001$	$10.250 \pm 0.001$	$90.6944 \pm 0.0006$	$9.3042 \pm 0.0006$
	DD	$89.5576 \pm 0.0005$	$10.2935 \pm 0.0005$	$90.7768 \pm 0.0004$	$9.1600 \pm 0.0004$
$B_s^0 \rightarrow \Lambda\bar{p}K^+$	LL	$4.434 \pm 0.002$	$95.573 \pm 0.002$	$4.781 \pm 0.002$	$95.219 \pm 0.002$
	DD	$4.0354 \pm 0.0008$	$95.9324 \pm 0.0008$	$4.3015 \pm 0.0006$	$95.6744 \pm 0.0006$
$\bar{B}^0 \rightarrow \Sigma^0\bar{p}\pi^+$	LL	$89.577 \pm 0.004$	$10.369 \pm 0.004$	$90.650 \pm 0.003$	$9.340 \pm 0.003$
	DD	$89.445 \pm 0.002$	$10.4415 \pm 0.002$	$90.702 \pm 0.001$	$9.214 \pm 0.001$
$\bar{B}_s^0 \rightarrow \Sigma^0\bar{p}K^+$	LL	$4.517 \pm 0.003$	$95.489 \pm 0.003$	$4.867 \pm 0.003$	$95.133 \pm 0.003$
	DD	$4.068 \pm 0.001$	$95.9015 \pm 0.0014$	$4.3368 \pm 0.0009$	$95.6337 \pm 0.0009$

Table F.8: PID efficiencies of the proton selection cut for both years. The values and their uncertainties are determined by the PIDCalib package. The bachelor meson PID efficiency is not included. There is no PID selection imposed on the  $\Lambda$  daughters.

Decay mode	Reco.	$\varepsilon_{p \rightarrow p}(\%)$	
		2011	2012
$\bar{B}^0 \rightarrow \Lambda \bar{p} \pi^+$	LL	$79.577 \pm 0.034$	$82.462 \pm 0.019$
	DD	$79.968 \pm 0.022$	$83.0135 \pm 0.009$
$B_s^0 \rightarrow \Lambda \bar{p} K^+$	LL	$79.430 \pm 0.034$	$82.244 \pm 0.019$
	DD	$79.642 \pm 0.021$	$82.771 \pm 0.009$
$\bar{B}^0 \rightarrow \Sigma^0 \bar{p} \pi^+$	LL	$80.095 \pm 0.082$	$82.889 \pm 0.045$
	DD	$80.363 \pm 0.060$	$83.391 \pm 0.022$
$\bar{B}_s^0 \rightarrow \Sigma^0 \bar{p} K^+$	LL	$80.23 \pm 0.06$	$82.965 \pm 0.033$
	DD	$80.822 \pm 0.043$	$83.808 \pm 0.016$
$\bar{B}^0 \rightarrow \Lambda \bar{p} \rho^+$	LL	$83.18 \pm 0.11$	$85.387 \pm 0.066$
	DD	$83.859 \pm 0.053$	$86.332 \pm 0.029$
$\bar{B}_s^0 \rightarrow \Lambda \bar{p} K^{*+}$	LL	$82.73 \pm 0.09$	$85.110 \pm 0.053$
	DD	$83.353 \pm 0.048$	$85.7935 \pm 0.027$

## F.6 Variation of the Efficiency Across the Dalitz Plot

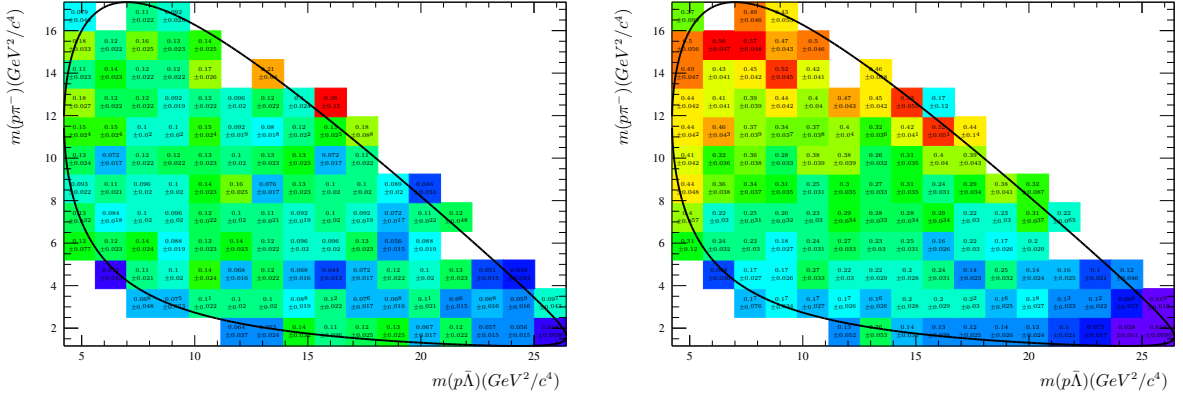


Figure F.1: Plot of the efficiency as function of the two Dalitz plot variables  $\varepsilon(m^2(\Lambda \bar{p}), m^2(\bar{p} h^+))$  for the  $\bar{B}^0 \rightarrow \Lambda \bar{p} \pi^+$  mode in 2011 LL (left) and DD(right).

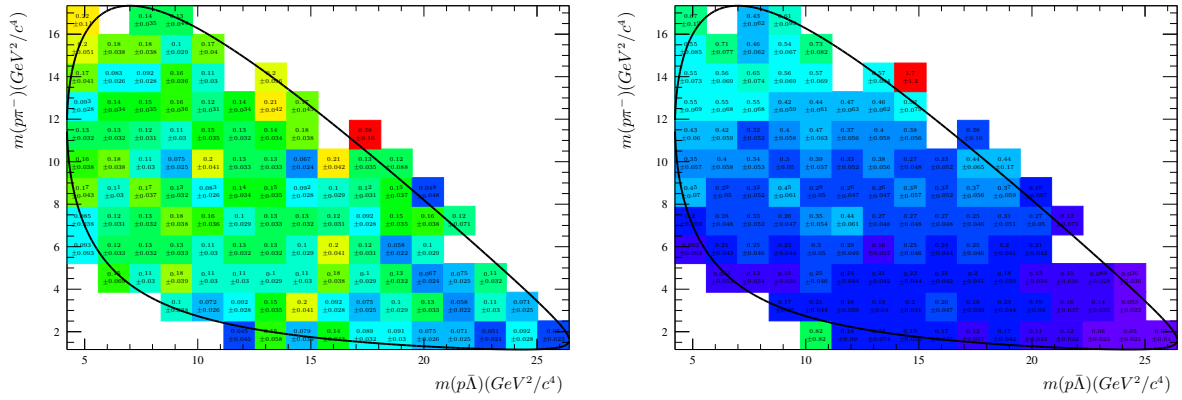


Figure F.2: Plot of the efficiency as function of the two Dalitz plot variables  $\varepsilon(m^2(\Lambda\bar{p}), m^2(\bar{p}h^+))$  for the  $\bar{B}^0 \rightarrow \Lambda\bar{p}\pi^+$  mode in 2012a LL (left) and DD(right).

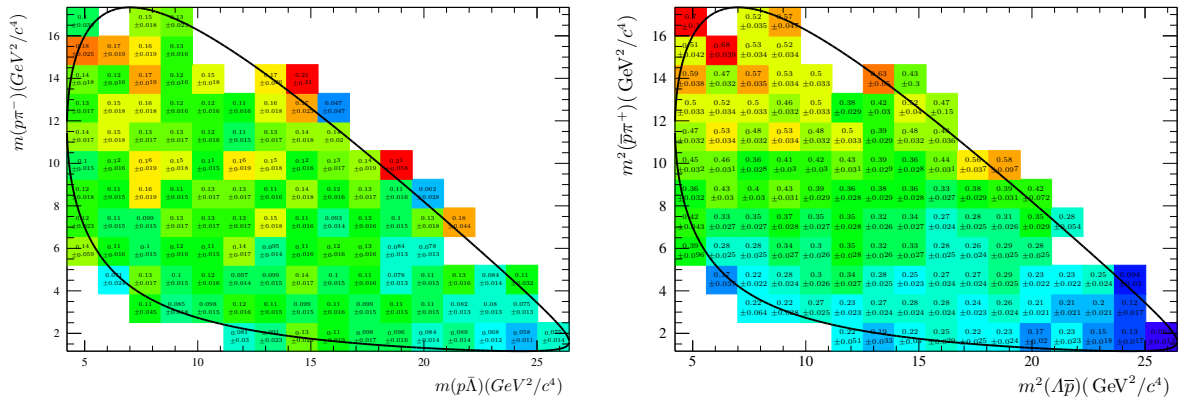


Figure F.3: Plot of the efficiency as function of the two Dalitz plot variables  $\varepsilon(m^2(\Lambda\bar{p}), m^2(\bar{p}h^+))$  for the  $\bar{B}^0 \rightarrow \Lambda\bar{p}\pi^+$  mode in 2012b LL (left) and DD(right).

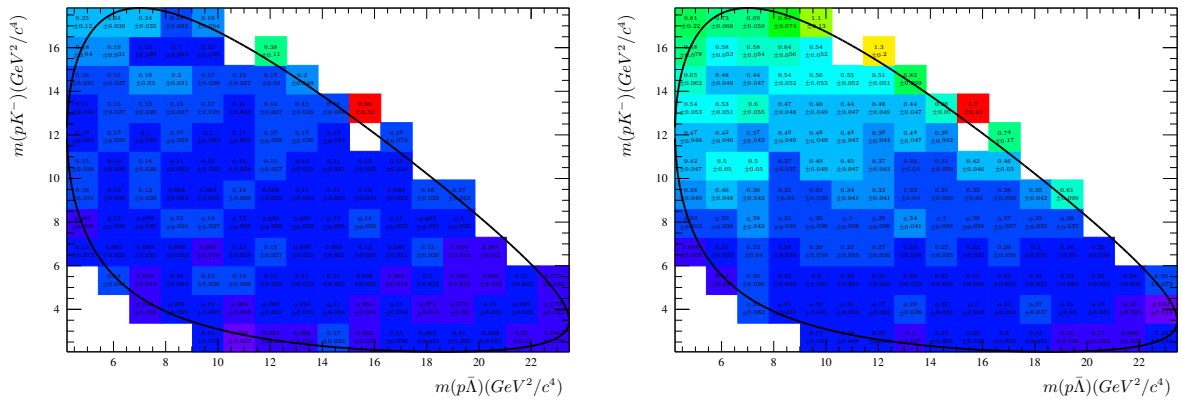


Figure F.4: Plot of the efficiency as function of the two Dalitz plot variables  $\varepsilon(m^2(\Lambda\bar{p}), m^2(\bar{p}h^+))$  for the  $\bar{B}_s^0 \rightarrow \Lambda\bar{p}K^+$  mode in 2011 LL (left) and DD(right).

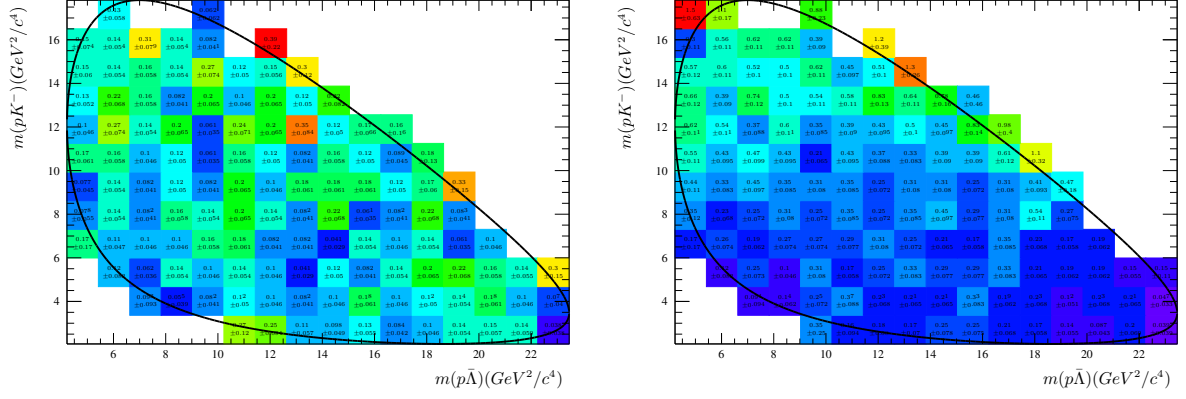


Figure F.5: Plot of the efficiency as function of the two Dalitz plot variables  $\varepsilon(m^2(\Lambda\bar{p}), m^2(\bar{p}h^+))$  for the  $\bar{B}_s^0 \rightarrow \Lambda\bar{p}K^+$  mode in 2012a LL (left) and DD(right).

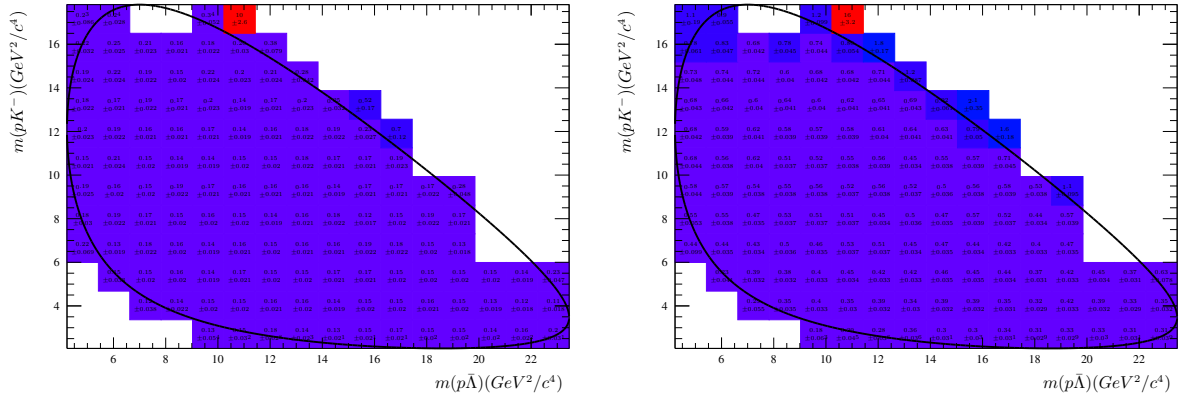


Figure F.6: Plot of the efficiency as function of the two Dalitz plot variables  $\varepsilon(m^2(\Lambda\bar{p}), m^2(\bar{p}h^+))$  for the  $\bar{B}_s^0 \rightarrow \Lambda\bar{p}K^+$  mode in 2012b LL (left) and DD(right).

# Appendix G

## List of Shape Parameters

Table G.1: Shape parameters for the  $\bar{B}^0 \rightarrow A\bar{p}\pi^+$  mode used in the corresponding samples. For the  $\pi$  hypothesis a sum of two Novosibirsk functions is used with the parameters  $\mu_i$ ,  $\sigma_i$ , and  $\alpha_i$ , the fraction between these two is described by  $f$ . For the  $K$  hypothesis a sum of a Gaussian, with parameters  $\mu$  and  $\sigma$ , and the modified Fermi-Function, with the parameters  $T$ ,  $m_0$ , and  $a$ , is used, the fraction is again given by  $f$ . The fit results are shown in Fig. 3.22.

LL		DD	
$\pi$ hypothesis	$K$ hypothesis	$\pi$ hypothesis	$K$ hypothesis
$\mu_1 = 5281.31 \text{ MeV}/c^2$	$\mu = 5325.6 \text{ MeV}/c^2$	$\mu_1 = 5283.58 \text{ MeV}/c^2$	$\mu = 5323.7 \text{ MeV}/c^2$
$\sigma_1 = 12.2 \text{ MeV}/c^2$	$\sigma = 14.9 \text{ MeV}/c^2$	$\sigma_1 = 13.55 \text{ MeV}/c^2$	$\sigma = 18.06 \text{ MeV}/c^2$
$\alpha_1 = -0.0004$	$m_0 = 5314.6 \text{ MeV}/c^2$	$\alpha_1 = 0.481$	$m_0 = 5330 \text{ MeV}/c^2$
$\mu_2 = 5274.9 \text{ MeV}/c^2$	$T = 301 (\text{MeV}/c^2)^{-1}$	$\mu_2 = 5278.97 \text{ MeV}/c^2$	$T = 194 (\text{MeV}/c^2)^{-1}$
$\sigma_2 = 29.7 \text{ MeV}/c^2$	$a = 36.5 (\text{MeV}/c^2)^{-1}$	$\sigma_2 = 12.82 \text{ MeV}/c^2$	$a = 33.3 (\text{MeV}/c^2)^{-1}$
$\alpha_2 = 0.009$	$f = 0.833$	$\alpha_2 = -0.2198$	$f = 0.52$
$f = 0.833$		$f = 0.366$	

Table G.2: Shape parameters for the  $\bar{B}_s^0 \rightarrow A\bar{p}K^+$  mode used in the corresponding samples. For the  $K$  hypothesis, a sum of two Novosibirsk functions is used, with the parameters  $\mu_i$ ,  $\sigma_i$ , and  $\alpha_i$ , the fraction between these two is described by  $f$ . For the  $\pi$  hypothesis, a sum of a Gaussian, with parameters  $\mu$  and  $\sigma$ , and the modified Fermi-Function, with the parameters  $T$ ,  $m_0$ , and  $a$ , is used, the fraction is again given by  $f$ . The fit results are shown in Fig. 3.23.

LL		DD	
$\pi$ hypothesis	$K$ hypothesis	$\pi$ hypothesis	$K$ hypothesis
$\mu = 5323.3 \text{ MeV}/c^2$	$\mu_1 = 5376.88 \text{ MeV}/c^2$	$\mu = 5325.81 \text{ MeV}/c^2$	$\mu_1 = 5362.0 \text{ MeV}/c^2$
$\sigma = 19.6 \text{ MeV}/c^2$	$\sigma_1 = 12.39 \text{ MeV}/c^2$	$\sigma = 17.81 \text{ MeV}/c^2$	$\sigma_1 = 28.7 \text{ MeV}/c^2$
$m_0 = 5269$	$\alpha_1 = -0.0113$	$m_0 = 5299 \text{ MeV}/c^2$	$\alpha_1 = -0.0410$
$T = 124 (\text{MeV}/c^2)^{-1}$	$\mu_2 = 5365.5 \text{ MeV}/c^2$	$T = 220 (\text{MeV}/c^2)^{-1}$	$\mu_2 = 5367.78 \text{ MeV}/c^2$
$a = 56 (\text{MeV}/c^2)^{-1}$	$\sigma_2 = 30.5 \text{ MeV}/c^2$	$a = 89 (\text{MeV}/c^2)^{-1}$	$\sigma_2 = 11.92 \text{ MeV}/c^2$
$f = 0.221$	$\alpha_2 = 0.029$	$f = 0.811$	$\alpha_2 = -0.0165$
	$f = 0.872$		$f = 0.108$



Table G.3: Shape parameters for the  $\bar{B}^0 \rightarrow \Sigma^0 \bar{p} \pi^+$  mode used in the corresponding samples. For the LL case under  $\pi$  hypothesis, a single modified Fermi-function, with the parameters  $T$ ,  $m_0$  is used and a sum of a Novosibirsk functions, with the parameters  $\mu_1$ ,  $\sigma_1$ , and  $\alpha$ , and a Gaussian, with the parameters  $\mu_2$  and  $\sigma_2$ , the fraction is given by  $f$ . For the  $K$  hypothesis, a modified Fermi-function, with the parameters  $T$ ,  $m_0$ , and  $a$ , is used. The fit results are shown in Fig. 3.24.

LL		DD	
$\pi$ hypothesis	$K$ hypothesis	$\pi$ hypothesis	$K$ hypothesis
$m_0 = 5220.4 \text{ MeV}/c^2$ $T = 331 (\text{MeV}/c^2)^{-1}$ $a = 66.0 (\text{MeV}/c^2)^{-1}$	$m_0 = 5161 \text{ MeV}/c^2$ $T = 237 (\text{MeV}/c^2)^{-1}$ $a = 197 (\text{MeV}/c^2)^{-1}$	$\mu_1 = 5201.4 \text{ MeV}/c^2$ $\sigma_1 = 55.8 \text{ MeV}/c^2$ $\alpha_1 = 0.511$ $\mu_2 = 5310 \text{ MeV}/c^2$ $\sigma_2 = 125 \text{ MeV}/c^2$ $\alpha_2 = -0.2198$ $f = 0.9951$	$m_0 = 5168 \text{ MeV}/c^2$ $T = 235 (\text{MeV}/c^2)^{-1}$ $a = 196 (\text{MeV}/c^2)^{-1}$

Table G.4: Shape parameters for the  $\bar{B}_s^0 \rightarrow \Sigma^0 \bar{p} K^+$  mode used in the corresponding samples. For the  $\pi$  hypothesis, a single modified Fermi-function, with the parameters  $T$ ,  $m_0$  is used. For LL under  $K$  hypothesis, a sum a modified Fermi-function, with the parameters  $T$ ,  $m_0$ , and  $a$ , and a Novosibirsk, with the parameters  $\mu$ ,  $\sigma$ , and  $\alpha$ , is used, the fraction is given by  $f$ . For DD under  $K$  hypothesis, a sum of two Novosibirsk functions is used, with the parameters  $\mu_i$ ,  $\sigma_i$ , and  $\alpha_i$ , the fraction is determined by  $f$ . The fit results are shown in Fig. 3.25.

LL		DD	
$\pi$ hypothesis	$K$ hypothesis	$\pi$ hypothesis	$K$ hypothesis
$m_0 = 5272 \text{ MeV}/c^2$ $T = 386 (\text{MeV}/c^2)^{-1}$ $a = 57.9 (\text{MeV}/c^2)^{-1}$	$\mu = 5278.4 \text{ MeV}/c^2$ $\sigma = 56.8 \text{ MeV}/c^2$ $\alpha = 0.359$ $m_0 = 5292 \text{ MeV}/c^2$ $T = 3 (\text{MeV}/c^2)^{-1}$ $a = 207 (\text{MeV}/c^2)^{-1}$ $f = 0.998$	$m_0 = 5256 \text{ MeV}/c^2$ $T = 300 (\text{MeV}/c^2)^{-1}$ $a = 70.9 (\text{MeV}/c^2)^{-1}$	$\mu_1 = 5200.7 \text{ MeV}/c^2$ $\sigma_1 = 61.5 \text{ MeV}/c^2$ $\alpha_1 = -0.0886$ $\mu_2 = 5297.2 \text{ MeV}/c^2$ $\sigma_2 = 43.7 \text{ MeV}/c^2$ $\alpha_2 = 0.440$ $f = 0.297$

# Appendix H

## Additional Fit information

### H.1 Fit to the Full Data with Dalitz Plot Corrected Efficiencies

Table H.1: Fit yield parameters for the full Dalitz plot using the recalculated efficiencies. It should be noted that the  $\Sigma^0$  ratios have no physical meaning per construction.

Floating parameter	Fit value and uncertainties
$N_{11}^{LL}(\bar{B}^0 \rightarrow \Lambda \bar{p} \pi^+)$	$43.0^{+8.4}_{-7.6}$
$N_{12}^{LL}(\bar{B}^0 \rightarrow \Lambda \bar{p} \pi^+)$	$149.1^{+16.4}_{-15.5}$
$\gamma_{\bar{B}_s^0 \rightarrow \Lambda \bar{p} K^+}$	$0.392^{+0.044}_{-0.040}$
$\gamma_{\bar{B}^0 \rightarrow \Sigma^0 \bar{p} \pi^+}$	$2.8^{+2.6}_{-2.5} \times 10^{-5}$
$\gamma_{\bar{B}_s^0 \rightarrow \Sigma^0 \bar{p} K^+}$	$3.9^{+1.6}_{-1.5} \times 10^{-5}$
$N_{11,\pi,LL}^{Bkg}$	$145.1^{+13.5}_{-12.9}$
$N_{12,\pi,LL}^{Bkg}$	$945.9^{+33.8}_{-33.2}$
$N_{11,\pi,DD}^{Bkg}$	$590.9^{+28.5}_{-27.9}$
$N_{12,\pi,DD}^{Bkg}$	$2813.4^{+62.1}_{-61.6}$
$N_{11,K,LL}^{Bkg}$	$77.2^{+10.3}_{-9.7}$
$N_{12,K,LL}^{Bkg}$	$360.0^{+22.9}_{-22.3}$
$N_{11,K,DD}^{Bkg}$	$209^{+17.0}_{-16.3}$
$N_{12,K,DD}^{Bkg}$	$972.1^{+36.2}_{-35.6}$

Table H.2: Shape parameters for the full Dalitz plot using the recalculated efficiencies.

Floating parameter	Fit value and uncertainties
$\Delta m$	$4.54^{+0.89}_{-0.88}$
$a_{11,\pi,LL}^{Bkg}$	$-12.2^{+4.2}_{-4.3} \times 10^{-4}$
$a_{12,\pi,LL}^{Bkg}$	$-13.3^{+1.7}_{-1.7} \times 10^{-4}$
$a_{11,\pi,DD}^{Bkg}$	$-10.5^{+2.1}_{-2.1} \times 10^{-4}$
$a_{12,\pi,DD}^{Bkg}$	$-7.85^{+0.95}_{-0.95} \times 10^{-4}$
$a_{11,K,LL}^{Bkg}$	$-1.8^{+5.8}_{-5.9} \times 10^{-4}$
$a_{12,K,LL}^{Bkg}$	$-7.4^{+2.7}_{-2.8} \times 10^{-4}$
$a_{11,K,DD}^{Bkg}$	$-12.0^{+3.7}_{-3.8} \times 10^{-4}$
$a_{12,K,DD}^{Bkg}$	$-3.2^{+1.6}_{-1.7} \times 10^{-4}$

Table H.3: Efficiency related parameters for the full Dalitz plot using the recalculated efficiencies. Except  $r_{11}^{\text{DD}}$  and  $r_{12}^{\text{DD}}$  all determined through Gaussian constraints.

Floating parameter	Fit value and uncertainties
$r_{11}^{\text{DD}}$	$1.05^{+0.27}_{-0.21}$
$r_{12}^{\text{DD}}$	$0.704^{+0.098}_{-0.085}$
$r_{\text{LL/DD},11}^{\text{MC}}$	$0.311^{+0.023}_{-0.023}$
$r_{\text{LL/DD},12}^{\text{MC}}$	$0.303^{+0.011}_{-0.011}$
$\delta_{\text{LL},11}^{\bar{B}_s^0 \rightarrow \Lambda \bar{p} K^+}$	$1.124^{+0.089}_{-0.088}$
$\delta_{\text{LL},12}^{\bar{B}_s^0 \rightarrow \Lambda \bar{p} K^+}$	$1.300^{+0.049}_{-0.049}$
$\delta_{\text{DD},11}^{\bar{B}_s^0 \rightarrow \Lambda \bar{p} K^+}$	$1.124^{+0.067}_{-0.067}$
$\delta_{\text{DD},12}^{\bar{B}_s^0 \rightarrow \Lambda \bar{p} K^+}$	$1.271^{+0.069}_{-0.069}$
$\delta_{\text{LL},11}^{\bar{B}^0 \rightarrow \Sigma^0 \bar{p} \pi^+}$	$2092^{+179}_{-179}$
$\delta_{\text{LL},12}^{\bar{B}^0 \rightarrow \Sigma^0 \bar{p} \pi^+}$	$3752^{+205}_{-205}$
$\delta_{\text{DD},11}^{\bar{B}^0 \rightarrow \Sigma^0 \bar{p} \pi^+}$	$1970^{+115}_{-115}$
$\delta_{\text{DD},12}^{\bar{B}^0 \rightarrow \Sigma^0 \bar{p} \pi^+}$	$3757^{+122}_{-122}$
$\delta_{\text{LL},11}^{\bar{B}_s^0 \rightarrow \Sigma^0 \bar{p} K^+}$	$4943^{+349}_{-349}$
$\delta_{\text{LL},12}^{\bar{B}_s^0 \rightarrow \Sigma^0 \bar{p} K^+}$	$11400^{+454}_{-454}$
$\delta_{\text{DD},11}^{\bar{B}_s^0 \rightarrow \Sigma^0 \bar{p} K^+}$	$4678^{+243}_{-243}$
$\delta_{\text{DD},12}^{\bar{B}_s^0 \rightarrow \Sigma^0 \bar{p} K^+}$	$10077^{+260}_{-260}$

## H.2 Fit to the Full Data with Dalitz Plot Corrected Efficiencies for the Enhancement Only.

Table H.4: Fit yield parameters for the enhancement only region of the Dalitz plot using the recalculated efficiencies. It should be noted that the  $\Sigma^0$  ratios have no physical meaning per construction.

Floating parameter	Fit value and uncertainties
$N_{11}^{LL}(\bar{B}^0 \rightarrow \Lambda \bar{p} \pi^+)$	$43.8^{+7.7}_{-7.0}$
$N_{12}^{LL}(\bar{B}^0 \rightarrow \Lambda \bar{p} \pi^+)$	$137.3^{+15.2}_{-13.9}$
$r_{\bar{B}_s^0 \rightarrow \Lambda \bar{p} K^+}$	$0.355^{+0.039}_{-0.036}$
$r_{\bar{B}^0 \rightarrow \Sigma^0 \bar{p} \pi^+}$	$3.0^{+2.1}_{-2.0} \times 10^{-5}$
$r_{\bar{B}_s^0 \rightarrow \Sigma^0 \bar{p} K^+}$	$2.8^{+1.4}_{-1.3} \times 10^{-5}$
$N_{11,\pi,LL}^{Bkg}$	$58.3^{+9.2}_{-8.5}$
$N_{12,\pi,LL}^{Bkg}$	$546.4^{+26.2}_{-25.2}$
$N_{11,\pi,DD}^{Bkg}$	$401.7^{+23.5}_{-22.7}$
$N_{12,\pi,DD}^{Bkg}$	$1834.1^{+50.5}_{-50.1}$
$N_{11,K,LL}^{Bkg}$	$29.9^{+6.8}_{-6.1}$
$N_{12,K,LL}^{Bkg}$	$208.6^{+17.2}_{-16.7}$
$N_{11,K,DD}^{Bkg}$	$122.5^{+13.6}_{-12.6}$
$N_{12,K,DD}^{Bkg}$	$640.9^{+29.8}_{-29.1}$

Table H.5: Shape parameters for the enhancement only region of the Dalitz plot using the recalculated efficiencies.

Floating parameter	Fit value and uncertainties
$\Delta m$	$3.79^{+0.81}_{-0.81}$
$a_{11,\pi,LL}^{Bkg}$	$-20.5^{+6.9}_{-7.2} \times 10^{-4}$
$a_{12,\pi,LL}^{Bkg}$	$-11.3^{+2.2}_{-2.2} \times 10^{-4}$
$a_{11,\pi,DD}^{Bkg}$	$-7.8^{+2.6}_{-2.5} \times 10^{-4}$
$a_{12,\pi,DD}^{Bkg}$	$-7.2^{+1.2}_{-1.2} \times 10^{-4}$
$a_{11,K,LL}^{Bkg}$	$-22^{+11}_{-12} \times 10^{-4}$
$a_{12,K,LL}^{Bkg}$	$-6.3^{+3.6}_{-3.7} \times 10^{-4}$
$a_{11,K,DD}^{Bkg}$	$-11.4^{+4.9}_{-5.1} \times 10^{-4}$
$a_{12,K,DD}^{Bkg}$	$-6.0^{+2.1}_{-2.1} \times 10^{-4}$

Table H.6: Efficiency related parameters for the enhancement only region of the Dalitz plot using the recalculated efficiencies. Except  $r_{11}^{\text{DD}}$  and  $r_{12}^{\text{DD}}$  all determined through Gaussian constraints.

Floating parameter	Fit value and uncertainties
$r_{11}^{\text{DD}}$	$1.00^{+0.23}_{-0.18}$
$r_{12}^{\text{DD}}$	$0.80^{+0.11}_{-0.09}$
$r_{\text{LL/DD},11}^{\text{MC}}$	$0.311^{+0.023}_{-0.023}$
$r_{\text{LL/DD},12}^{\text{MC}}$	$0.303^{+0.011}_{-0.011}$
$\delta_{\text{LL},11}^{\bar{B}_s^0 \rightarrow A\bar{p}K^+}$	$1.126^{+0.088}_{-0.088}$
$\delta_{\text{LL},12}^{\bar{B}_s^0 \rightarrow A\bar{p}K^+}$	$1.293^{+0.050}_{-0.049}$
$\delta_{\text{DD},11}^{\bar{B}_s^0 \rightarrow A\bar{p}K^+}$	$1.12^{+0.07}_{-0.07}$
$\delta_{\text{DD},12}^{\bar{B}_s^0 \rightarrow A\bar{p}K^+}$	$1.28^{+0.07}_{-0.07}$
$\delta_{\text{LL},11}^{\bar{B}_s^0 \rightarrow \Sigma^0 \bar{p}\pi^+}$	$2100^{+179}_{-179}$
$\delta_{\text{LL},12}^{\bar{B}_s^0 \rightarrow \Sigma^0 \bar{p}\pi^+}$	$3748^{+206}_{-206}$
$\delta_{\text{DD},11}^{\bar{B}_s^0 \rightarrow \Sigma^0 \bar{p}\pi^+}$	$1969^{+115}_{-116}$
$\delta_{\text{DD},12}^{\bar{B}_s^0 \rightarrow \Sigma^0 \bar{p}\pi^+}$	$3756^{+122}_{-121}$
$\delta_{\text{LL},11}^{\bar{B}_s^0 \rightarrow \Sigma^0 \bar{p}K^+}$	$4933^{+351}_{-348}$
$\delta_{\text{LL},12}^{\bar{B}_s^0 \rightarrow \Sigma^0 \bar{p}K^+}$	$11371^{+456}_{-454}$
$\delta_{\text{DD},11}^{\bar{B}_s^0 \rightarrow \Sigma^0 \bar{p}K^+}$	$4693^{+241}_{-245}$
$\delta_{\text{DD},12}^{\bar{B}_s^0 \rightarrow \Sigma^0 \bar{p}K^+}$	$10082^{+261}_{-260}$

### H.3 Fit to the Full Data in Order to Determine for $\mathcal{A}_T$ with Dalitz Plot Corrected Efficiencies Including Dilution Effects

Table H.7: Asymmetry parameters for the  $\mathcal{A}_T$  fit.

Floating parameter	Fit value and uncertainties
$A_T$	$1.0^{+37.1}_{-37.3}$
$\mathcal{A}_T$	$7.6^{+26.9}_{-27.1}$

Table H.8: Fit yield parameters for the  $\mathcal{A}_T$  fit for the  $\bar{B}^0 \rightarrow \Lambda \bar{p} \pi^+$  and  $\mathcal{O} < 0$  sample.

Floating parameter	Fit value and uncertainties
$N_{11}^{LL}(\bar{B}^0 \rightarrow \Lambda \bar{p} \pi^+)$	$10.4^{+2.6}_{-2.2}$
$N_{12}^{LL}(\bar{B}^0 \rightarrow \Lambda \bar{p} \pi^+)$	$36.0^{+6.0}_{-5.4}$
$\gamma_{\bar{B}_s^0 \rightarrow \Lambda \bar{p} K^+}$	$0.34^{+0.10}_{-0.08}$
$\gamma_{\bar{B}^0 \rightarrow \Sigma^0 \bar{p} \pi^+}$	$0.0^{+3.4}_{-3.6} \times 10^{-5}$
$\gamma_{\bar{B}_s^0 \rightarrow \Sigma^0 \bar{p} K^+}$	$2.8^{+2.6}_{-2.3} \times 10^{-5}$
$N_{11,\pi,LL}^{Bkg}$	$27.3^{+5.8}_{-5.2}$
$N_{12,\pi,LL}^{Bkg}$	$158.3^{+13.6}_{-13.2}$
$N_{11,\pi,DD}^{Bkg}$	$106.4^{+11.2}_{-11.2}$
$N_{12,\pi,DD}^{Bkg}$	$492.1^{+23.6}_{-25.5}$
$N_{11,K,LL}^{Bkg}$	$6.8^{+3.4}_{-2.7}$
$N_{12,K,LL}^{Bkg}$	$49.4^{+8.4}_{-7.8}$
$N_{11,K,DD}^{Bkg}$	$32.0^{+6.7}_{-6.0}$
$N_{12,K,DD}^{Bkg}$	$165.4^{+15.4}_{-14.7}$

Table H.9: Fit yield parameters for the  $\mathcal{A}_T$  fit for the  $\bar{B}^0 \rightarrow \Lambda \bar{p} \pi^+$  and  $\mathcal{O} > 0$  sample.

Floating parameter	Fit value and uncertainties
$\gamma_{\bar{B}_s^0 \rightarrow \Lambda \bar{p} K^+}$	$0.310^{+0.096}_{-0.075}$
$\gamma_{\bar{B}^0 \rightarrow \Sigma^0 \bar{p} \pi^+}$	$1.4^{+4.1}_{-1.4} \times 10^{-5}$
$\gamma_{\bar{B}_s^0 \rightarrow \Sigma^0 \bar{p} K^+}$	$4.9^{+3.5}_{-3.0} \times 10^{-5}$
$N_{11,\pi,LL}^{Bkg}$	$21.7^{+5.7}_{-5.0}$
$N_{12,\pi,LL}^{Bkg}$	$143.7^{+13.2}_{-12.5}$
$N_{11,\pi,DD}^{Bkg}$	$110.1^{+12.5}_{-11.8}$
$N_{12,\pi,DD}^{Bkg}$	$505.5^{+26.2}_{-25.4}$
$N_{11,K,LL}^{Bkg}$	$12.8^{+4.5}_{-3.7}$
$N_{12,K,LL}^{Bkg}$	$44.5^{+8.2}_{-7.4}$
$N_{11,K,DD}^{Bkg}$	$38.8^{+7.7}_{-7.0}$
$N_{12,K,DD}^{Bkg}$	$179.0^{+14.5}_{-13.8}$

Table H.10: Fit yield parameters for the  $\mathcal{A}_T$  fit for the  $B^0 \rightarrow \bar{\Lambda}p\pi^-$  and  $\mathcal{O} < 0$  sample.

Floating parameter	Fit value and uncertainties
$N_{11}^{\text{LL}}(\bar{B}^0 \rightarrow \Lambda\bar{p}\pi^+)$	$12.1^{+2.7}_{-2.3}$
$N_{12}^{\text{LL}}(\bar{B}^0 \rightarrow \Lambda\bar{p}\pi^+)$	$34.9^{+5.7}_{-5.1}$
$r_{\bar{B}_s^0 \rightarrow \Lambda\bar{p}K^+}$	$0.45^{+0.12}_{-0.10}$
$r_{\bar{B}^0 \rightarrow \Sigma^0\bar{p}\pi^+}$	$0.0^{+3.4}_{-3.6} \times 10^{-5}$
$r_{\bar{B}_s^0 \rightarrow \Sigma^0\bar{p}K^+}$	$2.2^{+2.0}_{-1.8} \times 10^{-5}$
$N_{11,\pi,\text{LL}}^{\text{Bkg}}$	$19.2^{+5.1}_{-4.4}$
$N_{12,\pi,\text{LL}}^{\text{Bkg}}$	$127.2^{+12.1}_{-11.8}$
$N_{11,\pi,\text{DD}}^{\text{Bkg}}$	$132.0^{+12.3}_{-12.8}$
$N_{12,\pi,\text{DD}}^{\text{Bkg}}$	$489.5^{+23.5}_{-24.4}$
$N_{11,K,\text{LL}}^{\text{Bkg}}$	$13.8^{+4.4}_{-3.7}$
$N_{12,K,\text{LL}}^{\text{Bkg}}$	$66.6^{+9.8}_{-9.2}$
$N_{11,K,\text{DD}}^{\text{Bkg}}$	$27.1^{+6.5}_{-5.7}$
$N_{12,K,\text{DD}}^{\text{Bkg}}$	$152.0^{+14.6}_{-13.9}$

Table H.11: Fit yield parameters for the  $\mathcal{A}_T$  fit for the  $B^0 \rightarrow \bar{\Lambda}p\pi^-$  and  $\mathcal{O} > 0$  sample.

Floating parameter	Fit value and uncertainties
$r_{\bar{B}_s^0 \rightarrow \Lambda\bar{p}K^+}$	$0.33^{+0.10}_{-0.08}$
$r_{\bar{B}^0 \rightarrow \Sigma^0\bar{p}\pi^+}$	$6.6^{+3.9}_{-3.4} \times 10^{-5}$
$r_{\bar{B}_s^0 \rightarrow \Sigma^0\bar{p}K^+}$	$0.0^{+1.2}_{-0.0} \times 10^{-5}$
$N_{11,\pi,\text{LL}}^{\text{Bkg}}$	$16.1^{+4.9}_{-4.2}$
$N_{12,\pi,\text{LL}}^{\text{Bkg}}$	$162.4^{+14.1}_{-13.4}$
$N_{11,\pi,\text{DD}}^{\text{Bkg}}$	$85.7^{+12.0}_{-11.3}$
$N_{12,\pi,\text{DD}}^{\text{Bkg}}$	$457.2^{+25.0}_{-24.4}$
$N_{11,K,\text{LL}}^{\text{Bkg}}$	$12.1^{+4.0}_{-3.3}$
$N_{12,K,\text{LL}}^{\text{Bkg}}$	$6.7^{+8.7}_{-8.0}$
$N_{11,K,\text{DD}}^{\text{Bkg}}$	$39.6^{+7.3}_{-6.5}$
$N_{12,K,\text{DD}}^{\text{Bkg}}$	$179.0^{+14.5}_{-13.8}$

Table H.12: Shape parameters for the  $\mathcal{A}_T$  fit for the  $\bar{B}^0 \rightarrow \Lambda\bar{p}\pi^+$  and  $\mathcal{O} < 0$  sample.

Floating parameter	Fit value and uncertainties
$\Delta m$	$4.18^{+0.80}_{-0.80}$
$a_{11,\pi,\text{LL}}^{\text{Bkg}}$	$-12.2^{+8.8}_{-9.1} \times 10^{-4}$
$a_{12,\pi,\text{LL}}^{\text{Bkg}}$	$-10.8^{+3.6}_{-3.6} \times 10^{-4}$
$a_{11,\pi,\text{DD}}^{\text{Bkg}}$	$-5.6^{+4.3}_{-4.3} \times 10^{-4}$
$a_{12,\pi,\text{DD}}^{\text{Bkg}}$	$-6.6^{+2.0}_{-2.0} \times 10^{-4}$
$a_{11,K,\text{LL}}^{\text{Bkg}}$	$-1.9^{+2.5}_{-2.5} \times 10^{-4}$
$a_{12,K,\text{LL}}^{\text{Bkg}}$	$-6.8^{+3.4}_{-3.4} \times 10^{-4}$
$a_{11,K,\text{DD}}^{\text{Bkg}}$	$-10.1^{+4.0}_{-4.0} \times 10^{-4}$
$a_{12,K,\text{DD}}^{\text{Bkg}}$	$-3.8^{+2.0}_{-2.0} \times 10^{-4}$

Table H.13: Shape parameters for the  $\mathcal{A}_T$  fit for the  $\bar{B}^0 \rightarrow \bar{\Lambda} p \pi^+$  and  $\mathcal{O} > 0$  sample.

Floating parameter	Fit value and uncertainties
$a_{11,\pi,LL}^{\text{Bkg}}$	$-19.0^{+9.2}_{-9.8} \times 10^{-4}$
$a_{12,\pi,LL}^{\text{Bkg}}$	$-13.1^{+3.8}_{-3.8} \times 10^{-4}$
$a_{11,\pi,DD}^{\text{Bkg}}$	$-5.0^{+4.2}_{-4.} \times 10^{-4}$
$a_{12,\pi,DD}^{\text{Bkg}}$	$-5.7^{+1.9}_{-1.9} \times 10^{-4}$
$a_{11,K,LL}^{\text{Bkg}}$	$-2.3^{+2.1}_{-2.1} \times 10^{-4}$
$a_{12,K,LL}^{\text{Bkg}}$	$-7.3^{+4.0}_{-4.0} \times 10^{-4}$
$a_{11,K,DD}^{\text{Bkg}}$	$-9.6^{+3.5}_{-3.5} \times 10^{-4}$
$a_{12,K,DD}^{\text{Bkg}}$	$-3.3^{+1.8}_{-1.8} \times 10^{-4}$

Table H.14: Shape parameters for the  $\mathcal{A}_T$  fit for the  $B^0 \rightarrow \bar{\Lambda} p \pi^-$  and  $\mathcal{O} < 0$  sample.

Floating parameter	Fit value and uncertainties
$a_{11,\pi,LL}^{\text{Bkg}}$	$-23.6^{+10.0}_{-10.2} \times 10^{-4}$
$a_{12,\pi,LL}^{\text{Bkg}}$	$-7.1^{+3.6}_{-3.7} \times 10^{-4}$
$a_{11,\pi,DD}^{\text{Bkg}}$	$-11.0^{+4.1}_{-4.1} \times 10^{-4}$
$a_{12,\pi,DD}^{\text{Bkg}}$	$-8.0^{+2.0}_{-2.0} \times 10^{-4}$
$a_{11,K,LL}^{\text{Bkg}}$	$-3.1^{+2.8}_{-2.8} \times 10^{-4}$
$a_{12,K,LL}^{\text{Bkg}}$	$-5.5^{+3.1}_{-3.1} \times 10^{-4}$
$a_{11,K,DD}^{\text{Bkg}}$	$-7.4^{+2.8}_{-2.8} \times 10^{-4}$
$a_{12,K,DD}^{\text{Bkg}}$	$-3.6^{+2.1}_{-2.1} \times 10^{-4}$

Table H.15: Shape parameters for the  $\mathcal{A}_T$  fit for the  $B^0 \rightarrow \bar{\Lambda} p \pi^-$  and  $\mathcal{O} > 0$  sample.

Floating parameter	Fit value and uncertainties
$a_{11,\pi,LL}^{\text{Bkg}}$	$-21.8^{+10.0}_{-10.4} \times 10^{-4}$
$a_{12,\pi,LL}^{\text{Bkg}}$	$-8.9^{+3.4}_{-3.5} \times 10^{-4}$
$a_{11,\pi,DD}^{\text{Bkg}}$	$-10.2^{+4.7}_{-4.7} \times 10^{-4}$
$a_{12,\pi,DD}^{\text{Bkg}}$	$-4.5^{+2.0}_{-2.0} \times 10^{-4}$
$a_{11,K,LL}^{\text{Bkg}}$	$-2.0^{+1.5}_{-1.5} \times 10^{-4}$
$a_{12,K,LL}^{\text{Bkg}}$	$-4.3^{+2.4}_{-2.4} \times 10^{-4}$
$a_{11,K,DD}^{\text{Bkg}}$	$-5.6^{+2.3}_{-2.3} \times 10^{-4}$
$a_{12,K,DD}^{\text{Bkg}}$	$-3.0^{+1.8}_{-1.8} \times 10^{-4}$



Table H.16: Efficiency related parameters for the  $\mathcal{A}_T$  fit. Except  $r_{11}^{\text{DD}}$  and  $r_{12}^{\text{DD}}$  all determined through Gaussian constraints.

Floating parameter	Fit value and uncertainties
$r_{11}^{\text{DD}}$	$1.44^{+0.42}_{-0.32}$
$r_{12}^{\text{DD}}$	$0.84^{+0.19}_{-0.15}$
$r_{\text{LL/DD},11}^{\text{MC}}$	$0.317^{+0.004}_{-0.005}$
$r_{\text{LL/DD},12}^{\text{MC}}$	$0.2801^{+0.0020}_{-0.0013}$
$\delta_{\text{LL},11}^{\bar{B}_s^0 \rightarrow \Lambda \bar{p} K^+}$	$1.15^{+0.07}_{-0.07}$
$\delta_{\text{LL},12}^{\bar{B}_s^0 \rightarrow \Lambda \bar{p} K^+}$	$1.31^{+0.05}_{-0.05}$
$\delta_{\text{DD},11}^{\bar{B}_s^0 \rightarrow \Lambda \bar{p} K^+}$	$1.10^{+0.04}_{-0.04}$
$\delta_{\text{DD},12}^{\bar{B}_s^0 \rightarrow \Lambda \bar{p} K^+}$	$1.129^{+0.026}_{-0.026}$
$\delta_{\text{LL},11}^{\bar{B}^0 \rightarrow \Sigma^0 \bar{p} \pi^+}$	$2114^{+170}_{-170}$
$\delta_{\text{LL},12}^{\bar{B}^0 \rightarrow \Sigma^0 \bar{p} \pi^+}$	$3693^{+201}_{-201}$
$\delta_{\text{DD},11}^{\bar{B}^0 \rightarrow \Sigma^0 \bar{p} \pi^+}$	$1906^{+86}_{-86}$
$\delta_{\text{DD},12}^{\bar{B}^0 \rightarrow \Sigma^0 \bar{p} \pi^+}$	$3589^{+98}_{-98}$
$\delta_{\text{LL},11}^{\bar{B}_s^0 \rightarrow \Sigma^0 \bar{p} K^+}$	$4962^{+321}_{-321}$
$\delta_{\text{LL},12}^{\bar{B}_s^0 \rightarrow \Sigma^0 \bar{p} K^+}$	$11219^{+444}_{-444}$
$\delta_{\text{DD},11}^{\bar{B}_s^0 \rightarrow \Sigma^0 \bar{p} K^+}$	$4535^{+163}_{-163}$
$\delta_{\text{DD},12}^{\bar{B}_s^0 \rightarrow \Sigma^0 \bar{p} K^+}$	$9639^{+210}_{-210}$

# Bibliography

- [1] C. Q. Geng and Y. K. Hsiao, “T violation in baryonic B decays,” *Int. J. Mod. Phys. A* **21** (2006) 897–900, arXiv:hep-ph/0509235 [hep-ph].
- [2] C. Q. Geng and Y. K. Hsiao, “Direct CP and T Violation in Baryonic B Decays,” *Int. J. Mod. Phys. A* **23** (2008) 3290–3295, arXiv:0801.0022 [hep-ph].
- [3] J. H. Christenson, J. W. Cronin, V. L. Fitch, and R. Turlay, “Evidence for the 2 pi Decay of the k(2)0 Meson,” *Phys. Rev. Lett.* **13** (1964) 138–140.
- [4] **CPLEAR** Collaboration, A. Angelopoulos *et al.*, “First direct observation of time reversal noninvariance in the neutral kaon system,” *Phys. Lett.* **B444** (1998) 43–51.
- [5] **BaBar** Collaboration, J. P. Lees *et al.*, “Observation of Time Reversal Violation in the  $B^0$  Meson System,” *Phys. Rev. Lett.* **109** (2012) 211801, arXiv:1207.5832 [hep-ex].
- [6] C.-N. Yang and R. L. Mills, “Conservation of Isotopic Spin and Isotopic Gauge Invariance,” *Phys. Rev.* **96** (1954) 191–195.
- [7] J. Charles *et al.*, “Ckmfitter group,” *Eur. Phys. J.* **C41** (2005) 1–131.
- [8] S. L. Glashow, J. Iliopoulos, and L. Maiani, “Weak Interactions with Lepton-Hadron Symmetry,” *Phys. Rev.* **D2** (1970) 1285–1292.
- [9] M. A. Shifman, A. Vainshtein, and V. I. Zakharov, “QCD and Resonance Physics. Sum Rules,” *Nucl.Phys.* **B147** (1979) 385–447.
- [10] S. J. Brodsky and G. R. Farrar, “Scaling Laws for Large Momentum Transfer Processes,” *Phys.Rev.* **D11** (1975) 1309.
- [11] R. Omnes, “Regge poles,” *Annual Review of Nuclear Science* **16** (1966) no. 1, 263–290.
- [12] **Particle Data Group** Collaboration, K. Olive *et al.*, “Review of particle physics,” *Chin. Phys.* **C38** (2014) 090001.
- [13] T. Leddig, *Search for the decay  $B^- \rightarrow \Lambda_c^+ \bar{p} \ell^- \bar{\nu}_\ell$  with the BABAR detector*. PhD thesis, Rostock U., 2014. arXiv:1505.04733 [hep-ex].  
<http://inspirehep.net/record/1370690/files/arXiv:1505.04733.pdf>.
- [14] H.-Y. Cheng and K.-C. Yang, “Three-body charmful baryonic B decays  $\bar{B} \rightarrow D^{(*)} N \bar{N}$ ,” *Phys. Rev.* **D66** (2002) 094009, arXiv:hep-ph/0208185.
- [15] J. L. Rosner, “Low-Mass Baryon-Antibaryon Enhancements in B Decays,” *Phys. Rev.* **D68** (2003) 014004, arXiv:hep-ph/0303079.
- [16] C.-H. Chen, H.-Y. Cheng, C. Q. Geng, and Y. K. Hsiao, “Charmful Three-body Baryonic B decays,” *Phys. Rev.* **D78** (2008) 054016, arXiv:0806.1108 [hep-ph].

- [17] Y.-K. Hsiao, “Charmful baryonic  $B \rightarrow B\bar{B}'M_c$  decays,” *Int. J. Mod. Phys.* **A24** (2009) 3638–3644, arXiv:0902.4831 [hep-ph].
- [18] M. K. Gaillard, B. W. Lee, and J. L. Rosner, “Search for Charm,” *Rev. Mod. Phys.* **47** (1975) 277–310.
- [19] J. R. Ellis, M. K. Gaillard, and D. V. Nanopoulos, “On the Weak Decays of High Mass Hadrons,” *Nucl. Phys.* **B100** (1975) 313.
- [20] **LHCb** Collaboration, R. Aaij *et al.*, “Evidence for CP Violation in  $B^+ \rightarrow p\bar{p}K^+$  Decays,” *Phys. Rev. Lett.* **113** (2014) no. 14, 141801, arXiv:1407.5907 [hep-ex].
- [21] **ARGUS** Collaboration, H. Albrecht *et al.*, “Direct Evidence for  $W$  Exchange in Charmed Meson Decay,” *Phys. Lett.* **B158** (1985) 525.
- [22] **Belle** Collaboration, M. Z. Wang *et al.*, “Observation of  $\bar{B}^0 \rightarrow \Lambda\bar{p}\pi^+$ ,” *Phys. Rev. Lett.* **90** (2003) 201802, arXiv:hep-ex/0302024 [hep-ex].
- [23] C.-K. Chua and W.-S. Hou, “Three body baryonic anti-B  $\rightarrow$  Lambda anti-p pi decays and such,” *Eur. Phys. J.* **C29** (2003) 27–35, arXiv:hep-ph/0211240 [hep-ph].
- [24] **Belle** Collaboration, M. Z. Wang *et al.*, “Study of  $B^+ \rightarrow p\bar{\Lambda}\gamma$ ,  $B^+ \rightarrow p\bar{\Lambda}\pi^0$  and  $\bar{B}^0 \rightarrow \Lambda\bar{p}\pi^+$ ,” *Phys. Rev.* **D76** (2007) 052004, arXiv:0704.2672 [hep-ex].
- [25] **BaBar** Collaboration, B. Aubert *et al.*, “Measurement of the Branching Fraction and anti-Lambda Polarization in  $B^0 \rightarrow \Lambda p\pi^-$ ,” *Phys. Rev.* **D79** (2009) 112009, arXiv:0904.4724 [hep-ex].
- [26] M. Martinelli, “CP-violating triple-product asymmetries in Charm decays,” in *8th International Workshop on the CKM Unitarity Triangle (CKM 2014) Vienna, Austria, September 8-12, 2014*. 2014. arXiv:1411.4140 [hep-ex].  
<http://inspirehep.net/record/1328483/files/arXiv:1411.4140.pdf>.
- [27] M. Duraisamy and A. Datta, “The Full  $B \rightarrow D^*\tau^- \bar{\nu}_\tau$  Angular Distribution and CP violating Triple Products,” *JHEP* **09** (2013) 059, arXiv:1302.7031 [hep-ph].
- [28] S. K. Patra and A. Kundu, “CPT violation and triple-product correlations in B decays,” *Phys. Rev.* **D87** (2013) no. 11, 116005, arXiv:1305.1417 [hep-ph].
- [29] R. H. Dalitz, “On the analysis of  $\tau$ -meson data and the nature of the  $\tau$ -meson,” *Phil. Mag.* **44** (1953) 1068–1080.
- [30] **LHCb** Collaboration, R. Aaij *et al.*, “Measurement of  $\sigma(pp \rightarrow b\bar{b}X)$  at  $\sqrt{s} = 7$  TeV in the forward region,” *Phys. Lett.* **B694** (2010) 209–216, arXiv:1009.2731 [hep-ex].
- [31] **LHCb** Collaboration, A. A. Alves, Jr. *et al.*, “The LHCb Detector at the LHC,” *JINST* **3** (2008) S08005.
- [32] **LHCb** Collaboration, R. Aaij *et al.*, “LHCb Detector Performance,” *Int.J.Mod.Phys.* **A30** (2015) no. 07, 1530022, arXiv:1412.6352 [hep-ex].
- [33] **LHCb** Collaboration, “LHCb VELO TDR: Vertex locator. Technical design report,”.
- [34] R. E. Kalman, “A new approach to linear filtering and prediction problems,” *Transactions of the ASME—Journal of Basic Engineering* **82** (1960) no. Series D, 35–45.
- [35] W. D. Hulsbergen, “Decay chain fitting with a Kalman filter,” *Nucl. Instrum. Meth.* **A552** (2005) 566–575, arXiv:physics/0503191 [physics].
- [36] J. Podolanski and R. Armenteros, “iii. analysis of v-events,” *The London, Edinburgh, and Dublin Philosophical Magazine and Journal of Science* **45** (1954) no. 360, 13–30.

- [37] M. Nicholas and S. Ulam, “The monte carlo method,” *Journal of the American Statistical Association* **44** (1949) no. 247, 335–341.
- [38] T. Sjostrand, S. Mrenna, and P. Z. Skands, “A Brief Introduction to PYTHIA 8.1,” *Comput. Phys. Commun.* **178** (2008) 852–867, arXiv:0710.3820 [hep-ph].
- [39] **LHCb** Collaboration, I. Belyaev *et al.*, “Handling of the generation of primary events in Gauss, the LHCb simulation framework,” *J. Phys. Conf. Ser.* **331** (2011) 032047.
- [40] D. J. Lange, “The EvtGen particle decay simulation package,” *Nucl. Instrum. Meth.* **A462** (2001) 152–155.
- [41] P. Golonka and Z. Was, “PHOTOS Monte Carlo: A Precision tool for QED corrections in  $Z$  and  $W$  decays,” *Eur. Phys. J.* **C45** (2006) 97–107, arXiv:hep-ph/0506026 [hep-ph].
- [42] **LHCb** Collaboration, M. Clemencic, G. Corti, S. Easo, C. R. Jones, S. Miglioranza, M. Pappagallo, and P. Robbe, “The LHCb simulation application, Gauss: Design, evolution and experience,” *J. Phys. Conf. Ser.* **331** (2011) 032023.
- [43] **GEANT4** Collaboration, S. Agostinelli *et al.*, “GEANT4: A Simulation toolkit,” *Nucl. Instrum. Meth.* **A506** (2003) 250–303.
- [44] **LHCb** Collaboration, S. B., “Updated average  $f_s/f_d$   $b$ -hadron production fraction ratio for 7 TeV  $pp$  collisions,”.
- [45] **LHCb** Collaboration, R. Aaij *et al.*, “Measurement of  $b$ -hadron production fractions in 7 TeV  $pp$  collisions,” *Phys. Rev.* **D85** (2012) 032008, arXiv:1111.2357 [hep-ex].
- [46] C.-K. Chua, W.-S. Hou, and S.-Y. Tsai, “Charmless three-body baryonic  $B$  decays,” *Phys. Rev.* **D66** (2002) 054004, arXiv:hep-ph/0204185 [hep-ph].
- [47] S. Arunagiri and C. Q. Geng, “ $T$  violating triple product asymmetries  $\Lambda_b^0 \rightarrow \Lambda \pi^+ \pi^-$  in decay,” *Phys. Rev.* **D69** (2004) 017901, arXiv:hep-ph/0307307 [hep-ph].
- [48] D. O’Hanlon *et al.*, “Search for  $\Lambda_b^0(\Xi_b) \rightarrow \Lambda h$ ,” *LHCb Analysis Note ANA-2014-051* (2015) .
- [49] P. Speckmayer, A. Hocker, J. Stelzer, and H. Voss, “The toolkit for multivariate data analysis: Tmva 4,” *J. Phys. Conf. Ser.* **219** (2010) 032057.
- [50] A. Hicheur, I. Bediaga, A. Cavalcante, M. Cruz, C. Gobel, J. Miranda, A. Massafferri, J. Helder, J. Otalora, A. Gomes, I. Nasteva, A. Reis, and F. Rodrigues, “Study of  $B^\pm \rightarrow p\bar{p}h^\pm$  decays with 2011+2012 data,”. <https://cds.cern.ch/record/1665617>.
- [51] A. Hoecker *et al.*, “TMVA 4 - Toolkit for Multivariate Data Analysis with ROOT Users Guide,”. <http://tmva.sourceforge.net/docu/TMVAUsersGuide.pdf>.
- [52] **LHCb** Global Particle ID, “PIDCalib Package,”. <https://twiki.cern.ch/twiki/bin/view/LHCb/PIDCalibPackage>.
- [53] **BaBar** Collaboration, J. P. Lees *et al.*, “Evidence for the baryonic decay  $\bar{B}^0 \rightarrow D^0 \Lambda \bar{\Lambda}$ ,” *Phys. Rev.* **D89** (2014) no. 11, 112002, arXiv:1401.5990 [hep-ex].
- [54] **Belle** Collaboration, H. Ikeda *et al.*, “A detailed test of the CsI(Tl) calorimeter for BELLE with photon beams of energy between 20-MeV and 5.4-GeV,” *Nucl. Instrum. Meth.* **A441** (2000) 401–426.
- [55] J. Gaiser, “Charmonium spectroscopy from radiative decays of the  $J/\psi$  and  $\psi'$ ,”. SLAC-0255.
- [56] **ARGUS** Collaboration, H. Albrecht *et al.*, “Reconstruction of B Mesons,” *Phys. Lett.* **B185** (1987) 218.

- [57] M. Pivk and F. L. Diberder, “: A statistical tool to unfold data distributions,” *Nuclear Instruments and Methods in Physics Research Section A: Accelerators, Spectrometers, Detectors and Associated Equipment* **555** (2005) no. 12, 356 – 369.  
<http://www.sciencedirect.com/science/article/pii/S0168900205018024>.
- [58] **Belle** Collaboration, E. Solovieva *et al.*, “Evidence for  $\bar{B}_s^0 \rightarrow \Lambda_c^+ \bar{\Lambda} \pi^-$ ,” *Phys. Lett.* **B726** (2013) 206–210, [arXiv:1304.6931](https://arxiv.org/abs/1304.6931) [hep-ex].
- [59] **BES** Collaboration, J. Z. Bai *et al.*, “Observation of a near-threshold enhancement in the  $p \bar{p}$  mass spectrum from radiative  $J/\psi \rightarrow \gamma p \bar{p}$  decays,” *Phys. Rev. Lett.* **91** (2003) 022001, [arXiv:hep-ex/0303006](https://arxiv.org/abs/hep-ex/0303006).
- [60] **Belle, BaBar** Collaboration, A. J. Bevan *et al.*, “The Physics of the B Factories,” *Eur. Phys. J.* **C74** (2014) 3026, [arXiv:1406.6311](https://arxiv.org/abs/1406.6311) [hep-ex].
- [61] M. Suzuki, “Lambda hyperon as helicity analyzer of s quark in B decay,” *J. Phys.* **G29** (2003) B15, [arXiv:hep-ph/0208060](https://arxiv.org/abs/hep-ph/0208060) [hep-ph].

# Acknowledgements

I am grateful for the support I received from many different sources throughout the endeavour that resulted in the thesis. First and foremost I'd like to thank Priv.-Doz. Roland Waldi for giving me the opportunity to graduate in his group and trusting me with this yet unexplored topic.

I would particularly like to thank Eduardo Rodrigues for his support during the last one and a half years. His aid in technical and organisational matters was invaluable especially for an LHCb newcomer as myself. Furthermore, I'd like to thank the Warwick LHCb group and especially Rafael Silva Coutinho for providing technical support and for their initial work on the stripping line. I'd like to thank the LHCb collaboration and the BnoC working group in particular for the computing and technical support throughout the years.

Next I'd like to thank my former bachelor and master students, especially Kai-Uwe Goetz, Nis Meinert, Harald Viemann, and Robert Zillmer for the friendly working atmosphere and the opportunity to hand over my experiences. I'd like to thank my former colleagues Dr. Marcus Ebert and Dr. Torsten Leddig for volunteering to provide comments on this thesis.

Finally I'd like to thank my friends and family for the support and keeping in touch with the rest of the world.



# Selbständigkeitserklärung

**Doktorandinnen/Doktoranden-Erklärung gemäß 4 Absatz 1 Buchstaben g und h der Promotionsordnung der Mathematisch-Naturwissenschaftlichen Fakultät der Universität Rostock**

*Name* Voß, Christian

*Anschrift* Aleksis-Kivi Straße 16, 18106 Rostock

Ich habe eine Dissertation zum Thema

*Measurement of the Time Reversal Asymmetry for the Decay  $\bar{B}^0 \rightarrow \Lambda \bar{p} \pi^+$   
and Observation of the Decay  $\bar{B}_s^0 \rightarrow \Lambda \bar{p} K^+$  with the LHCb Experiment*

an der Mathematisch-Naturwissenschaftlichen Fakultät der Universität Rostock angefertigt. Dabei wurde ich von Herrn **Dr. Roland Waldi** betreut.

Ich gebe folgende Erklärung ab:

1. Die Gelegenheit zum vorliegenden Promotionsvorhaben ist mir nicht kommerziell vermittelt worden. Insbesondere habe ich keine Organisation eingeschaltet, die gegen Entgelt Betreuerinnen/Betreuer für die Anfertigung von Dissertationen sucht oder die mir obliegenden Pflichten hinsichtlich der Prüfungsleistungen für mich ganz oder teilweise erledigt.
2. Ich versichere hiermit an Eides statt, dass ich die vorliegende Arbeit selbstständig angefertigt und ohne fremde Hilfe verfasst habe. Dazu habe ich keine außer den von mir angegebenen Hilfsmitteln und Quellen verwendet und die den benutzten Werken inhaltlich und wörtlich entnommenen Stellen habe ich als solche kenntlich gemacht.

Rostock, den 17. Mai 2016